

Top-Down Cracking of Hot-Mix Asphalt Layers: Models for Initiation and Propagation

DETAILS

0 pages | null | PAPERBACK

ISBN 978-0-309-43013-5 | DOI 10.17226/22935

AUTHORS

BUY THIS BOOK

FIND RELATED TITLES

Visit the National Academies Press at NAP.edu and login or register to get:

- Access to free PDF downloads of thousands of scientific reports
- 10% off the price of print titles
- Email or social media notifications of new titles related to your interests
- Special offers and discounts



Distribution, posting, or copying of this PDF is strictly prohibited without written permission of the National Academies Press. (Request Permission) Unless otherwise indicated, all materials in this PDF are copyrighted by the National Academy of Sciences.

ACKNOWLEDGMENT

This work was sponsored by the American Association of State Highway and Transportation Officials (AASHTO), in cooperation with the Federal Highway Administration, and was conducted in the National Cooperative Highway Research Program (NCHRP), which is administered by the Transportation Research Board (TRB) of the National Academies.

COPYRIGHT INFORMATION

Authors herein are responsible for the authenticity of their materials and for obtaining written permissions from publishers or persons who own the copyright to any previously published or copyrighted material used herein.

Cooperative Research Programs (CRP) grants permission to reproduce material in this publication for classroom and not-for-profit purposes. Permission is given with the understanding that none of the material will be used to imply TRB, AASHTO, FAA, FHWA, FMCSA, FTA, Transit Development Corporation, or AOC endorsement of a particular product, method, or practice. It is expected that those reproducing the material in this document for educational and not-for-profit uses will give appropriate acknowledgment of the source of any reprinted or reproduced material. For other uses of the material, request permission from CRP.

DISCLAIMER

The opinions and conclusions expressed or implied in this report are those of the researchers who performed the research. They are not necessarily those of the Transportation Research Board, the National Research Council, or the program sponsors.

The information contained in this document was taken directly from the submission of the author(s). This material has not been edited by TRB.

THE NATIONAL ACADEMIES

Advisers to the Nation on Science, Engineering, and Medicine

The **National Academy of Sciences** is a private, nonprofit, self-perpetuating society of distinguished scholars engaged in scientific and engineering research, dedicated to the furtherance of science and technology and to their use for the general welfare. On the authority of the charter granted to it by the Congress in 1863, the Academy has a mandate that requires it to advise the federal government on scientific and technical matters. Dr. Ralph J. Cicerone is president of the National Academy of Sciences.

The **National Academy of Engineering** was established in 1964, under the charter of the National Academy of Sciences, as a parallel organization of outstanding engineers. It is autonomous in its administration and in the selection of its members, sharing with the National Academy of Sciences the responsibility for advising the federal government. The National Academy of Engineering also sponsors engineering programs aimed at meeting national needs, encourages education and research, and recognizes the superior achievements of engineers. Dr. Charles M. Vest is president of the National Academy of Engineering.

The **Institute of Medicine** was established in 1970 by the National Academy of Sciences to secure the services of eminent members of appropriate professions in the examination of policy matters pertaining to the health of the public. The Institute acts under the responsibility given to the National Academy of Sciences by its congressional charter to be an adviser to the federal government and, on its own initiative, to identify issues of medical care, research, and education. Dr. Harvey V. Fineberg is president of the Institute of Medicine.

The **National Research Council** was organized by the National Academy of Sciences in 1916 to associate the broad community of science and technology with the Academy's purposes of furthering knowledge and advising the federal government. Functioning in accordance with general policies determined by the Academy, the Council has become the principal operating agency of both the National Academy of Sciences and the National Academy of Engineering in providing services to the government, the public, and the scientific and engineering communities. The Council is administered jointly by both the Academies and the Institute of Medicine. Dr. Ralph J. Cicerone and Dr. Charles M. Vest are chair and vice chair, respectively, of the National Research Council.

The **Transportation Research Board** is one of six major divisions of the National Research Council. The mission of the Transportation Research Board is to provide leadership in transportation innovation and progress through research and information exchange, conducted within a setting that is objective, interdisciplinary, and multimodal. The Board's varied activities annually engage about 7,000 engineers, scientists, and other transportation researchers and practitioners from the public and private sectors and academia, all of whom contribute their expertise in the public interest. The program is supported by state transportation departments, federal agencies including the component administrations of the U.S. Department of Transportation, and other organizations and individuals interested in the development of transportation. www.TRB.org

www.national-academies.org

CONTENTS

Acknowledgments.....	iii
Executive Summary	1
1. Background.....	5
1.1 Problem Statement.....	5
1.2 Research Objective	5
1.3 Research Scope.....	6
2. Research Approach	9
3. Findings: The VECD-Based Model.....	12
3.1 Framework.....	12
3.1.1 Inputs Module.....	13
3.1.2 Material Property Sub-models.....	15
3.1.3 Analytical Sub-models	48
3.1.4 Performance Prediction Module.....	59
3.1.5 Output Module.....	69
3.1.6 Model Integration	72
3.2 Example Simulation.....	75
3.2.1 Introduction	75
3.2.2 Simulation Results and Discussion	76
3.3 Model Evaluation: Parametric Study.....	77
3.3.1 Introduction	77
3.3.2 Effect of Region	80
3.3.3 Effect of Structure	81
3.3.4 Effect of Unbound Layer Property	81
3.3.5 Effect of Asphalt Mixture Properties	82
3.4 Summary of Findings	83
4. Findings: The HMA-FM-Based System.....	85
4.1 Framework.....	85
4.1.1 Inputs Module and Indirect Tensile Test.....	86
4.1.2 Material Property Model	89
4.1.3 Pavement Response Model.....	92
4.1.4 Pavement Fracture Model.....	93
4.1.5 Outputs	96
4.1.6 Model Integration	96
4.2 Model Evaluation: Parametric Study.....	99
4.2.1 Effects of Material and Structural Properties	102
4.2.2 Effect of Traffic	110
4.2.3 Effect of Climate	111
4.3 Model Calibration and Validation	113

4.3.1 Summary of Top-down Cracking Performance Model Data	113
4.3.2 Model Calibration.....	123
4.3.3 Validation of Model	127
4.3.4 Final Model Predictions	132
4.4 Summary of Findings	137
5. Conclusions and Recommendations for Future Research	141
5.1 Conclusions.....	141
5.2 Recommendations for Future Research.....	142
References.....	146
Appendix A: Development of the VECD-Based Model.....	A-i
Appendix B: Development of the HMA-FM-Based Model	B-i
Appendix C: Simulation Tools	C-i

ACKNOWLEDGMENTS

The research reported herein was performed under NCHRP Project 1-42A by the Department of Civil and Coastal Engineering at the University of Florida (UF), and the Department of Civil, Construction, and Environmental Engineering at the North Carolina State University (NCSU). UF was the contractor for this study, with NCSU serving as the sub-contractor.

Dr. Reynaldo Roque, P.E., Professor of Civil Engineering at UF, was the Principal Investigator. The other authors of this report were Dr. Y. Richard Kim, Professor of Civil Engineering at NCSU, and Murthy N. Guddati, Associate Professor of Civil Engineering at NCSU; Jian Zou, Research Assistant and Ph.D. Candidate at UF; and Cheolmin Baek, Senganal Thirunavukkarasu, and B. Shane Underwood, Research Assistants and Ph.D. Candidates at NCSU. The work was done under the general supervision of Professor Roque at UF.

EXECUTIVE SUMMARY

It is well recognized that load-related top-down cracking, which initiates at or near the surface of the pavement and propagates downward, commonly occurs in hot mix asphalt (HMA) pavements. This phenomenon has been reported in many parts of the United States, as well as in Europe, Japan, and other countries. This mode of failure, however, cannot be explained by traditional fatigue mechanisms used to explain fatigue cracking that initiates at the bottom of the pavement. Therefore, this project was to identify or develop mechanistic-based models for predicting top-down cracking in HMA layers for use in mechanistic-empirical procedures for design and analysis of new and rehabilitated flexible pavements.

For years, many researchers have tried to identify key factors and fundamental mechanisms that may lead to top-down cracking initiation and propagation. From these efforts, it appeared that at least two major mechanisms would need to be considered to predict top-down cracking initiation. One mechanism is related to the bending-induced surface tension away from the tire (i.e., bending mechanism), which governs crack initiation in HMA layers of thin to medium thickness. The other is associated with the shear-induced near-surface tension at the tire edge (i.e., near-tire mechanism), which explains crack initiation in thicker HMA layers. The damage induced by either of the two major mechanisms becomes more critical as aging progresses. Also, top-down cracking initiation can be influenced by thermal stresses and the presence of damage zones. After crack initiation, the presence of cracks and the associated redistribution and intensification of stresses, particularly in the presence of stiffness gradients, plays a potentially critical role during crack propagation in the HMA layers.

In this project, two models were identified and selected for integration into a unified predictive system because of their unique features and capabilities to address the dominant mechanisms associated with top-down cracking. The two models were as follows:

- a viscoelastic continuum damage (VECD) model to predict crack initiation by modeling damage zones and their effect on response prior to cracking (i.e., damage zone effects), and
- an HMA fracture mechanics (HMA-FM) model to predict crack propagation by modeling the presence of macro cracks and their effect on response (i.e., macro crack effects).

However, the existing model components required significant further development before being suitable for integration and development of a top-down cracking performance prediction model for the Mechanistic-Empirical Pavement Design Guide (MEPDG). Therefore, the research focused on (1) finalizing and verifying the reasonableness of the two model components, and (2) developing for and integrating with the HMA-FM-based crack propagation model a simplified fracture energy-based crack initiation model.

Consequently, two enhanced models—a VECD-based crack initiation model and a HMA-FM-based crack growth model—were developed to serve as the major components of the targeted system. The primary role of the VECD-based model is to account for damage zone effects prior to cracking and to identify the time and location of crack initiation. Several important material property sub-models, including aging, healing, failure criteria, viscoplasticity, and thermal stress models, were developed, modified, and/or investigated, and then incorporated into the existing VECD model. These material sub-models were then converted into and/or combined with the structural sub-models. The integrated sub-model was implemented into the

VECD-FEP++ (which is a product of incorporating the VECD model into an in-house stand-alone finite element code FEP++), and an extrapolation method was developed for predicting top-down cracking initiation in HMA pavements. A parametric study was undertaken and showed that the VECD-based model provides reasonable predictions and trends for crack initiation.

The primary role of the HMA-FM-based model is to account for macro crack effects during crack propagation and to predict the propagation of cracks over time. This model has the following key elements:

- a critical condition concept that can accurately capture field observations and significantly reduce the computation time required for long-term pavement performance prediction;
- material property sub-models that account for changes in near-surface mixture properties with aging, including increase in stiffness (stiffening), reduction in fracture energy (embrittlement), and reduction in healing potential, which together make pavements more susceptible to top-down cracking over time.
- a thermal response model that predicts transverse thermal stresses, which can be an important factor in the top-down cracking mechanism; and
- a pavement fracture model that predicts crack growth over time, accounting for the effect of changes in geometry on stress distributions.

In addition, a simplified fracture energy-based approach for predicting crack initiation (i.e., a crack initiation model that does not consider damage zone effects) was developed and integrated with the HMA-FM-based model to demonstrate the capabilities of a completed system. A systematic parametric study showed that the integrated performance model provided

reasonable predictions and expected trends for both crack initiation and propagation. A limited calibration/validation using data from field sections indicated that the performance model reasonably represents and accounts for the most significant factors that influence top-down cracking. However, this performance model is not ready or intended for immediate implementation in the MEPDG because (1) the model should capture damage zone effects, for which the VECD-based model is needed, and (2) further verification of sub-models is needed.

In summary, the work performed clearly indicates that the VECD-based model and the HMA-FM-based model developed and evaluated in this project can form the basis for a top-down cracking model suitable for use in the MEPDG. Furthermore, the component models can form the basis for an improved performance model to predict multiple cracking distresses simultaneously, including top-down cracking, bottom-up cracking, and thermal cracking. The project also identified and recommended research efforts to develop calibrated/validated top-down cracking performance models for use in the MEPDG.

1. BACKGROUND

1.1 Problem Statement

It is now well accepted that top-down cracking (i.e., cracking that initiates at or near the surface of the pavement and propagates downward) commonly occurs in hot-mix asphalt (HMA) pavements. The phenomenon has been reported in many parts of the United States (1, 2, 3), as well as in Europe (4, 5), Japan (6), and other countries (7). This mode of failure cannot be explained by traditional fatigue mechanisms used to explain load-associated fatigue cracking that initiates at the bottom of the HMA layer. The lack of an appropriately verified description (i.e., model) of the mechanisms that lead to this type of cracking makes it difficult to consider this form of distress in the design process.

Several researchers have developed hypotheses regarding the mechanisms of top-down cracking (8). Some researchers have also proposed experimental methods that may provide the properties necessary to evaluate the susceptibility of HMA mixtures to this type of distress (9, 10). In addition, researchers have performed analytical work that has led to the development of preliminary models that offer the potential to predict the initiation and propagation of top-down cracks (8, 11, 12). However, only limited research has been performed to evaluate and validate these hypotheses, test methods, and models. Research was needed to further evaluate the causes of top-down fatigue cracking and to develop effective laboratory testing systems and models to account for it in design and allow for selection of HMA mixtures and pavement structures that are resistant to top-down fatigue cracking for the expected loading and environmental conditions.

1.2 Research Objective

The research focused on:

- 1) Finalizing the two primary model components (i.e., a viscoelastic continuum damage (VECD) model for crack initiation and an HMA fracture mechanics (HMA-FM) model for crack propagation), involving development and integration of sub-models that are relevant to dominant top-down cracking mechanisms into each model component;
- 2) Verifying the reasonableness of the two enhanced primary model components (i.e., the VECD-based model and the HMA-FM-based model); and
- 3) Developing for and integrating with the HMA-FM-based crack propagation model a simplified fracture energy-based crack initiation model to illustrate the potential of a completed system and to help formulate a plan for integrating, calibrating, and validating the two enhanced primary model components.

1.3 Research Scope

For years, many researchers have tried to identify key factors and fundamental mechanisms that may lead to top-down cracking initiation and propagation. From these efforts, it appeared that at least two major mechanisms would need to be considered to predict top-down cracking initiation. One mechanism is related to the bending-induced surface tension away from the tire (i.e., bending mechanism), which governs crack initiation in HMA layers of thin to medium thickness. The other mechanism is associated with the shear-induced near-surface tension at the tire edge (i.e., near-tire mechanism), which explains crack initiation in thicker HMA layers. The damage induced by either mechanism becomes more critical as aging progresses. Also, top-down cracking initiation can be influenced by thermal stresses and the presence of damage zones. After crack initiation, the presence of cracks and the associated redistribution and intensification of stresses, particularly in the presence of stiffness gradients, plays a potentially critical role during crack propagation in the HMA layers.

In this project, two models were identified and selected for further development (to form the basis of a comprehensive predictive system) because of their unique features and capabilities to address the dominant mechanisms associated with top-down cracking. The two models are as follows:

A viscoelastic continuum damage (VECD) model to predict crack initiation by modeling damage zones and their effect on response prior to cracking (i.e., damage zone effects). The capability of the VECD model to predict the performance of the pavement structure has been validated using different pavement structures. One example uses the FHWA Accelerated Load Facility (FHWA ALF) pavements and another example is the Korea Express Highway (KEC) test road in South Korea (13).

An HMA fracture mechanics (HMA-FM) model to predict crack propagation by modeling the presence of macro cracks and their effect on response (i.e., macro crack effects). The capability of the HMA-FM model to identify cracked from uncracked sections has been validated by using 27 field test sections selected throughout the state of Florida for evaluation of top-down cracking (14).

Because several factors (e.g., aging, healing, and thermal stress) and material property models (e.g., fracture energy, creep compliance rate, and characteristic damage curve) which are relevant to the dominant top-down cracking mechanisms were not addressed by the existing component models, sub-models that properly address these critical factors were developed and incorporated into each of these two models.

The primary role of the VECD-based model is to account for damage zone effects prior to cracking and to identify the time and location of crack initiation. A parametric study was undertaken to show how reasonable are the VECD-based model predictions and trends for crack initiation. The primary role of the HMA-FM-based model is to account for macro crack effects during crack propagation and to predict the propagation of cracks over time. To demonstrate the capabilities of a completed system, a simplified fracture energy-based crack initiation model (that does not consider damage zone effects) was developed and integrated with the HMA-FM-based model. A parametric study was carried out to show how reasonable are the integrated

performance model predictions for both crack initiation and propagation. A limited calibration/validation using data from field sections in Florida and Minnesota was conducted to demonstrate how reasonably the performance model represents and accounts for the most significant factors that influence top-down cracking. A broader calibration/validation is necessary after the VECD-based model is integrated with the HMA-FM-based model.

2. RESEARCH APPROACH

The research approach for this project consisted of the following five phases.

1. Determination of key elements that must be part of the top-down cracking predictive system.

These elements included two primary model components:

- A micro-damage effects model that predicts the damage induced in the HMA layer, the resulting reduction in modulus associated with the damage, and the change in stress-strain-energy response resulting from the modulus reduction. As discussed earlier, the VECD model was selected because of its ability to model damage zones and their effect on response prior to cracking. The capability of the VECD model to predict the performance of the pavement structure has been validated using different pavement structures (e.g., FHWA ALF pavements and the KEC test road in South Korea).
- A crack effects model that predicts the effect of cracks (which are regarded as discontinuities that reduce the effective cross-section of the pavement layer) on the stress, strain, and energy redistribution within the layer. The HMA-FM model was selected because of its ability to model the presence of macro cracks and their effect on response during crack propagation. The capability of the HMA-FM model to identify cracked from uncracked sections has been validated by using 27 field test sections selected throughout the state of Florida for evaluation of top-down cracking.

2. Identification and/or development of sub-models. Because the existing VECD and HMA-FM models did not account for several key factors and material property sub-models relevant to top-down cracking mechanisms, there was a need to identify and/or develop appropriate sub-models, as follows:

- Material property sub-models, including aging, healing, failure criteria, and thermal stress models for incorporation into the existing VECD model.
- Material property sub-models that account for changes in mixture properties (e.g., fracture energy, creep rate, and healing) with aging, and a thermal response model that predicts transverse thermal stresses for incorporation into the existing HMA-FM model.

3. Integration of sub-models into primary model components. The sub-models developed in Phase 2 were integrated into each of the existing models to form two enhanced primary model

components (i.e., a VECD-based crack initiation model and an HMA-FM-based crack propagation model) to form the basis of the targeted system. In addition, a simplified fracture energy-based crack initiation model was developed for and integrated with the HMA-FM-based model to demonstrate the capabilities of a completed system. This phase included the following:

- Integration of sub-models into the VECD model, including a sensitivity study to investigate the effect of each sub-model on pavement performance and two example simulations to demonstrate the full capabilities of the VECD-based crack initiation model;
- Integration of sub-models into the simplified fracture energy-based crack initiation model and into the HMA-FM model to form two core modules (i.e., the crack initiation simulation (CIS) and crack growth simulation (CGS) modules) based on a critical condition concept; and
- Integration of the CIS module with the CGS module (which resulted in a simplified HMA-FM-based performance model), including a sensitivity study to investigate the effects of sub-models (i.e., aging, healing, and thermal effects) on pavement performance.

4. Evaluation of the VECD-based and HMA-FM-based models. This evaluation included the following:

- Evaluation of the VECD-based model in a systematic parametric study to determine the reasonableness of the enhanced model.
- Evaluation of the simplified performance model (i.e., the product of integrating the simplified crack initiation model with the HMA-FM-based crack growth model) in a parametric study to show how reasonable are the model predictions for both crack initiation and propagation.

5. Calibration and validation of the simplified performance model. The simplified performance model was calibrated and validated using data from field sections to evaluate the accuracy of top-down cracking performance predictions in HMA layers using rheological and fracture properties of HMA mixtures. For most of the sections included in the calibration/validation studies, properties were available from tests performed in previous investigations (14). For test

sections for which properties were not available, Superpave IDT tests were performed on specimens obtained from field cores.

3.

FINDINGS: THE VECD-BASED MODEL

The primary feature of the VECD-based crack initiation model was to account for effects of damage zones on response prior to cracking. For this reason, several important material property sub-models, including aging, healing, failure criteria, viscoplasticity, and thermal stress models, were developed, modified, and/or investigated, and then incorporated into the existing VECD model. These material sub-models were then converted into and/or combined with the structural sub-models. The integrated model was implemented into the VECD-FEP++, and an extrapolation method was developed for predicting top-down cracking initiation in HMA pavements.

3.1 Framework

The overall framework guiding the VECD-FEP++ analysis is shown in Figure 3-1. The analysis is divided into five sub-modules: the input module, the material properties sub-models, the analytical sub-models, the performance prediction module, and the output module. These modules provide an analytical/computational method for identifying the location and time of crack initiation in the pavement structure. Each sub-model requires specific parameters to be obtained and/or determined. Table 3-1 summarizes the inputs for the VECD-based model along with the quantity of interest and test method for each input (a detailed description of the laboratory specimen fabrication and test method is given in Appendix A).

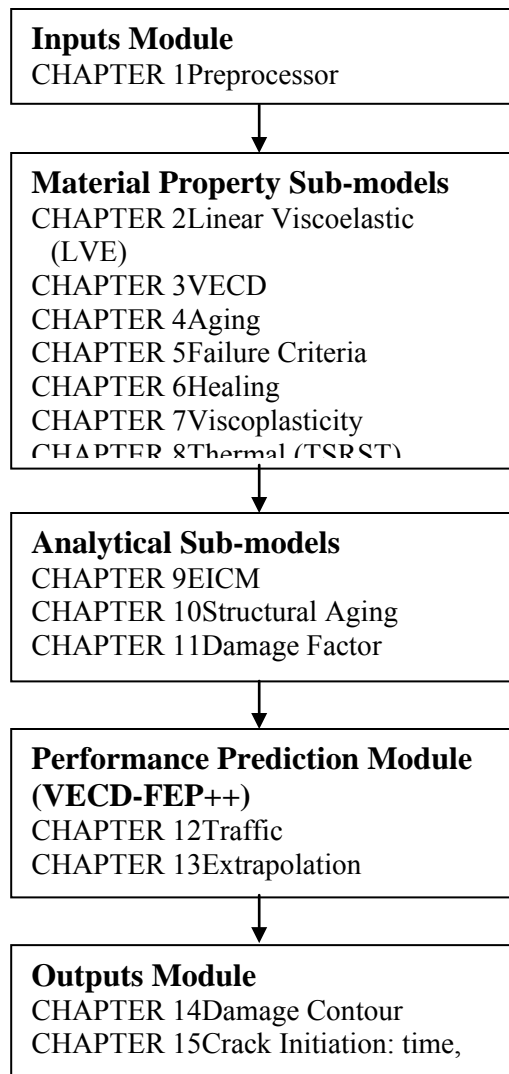


Figure 3-1. VECD-based model framework

3.1.1 Inputs Module

Preprocessors have been developed to facilitate easy and rapid analysis of pavement systems using the FEP++. Specifically, the preprocessor helps in the rapid development of input models for analysis and also helps in making consistent changes for repeated analysis. This tool is ANSI-compliant and developed with portable libraries, thus making it easy to transfer to other platforms.

Table 3-1. Inputs Required for the VECD-based Model

Input	Quantity of Interest	Test Method
LVE	Material coefficients (E_s, E_i, ρ_i)	Temperature/frequency sweep test
VECD	Material coefficients (a, b)	Monotonic direct tension test at 5°C, Constant crosshead cyclic test at 19°C
Aging	LVE and VECD with time	Same as above and long-term oven aging
Failure Criteria	Critical pseudo stiffness	Constant crosshead cyclic test
Healing	Change in pseudo stiffness with rest duration	Random loading and healing period cyclic tests
Viscoplasticity	Material coefficients (p, q, Y)	Monotonic direct tension test at 40°C
Thermal	Thermal expansion coefficient	Thermal expansion test, or from literature
EICM	Temperature distribution within a pavement structure	--
Structural Aging	Effective age of pavement materials with depth	Binder viscosity or $ G^* $ (A and VTS)
Damage Factor	Viscoplastic sensitivity	--
Traffic	Number of Equivalent Single Axle Loads (ESAL count)	--
Extrapolation	Number of analysis segments	--

The preprocessor provides

- Graphical forms for user input;
- Pavement loading with support for multiple moving loads—
 - a. Material data with support for elastic, viscoelastic, and viscoelastic continuum damage (VECD) models, and
 - b. Analysis parameters and finite element (FE) mesh customization;
- Pavement temperature profiles generated from the EICM;
- Data validation and consistency checks;
- Visualization of the finite element model (FEM), consisting of
 - a. A graphical view of the model and mesh;
 - b. Standard graphical operations, such as zoom, pan, rotate, etc.; and
 - c. Mesh information, such as node and cell numbers;
- Data persistence using a database for storing and retrieving input data; and
- One-click installer and user documentation.

3.1.2 Material Property Sub-models

A brief review of the concepts of the LVE model and the VECD model and their most important formulations are given in Appendixes A.1.2.1 and A.1.2.2, respectively; a review of both the viscoplastic and thermal stress models is given in Appendix A.1.2.5 and A.1.2.6. However, because the aging, healing, and failure criteria sub-models were developed in this project, the details of each are given below.

3.1.2.1 Aging model

The effect of aging in asphalt binders on the performance of asphalt aggregate mixtures is well recognized. Traditionally, the effects of binder aging on mixture performance have been investigated using two approaches. The first is to subject different asphalt binders to various aging conditions and measure the resultant changes in physical properties to assess the aging potential of the different binders. However, this approach does not account for the effect of aggregate particles and does not yield accurate and realistic information about the performance of the mixtures. The other approach is to subject the asphalt aggregate mixtures to various aging conditions and then measure the physical properties of the aged mixtures. Although this method is more realistic because the aging process is conducted directly on the mixtures, little work has been done to determine the best method for incorporating these changes in mixture properties due to aging into the framework of constitutive modeling or fatigue performance modeling (15).

The original VECD uniaxial constitutive model is based on the assumption that the material is a non-aging system. This study focuses on establishing an analytical/experimental methodology for incorporating the effects of aging in the current constitutive model.

3.1.2.1.1 Aging method for laboratory mixtures

NCHRP Project 9-23 has found that the Strategic Highway Research Program (SHRP) protocol is not sufficient to simulate field-aging behavior in the laboratory because of its inability

to account for variables such as field-aging conditions and mix properties (16). Nevertheless, the SHRP method

1. Is simple to implement;
2. Provides a general relationship between laboratory and field-aging behavior; and
3. Has been used successfully for previous studies conducted at NCSU (15).

In addition, because this part of the study focuses on developing a place-holder relationship for the aging effects in the current VECD model rather than on matching the laboratory aging to that of the field, it was decided to use the SHRP aging method in this study. Four levels of asphalt mixture aging were simulated, as follows (17):

- (1) Short-term aging (STA): The loose, uncompacted mixture is conditioned at 135°C for 4 hours and then compacted. Specimens are cored and cut for testing.
- (2) Long-term aging, Level 1 (LTA1): The aging procedure is the same as for STA, except the specimens are conditioned at 85°C for 2 days before testing after coring and cutting.
- (3) Long-term aging, Level 2 (LTA2): The aging procedure is the same as for STA, except the specimens are conditioned at 85°C for 4 days before testing after coring and cutting.
- (4) Long-term aging, Level 3 (LTA3): The aging procedure is the same as for STA, except the specimens are conditioned at 85°C for 8 days before testing after coring and cutting.

These aging processes for asphalt mixtures follow the AASHTO R30 specification (18), with the exception that three different long-term aging times are used. To minimize slump in the specimens during the oven aging procedure, the method suggested by the NCHRP 9-23 project, whereby the specimens are wrapped in wire mesh that is held in place by three steel clamps, was adopted. Diameter, height, weight, and air void percentage of all specimens were measured before and after oven aging. The differences in the dimensions were negligible; the dry weights were reduced by 0 to 0.5 g, and the air voids (%) increased by 0 to 0.5%, depending on the level of aging. The maximum specific gravity (G_{mm}) value may also change with aging; however, a

single G_{mm} value for the STA mixture was used for all the aged specimens. Therefore, it was concluded that no apparent damage occurred due to aging.

3.1.2.1.2 Materials and specimen preparation for laboratory testing

Two different mixtures were used for the aging study: A mix and AL mix. The A mix, one of the most common mixture types used in North Carolina, uses granite aggregate that was obtained from the Martin-Marietta quarry in Garner, NC. The aggregate structure is a fine 9.5 mm nominal maximum aggregate size (NMAS) mixture composed of 36% #78M stone, 25% dry screenings, 38% washed screenings, and 1% baghouse fines. The blended gradation is shown in Figure 3-2. An unmodified asphalt binder (PG 64-22) from Citgo in Wilmington, NC, was also used for this study. The asphalt content for the A mix is 5.7% by weight of the total mix.

After a series of laboratory tests, it was determined that this mix was insensitive to aging and thus did not meet the study goals. A weak trend was found between the VECD characterization parameters and the aging times. As a result, the AL mix was used because it was known to be prone to aging.

The AL mix consisted of AAD-1 asphalt binder and local limestone aggregate. The binder (PG 58-28) was obtained from the Materials Reference Library (MRL), and the local limestone aggregate was obtained from the Martin-Marietta Castle Hayne quarry. The aggregate structure is a fine 9.5 mm Superpave mixture composed of 50% # 78M stone, 33% 2S-sand, 14.5% dry screenings, and 2.5% baghouse fines. The blended gradation is shown in Figure 3-2. A Superpave mix design procedure was performed, and an optimal asphalt content of 6.2 % by weight of total mix was chosen. The mixing and compaction temperatures used for the study were 147°C and 135°C, respectively.

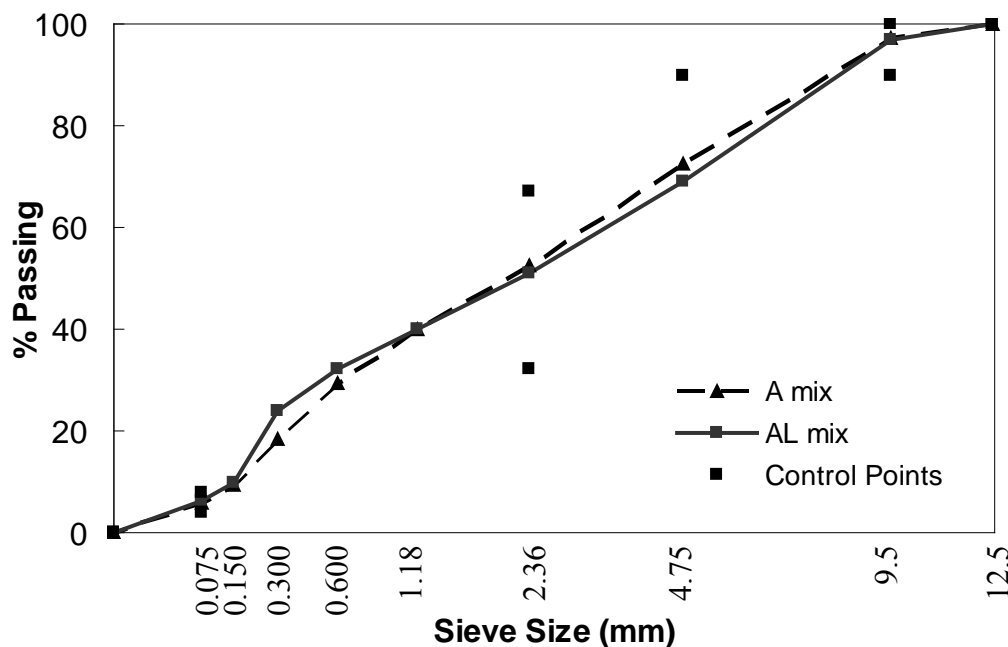


Figure 3-2. Mixture gradation

3.1.2.1.3 VECD characterization of aged mixtures

The A mix

The material characteristics of primary importance in VECD modeling are the LVE and damage characteristics. Figure 3-3 (a) and (b) present the replicate averaged dynamic modulus (E^*) master curves for four different aging levels of the A mix in both semi-log and log-log scales. In general, the stiffness increases with aging time, but the increases are small. This finding suggests that the short-time aging kinetics are more active than the long-time aging kinetics. Figure 3-3 also shows that the STA mixture exhibits similar stiffness characteristics at higher reduced frequencies (physically representing cooler temperatures and/or faster loading frequencies) than the LTA mixtures, but deviates from the LTA mixtures at approximately 1 Hz. Below this reduced frequency, the STA mixture shows lower modulus values than the LTA mixtures. Such a trend is expected because as temperature increases or frequency reduces the modulus gradient between the asphalt binder and aggregate particles becomes larger. As a result,

the effect of the asphalt binder properties on the total mixture behavior may become more noticeable. Similar trends can also be seen in the phase angle master curve graph, shown in Figure 3-3 (c); the three LTA mixtures exhibit similar phase angle values for all frequencies, but the STA mixture shows a different phase angle in the lower frequency range.

With regard to the damage characteristics, Figure 3-3 (d) indicates that the LTA3 mixture exhibits the most favorable damage characteristic curve, followed by the LTA2 and LTA1 mixtures and, finally, by the STA mixture. The differences among the aged mixtures are not significant and cannot be used directly to assess fatigue performance because the curves shown Figure 3-3 (d) do not account for stiffness effects, boundary conditions, or failure characteristics. The importance of these characteristics, as well as a method to account for them, is explained in the next section.

The AL mix

Figure 3-4 presents the averaged dynamic modulus mastercurves for the four different levels of aging of the AL mix in both semi-log and log-log scales. Compared to the A mix, the effect of aging on the dynamic modulus mastercurves is more significant over all of the frequency ranges. Moreover, a clearer trend with regard to aging time is observed with the AL mix when compared to the A mix. A similar trend can be seen in the phase angle mastercurves graph, shown in Figure 3-5.

To evaluate the statistical differences among the mastercurves for the various aging levels, all replicates results have been analyzed by the step-down bootstrap method (details of the analysis and results are presented in Appendix A.1.2.4). The results reveal that test data for the four aging levels are overall statistically different, except under the most extreme reduced frequencies.

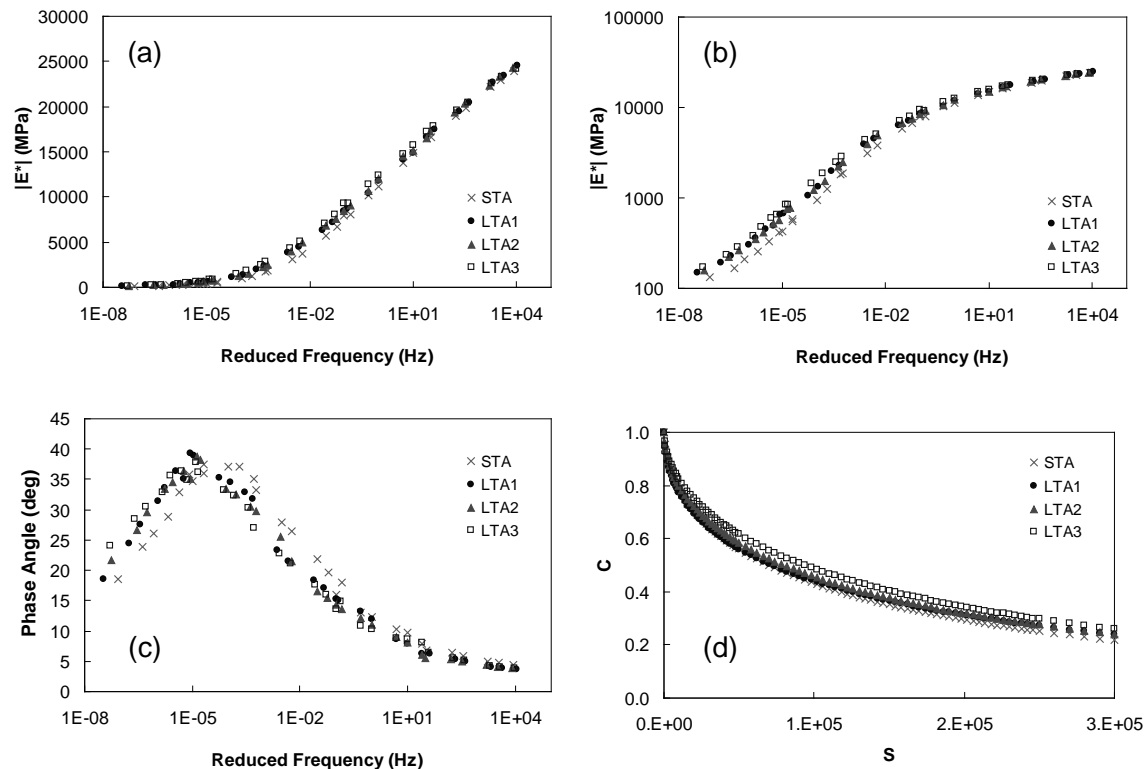


Figure 3-3. VECD characterization summary of the A mix: (a) dynamic modulus mastercurves in semi-log space, (b) dynamic modulus mastercurves in log-log space, (c) phase angle mastercurves, and (d) damage characteristic curves

With regard to the damage characteristics, the trend is the same as for the A mix where the damage characteristic curve for the LTA3 mixture is positioned the highest of all, followed by the LTA2 and LTA1 mixtures and, finally, by the STA mixture, as shown in Figure 3-6. However, the differences among the aged mixtures are more significant than those of the A mix.

Care should be taken in concluding from these observations that aging affects the mixture properties relative to performance. The aging effects must be quantified by considering both resistance to deformation (stiffness) and resistance to damage. Hence, the aging effects on pavement performance will be discussed in the next section along with the results of the FEP++ simulations.

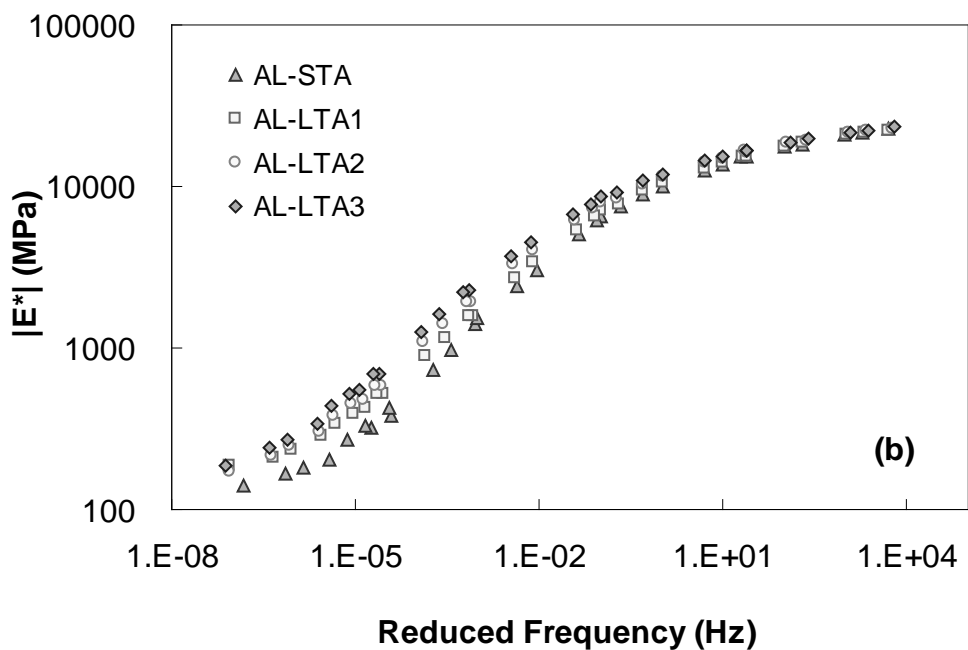
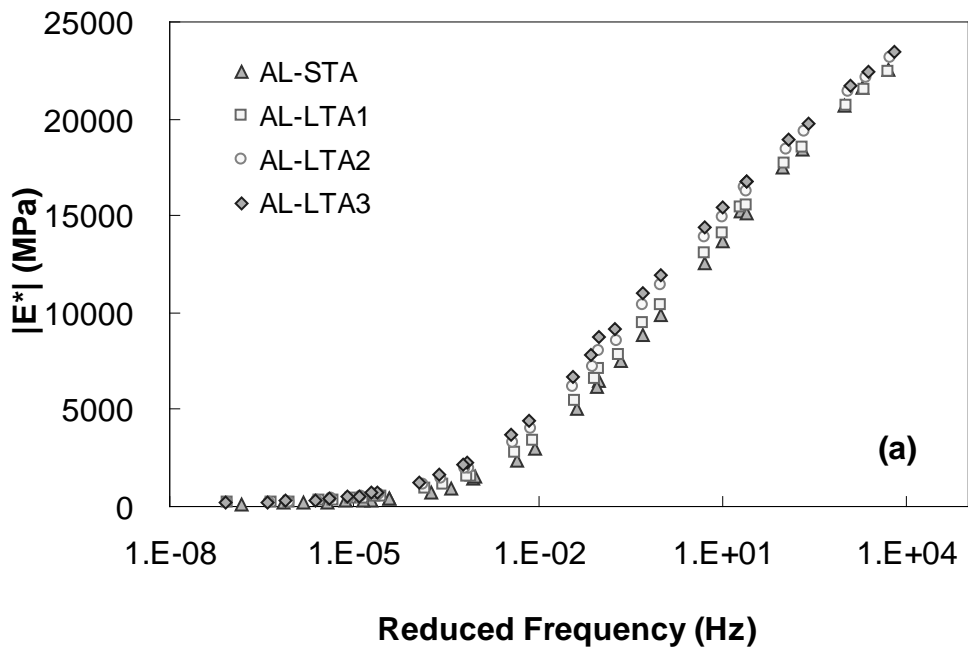


Figure 3-4. Dynamic modulus mastercurves for mixtures of the AL mix in: (a) semi-log space, and (b) log-log space

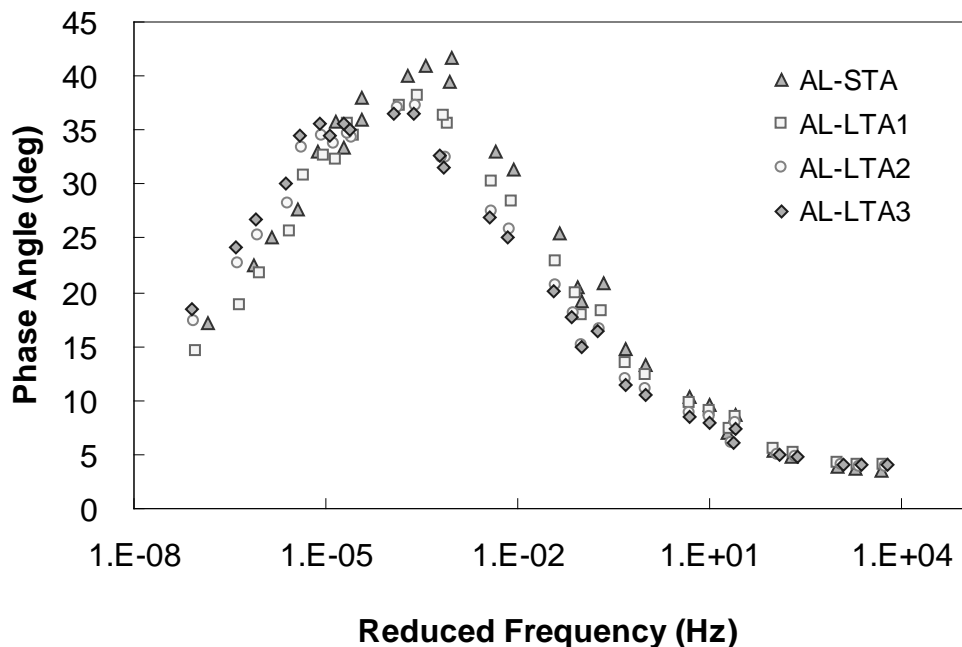


Figure 3-5. Phase angle mastercurves for mixtures of the AL mix

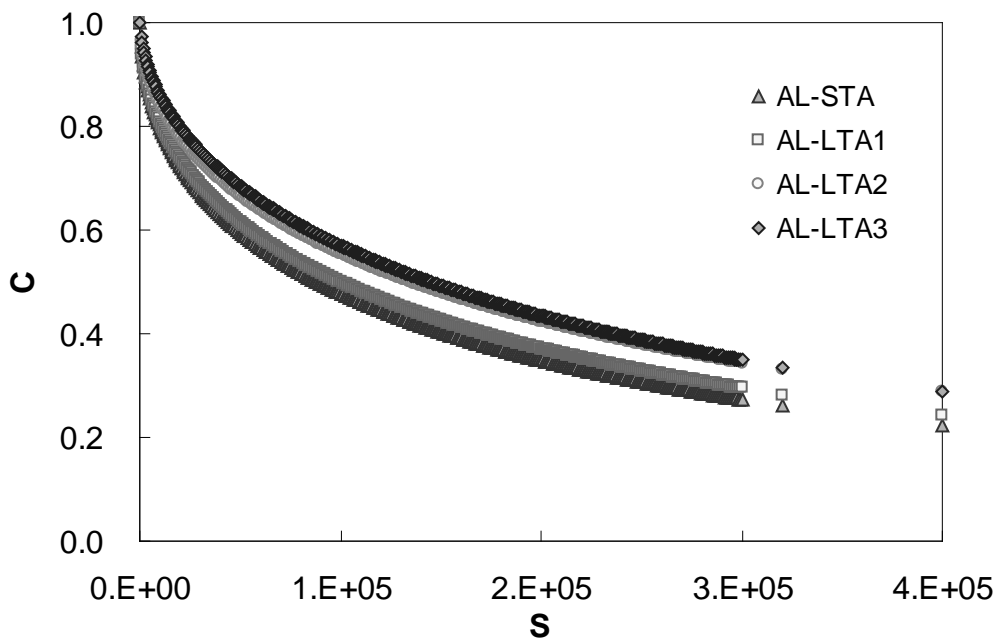


Figure 3-6. Damage characteristic curves for mixtures of the AL mix

3.1.2.1.4 Incorporation of aging effects into the VECD model

To incorporate the effects of aging into the VECD model, two major parameters must be evaluated: the viscoelastic properties and damage characteristics. It is analytically possible to

include the effects of aging in the formulation of the current constitutive model using another time variable that accounts for the aging time, as shown in Equations 3-1 and 3-2. The major advantage of this approach is that the interaction between loading and aging can be modeled realistically, thus allowing a more accurate evaluation of the effects of aged binders on mixture properties and the performance of the mixtures. Accounting for the effects of aging on the damage growth of asphalt aggregate mixtures using fundamental damage mechanics principles is probably the best approach to realistically simulate the interaction between damage and aging that occurs simultaneously in actual pavements.

The pseudo strain (ε^R) of an aged material under uniaxial conditions is represented by the hereditary integral (Equation 3-1).

$$\varepsilon^R = \frac{1}{E_R} \int_0^{\xi} E(t, \xi) \frac{d\varepsilon}{d\xi} d\xi \quad (3-1)$$

where ε^R is a particular reference modulus included for dimensional compatibility and typically taken as one.

Two time variables are used in this integral: the aging time, t , and the loading time, ξ (i.e., the time that has elapsed since the specimen was fabricated and ε is uniaxial strain). From this equation, the relaxation modulus (E) accounts for the aging effects; it is a function of aging time, loading time, and temperature, and is given as

$$E = E(t, t - \tau, T) = E(t, \xi) \quad (3-1)$$

where $\xi = (t - \tau) / a_T$, and a_T is the time-temperature (t - T) shift factor. Theoretically, Equation 3-2 results in the mastercurves of different aging times at a specific reference temperature. However, the relaxation mastercurves of the different aged mixtures could not simply be shifted horizontally or vertically to construct a single mastercurve that includes the

effects of aging. Moreover, solving Equation 3-1 with the two-dimensional relaxation modulus (Equation 3-2) is analytically difficult. Thus, an alternative, quasi-static approach was followed that takes advantage of the relatively long time scale of aging as compared to the time of loading.

As a result of an analytical investigation, it was found that the coefficients for the dynamic modulus mastercurve and damage characteristic curve, expressed by Equations 3-3 through 3-6, vary as either a power law or exponential model with aging time. To develop a final set of relationships between these coefficients and in-service aging time, the lab aging-to-field aging times suggested by SHRP (17) were selected. This relationship is as follows: 1 year for the STA mix, 4 years for the LTA1 mix, 7.5 years for the LTA2 mix, and 18 years for the LTA3 mix.

The relationships between aging time (t_e) and the LVE and VECD model coefficients are expressed by Equations 3-7 through 3-10. These equations show that the models have been formulated by using the ratio of aged values to original (un-aged) values so that the final function could be applied universally to other mixtures to simulate the aging effects. The model considers ways that the LVE and damage characteristics of a material vary with age. As expected, the model suggests that AC becomes stiffer and less time-dependent with age.

$$\log |E^*| = a + \frac{b}{1 + \frac{1}{e^{d+g \log(f_R)}}} \quad (3-2)$$

where $|E^*|$ is dynamic modulus, and f_R is reduced frequency.

$$\log(a_T) = \alpha_1 T^2 + \alpha_2 T + \alpha_3 \quad (3-3)$$

where a_T is time-temperature shift factor, and T is temperature.

$$\alpha = 1 + \frac{1}{u} \quad (3-5)$$

where u is the material constant related to material time dependence.

$$C = e^{mS^n} \quad (3-4)$$

where C is normalized pseudo secant modulus, and S is damage parameter.

$$\frac{a_{t_e}}{a_{t_0}} = t_e^{a1}, \quad \frac{b_{t_e}}{b_{t_0}} = t_e^{a2}, \quad \frac{d_{t_e}}{d_{t_0}} = t_e^{a3}, \quad \frac{g_{t_e}}{g_{t_0}} = t_e^{a4} \quad (3-5)$$

where a1, a2, a3, and a4 are regression constants.

$$\frac{\alpha1_{t_e}}{\alpha1_{t_0}} = t_e^{\alpha12}, \quad \frac{\alpha2_{t_e}}{\alpha2_{t_0}} = t_e^{\alpha22}, \quad \frac{\alpha3_{t_e}}{\alpha3_{t_0}} = t_e^{\alpha32} \quad (3-6)$$

where $\alpha12$, $\alpha22$, and $\alpha32$ are regression constants.

$$\frac{\alpha_{t_e}}{\alpha_{t_0}} = \frac{\alpha_{\max}}{\left(1 + \left(\frac{k1}{t_e}\right)^{k2}\right)^{k3}} \quad (3-7)$$

where α_{\max} , k1, k2, and k3 are regression constants.

$$\frac{m_{t_e}}{m_{t_0}} = \frac{1}{m1 + \frac{m2}{1 + e^{(m3+m4*t_e)}}}, \quad \frac{n_{t_e}}{n_{t_0}} = \frac{1}{n1 + \frac{n2}{1 + e^{(n3+n4*t_e)}}} \quad (3-8)$$

where m1, m2, m3, m4, n1, n2, n3, and n4 are regression constants.

The relationships between aging time and the LVE and VECD model coefficients are shown in Figure 3-7 through Figure 3-9. Generally, the sigmoidal coefficients (a, b, d, g), shift factor coefficients (α_1 , α_2 , α_3), and damage evolution rate (α) vary as a function of aging time in power relationships. The damage coefficients (m, n) change with aging time by following the sigmoidal type of function shown in Figure 3-9. The best fit relationship between the experimental results and the sigmoidal function was selected to represent the VECD model and, as a result, the relationship appears to be somewhat arbitrary. It cannot be stated definitively that rapid transition between years 7 and 12, as suggested by the model, will occur in reality.

However, a more thorough investigation into the correlation between the oven aging and field aging times for damage characteristics is beyond the scope of the current research.

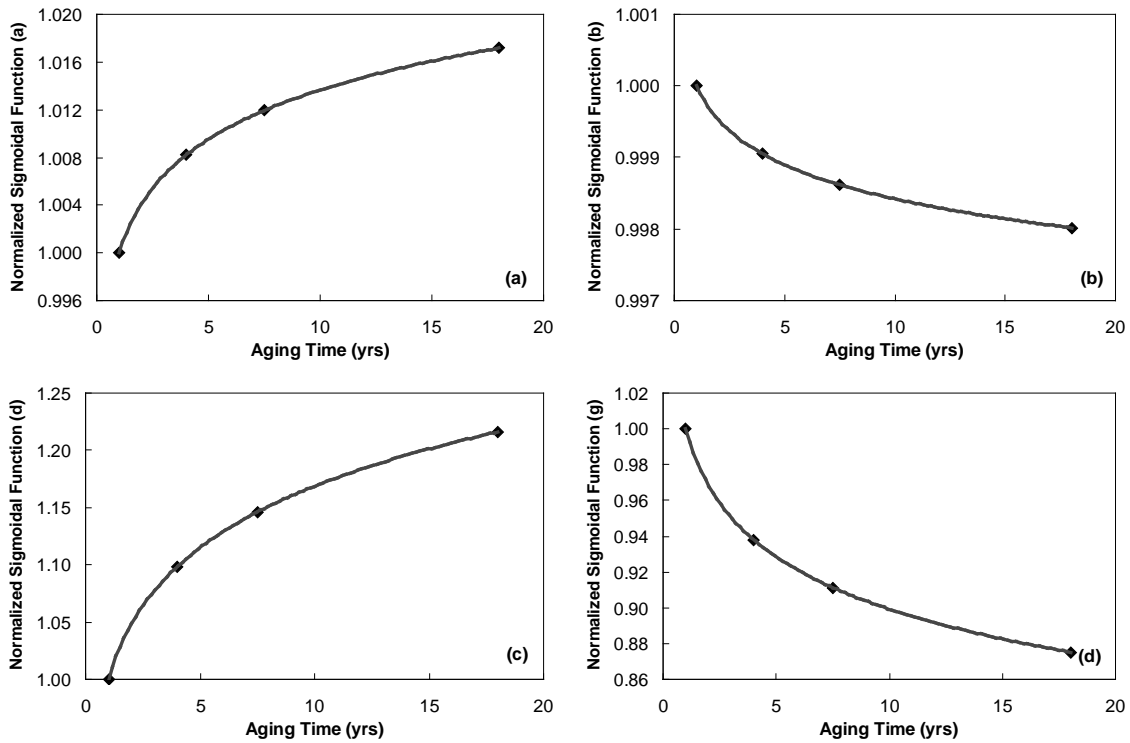


Figure 3-7. Relationship of sigmoidal functions to aging time

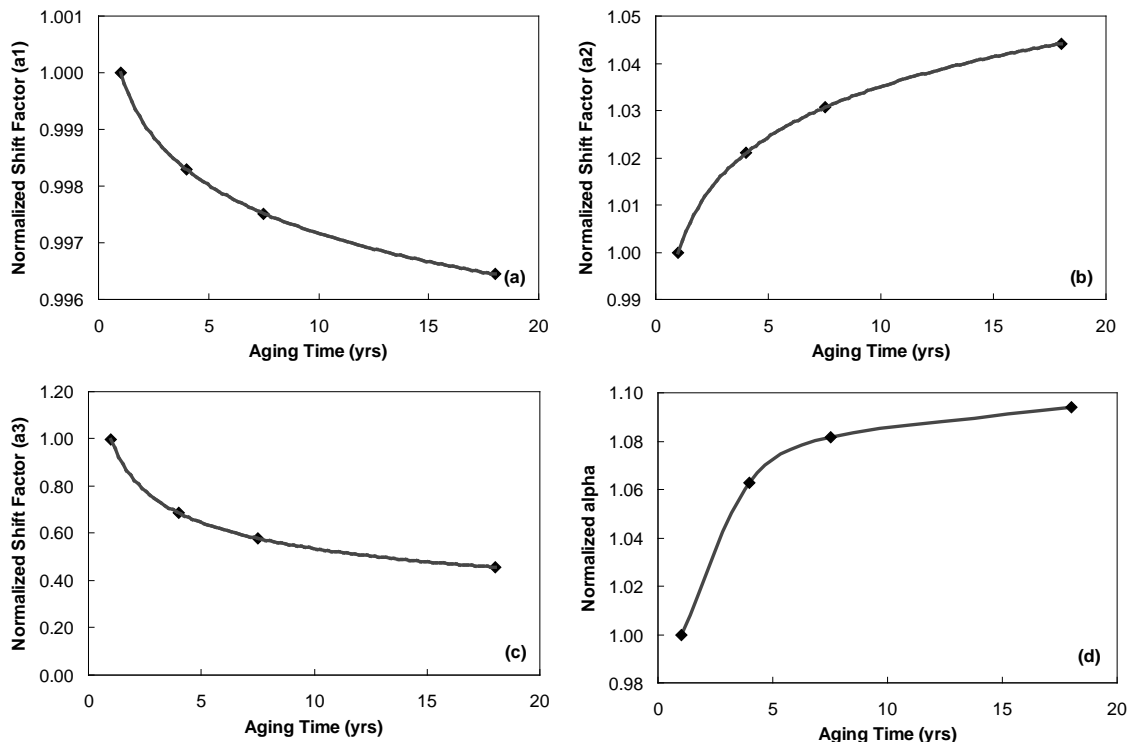


Figure 3-8. Relationship of shift factor coefficients and alpha to aging time

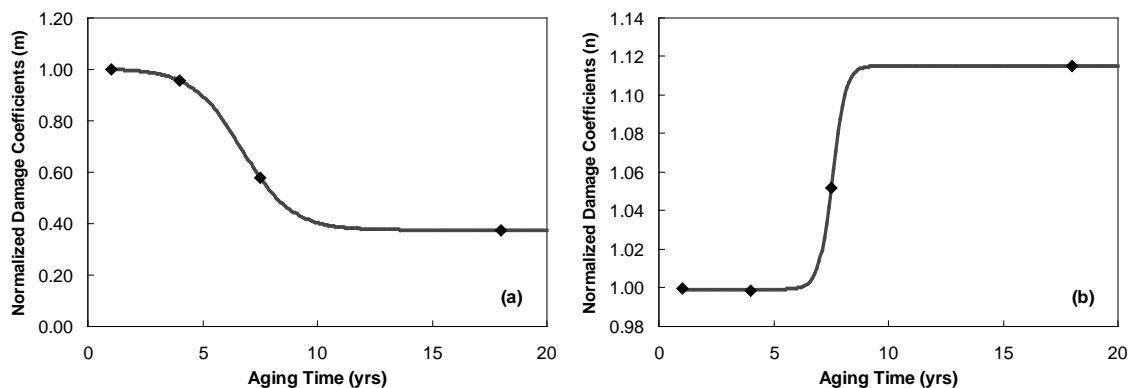


Figure 3-9. Relationship of damage coefficients to aging time

3.1.2.2 Failure criteria as functions of aging and temperature

Aging effects on the performance of asphalt mixtures must be evaluated in terms of the combined effects of stiffness, damage, and failure criteria. A series of cyclic fatigue tests has been conducted to investigate the effects of aging on these characteristics directly and closely. One important finding from this experimental work is that the failure of the specimen occurs at different degrees of damage, depending on the aging level of the mixture and the testing

temperature. This subsection compares the fatigue performance for mixtures aged at different levels, then presents a new method to analyze cyclic fatigue tests, and finally, presents the failure criteria used to interpret the FEP++ results. Detailed information on this new method for cyclic test analysis, the so-called Simplified VECD Model (S-VECD), is provided in Appendix A.1.2.2.4 along with material model fatigue life predictions that include a more general failure criterion to determine the capability and accuracy of the S-VECD (see Appendix A.1.2.3).

3.1.2.2.1 Cyclic fatigue tests

Cyclic fatigue tests using the AL mix were conducted for all four aged mixtures under controlled stress (CS) and controlled crosshead (CX) cyclic conditions. Two amplitudes, high and low, were applied at two temperatures, 5°C and 19°C. The test conditions and some important results, especially the number of cycles to failure (N_f), are summarized in Table 3-2.

To define the number of cycles to failure, the phase angle criterion suggested by Reese (19) is utilized because it seems to work well under both CX and CS test conditions. The phase angle quickly drops in the CX tests and suddenly increases in the CS tests once the specimen fails. One example from the test results for the AL-STA mixture is shown in Figure 3-10.

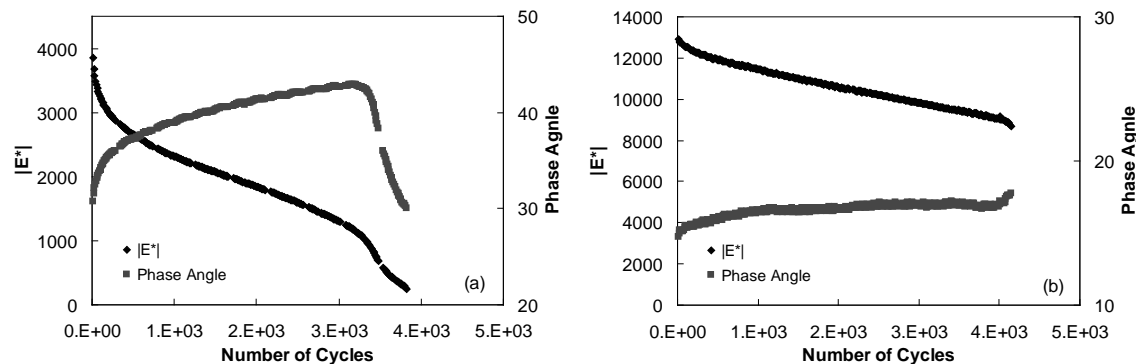


Figure 3-10. Dynamic modulus and phase angle versus load cycle for AL-STA mix: (a) the CX test (AL229), and (b) the CS test (AL248)

Overall, the dynamic modulus decreases and the phase angle increases according to the number of cycles until the specimen fails, which is when the localization of on-specimen strain starts.

Using the cyclic test results, comparisons can be made with regard to four conditions: (1) magnitude of the input, (2) testing mode, (3) temperature, and (4) aging level. However, care must be taken in comparing these results, because the conditions to be compared are not always the same (e.g., there may be a difference in on-specimen strain for each aged mixture).

Nonetheless, the comparisons led to the following conclusions:

1. Regardless of testing mode, temperature, and aging level, fatigue resistance decreases as the magnitude of the input increases;
2. By comparing the CX test results at a similar initial strain magnitude, as the temperature decreases or the aging time increases, the resulting initial stress magnitude increases and the number of cycles to failure (N_f) decreases; and
3. By comparing the CX test results at a similar initial stress magnitude, as the temperature decreases or the aging time increases, the resulting initial strain magnitude decreases and the number of cycles to failure (N_f) increases.

Overall, the different testing modes result in the opposite fatigue performance (e.g., the STA mix shows better performance in the CX tests, but the LTA3 mix shows better performance in the CS tests). It is known, based on energy principles, that stiff materials tend to perform better in CS test protocols, whereas soft materials yield better performance in CX tests, all other factors being equal. In this case, however, all the factors are not equal because aging has occurred, and has somewhat embrittled the LTA mixes. The experimental data suggest that this embrittlement may not be as significant for the CS tests. As noted above, soft materials should perform better in the CX test protocols, and because the softest mixture is also the least embrittled, i.e., the STA, the CX test results cannot be used reliably to determine the exact effects of this embrittlement process.

Table 3-2. Cyclic Fatigue Test Summary (Frequency of 10 Hz)

Mix ID	Specimen ID	Test Designation	Initial Stress Amplitude in Tension (kPa)	Initial Peak-to-Peak Strain (Microstrain)	N_f
AL-STA	AL229	19 ^a -CX ^b -H ^c	1,700	582	3,091
	AL232	19-CX-H	1,400	415	8,908
	AL231	19-CX-L	610	162	> 150,000
	AL246	19-CS-H	750	152	1,610
	AL238	19-CS-L	250	50	46,200
	AL233	5-CX-H	2,870	274	3,498
	AL239	5-CX-L	980	87	> 280,000
	AL248	5-CS-H	1,500	120	4,000
	AL247	5-CS-L	900	76	44,700
AL-LTA1	AL228	19-CX-H	1,790	466	3,613
	AL242	5-CX-H	2,900	259	3,100
	AL244	5-CX-L	920	74	> 280,000
	AL243	5-CS-H	1,500	107	4,590
	AL245	5-CS-L	900	66	77,000
AL-LTA2	AL225	19-CX-H	2,020	483	2,753
	AL250	5-CX-H	3,210	264	713
	AL241	5-CX-L	1,180	84	> 280,000
	AL249	5-CS-H	1,500	99	4,200
	AL240	5-CS-L	900	64	97,200
AL-LTA3	AL220	19-CX-H	2,030	419	1,383
	AL234	5-CX-H	3,220	253	800
	AL235	5-CX-L	1,810	134	> 280,000
	AL237	5-CS-H	1,500	95	8,900
	AL236	5-CS-L	900	52	167,000

^a Test temperature in degrees Celsius; ^b Test mode; ^c Relative magnitude: H=high, L=low

Damage characteristics from cyclic tests

Work by Underwood et al. (20) concluded that the damage characteristic curves obtained from CS, CX, and monotonic testing collapse into a single curve, indicating that the property represented by these curves is fundamental and independent of temperature and test type. Initially, the cyclic data for the aged mixtures were analyzed following the method by Underwood et al. (20) (details are provided in Appendix A.1.2.2.4), but the damage characteristic curves obtained from the different modes of testing did not collapse well, although the collapse in each test mode was acceptable. This analysis showed that the samples conditioned for the LTA mixes produced poorer results than those conditioned only for the STA mix. Thus,

some trials were conducted, and the resultant damage characteristic curves collapsed reasonably using two options taken from the originally suggested analysis method: (1) the α function is defined as $(1/u + 1)$ for the monotonic test and $(1/u)$ for the CX and CS tests, and (2) the correction factor, I , is set to one for all the cyclic tests. These differences in the current and earlier work for analyzing cyclic test results still need to be investigated. Because the definition of α in the original model is based on theoretical arguments and has been verified using STA materials only, its universality with regard to materials tested at other aging conditions was not verified in the original work (20). Figure 3-11 shows the damage characteristic curves of the AL-STA mixture obtained from the monotonic, CX, and CS tests. All the cyclic test data are included in this plot and collapse well with each other. The damage characteristic curves for all four aged mixtures are shown in Figure 3-12 for only the tests that have been performed under the same testing condition (i.e., 19-CX-H). The collapses are good except for the discrepancy between the monotonic and cyclic results of the LTA1 mixture.

3.1.2.2.2 Failure criterion

As shown in Appendix A.1.2.3.1, the general failure criterion developed in previous work is based on reduced frequency and does not include the aging effect on the failure. Because the failure criterion does not include aging time and because the reduced frequency basis approach is not amenable for use with the VECD-FEP++, a temperature-only based failure criterion has been developed that includes the aging effect in the failure definition.

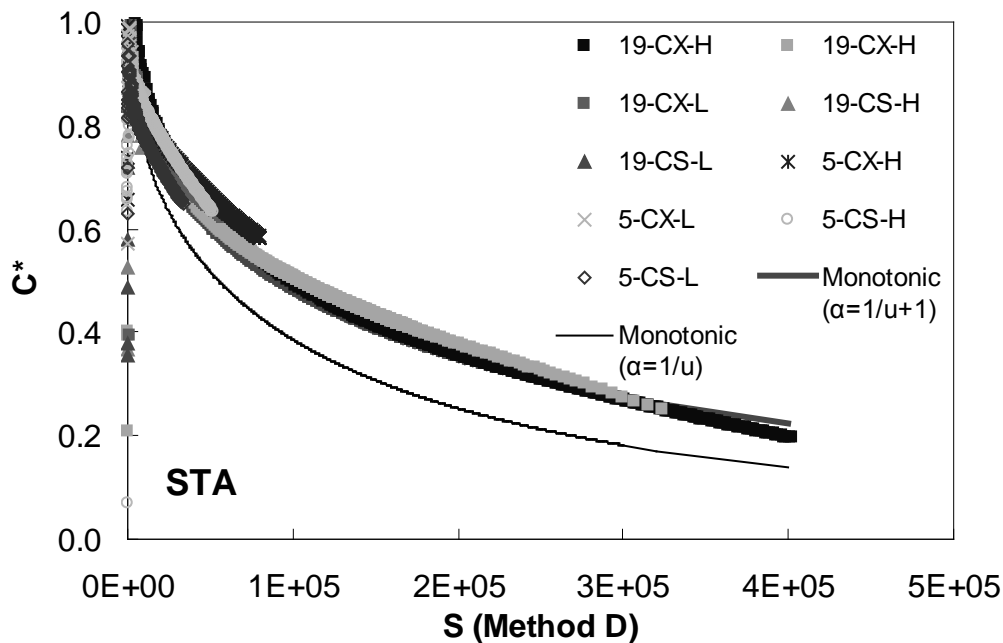


Figure 3-11. Damage characteristic curves of AL-STA mix (all cyclic test data included)

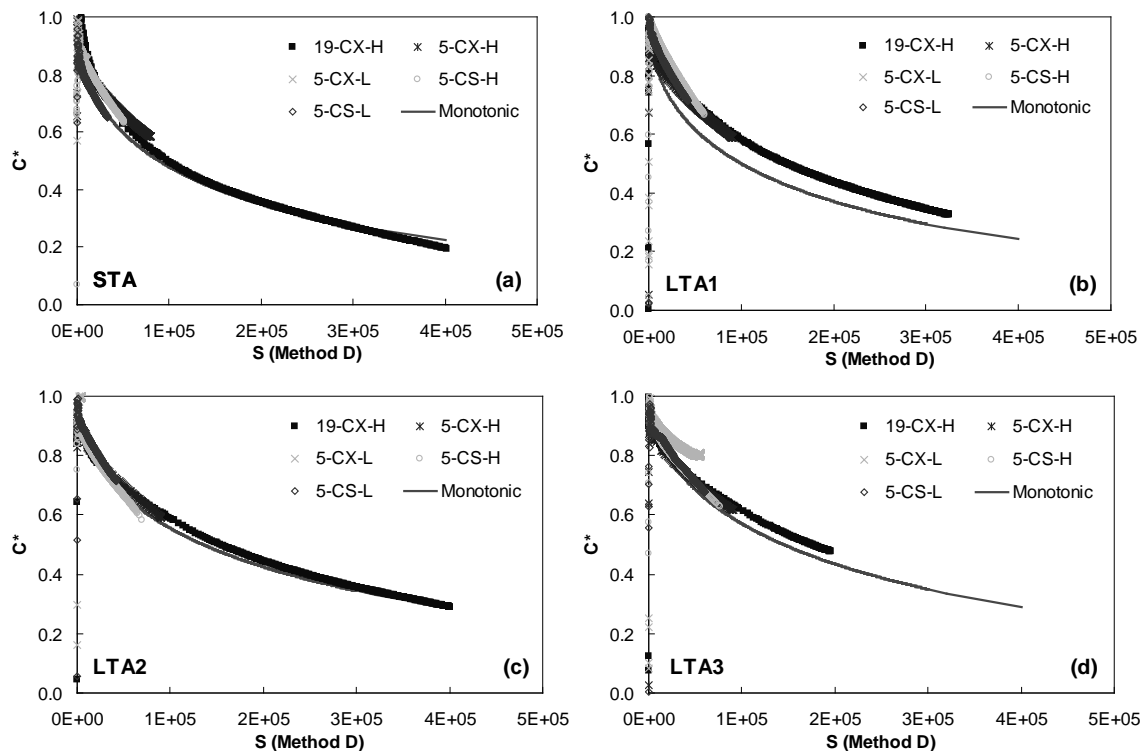


Figure 3-12. Damage characteristic curves of: (a) STA, (b) LTA1, (c) LTA2, and (d) LTA3 aged mixtures of AL mix

In Figure 3-13, the pseudo stiffness (C) values at failure are plotted against the test temperatures for the CX tests for all aged mixtures. The C values at failure decrease as the temperature increases for all aging levels. The aging effect on failure is most noticeable at 19°C. Such a trend can be expected because of the aforementioned tendency of AC to embrittle with age. On the other hand, all the aging mixes failed at similar C values at 5°C. This result is due mainly to the fact that AC is brittle enough at low temperatures that the aging effect is not significant.

Because of limited test data, it is assumed that the failure criterion varies linearly between 5°C and 19°C and is constant beyond this range. All data at 5°C are averaged, and that the LTA1 and LTA2 data are averaged because they show similar values, as shown in Figure 3-14. Therefore, the piecewise function is used for the failure criterion, as shown in Equation 3-11. Like the aging model, the failure criterion is formulated by the ratio of the aged value to the original (un-aged) value so that it can be universally applied to other mixtures according to the aging effect.

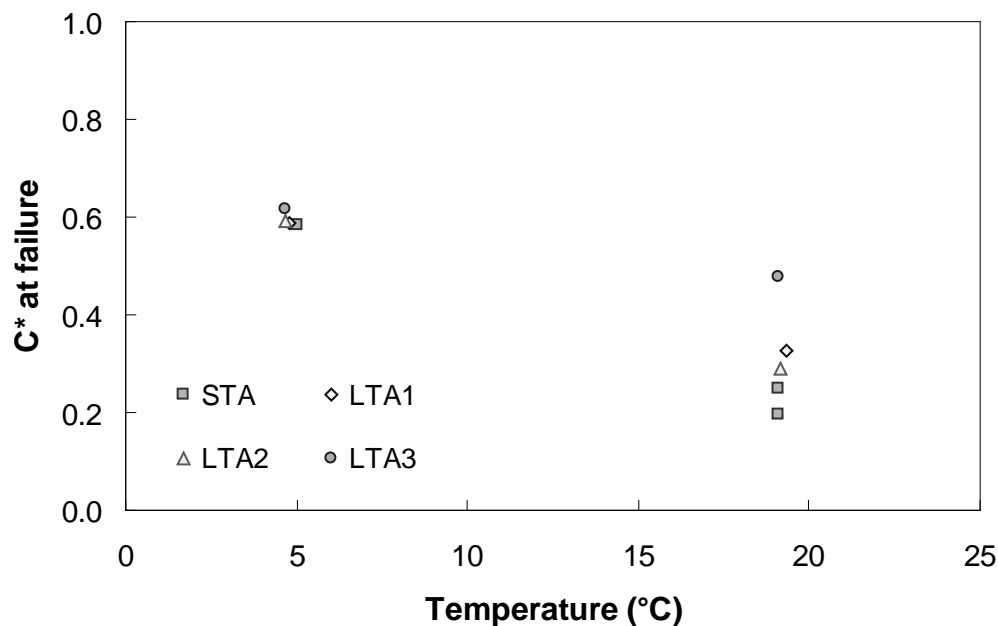


Figure 3-13. Variation of C at failure from cyclic fatigue tests

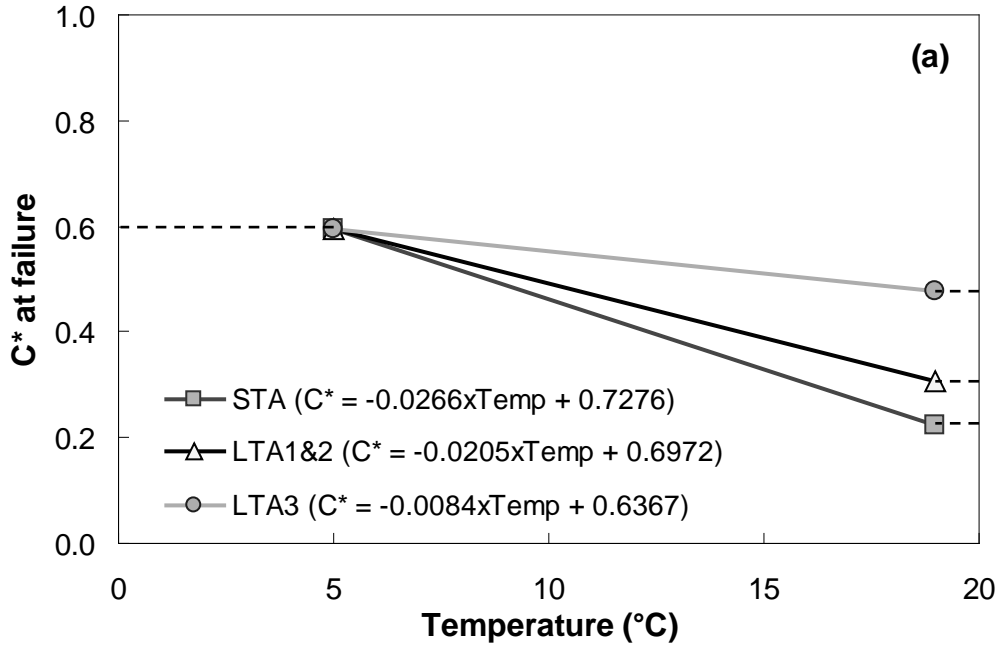


Figure 3-14. (a) Failure criterion

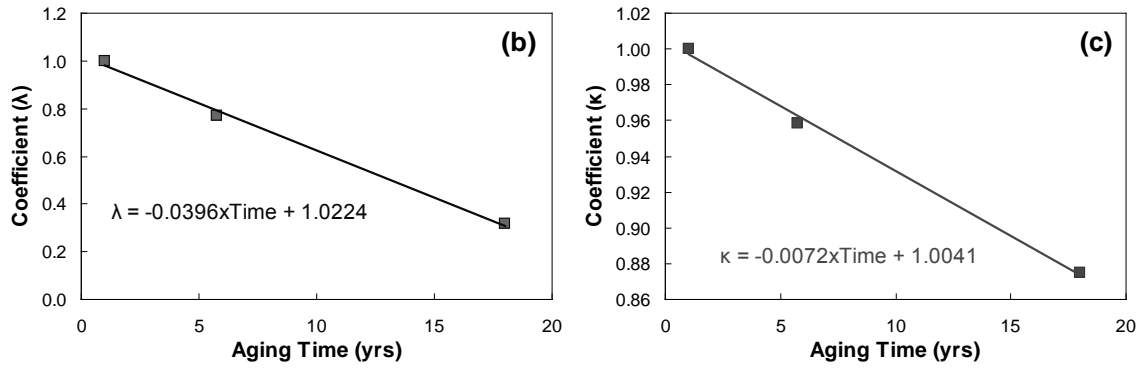


Figure 3-14. (b) and (c) variation of coefficients λ and κ as functions of temperature and aging, respectively

$$C_f = \begin{cases} \left(\frac{\lambda_{t_e}}{\lambda_{t_0}}\right) * 5 + \left(\frac{\kappa_{t_e}}{\kappa_{t_0}}\right) & T \leq 5^\circ C \\ \left(\frac{\lambda_{t_e}}{\lambda_{t_0}}\right) * T + \left(\frac{\kappa_{t_e}}{\kappa_{t_0}}\right) & 5^\circ C < T < 19^\circ C \\ \left(\frac{\lambda_{t_e}}{\lambda_{t_0}}\right) * 19 + \left(\frac{\kappa_{t_e}}{\kappa_{t_0}}\right) & T \geq 19^\circ C \end{cases} \quad (3-9)$$

where

$$\frac{\lambda_{t_e}}{\lambda_{t_0}} = \lambda 1 * t_e + \lambda 2,$$

$$\frac{\kappa_{t_e}}{\kappa_{t_0}} = \kappa 1 * t_e + \kappa 2, \text{ and}$$

$\lambda 1, \lambda 2, \kappa 1, \kappa 2 = \text{constant.}$

3.1.2.3 Healing model

As a placeholder for a fully mechanistic, potentially micromechanically motivated healing model, a simplified version of the phenomenological mechanical model, which was derived, characterized, and verified by Lee and Kim (21), has been applied. A simplified version of this model is used here because (1) the previous formulation, of which the healing model is a part, has certain shortcomings in its rigor, and (2) modifying the material model for the FEP++ would require significant time. The primary disadvantage of this model is the lack of characterization and verification data under various conditions needed for the FEP++ simulations. For this reason, an empirical adjustment has been made to improve the engineering reasonableness of the simplified model.

3.1.2.3.1 Previous formulation

The healing model formulation is encapsulated in the general framework of the VECD model, as it is coded in the FEP++. However, the healing model includes two additional damage parameters (S_2 and S_3) and pseudo stiffnesses (C_2 and C_3) that the current model does not include. The VECD model, shown in Equation 3-12, includes only a single damage parameter, S_1 , and material integrity term, C_1 . The additional terms are included mathematically in the healing function shown in Equation 3-13 where they are shown to physically represent the

increase in pseudo stiffness during the rest periods, $C_2(S_2)$, and the reduction in pseudo stiffness as the healed material is redamaged, $C_3(S_3)$. These material functions are independent of the amount of damage in the virgin material, i.e., $C_1(S_1)$.

$$\sigma = C_1(S_1) \varepsilon^R \quad (3-10)$$

$$\sigma = [C_1 + H] \varepsilon^R \quad (3-11)$$

where

$$H = [S_{B,i}^R + C_2(S_{2,i})] C_3(S_{3,i}) - C_1(S_1) - \sum_{j=1}^{i-1} S_{B,j}^R - S_{C,j}^R,$$

if both the healed and virgin materials are damaged (see Region 1 in Figure 3-15); or

$$H = \sum_{j=1}^{i-1} S_{B,j}^R - S_{C,j}^R,$$

if only the virgin material is damaged (see Region II in Figure 3-15).

Figure 3-15 schematically illustrates the model behavior in terms of pseudo stiffness for a single rest and reloading period. The evolution laws for the S_2 and S_3 damage parameters are given in Equations 3-14 and 3-15, respectively. The relationships between these damage parameters and their respective material integrity parameters are given by Equations 3-16 and 3-17. The coefficients for these equations, as characterized by Lee and Kim (21), are summarized in Table 3-3.

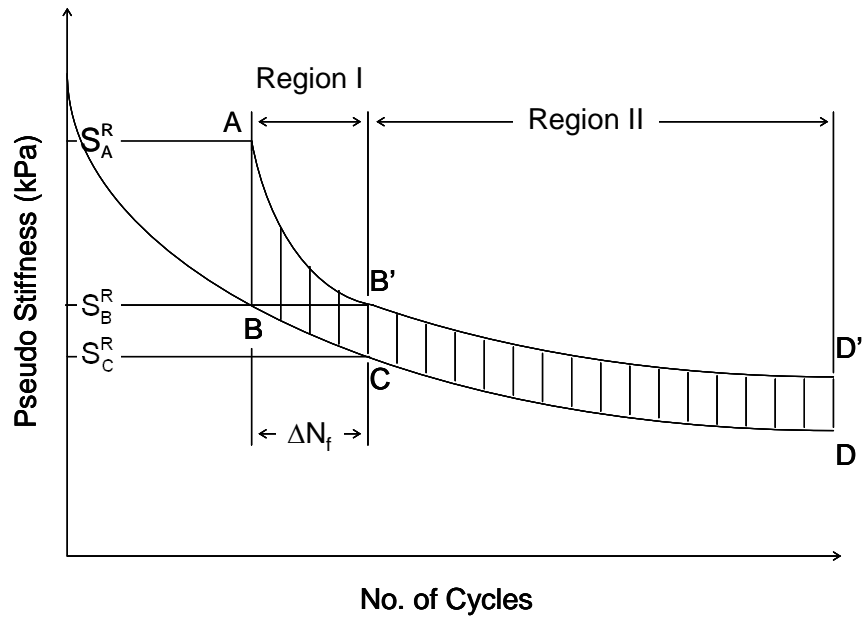


Figure 3-15. Effect of rest period on pseudo stiffness

$$S_2 = \int_0^{t_p} \left[\frac{1}{2} (\varepsilon^R)^2 \frac{\partial C_2}{\partial S_2} \right]^{\alpha_2} dt \quad (3-12)$$

$$\dot{S}_3 = \left[-\frac{S_A^R}{2} (\varepsilon^R)^2 \frac{\partial C_3}{\partial S_3} \right]^{\alpha_3} \quad (3-13)$$

$$C_2(S_2) = C_{20} + C_{21}(S_2)^{C_{22}} \quad (3-14)$$

$$C_3(S_3) = C_{30} - C_{31}(S_3)^{C_{32}} \quad (3-15)$$

Table 3-3. Healing Model Formulation Coefficients (21)

Coefficient	AAM Value	AAD Value
Function C_1		
C_{10}	0.9900	1.1000
C_{11}	0.0065	0.0764
C_{12}	0.4400	0.2000
α_1	2.6950	2.7860
Function C_2		
C_{20}	-0.3750	0.0015
C_{21}	0.0941	0.0004
C_{22}	0.2000	0.6200
α_2	1.7000	1.5000
Function C_3		
C_{30}	1.0100	1.0100
C_{31}	0.0019	0.0114
C_{32}	0.5500	0.3000
α_3	2.1000	2.0000
t-T Shift Factor		
α_1	0.0009	0.0012
α_2	-0.1602	-0.1843
α_3	3.3709	3.9471
T_R	25	25

3.1.2.3.2 Simplified formulation

The basic trends found in the above formulation and numerous experimental studies (15, 22, 23) are shown in Figure 3-16. In short, the more time that elapses between load applications, the more the pseudo stiffness will recover, and hence, the longer the fatigue life will be extended. The amount of recovery is most sensitive to the rest period duration, but the model also suggests that recovery is a function of the previous load intensity and the total cumulative amount of damage that exists in the material. The previous formulation includes these factors by including multiple parameters and damage functions. For the simplified model, an attempt is made to use only a single material function, $C_1(S_1)$, to accomplish the same objective. A closer examination of the previous formulation shows that it is not possible to directly quantify the increase in

pseudo stiffness healing with a single function because, as shown in Figure 3-15, the healed material is more sensitive to loading than the virgin material (i.e., the damage rate of the healed material is greater than that of the virgin material in Region I, while it is the same for the healed and virgin materials in Region II).

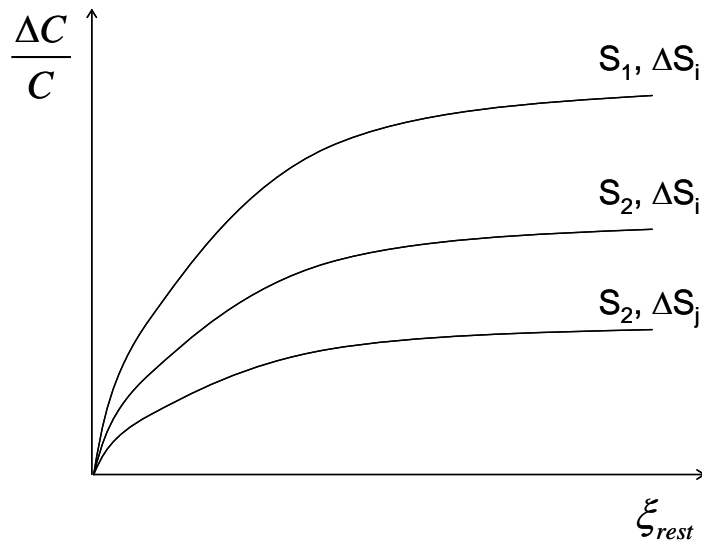


Figure 3-16. Effect of rest period on material healing

The basic concept of the simplified model is diagrammed schematically in Figure 3-17 where damage characteristic curves are shown for the first three cycles of loading. The points evenly labeled (0, 2, and 4) represent the pseudo stiffness values at the beginning of load pulses 1, 2 and 3. The points labeled with the odd numbers (1, 3, and 5) represent the pseudo stiffness values at the end of load pulses 1, 2 and 3. The single damage parameter model will predict that during the first cycle, damage will grow from point 0 to point 1. The simplified model would then suggest that during some rest period the material would heal back (i.e., recover) to point 2. Then, when loading begins for the second cycle, the damage would grow to point 3. Upon resting after the end of the second cycle, healing would increase the pseudo stiffness to point 4. Finally, after the third loading cycle, the damage would grow to point 5. In total, then, there are three different segments where damage is assumed to occur in the virgin material: from point 0

to point 1; from point 1 to point 3 (second cycle); and finally from point 3 to point 5 (third cycle). Similarly, there are only two segments where damage is assumed to occur in the healed material: from point 2 to point 1 (second cycle) and from point 4 to point 3 (third cycle). Between each of these points, though, a single damage function, $C_1(S_1)$, is used to compute the damage.

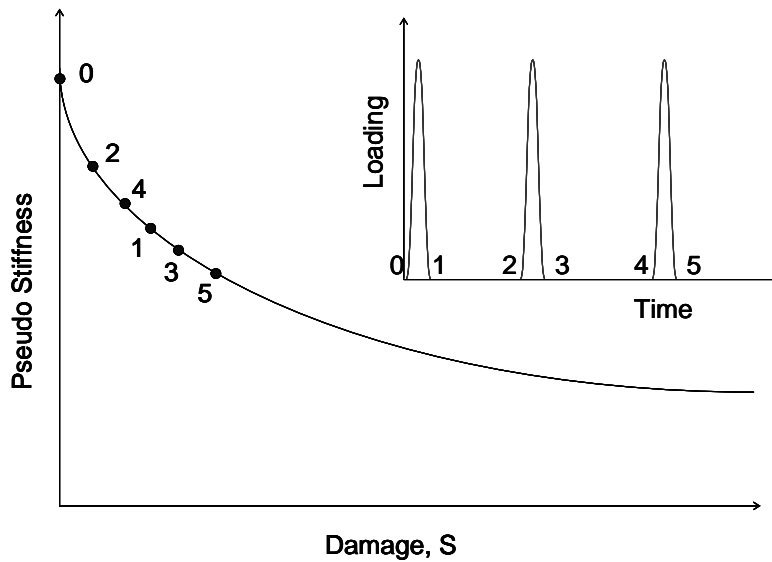


Figure 3-17. Conceptual schematic diagram for the simplified model

In order to use the previous formulation, a systematic factorial data set was created for the different rest periods (x 7), damage levels (x 9), and energy inputs, ΔS (x 7), which have values that could be expected in any given FEP++ simulation. For each of these combinations, the previous formulation was used to predict the pseudo stiffness at the end of the cycle after the rest period, i.e., point 3. Then, S_H in Equation 3-18 was determined through optimization to give the same pseudo stiffness value after a load pulse; e.g., damage was found at point 2, so when calculating damage growth, the resulting pseudo stiffness was equal to that at point 3. The pseudo stiffness at this healed damage level was then calculated using Equation 3-19, and finally used to compute the value of the change in pseudo stiffness (ΔC), which is the difference

between the pseudo stiffness values at point 1 and point 2. In order to apply the outcomes universally, the damage level, S , and energy input, ΔS , were normalized to the damage level at failure, S_f , and the change in pseudo stiffness was normalized to the pseudo stiffness level.

$$S_{i+1} = S_H + \left(-\frac{1}{2} (\varepsilon^R)^2 \frac{\partial C}{\partial S} \right)^{\alpha_1} \quad (3-16)$$

$$C_H(S_H) = C_{10} - C_{11} (S_H)^{C_{12}} \quad (3-17)$$

After calculating the change in pseudo stiffness for the multiple conditions, a regression model was characterized for easy use. The basic model is shown in Equation 3-20 where the coefficients are found to depend on the damage level and energy input, as seen in Equations 3-21 through 3-29. Note that the model is presented in terms of reduced rest time, ξ_{rest} , which is defined in Equation 3-30 by combining the physical rest period, t_{rest} , and the t-T shift factor function, which is a second order polynomial, at some reference temperature, T_R (25°C).

$$\frac{\Delta C_{Heal}}{C} = \frac{\kappa}{\left(1 + \left(\frac{\beta}{\xi_{rest}} \right)^\gamma \right)^{\delta/\gamma}} \quad (3-18)$$

$$\kappa = \kappa_1 \left(\frac{\Delta S}{S_f} \right)^{\kappa_2} \quad (3-19)$$

$$\kappa_1 = ae^{b \left(\frac{S}{S_f} \right)} \quad (3-20)$$

$$\kappa_2 = -c \left(\frac{S}{S_f} \right)^d \quad (3-21)$$

$$\beta = \beta_1 \left(\frac{\Delta S}{S_f} \right)^{\beta_2} \quad (3-22)$$

$$\beta_1 = fe^{g^*\left(\frac{S}{S_f}\right)^h + i^*\left(\frac{S}{S_f}\right)} \quad (3-23)$$

$$\beta_2 = -je^{k^*\left(\frac{S}{S_f}\right)} \quad (3-24)$$

$$\gamma = \gamma_1 \quad (3-25)$$

$$\gamma_1 = ye^{z^*\left(\frac{S}{S_f}\right)} \quad (3-28)$$

$$\delta = n + \left(\frac{o}{1 + e^{p+q\log\left(\frac{S}{S_f}\right)}} \right) \left(\frac{\Delta S}{S_f} \right)^{\delta_2} \quad (3-26)$$

$$\xi_{rest} = \frac{t_{rest}}{a_T} = \frac{t_{rest}}{10^{\alpha_1(T^2 - T_R^2) + \alpha_2(T - T_R)}} \quad (3-27)$$

The coefficients for this model are summarized in for AAD and AAM mixtures (21).

These two mixtures represent, respectively, a light healing and a heavy healing material. Because the model is normalized, i.e., it predicts the ratio of change in pseudo stiffness to current pseudo stiffness, $\Delta C/C$, it can be applied universally to other mixtures to simulate heavy healing and light healing. The strength of the characterized model is shown for the AAD mixture in Figure 3-18.

Table 3-4. Simplified Healing Model Coefficients

Coefficient	AAM Value	AAD Value
Function K		
a	0.1679	0.1657
b	2.2695	2.8865
c	0.0548	0.0261
d	0.2572	0.2379
Function β		
f	27.3913	1.5144
g	-1.5887	-4.7659
h	30.1058	5.0763
i	-5.8228	-3.3953
j	0.5070	0.5290
k	-8.1700	-3.0063
Function γ		
y	1.4707	1.2448
z	-1.6387	-1.6425
Function δ		
n	-0.3593	1.0526
o	30.1626	7.2289
p	2.8853	1.7666
q	-0.2850	-2.0453
$\bar{\delta}_2$	-0.0843	-0.1597

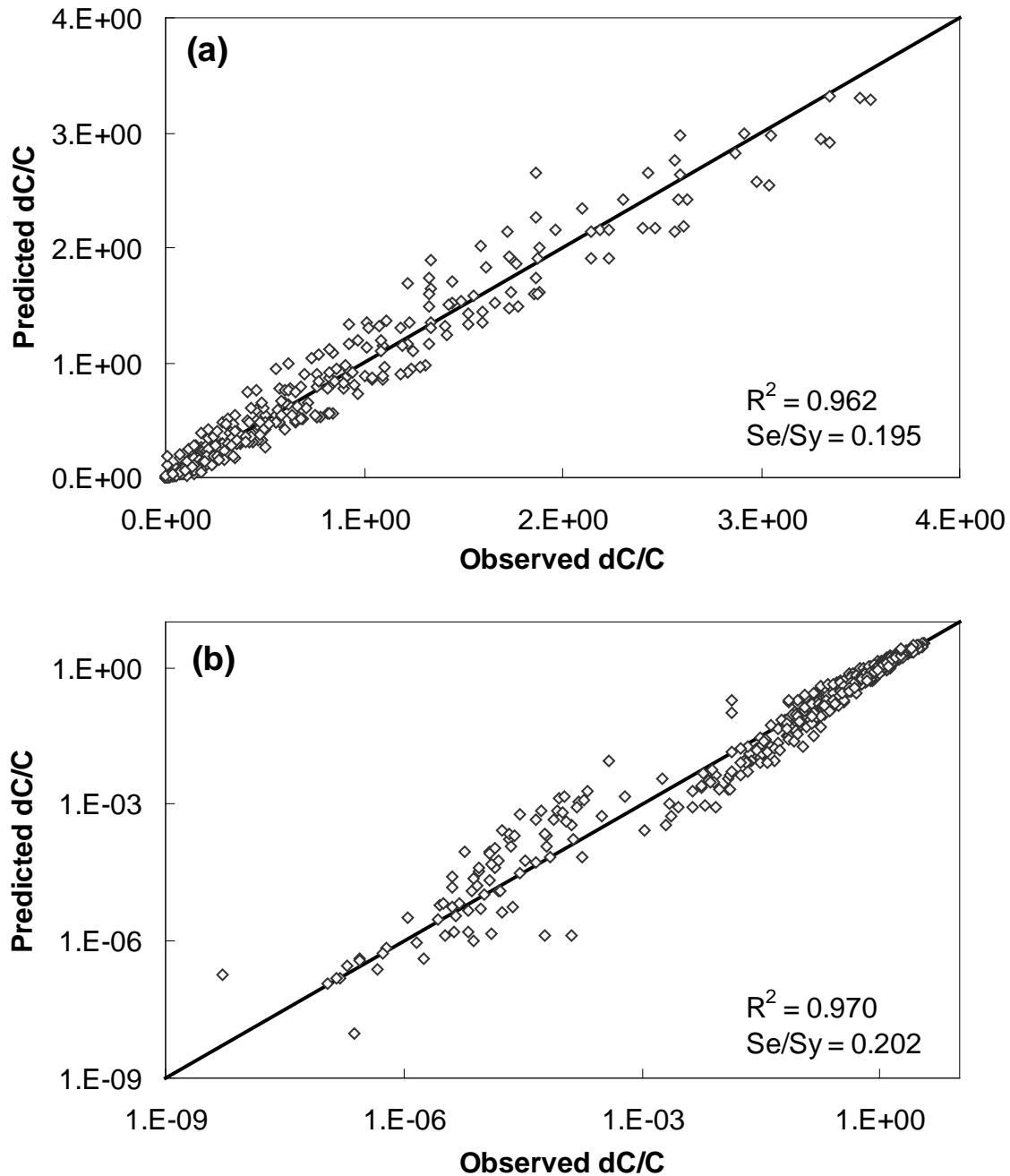


Figure 3-18. Strength of simplified model for AAD mixture in: (a) arithmetic and (b) logarithmic scales

3.1.2.3.3 Healing potential factors

One shortcoming of the simplified model, which has transferred from the previous formulation, is its handling of rest periods introduced before the healed material has been entirely redamaged (e.g., the rest periods in Region I). This issue is represented schematically in

Figure 3-19, but was not encountered during the development of the more robust healing model because the earlier work (21) did not include experiments in which the subsequent healing and redamaging occurred in Region I of the previous healing cycle. This situation is important in the context of FEP++ simulations because each load pulse is followed by a rest period and only a single load pulse is applied after each rest period. It is believed that the behavior suggested by the previous formulation, shown in Figure 3-19, is unrealistic, because the repeated redamaging of the healed material should actually limit the healing potential; thus, the response depicted in Figure 3-20 is deemed more appropriate.

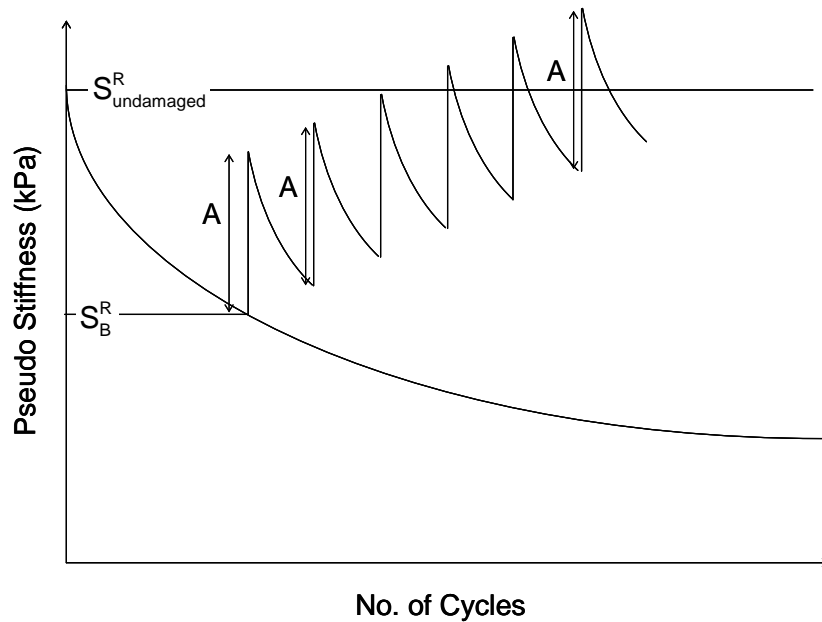


Figure 3-19. Effect of damage and healing in Region I using previous formulation

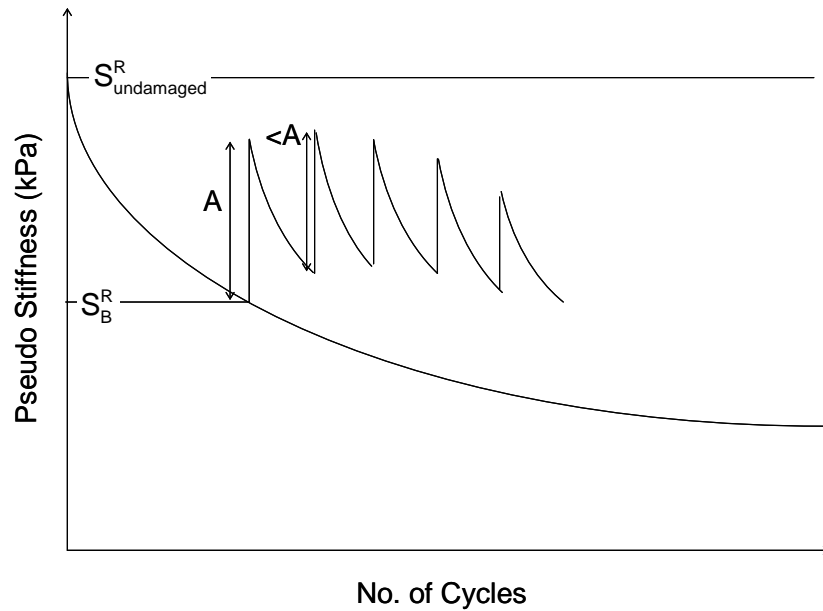


Figure 3-20. Representation of expected material behavior

Because not all damage occurs in the healed material, a correction factor was formulated to be a function of the total summed damage that occurs in the material. This correction factor is referred to as *healing potential factor-C*. Damage related to the redamage of healed material is considered to be negative damage, and the damage related to virgin material is considered to be positive damage. Referring to Figure 3-17, the damage that occurs from point 0 to point 1, point 1 to point 3 (second cycle), and finally point 3 to point 5 (third cycle) is calculated as a positive value. Then, the damage that occurs from point 2 to point 1 (second cycle) and from point 4 to point 3 (third cycle) is calculated as a negative value. If there is a net positive value, then the full healing potential suggested by Equation (3-18) is achieved. If, however, there is a net negative value, then the full healing potential is not reached, and the *healing potential factor-C* is less than one. The exact mathematical function used is shown in Equation 3-32.

Another correction factor, *healing potential factor-O*, is applied with the consideration that the healing potential generally reduces as the material becomes more damaged. In other words, even when the healing in a cycle occurs at newly damaged sites, i.e., when the total net damage

is positive, the healing potential should nonetheless decrease as the damage grows. This situation is believed to be related to the fact that high damage levels represent both an increase in crack density and an increase in the average size of the cracks. As the size of the cracks increases, the overall potential for healing should be adjusted. The mathematical formulation for this healing potential factor is shown in Equation 3-33. Because the value of *healing potential factor-O* is related to the maximum damage level (S) it always reflects an overall drop in healing potential in damaged materials, regardless of the type of damage, new or rehealed.

Figure 3-21 shows the healing potential factors, and Figure 3-22 represents each healing potential factor that will be used in the FEP++ simulation. The *healing potential factor-C* and *healing potential factor-O* are more important, respectively, in a single cycle and in overall periods within the simulation; therefore, both factors should be considered together, as shown in Equation 3-34.

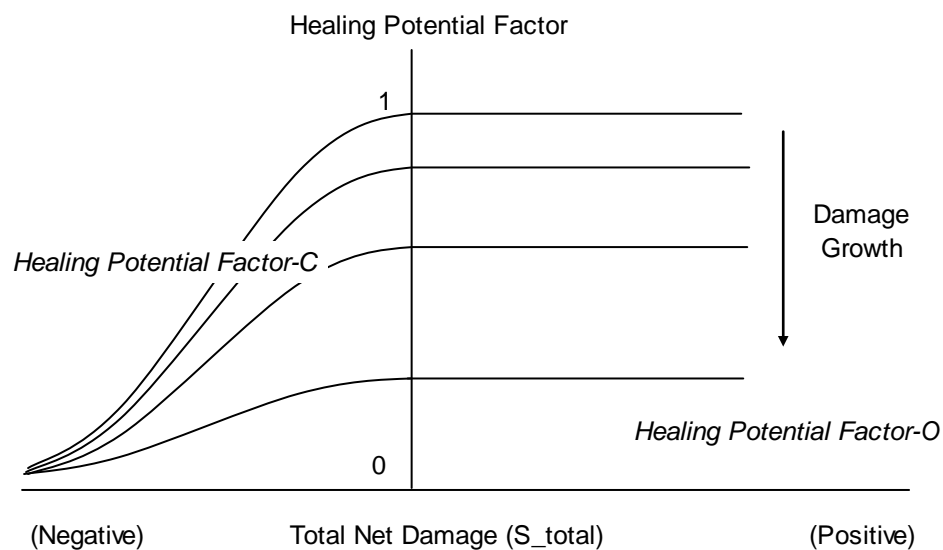


Figure 3-21. Effect of net damage growth on healing potential correction factor

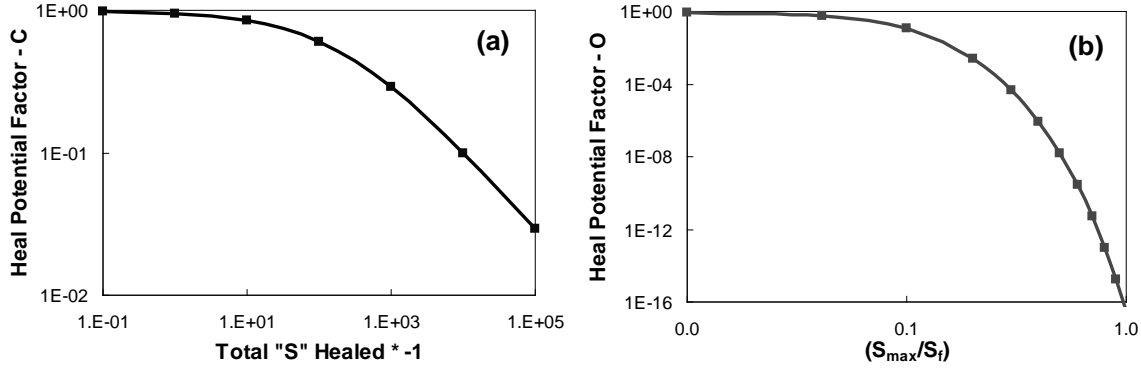


Figure 3-22. Healing potential factors

$$\Delta C_{Adjusted} = \Delta C_{Heal} * Healing\ Potential\ Factor \quad (3-28)$$

$$Healing\ Potential\ Factor - C = \begin{cases} 1 & S_t \geq 0 \\ \frac{1}{1+e^{y1+z1*\log(-1*S_t)}} & S_t < 0 \end{cases} \quad (3-29)$$

$$Healing\ Potential\ Factor - O = \frac{1}{1+e^{y2+z2*(S_{max}/S_f)}} \quad (3-30)$$

$$Healing\ Potential\ Factor = \begin{cases} \frac{1}{1+e^{y2+z2*(S_{max}/S_f)}} & S_t \geq 0 \\ \frac{1}{1+e^{y1+z1*\log(-1*S_t)}} * \frac{1}{1+e^{y2+z2*(S_{max}/S_f)}} & S_t < 0 \end{cases} \quad (3-31)$$

where

- S_{max} = maximum S in history,
- S_f = S at failure,
- S_t = total net damage, and
- $y1, y2, z1, z2$ = constant.

3.1.3 Analytical Sub-models

To predict pavement performance, the material sub-models must be converted to, or implemented into, structural models to consider the different structures, boundary conditions, climate conditions, etc. Consequently, three analytical sub-models have been developed: (1) a

structural aging model, (2) a damage correction factor (DCF) model, and (3) a temperature variation model.

3.1.3.1 Structural aging model

Details of the development of a material level aging model are provided in Section 3.2.2.1. The time scale used for the material level aging model corresponds physically only to that used for the top layer of a real pavement cross-section. To apply this model to different depths, the age of each sub-layer relative to that of the surface must be found. This goal is achieved by coupling the principles of the Global Aging System (GAS), first proposed by Mirza and Witzczak (24), with an effective time concept. A 10-year-old pavement can serve as an example of the effective time concept whereby after 10 years of service, the surface layer has aged 10 years, but the material at a depth of 3 inches may behave as the surface layer behaved when the pavement was only 4 years old. In this example then, the effective time of the sub-layer 3 inches from the surface 10 years after construction is 4 years. To compute the material properties of this sub-layer at year ten, material aging models described in Section 3.2.2.1.4 (Figure 3-7 through Figure 3-9) can be used to find the value of the coefficients at 4 years.

The GAS model was used to determine the effective time of a given pavement structure. The GAS model predicts the viscosity of the asphalt binder as a function of depth, mean annual air temperature (MAAT) representing the effect of geographical location, and rolling thin film oven (RTFO) binder viscosity. The effective time is determined by finding, for some physical time and depth, the time that gives the same viscosity for the binder at the pavement surface. A flow chart of the structural aging model, including the equiviscosity concept as well as the plot of effective time versus depth for a typical simulation, is shown in Figure 3-23.

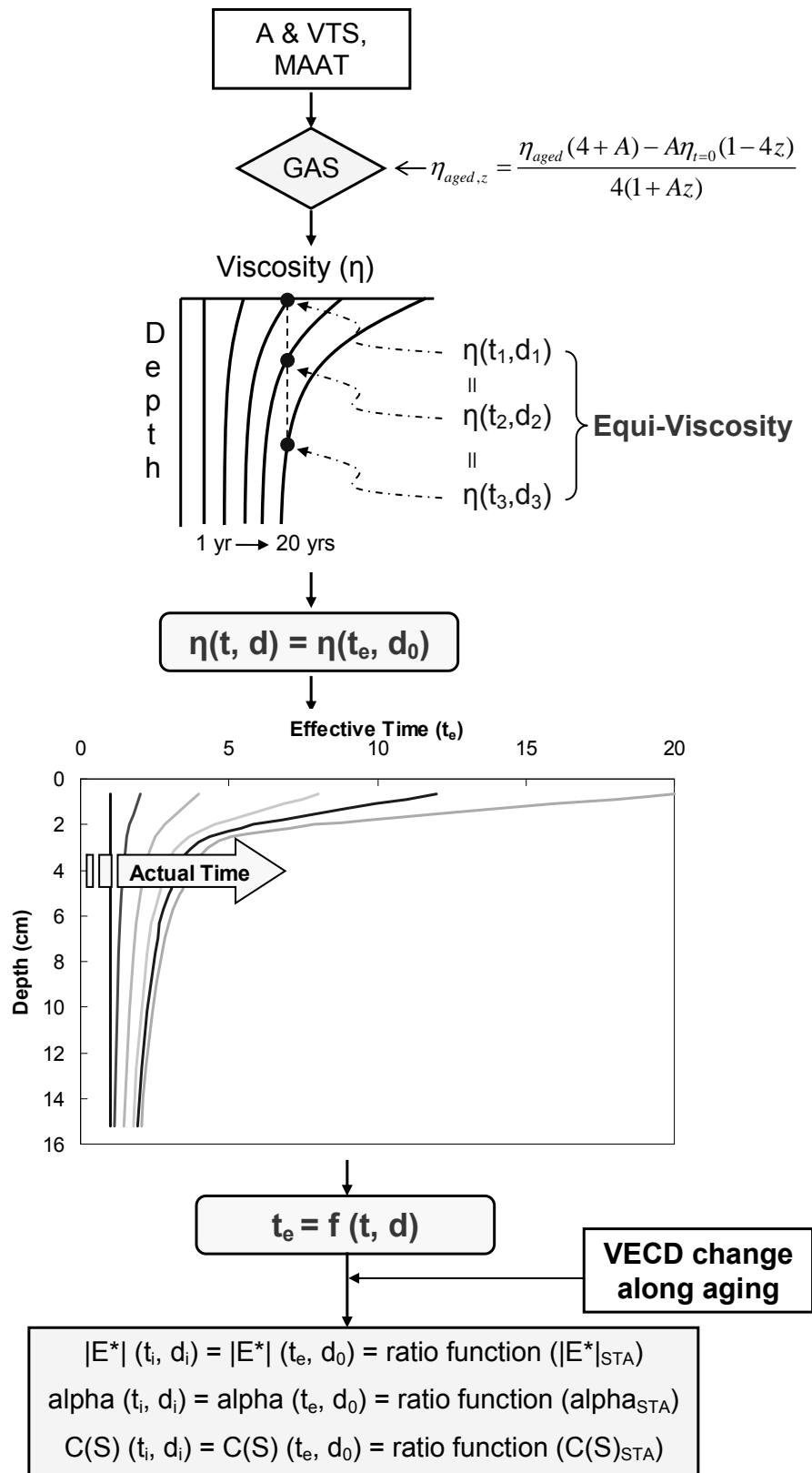


Figure 3-23. Structural aging model

As the GAS model is a function of the MAAT, the effective time varies for different climatic regions. To represent the wide range of conditions encountered in the United States, five regions are included in the study. These regions were selected based on the AASHTO climatic classification (25) and consist of (1) wet, freeze-thaw cycling (Washington, D.C.); (2) wet, hard freeze, spring thaw (Chicago, Illinois); (3) wet, no freeze (Tallahassee, Florida); (4) dry, freeze-thaw cycling (Dallas, Texas); and (5) dry, hard freeze, spring thaw (Laramie, Wyoming). Figure 3-24 is the plot of effective time at 20 years versus pavement depth for the five regions. The temperature in the legend is the MAAT for each region. The higher the MAAT, the higher the effective time at the same depth, which indicates that the aging effect is more significant for a higher MAAT region.

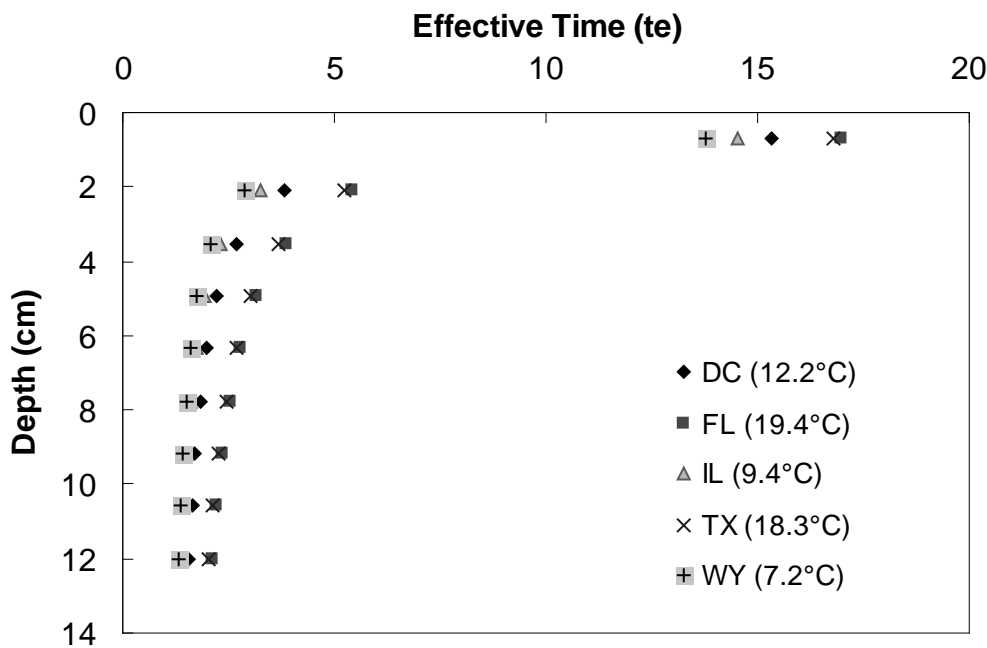


Figure 3-24. Effective time contours for various regions

3.1.3.2 Damage correction factor

The current framework uses the VECD material model, which does not account for viscoplasticity and results in an overprediction of stress and increase in damage.

The viscoplasticity of a given material and structure is considered by applying the damage correction factor (DCF). The DCF is calculated by combining the simple strain-hardening viscoplastic material model (discussed in Appendix A.1.2.5) with the LVE stress and strain responses of the pavement under consideration. These responses are predicted by using the FEP++ software and turning off the damage functionality. The linear strain responses are adjusted to account for viscoplasticity, and then these adjusted strain responses are used to find an effective viscoelastoplastic modulus. A second run of the FEP++ was performed using the effective modulus values. Comparisons made between the responses of the first and second FEP++ runs revealed the sensitivity of the given pavement structure and materials to variations in viscoplastic strain. This sensitivity is reflected by a damage factor, which varies from 0 to 1. A value of 0 reflects a condition where the material is either very sensitive to structural viscoplastic effects and/or materially sensitive; conversely, a value of 1 reflects a condition where both structural and material viscoplastic effects are not very important (e.g., during winter).

The idea behind this scheme is that a pavement simulation is neither in controlled stress nor controlled strain mode but somewhere in between. In a stress-controlled situation, the strain computed in the simulation corresponds to the viscoelastic strain and fully contributes to damage. However, in a strain-controlled situation, the viscoelastic strain that contributes to damage is significantly weaker than the strain computed in the simulation. Thus, depending on which end of the spectrum the analysis lies, the amount of strain that contributes to damage varies significantly. To account for this unpredictability, the DCF has been introduced and is defined as

$$DCF = (1 - \beta) \left(\frac{\varepsilon_{ve}^{dmg}}{\varepsilon_{fem}} \right) + \beta, \quad (3-32)$$

where

- ε_{fem} = the strain computed by an FEP++ simulation,
 ε_{ve}^{dmg} = the strain contributing to damage, and
 β = a factor that is 0 for control strain and 1 for control stress.

Thus, the problem of significant damage due to total strain can be handled by using the DCF to scale the strain used in the damage calculation. The method used to calculate the DCF is as follows.

First, the stress and strain in the pavement are computed using viscoelastic analysis. Because the main interest is vertical cracking, the radial stress and strain (denoted as σ_{ve} and ε_{ve} , respectively) are used in this analysis. Now, the viscoplastic strain, ε_{vp} , can be approximated using the simple strain-hardening material model, Equation 3-36, and the viscoelastic stress computed in the previous step. Then, to approximate the structural effects of this viscoplastic strain, an effective viscoelastoplastic relaxation modulus, E_i^{eff} , is computed by scaling the Prony coefficients in Equation 3-37 using Equation 3-38, as follows:

$$\varepsilon_{vp} = \left(\frac{p+1}{Y} \right)^{\frac{1}{p+1}} \left(\int_0^t \sigma^q dt \right)^{\frac{1}{p+1}}. \quad (3-36)$$

where

- ε_{vp} = the viscoplastic strain,
 p, q, Y = the material coefficients.

$$E(t) = E_\infty + \sum_{i=1}^m E_i e^{-t/\rho_i} \quad (3-37)$$

where

- $E(t)$ = the relaxation modulus,
 E_∞ = the elastic modulus,
 E_i = the modulus of the i^{th} Maxwell element (fitting coefficient), and

ρ_i = the relaxation time (fitting coefficient).

$$E_i^{eff} = \left(\frac{\varepsilon_{ve}}{\varepsilon_{ve} + \varepsilon_{vp}} \right) E_i \quad (3-38)$$

A second analysis was performed using the effective viscoelastoplastic Prony coefficients instead of the viscoelastic Prony coefficients. The stress and strain obtained from this analysis are referred to as the effective stress and strain and denoted as σ_{ve}^{eff} and ε_{ve}^{eff} , respectively.

The mode-of-loading factor β is then obtained by comparing the effective stress and strain (σ_{ve}^{eff} and ε_{ve}^{eff}) to the original stress and strain (σ_{ve} and ε_{ve}):

$$\begin{aligned} \sigma_{eff} &= (1 - \beta) \frac{E_{eff}}{E_{ve}} \sigma_{ve} + \beta \sigma_{ve} \\ \varepsilon_{eff} &= (1 - \beta) \varepsilon_{ve} + \beta \varepsilon_{eff} \end{aligned} \quad (3-39)$$

where β is a factor that is 0 for controlled strain and 1 for controlled stress. Equation 3-39 gives two values of β , and hence their average is taken as the degree of controlled stress:

$$\beta_{avg} = 0.5 \left(\left(1.0 - \frac{\frac{\sigma_{ve}}{E_i} - 1.0}{\frac{\sigma_{ve}^{eff}}{E_i} - 1.0} \right) + \frac{\frac{\varepsilon_{ve}^{eff}}{E_i} - 1.0}{\frac{\varepsilon_{ve}}{E_i} - 1.0} \right). \quad (3-40)$$

Finally, the DCF is given by

$$DCF = 0.5 \left(\frac{\frac{\sigma_{ve}}{E_i} - 1.0}{\frac{\sigma_{ve}^{eff}}{E_i} - 1.0} + \left(1.0 - \frac{\frac{\varepsilon_{ve}^{eff}}{E_i} - 1.0}{\frac{\varepsilon_{ve}}{E_i} - 1.0} \right) \right). \quad (3-41)$$

Because the strain-hardening viscoplastic model is valid only for tension, the DCF is taken to be 1 for the region in which the radial stress is compressive.

3.1.3.3 Temperature variation

The variation of temperature in a pavement has two effects: a change in stiffness of the AC and a change in the thermal stress due to thermal expansion of the material. Thermal stress is generated in the pavement depending on the boundary conditions. These two effects of temperature have been implemented in the FEP++.

The actual temperature variation used for the pavement performance prediction is generated from the EICM. Temperature profiles generated from the EICM are input directly into the FEP++ preprocessor.

3.1.3.3.1 Temperature profile

Five regions have been selected based on the six climatic zones identified by the *AASHTO Guide for Design of Pavement Structures* (25) to represent the wide range of temperature variation in the United States. The regions selected for this analysis are the same as those used in evaluating aging. They are (1) wet, freeze-thaw cycling (Washington, D.C.); (2) wet, hard freeze, spring thaw (Chicago, Illinois); (3) wet, no freeze (Tallahassee, Florida); (4) dry, freeze-thaw cycling (Dallas, Texas); and (5) dry, hard freeze, spring thaw (Laramie, Wyoming). Figure 3-25 and Figure 3-26 show the variation of temperature and temperature rates in 2001 for each of the five regions; the numbers in the legend signify the month. Each month's data are the averaged data for that month at 0.7 cm below the surface of the pavement. Although a detailed method for pavement performance prediction is explained later, it has been determined that analysis on a monthly basis with three segments of a day might be appropriate for long-term simulations, such as 20 years. Based on temperature and rate profiles, three segments of a day are indicated by vertical divisions in the plots, as follows: 5:00 AM – 2:00 PM (5:00 – 14:00) for the heating cycle; 2:00 PM – 9:00 PM (14:00 – 21:00) for the cooling cycle; and 9:00 PM – 5:00 AM (21:00 – 5:00) for the constant cycle. Temperature profiles according to depth can also be obtained for

the same time segments and will be input for the simulation. Further, these segments generally follow daily traffic distributions.

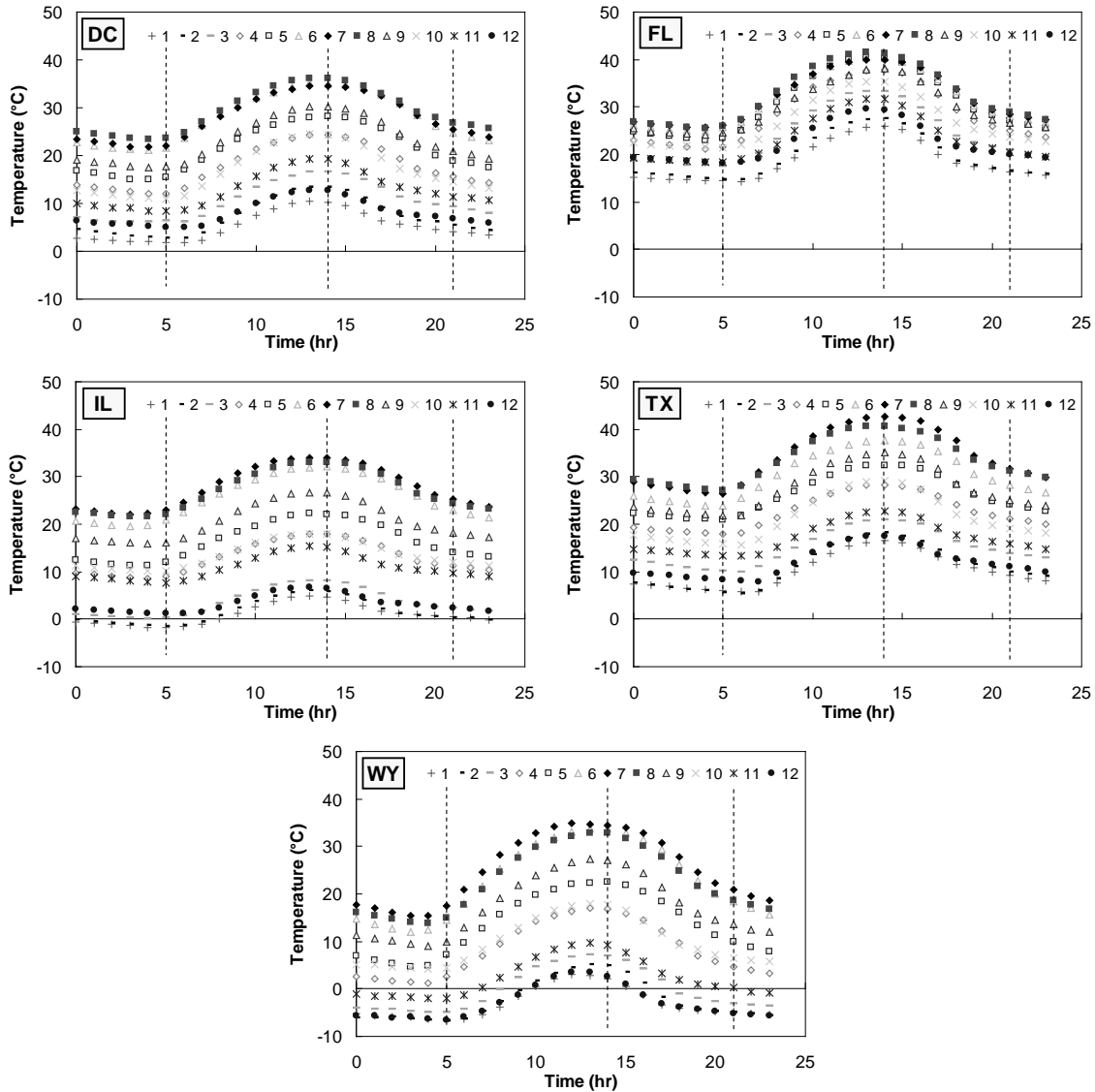


Figure 3-25. Temperature variation (at 0.7 cm below pavement surface)

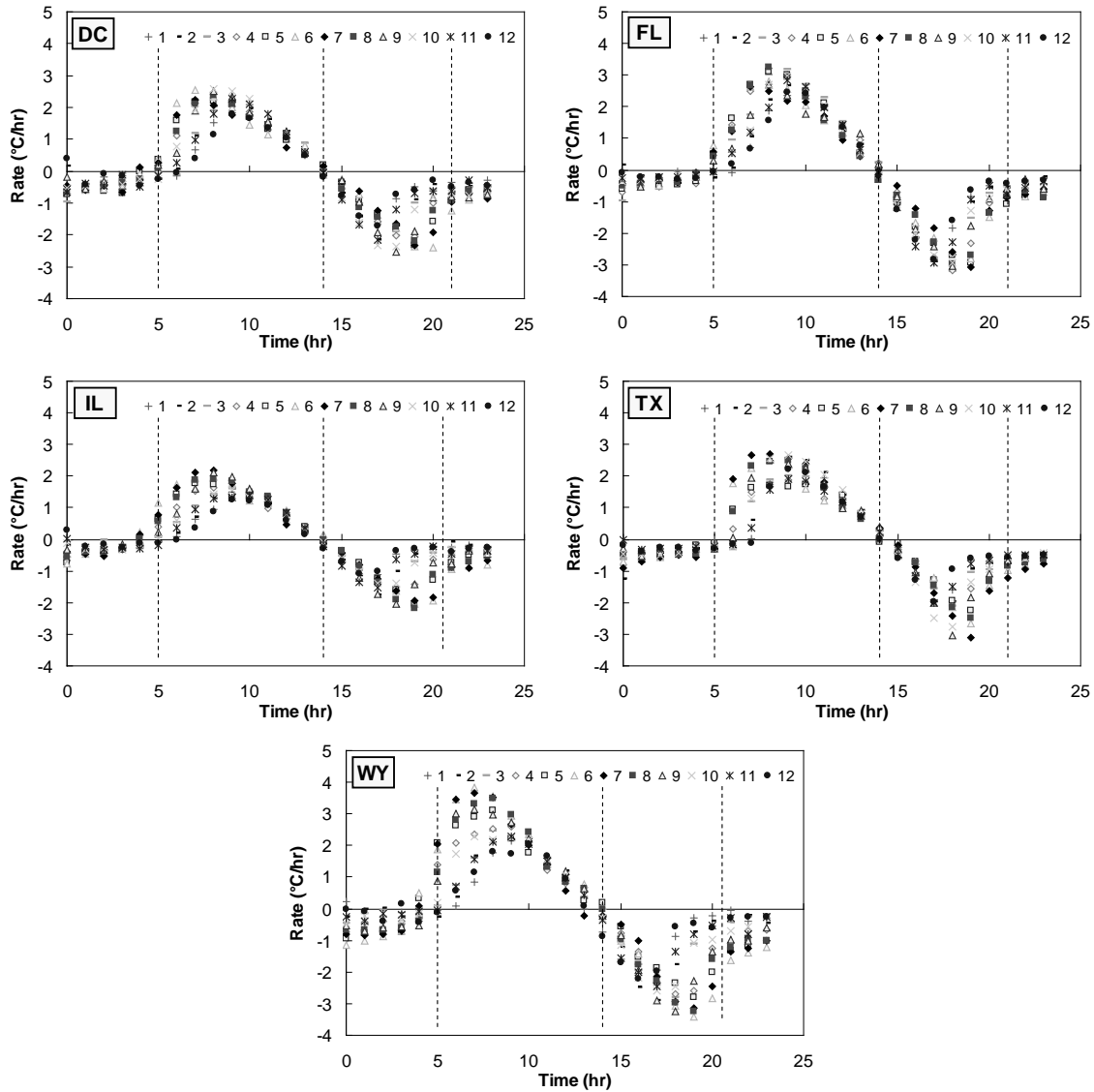


Figure 3-26. Temperature rate variation (at 0.7 cm below pavement surface)

3.1.3.3.2 Stiffness change as a function of temperature

For material level modeling, the change in stiffness in AC due to temperature is taken into account using the concept of reduced time (see Equation 3-42). The t-T shift factor is obtained from the characterization of the relaxation modulus of the material using dynamic modulus tests at different frequencies and temperatures. The reduced time is calculated with respect to a reference temperature and captures the history of temperature variations in the material.

$$\xi(t) = \int_0^t \frac{1}{a_T(\tau)} d\tau, \quad (3-42)$$

where

$$\begin{aligned} \xi(t) &= \text{the reduced time,} \\ a_T &= \text{the time-temperature shift factor.} \end{aligned}$$

In the computational implementation, all analyses were performed in terms of physical time, but the relaxation modulus was adjusted to the temperature of interest. This adjustment approach is similar in concept to the reduced time approach and is possible due to the use of a state variable formulation for stress and strain (*cf.* reference 26) and can be performed efficiently by adjusting the relaxation times in Equation 3-37 by Equation 3-43.

$$\hat{\rho}_i(t) = \frac{\rho_i}{a_T(t)}. \quad (3-43)$$

3.1.3.3 Thermal stress

Thermal stress in the material is incorporated by defining the mechanical strain, $\varepsilon_m(t)$, as follows:

$$\{\varepsilon_m(t)\} = \{\varepsilon(t)\} - \{\alpha_E\}(T - T_0), \quad (3-44)$$

where

$$\begin{aligned} \{\varepsilon(t)\} &= \text{the strain in the material,} \\ \{\alpha_E\} &= \text{the coefficient of isotropic thermal expansion for the material in three} \\ &\quad \text{dimensions,} \\ T &= \text{the current temperature, and} \\ T_0 &= \text{the reference temperature at which there is no initial stress.} \end{aligned}$$

The constitutive law for a viscoelastic material undergoing damage is given as

$$\{\sigma\} = [D]\{\varepsilon_m^R\}, \quad (3-45)$$

where

$$\begin{aligned} \{\sigma\} &= \text{the stress vector,} \\ [D] &= \text{the stiffness matrix that is a function of damage, and} \\ \{\varepsilon_m^R\} &= \text{the vector of mechanical pseudo strain, computed using the state} \\ &\quad \text{variable solution to pseudo strain (26).} \end{aligned}$$

3.1.4 Performance Prediction Module

The performance of a pavement can be characterized by predicting the damage accumulation. Using a suitable failure criterion that relates the damage parameter to the onset of cracking in a uniaxial test, the crack initiation points in the pavement under fatigue cracking can be predicted. However, when the period of interest is in the order of years, it becomes computationally impossible to simulate pavement performance. Consequently, an extrapolation method is introduced so that the simulations run in a more time-efficient manner.

3.1.4.1 VECD FEP++

The VECD FEP++ is a finite-element implementation of the VECD model (27). The model assumes that a material is isotropic when undamaged and that damage growth under loading leads to local transverse isotropy (i.e., the material has a local axis of symmetry oriented along the maximum principal stress direction, which is perpendicular to the crack direction). This model is currently used in modeling tensile damage and offers capabilities for modeling the damage progression in a viscoelastic material and the three-dimensional state of stress and strain. It also accounts for the effects of anisotropy in the material as a result of cracking in one direction.

The current framework of the VECD FEP++ is formulated for the axisymmetric case, but can be extended easily to three dimensions. The finite-element model (FEM) implementation enables the redistribution of stress in pavements that are being damaged, which is an important

phenomenon to be captured. The FEM implementation is also useful in studying the effects of layers with different stiffness values. By running the FEM simulation of a pavement for numerous cycles of fatigue loading, the progression of damage in the pavement over time may be observed, and critical points in the pavement that show early degradation can be noted. Using a suitable failure criterion that relates the damage parameter to the onset of cracking in a uniaxial test, the crack initiation points in the pavement under fatigue cracking can be predicted, and the life of the pavement can be better understood. Additionally, the program can be used in ranking the performance of pavements constructed from different asphalt mixtures.

The performance of a pavement can be characterized by predicting the damage accumulation and using a failure criterion to judge the state of the pavement. This evaluation can be achieved by using an FEM simulation with the VECD model over the period of interest. However, when the period of interest is in the order of years, it becomes computationally impossible to simulate the pavement performance. In these cases, approximate schemes are introduced so that the simulations run in a more time-efficient manner.

The FEP++ uses an extrapolation scheme that can significantly reduce the running time while still capturing the essential characteristics. The current scheme computes the damage caused by load and thermal variations at representative times in a day. These data are then extrapolated using a nonlinear scheme to obtain the total damage accumulation in a given month. This damage is then applied to the pavement as the initial condition for the next month's simulation. This process is continued for the entire simulation period.

3.1.4.2 Traffic

Traffic loading is a complicated characteristic to quantify and include in pavement simulations. Complexities arise due to the statistical distribution of the numerous different axle types available, each with its own load level distribution. Predicting the exact distribution of the

various vehicle loadings and their accompanying load level distributions is an imprecise science at best, and predicting the order of the loadings is impossible. Furthermore, predicting the sequential effects of different loading configurations becomes computationally time consuming. Although, at any instant in time, the exact traffic history will determine the pavement performance, over time an averaging effect occurs such that the exact sequence of loading is not that critical. In light of this statistical effect and in order to simulate pavement performance in a reasonable amount of time, the concept of equivalent single-axle loads (ESALs) is used.

For all of the subsequent pavement simulations, loading consists of 10 million ESALs equally distributed over the three daily simulation periods (as defined in Section 3.2.3.3.1) and for a 20-year period. This distribution translates to approximately 41,700 loadings each month or 450 for each of the three daily simulation periods. Traffic growth factors and loading distributions other than uniform distribution could have been used, but these factors were not investigated in this study. Each load is assumed to last for 0.1 second and, as a consequence of the uniform loading distribution, the rest period between each loading is constant and equal to approximately 62.1 seconds. These loading and rest times ensure compatibility between the total simulation time and the physical time.

The representative load consists of a single axle with an 80 kN (18 kip) load and tires inflated to 689 kPa (100 psi). It was assumed that the axle would be wide enough that the damage induced by each tire would be independent of that of the other. This assumption was verified through examinations of the damage contours that revealed little damage growth at distances of 0.5 m (1.6 ft) from the wheel center. Due to this damage independence and due to the axisymmetric nature of the current work, the simulations can take advantage of symmetry

and analyze a single side of the tire load. Currently, the effect of wheel wander is not considered in the simulations.

3.1.4.3 Extrapolation

The basic idea behind extrapolation is to use the damage growth law to obtain an approximate expression for the damage growth rate. The growth law is given by

$$\frac{\partial S}{\partial t} = \left(-\frac{\partial W^R}{\partial S} \right)^\alpha = \left(-\frac{\partial C}{\partial S} \right)^\alpha \frac{(\varepsilon^R)^2}{2}, \quad (3-46)$$

where

$$\begin{aligned} W^R &= \text{pseudo strain energy density function, } W^R = \frac{1}{2}(\varepsilon^R)C, \\ \varepsilon^R &= \text{pseudo strain,} \\ t &= \text{total duration of a load cycle,} \\ C &= \text{pseudo stiffness,} \\ S &= \text{damage, and} \\ \alpha &= \text{damage evolution rate.} \end{aligned}$$

Using a change of variables and Equation 3-46, the growth rate of the pseudo stiffness can be written as

$$\frac{\partial C}{\partial t} = \frac{\partial S}{\partial t} \frac{\partial C}{\partial S} = \left(\frac{\partial C}{\partial S} \right)^{\alpha+1} \frac{(\varepsilon^R)^2}{2}, \quad (3-47)$$

or equivalently as

$$\frac{\partial C}{\partial N} = \int_0^t \left(\frac{\partial C}{\partial S} \right)^{\alpha+1} \frac{(\varepsilon^R)^2}{2} dt, \quad (3-48)$$

where N is a load cycle.

The pseudo stiffness and damage parameters, C and S , are related by

$$\ln(C) = mS^n, \quad (3-49)$$

which, upon differentiation, yields

$$\frac{\partial C}{\partial S} = m^{1/n} n C (\ln C)^{1-1/n}. \quad (3-50)$$

Finally, assuming the pseudo strain, ε^R , remains constant during a cycle,

$$\frac{\partial C}{\partial N} = A C^{(\alpha+1)} (\ln C)^{(\alpha+1)(1-1/n)}, \quad (3-51)$$

where A is the constant over the duration of the cycle.

The above relationship can be solved numerically using the results from the FEM simulation as the initial condition to obtain an approximate value of the pseudo stiffness and, hence, the damage, at the end of the extrapolation period. The equations for the numerical scheme to solve Equation 3-51 are given by

$$\begin{aligned} C_{i+1}^{end} &= C_{i+1}^{begin} + A (C_{i+1}^{begin})^{(\alpha+1)} \left(-\ln (C_{i+1}^{begin}) \right)^{(\alpha+1)(1-1/n)}, \\ C_{i+1}^{begin} &= C_i^{end} + \Delta C_i^{heal}, \\ A &= \frac{C_i^{end} - C_i^{begin}}{(C_i^{begin})^{(\alpha+1)} \times \left(-\ln (C_i^{begin}) \right)^{(\alpha+1)(1-1/n)}}, \end{aligned} \quad (3-52)$$

where

- C_i^{begin} = the pseudo stiffness at the beginning of cycle i ,
- C_i^{end} = the pseudo stiffness at the end of cycle i , and
- ΔC_i^{heal} = the recovered stiffness due to healing in cycle i .

3.1.4.4 Damage calculation summary

A flow chart of the total damage calculation process, including extrapolation, is shown in Figure 3-27. This flow chart outlines the combination of elements discussed previously: traffic loading, thermal considerations, damage factor, daily divisions for damage calculation, healing, etc. To verify the accuracy of some of the simplifications, particularly the extrapolation scheme, a simulation was performed using the FEP++ software without any extrapolation. In a real pavement simulation, the number of cycles simulated in an analysis step would be closer to

13,000, but predicting this many cycles without extrapolation would require a significant amount of time. Instead, the simulation was carried out for only about 1,300 cycles, and comparisons were made at this number of cycles.

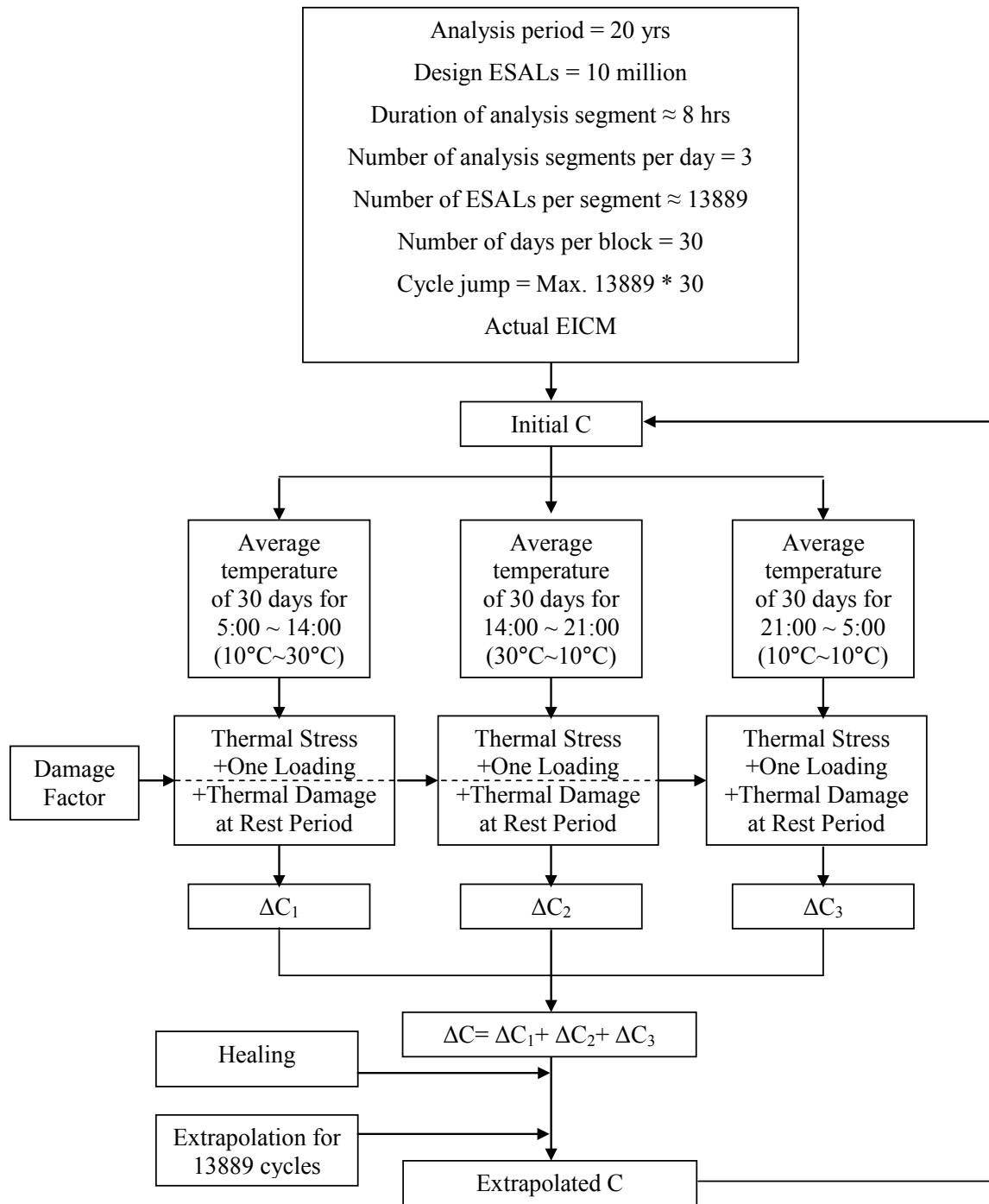


Figure 3-27. Extrapolation flow chart

The results of two different cases, (a) a healing-dominant case and (b) a damage-dominant case, are shown in Figure 3-28, along with the results based on the extrapolation. To compute the extrapolated value, the damage growth in the selected cell for the first cycle was extracted from the VECD-FEP++ analysis and input into a spreadsheet-implemented version of the extrapolation algorithm. The spreadsheet-based algorithm is used here for convenience only. In a full simulation, the extrapolation process is completed automatically in the VECD-FEP++ software. Figure 3-28 shows that the extrapolation algorithm effectively matches the output from the complete analysis at 1,300 cycles. The figure also shows that the agreement between the reference simulation and the extrapolated simulation decreases as the number of cycles increases, together with a tendency for the pseudo stiffness to approach an asymptotic value. Thus, it is expected that the differences observed in the extrapolation to 1,300 cycles would be similar to the differences observed at 13,000 cycles. Direct proof of this hypothesis was not performed due to the time necessary to create a reference simulation for 13,000 cycles.

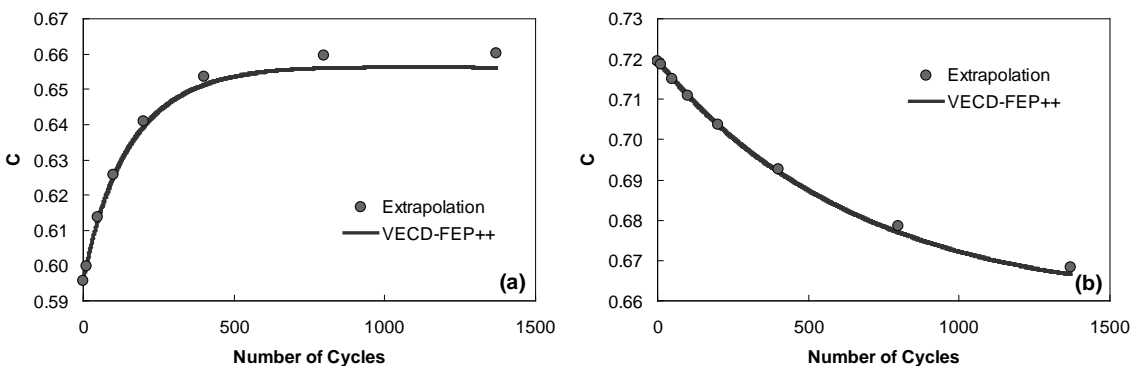


Figure 3-28. Effect of extrapolation calculation on predicted damage growth: (a) healing-dominant case and (b) damage-dominant case

3.1.4.5 Thermal stress calculation

In the current simulation extrapolation scheme, the temperature for a given month is averaged for each of the time segments identified in Section 3.2.3.3.1. This method is acceptable for computing the stress and damage due to mechanical loading, but could yield erroneous

thermal damage results because it effectively smoothes some of the more extreme events. The thermal stress-related damage calculations are much more sensitive to changes in temperature because these damage calculations are directly proportional to the temperature raised to the VECD damage power, α . This proportionality can be observed by substituting the thermal strain, Equation 3-44, into the pseudo strain calculation, Equation 3-53, and then combining the result with the derived evolution law, Equation 3-54. Conversely, the temperature dependence for mechanical damage enters indirectly into the constitutive model by changes in reduced time in the calculation of the pseudo strain. This indirect entry does not mean that the mechanical damage is not sensitive to temperature, only that it is less sensitive to temperature than is thermal damage.

$$\varepsilon^R = \frac{1}{E_R} \int_0^t E(t-\tau) \frac{d\varepsilon}{d\tau} d\tau, \quad (3-53)$$

$$dS = \left(-\frac{1}{2} (\varepsilon^R)^2 \Delta C \right)^{\alpha/1+\alpha} \times (\Delta\xi)^{1/1+\alpha} \quad (3-54)$$

To compute the thermal damage more accurately, the theoretically observed proportionality between thermal damage and temperature raised to the VECD α was used. Equation 3-55 shows the averaging function that was applied to generate the weighted average temperature. Figure 3-29 provides a comparison of the average and weighted average temperature values computed for a daily temperature cycle. In this figure, the lines represent the daily temperature cycles for the 31 days of December for Laramie, Wyoming. The circles represent the mathematical average temperature, and the squares represent the weighted average temperature. Figure 3-29 shows that the overall average temperatures are not that different from each other.

$$T_{WA} = \left(\frac{\sum_{i=1}^N T^{\alpha}}{N} \right)^{1/\alpha} \quad (3-55)$$

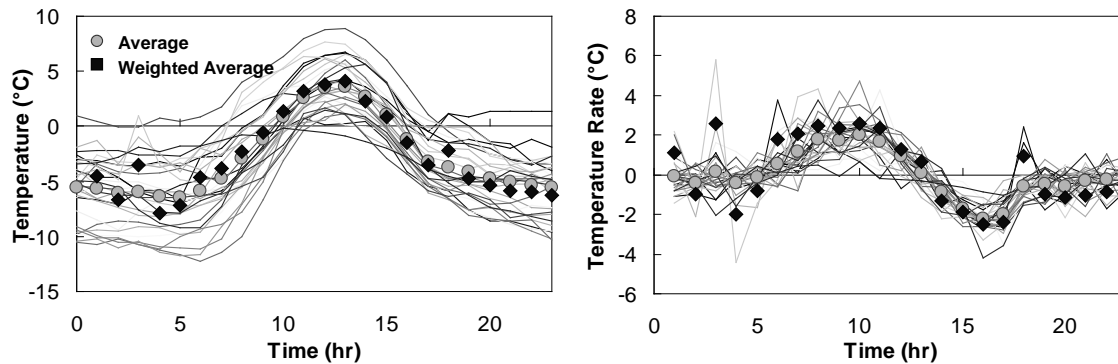


Figure 3-29. Original versus weighted average temperature and temperature rate for WY-Dec

To assess the consequences of these differences, the thermally induced damage was computed for each case and used in the extrapolation scheme. Coincident with this prediction, a rigorous time-wise analysis was performed using the daily temperature variations. Comparisons between the rigorous calculation and the average temperature calculations are shown in Figure 3-30. In this figure, the weighted average and arithmetic average predictions are shown only at the end of the month because they have been included in the extrapolation process. From Figure 3-30 it is clear that, even though the two averaging techniques yield only a slight difference according to Figure 3-29, the weighted average technique yields the more accurate solution for thermal-related damage.

For computational efficiency, the FEP++ uses only a single thermal gradient to compute the damage due to both thermal and mechanical loading. Thus, it is important that the method that yields acceptably accurate calculations for the thermal case does not yield unrealistic answers for the mechanical loading. The effect of using the weighted average technique in lieu of the arithmetic average is assessed by performing a limited simulation using both methods. The

results of this simulation are shown in Figure 3-31. In this figure, the x-axis shows the damage calculated via the arithmetic average temperature, and the y-axis shows the damage calculated via the weighted average temperature. These calculations were performed for each of the three daily time increments. Because both approaches yield basically the same amount of mechanical-related damage, and because the arithmetic average technique results in accuracy issues for thermal damage, the weighted average temperature was chosen for further analysis.

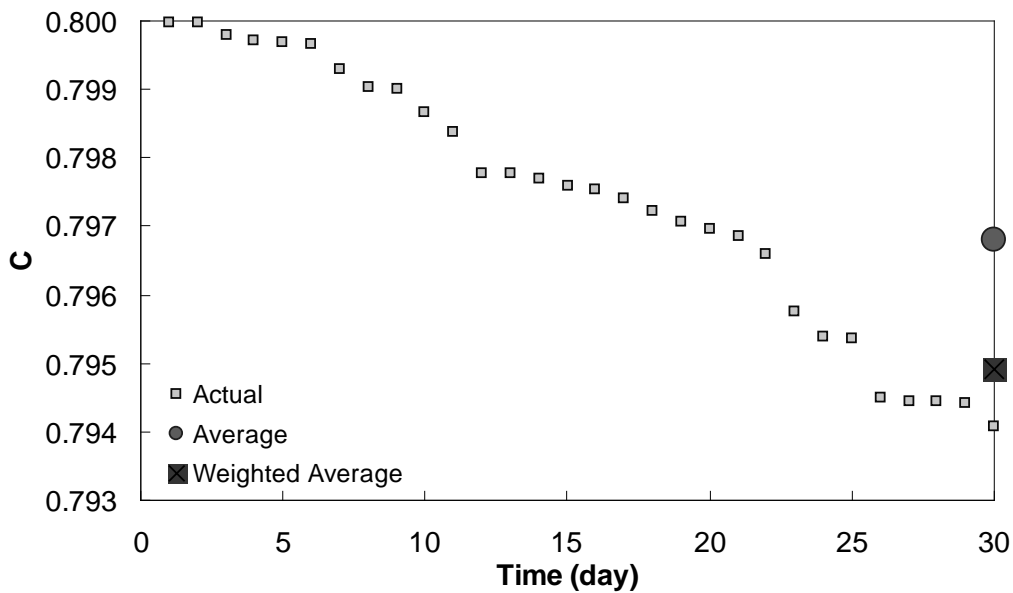


Figure 3-30. Damage accumulation at loading edge of pavement surface for WY-Dec

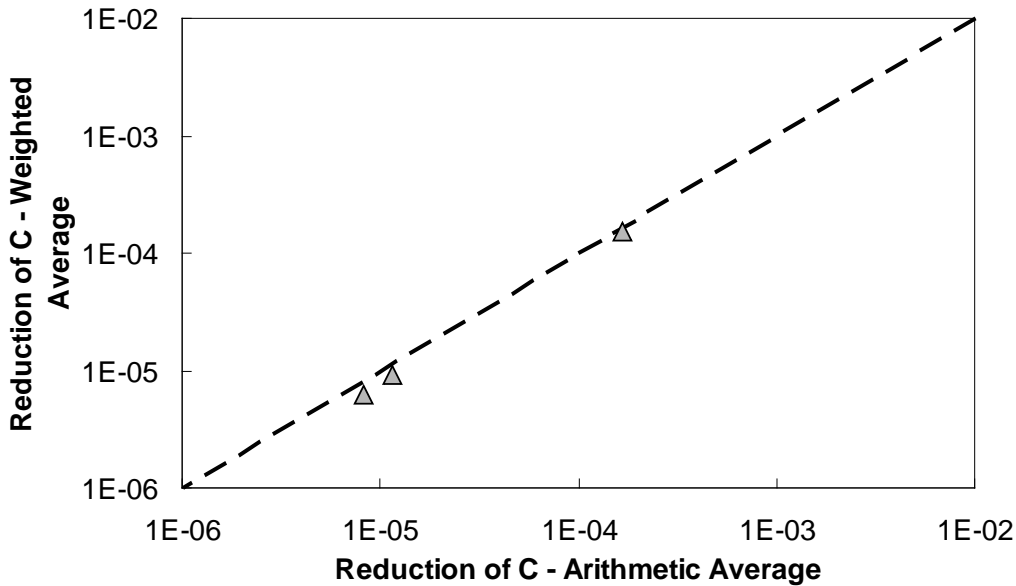


Figure 3-31. Arithmetic versus weighted average temperature and temperature rate for WY-Dec

3.1.5 Output Module

The output module consists of the tools and techniques necessary to view and interpret the VECD-FEP++ performance predictions. It creates a single file that can be opened, processed, and manipulated to view visual interpretations (contours) of the predicted damage, stress distribution, or other quantities of interest. This file can also be processed to extract different indices to quantify the visual observations.

3.1.5.1 Output in the form of a contour plot

Example contour plots and typical values are shown in Figure 3-32 a, b, c, and d for radial stress, radial strain, pseudo stiffness, and the condition index, respectively. Through qualitative observations of these contour plots, the damage distribution and evolution in the overall pavement structure can be captured easily. More importantly, because the VECD-FEP++ does not assume the location where the damage is concentrated, and usually the severe damage occurs in small areas (i.e., a few structural elements as compared to several thousands of elements within the whole pavement structure), the damage concentration needs to be tracked for the

entire structure. The contour plots in Figure 3-32 show the grids that represent the elements that build the AC layers in the pavement structure. For the sensitivity analysis, the element size of 1.4 cm by 1.4 cm was determined for the AC layers. Moreover, significant damage in an element of this size could be considered to be the initiation of cracking, based on field observations.

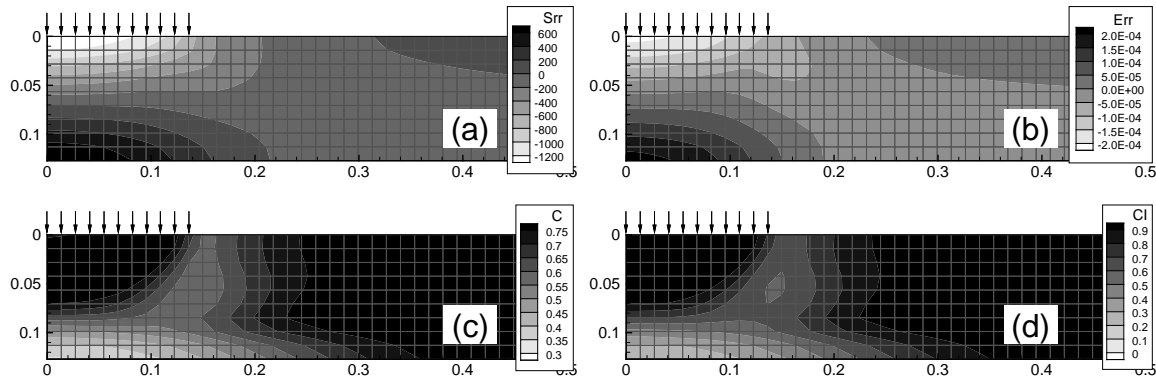


Figure 3-32. Examples of contour plots for: (a) radial stress, (b) radial strain, (c) pseudo stiffness, and (d) the condition index

3.1.5.2 Quantification of cracking prediction

A scaled parameter, referred to as the condition index (CI) and defined by Equation 3-56, was computed for each element in the pavement structure to interpret the loss in material integrity. The CI is a variable that ranges from 0 to 1, with 0 being failure according to the material level criteria discussed in Subsection 3.2.2.2 (see Figure 3-13), and 1 representing a completely intact body.

$$CI = \frac{C_i - C_{f,i}}{C_{intact} - C_{f,i}} \quad (3-56)$$

where

- CI = the condition index,
- C_{intact} = the intact pseudo stiffness value,
- C_i = pseudo stiffness at instant i , and
- $C_{f,i}$ = failure pseudo stiffness at instant i .

3.1.5.3 Output in the form of a stacked bar graph

Examining the damage contours has some advantages, but it is not the most efficient analytical method for evaluating the many cases that are simulated in this work. To better quantify the simulation results, a quantity termed the *condition index area* is employed. This quantity is defined as the percentage of the total investigation area with CI values of 0-0.2, 0.2-0.4, 0.4-0.6, 0.6-0.8, and 0.8-1. To appropriately represent the pavement condition, the area from the load center to 0.5 meters in the horizontal direction and from the pavement surface to the bottom of the AC layer in the vertical direction has been chosen for the analysis (see Figure 3-32). The respective effects of top-down and bottom-up cracking can be determined using this quantity by separately calculating the CI for the upper and lower halves of the pavement structure. Once computed for each block (0-0.2, 0.2-0.4, etc.) the CI area (%) can be shown graphically using a stacked bar graph. Figure 3-33 shows an example stacked bar graph for the CI area that was calculated from the CI contour plot in Figure 3-32 (d).

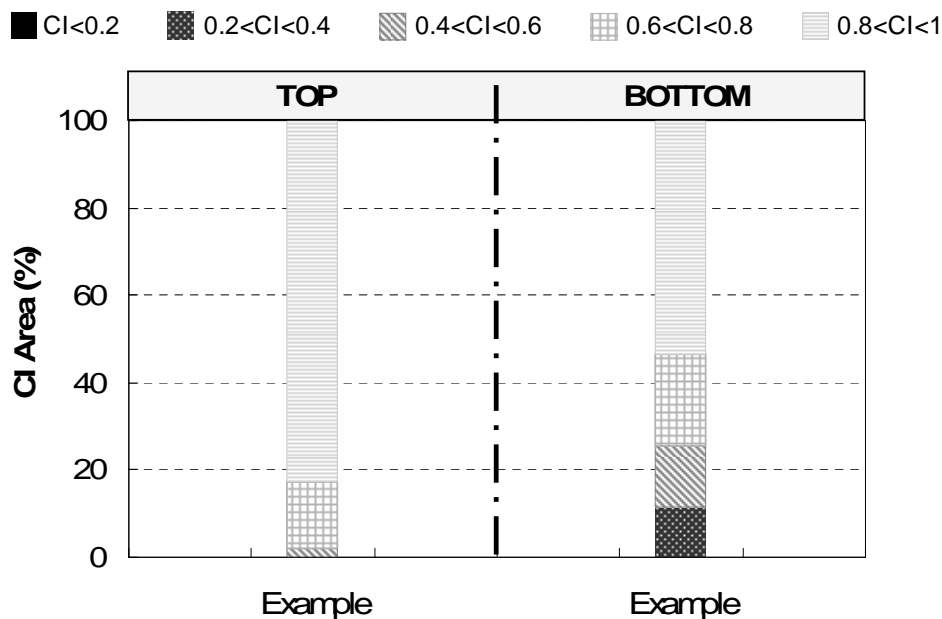


Figure 3-33. Example of condition index area

3.1.6 Model Integration

Reasonableness and sensitivity studies were carried out by a series of FEP++ simulations to show whether or not the framework development and integration into the VECD-FEP++ were performed correctly. First, a reasonableness check was performed to verify the proper implementation of the VECD model, and hence, the analytical sub-models (healing, aging, thermal damage, etc.) were not included. Second, a sensitivity check was conducted to investigate the effect of each analytical sub-model on pavement performance. From the sensitivity studies it was revealed that the sub-models affect pavement performance in different ways and to varying degrees (details of these studies are illustrated in Appendix A).

Two pavement structures, as shown in Figure 3-34, were investigated: thin (127 mm or 5 in.) and thick (304.8 mm or 12 in.). Two AC mixes, the Control and SBS mixes used in the FHWA ALF research, were selected for the simulation because all the necessary model data for both mixes were available, and it has been reported that both mixes show significantly different performance behavior (28). The aggregate gradation, asphalt content, and target air void levels are the same for both mixtures, as shown in Table 3-5.

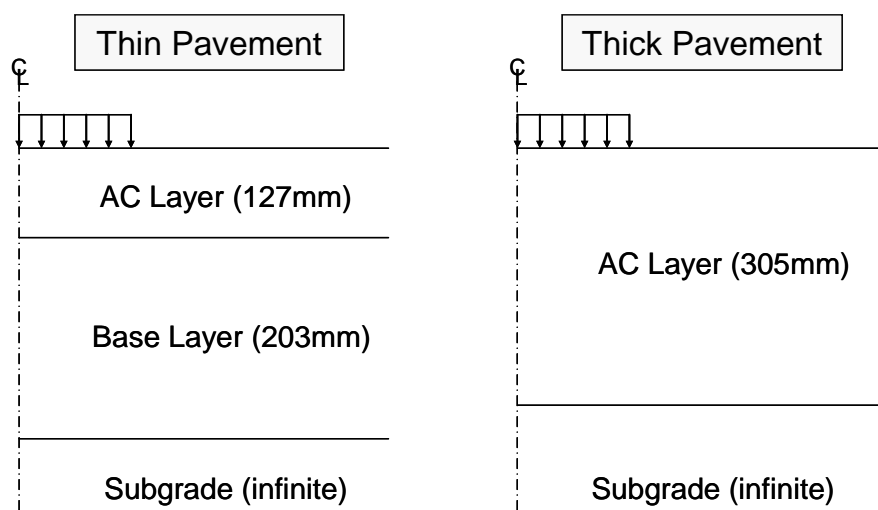


Figure 3-34. Pavement structures for FEP++ simulation

Results from the material characterization show large differences in the material responses (see Figure 3-35). The base layer for the thin pavement structure was 203 mm (8 in.) thick, and the subgrade for both structures was considered to be semi-infinite. The AC layers were modeled using the VECD model and additional analytical models to include such factors as aging, healing, damage factors, and thermal stress. The unbound material layers were assumed to be linear elastic at three different levels of modulus values (weak, medium, strong), as presented in Table 3-6. The moduli of both the base layer and subgrade materials were varied to yield either a weak, moderate, or strong support condition. Depending on the purpose of the simulation, the appropriate pavement temperature was selected from the five regional temperature profiles generated from the EICM. The temperatures varied in accordance with time and depth within a given AC layer. To simulate the variations in temperature with depth, each row of elements in the FEM mesh was assigned a different temperature consistent with the EICM output at the average depth of the row. A moving load was simulated by applying a 0.1-second haversine loading pulse with a magnitude of 40 kN (9 kip) and contact pressure of 689 kPa (100 psi) on the pavement surface, followed by 62.1 seconds of rest.

Table 3-5. Volumetric Properties of Laboratory Mixtures for ALF Pavements

Mix Designation	Control	SBS
Binder Type	Unmodified	Styrene Butadiene Styrene
Binder Grade	PG 70-22	PG 70-28
Binder Content	5.30%	
NMSA*	12.5 mm	
Target Air Voids	4%	
Sieve Size	Gradation, % Passing	
37.5 mm	100.0	
25.0 mm	100.0	
19.0 mm	100.0	
12.5 mm	93.8	
9.5 mm	85.2	
4.75 mm	56.0	
2.36 mm	35.6	
1.18 mm	25.1	
0.600 mm	18.4	
0.300 mm	13.1	
0.150 mm	9.3	
0.075 mm	6.7	

* Nominal Maximum Size Aggregate

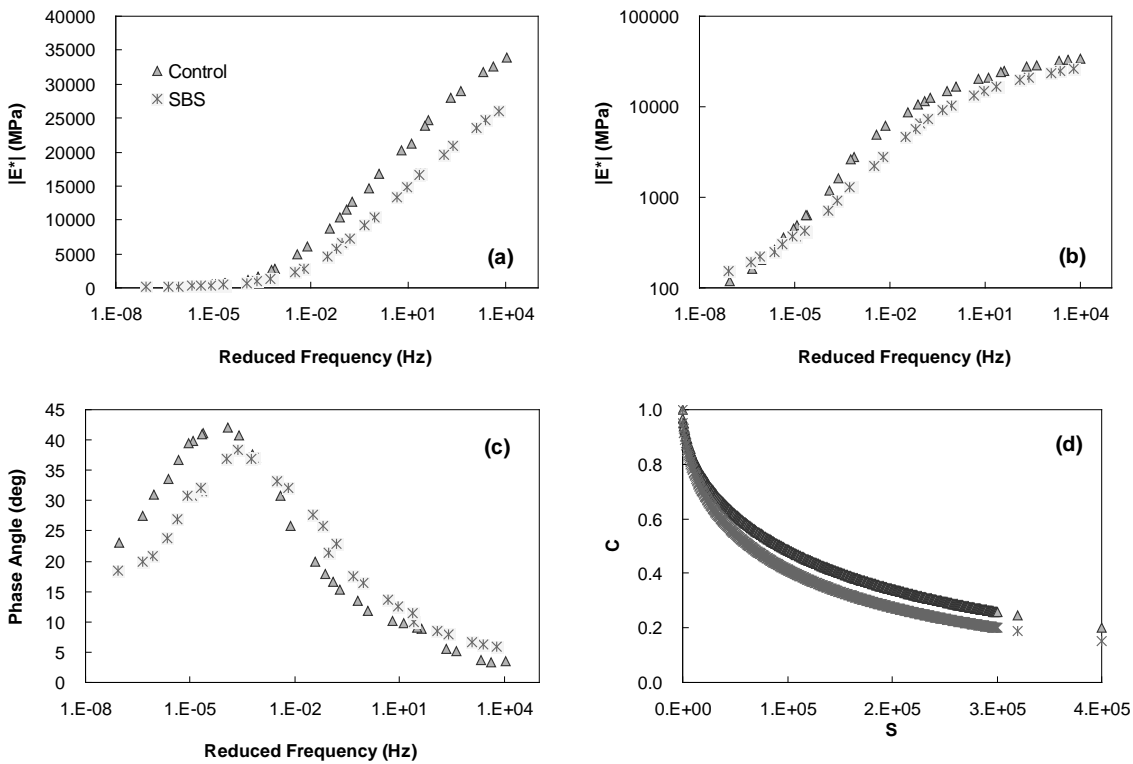


Figure 3-35. Characteristics of Control and SBS mixtures for FEP++ simulation: (a) $|E^*|$ mastercurve in semi-log scale; (b) $|E^*|$ mastercurve in log-log scale; (c) phase angle mastercurve; and (d) damage characteristic curve

Table 3-6. Elastic Modulus of Unbound Layers

Layer	Elastic Modulus, MPa (ksi)		
	Weak	Moderate	Strong
Base Layer	138 (20)	276 (40)	552 (80)
Subgrade	41 (6)	83 (12)	166 (24)

To save computational time for the example simulation and parametric study, the simulations were performed until one element reached a pseudo stiffness value of 0.25 or until 10 years had been simulated. In the case of the thin pavement, the length of time was somewhat longer than a full year, but the thick pavement was simulated for the full 10 years. The pseudo stiffness value of 0.25 has been found to describe the failure point of monotonic direct tension tests and is a conservative value for the failure point of cyclic fatigue tests. Based on experience and some limited trials, it was found that when one element reached a pseudo stiffness value of 0.25, the CI was zero or close to zero for many elements (including those neighboring the element with the pseudo stiffness value of 0.25). The failure criterion for any one element, e.g., that used in defining the CI, was always based on the criterion described in Section 3.2.2.2.

3.2 Example Simulation

3.2.1 Introduction

An example simulation of the FEP++ using the VECD model and all accompanying analytical sub-models was carried out to demonstrate the capabilities of the modeling approach. For this example problem, a single region – wet, freeze-thaw cycling for Washington, D.C. – was chosen. Only a single support condition, *moderate*, was used for this example, and all other factors were fixed, except the pavement thickness, which was evaluated at the 127 mm (5 in.) and 305 mm (12 in.) levels. All of the analytical sub-models were active for these simulations. The simulation details are summarized in Table 3-7.

Table 3-7. Simulation Details for Example Simulation

Item	Number of Cases	Details
Region	1	DC
Structure	2	Thin (127 mm or 5 in.), Thick (304.8 mm or 12 in.)
AC Material	1	ALF Control
Support Condition	1	Moderate
Aging	1	Yes
Healing	1	High
Thermal Stress	1	High Thermal Coefficient
Damage Factor	1	5-yr Average EICM
Climate	1	5-yr EICM Repeated
Load Level	1	40 kN (9 kip)
Contact Pressure	1	689 kPa (100 psi)
Total Number of Cases	2	

3.2.2 Simulation Results and Discussion

Results from the simulation are presented by stacked bar graphs for the CI areas shown for the thin and thick pavements in Figure 3-36 and Figure 3-37, respectively (contour plots for the same simulation results can be found in Appendix A). In Figure 3-36 and Figure 3-37, the simulation month number (all simulations began in July) and the abbreviated month that corresponds to the simulation are shown on the x-axis. Figure 3-36 shows the results for the months of October through July of the first simulation year for the thin pavement. Figure 3-37 presents the final nine months of the thick pavement simulation.

A few observations can be made from Figure 3-36 and Figure 3-37. First, it is evident that the damage in the thin pavement section is much larger than the damage in the thick pavement at the equivalent time. This result is to be expected because both simulations were conducted for the equivalent of a 10 million ESAL. It is also observed from examining the damage evolution between the months of April and July that pavement healing may constitute a major component of a pavement's total fatigue performance. However, it is seen, through the mechanisms associated with repeated loading, healing and aging, that the thick pavement shows an area of concentrated damage at the pavement surface near the wheel load edge. Therefore, it appears that

healing is more effective near the pavement surface of a thin pavement than that of a thick pavement (i.e., the thick pavement appears to heal better at the bottom of the pavement than does the thin pavement).

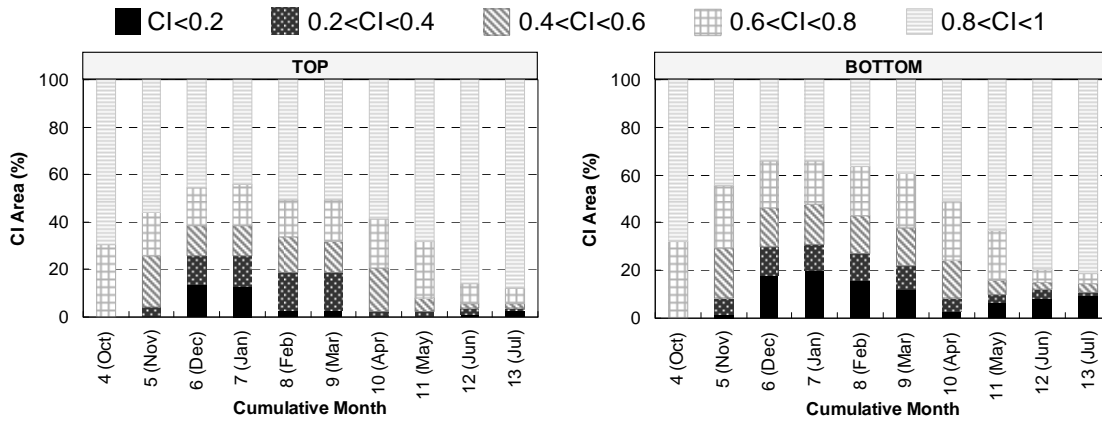


Figure 3-36. Condition index area (%) for thin pavement simulation

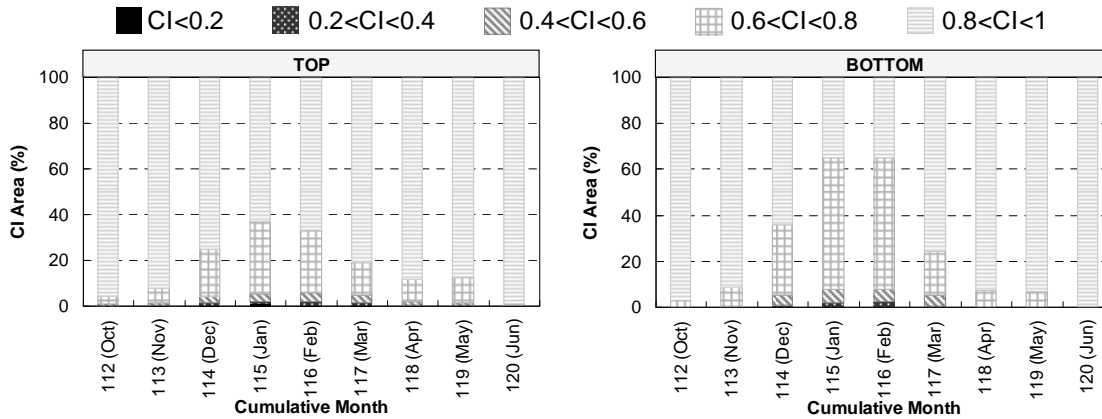


Figure 3-37. Condition index area (%) for thick pavement simulation

3.3 Model Evaluation: Parametric Study

3.3.1 Introduction

A systematic evaluation using the VECD-FEP++ code was carried out to gain insight into the parameters most responsible for the development and/or dominance of top-down cracking. Combinations of three regions (DC, FL, and WY), two structures (thin and thick pavements), two materials (Control ALF and SBS ALF) and two support conditions (weak and strong) were investigated so that simple and interactive variables could be studied. The factorial levels are

summarized in Table 3-8. The most important factors identified, for which all the necessary inputs were available, are material type (modified versus unmodified), pavement thickness (thick versus thin), climate (wet, no freeze versus wet, freeze-thaw cycling versus dry, hard freeze, spring thaw), and support condition (weak versus strong).

The CI area graphs are shown for the thin and thick pavements in Figure 3-38 and 3-39, respectively. The results for the thin pavements are all at the end of the ninth month (March), whereas the results for the thick pavements are also for March, but at year 10 (contour plots for the same simulation results are provided in Appendix A to show overall trends). The naming convention used for the different simulations is by letter and in the following order: pavement type, thick (T) or thin (t); material type, ALF control (C) or ALF SBS (S); and support condition, weak (W) or strong (S).

Table 3-8. Simulation Details for the Parametric Study

Item	Number of Cases	Details
Region	3	DC, FL, WY
Structure	2	Thin (127 mm or 5 in.), Thick (304.8 mm or 12 in.)
AC Material	2	ALF Control vs. ALF SBS
Support Condition	2	Weak vs. Strong
Aging	1	Yes
Healing	1	High
Thermal Stress	1	High Thermal Coefficient
Damage Factor	1	5-yr Average EICM
Climate	1	5-yr EICM Repeated
Load Level	1	40 kN (9 kip)
Contact Pressure	1	689 kPa (100 psi)
Total Number of Cases	24	Combination of all cases

The stacked bar graphs for the CI areas were calculated for March to best demonstrate the observed trends. The magnitude of these trends varies somewhat from month to month due to the relative effects of the different analytical sub-models. Healing, for example, may substantially reduce the amount of accumulated damage during the summer months by slightly different amounts in Wyoming and in Florida. However, it was observed that even with these differences,

the major trends do not change substantially, and that these trends are observed most clearly in March.

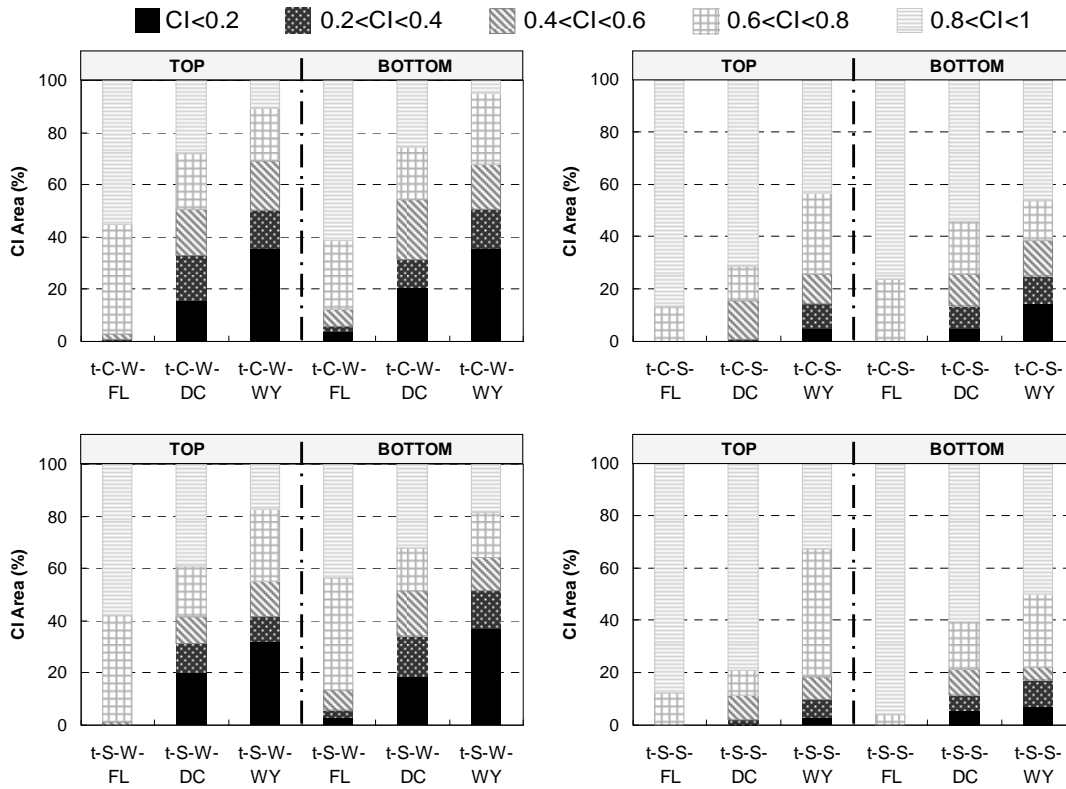


Figure 3-38. Condition index area (%) for thin pavement

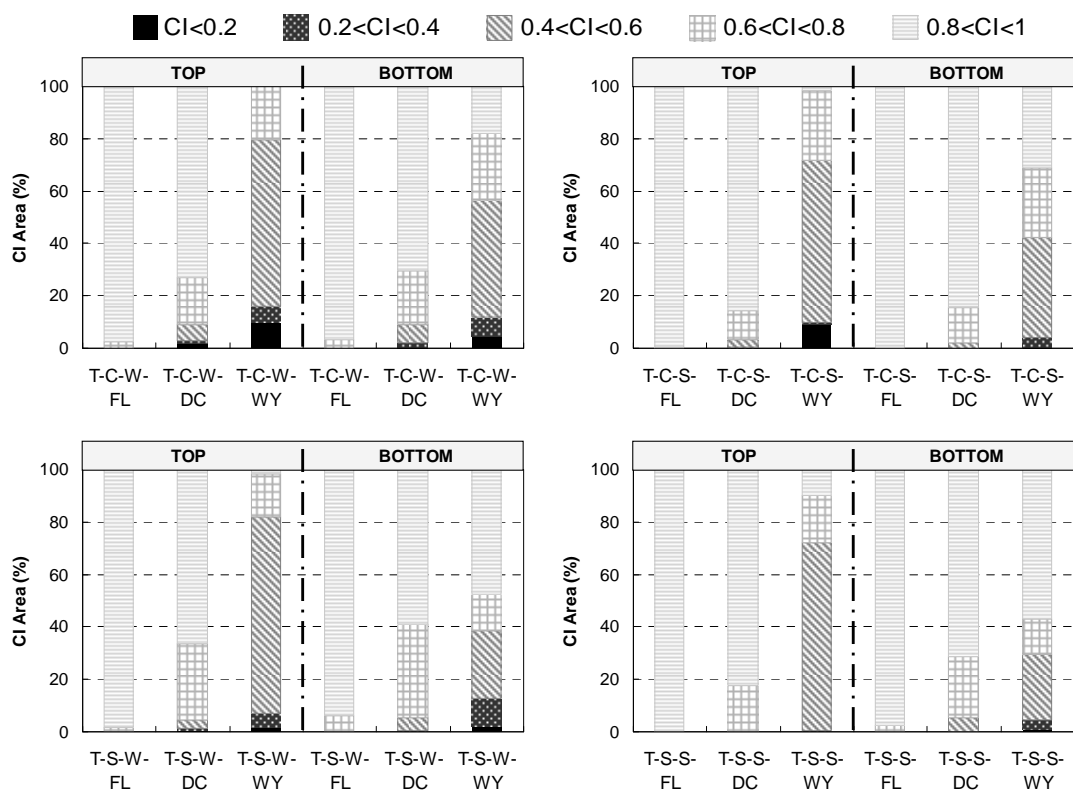


Figure 3-39. Condition index area (%) for thick pavement

3.3.2 Effect of Region

A comparison of the results at a consistent thickness and time for pavements constructed with similar materials indicates that the more extreme and cooler climates, as compared to less extreme and warmer climates, tend to show a higher concentration of highly damaged areas at both the top and bottom of the pavement (e.g., damage accumulates much more quickly in Wyoming than in Florida) because of the relatively stiff PG 70-22 binder used in the mixtures. Thus, mixtures with these binders would likely not be used in a climate such as that of Wyoming. The key factors that may lead to this increased damage accumulation are (1) increased thermal damage potential and (2) decreased healing potential. Both factors worsen due to extreme temperature variations and generally cool temperatures. Longitudinal thermal stress was used to calculate the associated thermal damage, which tends to overestimate the thermal effect. In the future, transverse thermal stress should be used, which is limited by the maximum

frictional resistance that can develop between the HMA surface and base layers. The SBS material tends to soften the regional differences slightly as does the use of a strong support condition. The support condition effect is more prevalent for the thin pavement. Care should be taken when considering these support conditions, though, because they do not account for differences due to support layer moisture or freeze/thaw action.

3.3.3 Effect of Structure

Structural effects are found to be similar to those shown previously in Figure 3-36 and Figure 3-37. Specifically, for the same traffic conditions, a thin pavement shows more significant damage earlier than a thick pavement. Also, thin pavements tend to show high damage zones at both the top and the bottom of the pavement structure that start to grow from the early stages of loading. Thick pavements, on the other hand, tend to develop damage at a much slower rate than thin pavements and also tend to show higher concentrations of damage near the pavement surface. These differences are exacerbated by cooler and more extreme temperature conditions. It should be noted that the designation of a pavement as *thin* or *thick* is somewhat arbitrary; it is defined as *thin* or *thick* relative to traffic loadings. For example, a 127 mm (5 in.) pavement may be considered thin for the case of 10 million ESALs, but would be considered thick for a significantly less loading (e.g., 100,000 ESALs).

3.3.4 Effect of Unbound Layer Property

The support layer stiffness has an important effect on the distribution of damage in the pavement structure. In general, weak support results in more extensive and more severe damage growth than strong support. This effect is more pronounced in thin pavements, but tends to have a more significant effect on damage at the top of the pavement in thick pavements. The effect is also more pronounced in cooler and more extreme climatic conditions.

3.3.5 Effect of Asphalt Mixture Properties

From the thin pavement simulation, it appears that the SBS material results in improved performance with regard to damage at the bottom of the pavement but slightly poorer performance in terms of damage at the top of the pavement for the one month considered. The damage progression from October through June is shown in Figure 3-40. From examining the behavior at the end of June, it is clear that the SBS material shows an overall benefit in the minimum CI levels for both top-down and bottom-up related damage. This difference occurs because the damage in SBS pavements tends to slow considerably during the summer months due to the overall lower modulus of the SBS material relative to the Control pavement and the tendency of the SBS pavement to exhibit more viscoplastic behavior at high temperatures and thus to have a more favorable DCF than the Control pavement. However, the healing potential function applied in this simulation is the same for both the Control and SBS materials.

The same basic mechanisms that are active in the thin pavement are also active in the thick pavement, although the effects are somewhat less noticeable due to the less extreme temperature variations at the bottom of the pavement structure in the thick pavement. The effect of the SBS material is also seen more clearly in the thick pavement, irrespective of potential differences in healing and the DCF. In the early stages (year 1), the SBS pavements tend to show a lower minimum CI value than do the Control materials. However, a transition begins to occur around year 5 when the SBS material tends to show a larger damaged area, but this damaged area has a higher minimum CI value than the corresponding Control section. This effect appears to be slightly more pronounced for the Wyoming climatic condition.

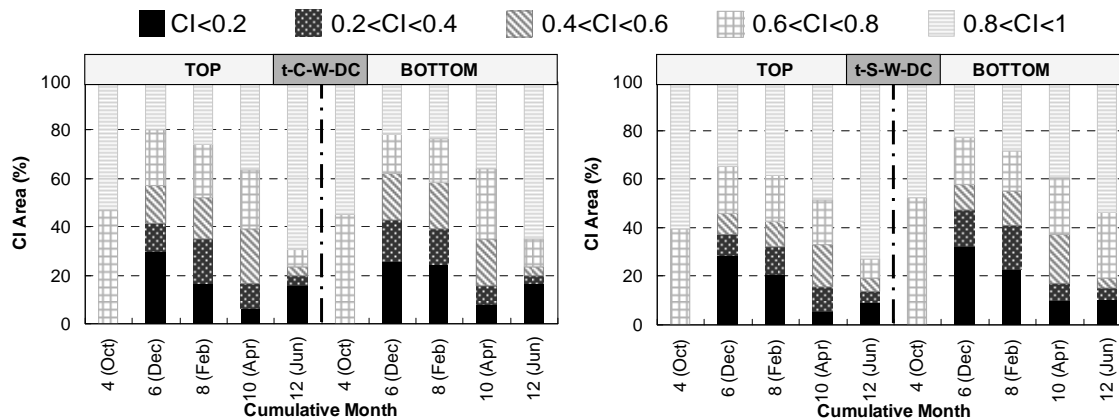


Figure 3-40. Damage progression and healing in SBS and Control pavements

3.4 Summary of Findings

An enhanced VECD-based model for predicting the initiation of top-down cracking in HMA layers has been established in this portion of the study. This effort was accomplished by developing, modifying, and/or investigating several important material property models, such as an aging model, healing model, failure criteria, viscoplasticity, and thermal stress, and then incorporating these sub-models into the existing VECD model. The material models were converted to and/or combined with the structural models. These sub-models were implemented into the VECD-FEP++, and an extrapolation method for predicting top-down cracking initiation was developed.

Reasonableness and sensitivity studies were undertaken to verify that the framework development and implementation into the VECD-FEP++ were performed correctly. A sensitivity study to investigate the effect of each sub-model on pavement performance revealed that each sub-model affects pavement performance in different ways and to varying degrees. To demonstrate the full capabilities of the VECD-FEP++, two example simulations were carried out, and the results indicated that the interactions among the sub-models and overall trends in terms of pavement behavior were captured successfully.

A systematic evaluation using the VECD-FEP++ was carried out to gain insight into the parameters most responsible for the development and/or dominance of top-down cracking. In general, more damage at both the top and bottom of the pavement was observed in the case of a cold climate, thin structure, weak support layer, and the use of the Control mixture. However, because the longitudinal thermal stress was used to calculate the associated thermal damage, the thermal effect in cold climates may have been overestimated. It was also found that thin pavements tend to show more damage at the bottom of the pavement, whereas thick pavements tend to show a higher concentration of damage at the top of the pavement.

CHAPTER 4

FINDINGS: THE HMA-FM-BASED SYSTEM

The primary feature of the HMA-FM-based crack propagation model was to account for effects of macro cracks during crack propagation. This model was comprised of the following key elements:

1. A critical condition concept that can more accurately capture field observations and significantly reduces the computation time required for long-term pavement performance prediction.
2. Material property sub-models that account for changes in near-surface mixture properties with aging [e.g., increase in stiffness (stiffening), reduction in fracture energy (embrittlement), and reduction in healing potential] which make pavements more susceptible to top-down cracking.
3. A thermal response model that predicts transverse thermal stresses that can be an important part of the top-down cracking mechanism.
4. A pavement fracture model that predicts crack growth with time, accounting for the effect of changes in geometry on stress distributions.

In addition, a simplified fracture energy-based approach for crack initiation (i.e., a crack initiation model without considering damage zone effects) was developed and integrated with the HMA-FM-based model to illustrate the capabilities of a completed system (which was named the top-down cracking performance model).

4.1 Framework

As shown in Figure 0-1, the overall framework of the integrated system has five main parts: (1) the inputs module, (2) the material property model, (3) indirect tensile test, (4) pavement response model, and (5) pavement fracture model.

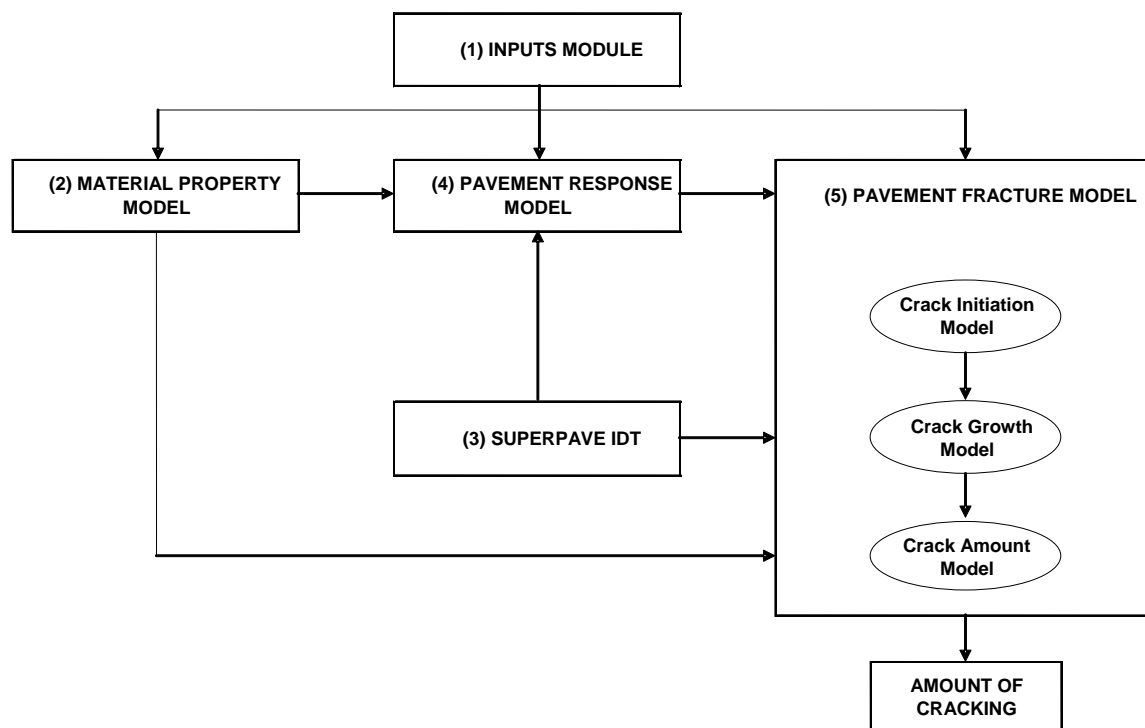


Figure 0-1. Framework of the top-down cracking performance model

4.1.1 Inputs Module and Indirect Tensile Test

The inputs module provides pavement material and structural properties, temperatures within HMA layer (as predicted using an enhanced integrated climatic model), and traffic volume (in ESALs). Because the use of load spectra to represent the traffic would have significantly increased the complexity of model development and its use on model accuracy was unknown, the research team decided to express the traffic in terms of ESALs (assuming an even spacing of ESALs over time). Table 0-1 summarizes the sub-models of the HMA-FM-based system along with the input requirements.

Table 0-1. Input required for sub-models of the HMA-FM-based system

Sub-model	Sub-model component	Input requirement
Material property model	AC stiffness aging model	- Basic mixture characteristics (gradation, binder type, mix volumetrics)
	AC tensile strength aging model	- Temperature, loading time, and aging time - Stiffness (from AC stiffness aging model)
	Fracture energy limit aging model	- Material coefficients a_n - Stiffness (from AC stiffness aging model)
	Healing model	- Initial fracture energy - Aging parameter k_1 (to be determined in calibration) - Stiffness (from AC stiffness aging model) - Initial fracture energy - Critical stiffnesses.
Pavement response model	Load response model	- Structural properties of each layer (thickness, modulus, and Poisson's ratio) - Stiffness (from AC stiffness aging model) - Equivalent single axle load
	Thermal response model	- Structural property of AC layer (thickness) - Relaxation modulus master curve parameters: E_i, λ_i, η_v - Temperature and thermal contraction coefficient

Table 0-1. Continued

Sub-model	Sub-model component	Input requirement
Pavement fracture model	Crack initiation model	<ul style="list-style-type: none"> - Load and thermal-induced stresses (from response models) - Creep compliance master curve parameters: m, D_1, η_v - Mixture fracture and healing properties (from material property model) - Traffic (in ESALs)
	Crack growth model	<ul style="list-style-type: none"> - Time and location of initial crack (from crack initiation model) - Structural properties of each layer (thickness, modulus, and Poisson's ratio) - Stiffness (from AC stiffness aging model) - Thermal-induced stresses (from thermal response model) - Stress intensity factor for an edge crack - Creep compliance master curve parameters: m, D_1, η_v - Mixture fracture and healing properties (from material property model) - Traffic (in ESALs)
	Crack amount model	<ul style="list-style-type: none"> - Change of crack depth over time (from crack growth model)

The Superpave indirect tensile test (IDT) developed as part of the Strategic Highway Research Program (SHRP) (29) was used to determine damage and fracture properties on field cores as part of the calibration efforts. Three types of tests were performed with the Superpave IDT: resilient modulus, creep compliance (for damage rate), and tensile strength (for fracture energy limit).

4.1.2 Material Property Model

Based on a brief review of the HMA-FM model and its relevant material property models, four important sub-models were developed, including aging models for asphalt concrete (AC) stiffness, tensile strength, and fracture energy (FE) limit, and a healing model. A summary of these sub-models is presented below (details of the development of the new models are presented in Appendix B).

The AC stiffness aging model was developed on the basis of a binder aging model (24) and a dynamic modulus model (30). In this model, the following empirical equation was identified to consider the aging effect on mixture stiffness,

$$|E^*|_t = |E^*|_0 \frac{\log \eta_t}{\log \eta_0} \quad (0-1)$$

where $|E^*|_t$ and $|E^*|_0$ represent the stiffnesses corresponding to aged and unaged conditions, respectively, and η_t and η_0 correspond to the aged and unaged binder viscosity. The AC tensile strength aging model was developed by directly relating tensile strength to the AC stiffness aging model based on the following relationship developed by Deme and Young (31),

$$S_t = \sum_{n=0}^5 a_n \cdot (\log S_f)^n \quad (0-2)$$

where S_f is the tensile stiffness at a loading time of 1800 seconds that can be obtained from the AC stiffness aging model by considering a reduction factor from compression to tension. The constants a_n are as follows:

$$\begin{aligned} a_0 &= 284.01, & a_1 &= -330.02, & a_2 &= 151.02, & a_3 &= -34.03, \\ a_4 &= 3.7786, & a_5 &= -0.1652 \end{aligned}$$

The FE limit surface aging model was conceived and expressed in the following form:

$$FE_f(t) = FE_i - (FE_i - FE_{\min}) \cdot [S_n(t)]^{k_1} \quad (0-3)$$

where, FE_i is the initial fracture energy. FE_{\min} is the minimum value of the FE limit after a sufficiently long aging period t_{inf} . In this research, FE_{\min} was determined based on experience (field specimens) to be 0.2 kJ/m^3 , and t_{inf} was chosen as 50 years. k_1 is an aging parameter to be determined from calibration. $S_n(t)$ is the normalized change of stiffness at the surface of the AC layer, and is expressed as

$$S_n(t) = \frac{S(t) - S_0}{S_{\max} - S_0} \quad (0-4)$$

where $S(t)$ is the stiffness at the surface of the AC layer. S_0 and S_{\max} are $S(t)$ when t is set as 0 and 50 years, respectively. Therefore, it can be seen that $S_n(t)$ is a parameter that varies between zero and one. The following relationship was conceived to describe the FE limit versus depth relation:

$$FE_f(t, z) = FE_i - [FE_i - FE_f(t)] \cdot S(t, z) / S(t) \quad (0-5)$$

where $S(t, z)$ is the general expression for AC stiffness. Based on the FE limit aging model, the DCSE limit aging model was developed and is expressed as follows:

$$DCSE_f(t, z) = FE_f(t, z) - [S_i(t, z)]^2 / [2 \cdot S(t, z)] \quad (0-6)$$

where, $S_i(t, z)$ is the general expression for AC tensile strength.

The development of a healing model was completed in two steps. First, a mixture level healing model was obtained based on the research by Kim and Roque (32). As a further step, possible improvements to this model for application in real pavement sections were investigated. This effort resulted in a simplified empirically based healing model that has three components: (1) a maximum healing potential aging model, (2) a daily-based healing criterion, and (3) a yearly-based healing criterion.

The maximum healing potential surface aging model developed in this study is described by the following relationship:

$$h_{ym}(t) = 1 - [S_n(t)]^{FE_i/1.67} \quad (0-7)$$

where t is time in years. The maximum healing potential versus depth relation is

$$h_{ym}(t, z) = 1 - [1 - h_{ym}(t)] \cdot \frac{S(t, z)}{S(t)} \quad (0-8)$$

where $S(t, z)$ is the general expression for AC stiffness, and $S(t)$ is the stiffness at the surface of AC layer.

The daily-based healing criterion was developed to estimate the recovered damage on any particular day. It was assumed that the damage generated in a day would be healed according to a daily normalized healing parameter h_{dn} which is defined as

$$h_{dn} = 1 - \frac{DCSE_{d_remain}}{DCSE_{d_induced}} \quad (0-9)$$

where $DCSE_{d_induced}$ is the dissipated energy induced during the day, and $DCSE_{d_remain}$ is the dissipated energy remaining at the end of the day after healing. Thus

$$DCSE_{d_remain} = DCSE_{d_induced} \cdot (1 - h_{dn}) \quad (0-10)$$

The daily normalized healing parameter depends on depth, time, and temperature. In this study, h_{dn} was correlated with the daily lowest stiffness (S_{low}) of the AC layer because the healing potential is believed to be closely related to the AC material's capacity to flow. Given that S_{low} is the lowest stiffness of a day, it represents the highest flow capacity of the material on that day, which was used to estimate the material's healing potential.

The yearly-based healing criterion was developed to address continuous healing. In this healing criterion, it was assumed that all damage accumulated during a yearly period (started from July 1st) can be at least partially healed according to a yearly normalized healing parameter, h_{yn} , which is defined as

$$h_{yn} = 1 - \frac{DCSE_{y_remain}}{DCSE_{y_induced}} \quad (0-11)$$

where $DCSE_{y_induced}$ is the dissipated energy induced during the year, and $DCSE_{y_remain}$ is the dissipated energy remaining at the end of the year after healing. Thus

$$DCSE_{y_remain} = DCSE_{y_induced} \cdot (1 - h_{yn}) \quad (0-12)$$

The yearly normalized healing parameter h_{yn} was determined based on an averaged daily lowest stiffness, S_{lowa} , over a prolonged period, T_p (i.e., the last 40 days of the yearly period being analyzed).

4.1.3 Pavement Response Model

The pavement response model has two sub-models: (1) a load response model and (2) a thermal response model. A brief summary of these sub-models is presented below (a detailed illustration of these two models is given in Appendix B).

The load response model was primarily used to predict bending-induced maximum surface tensile stresses away from the tire. The model first estimated the AC modulus based on the temperature profiles and aging conditions. The load-induced tensile stresses at the pavement

surface were then predicted using 3-dimensional (3-D) linear-elastic analyses (LEA). The model automatically searched for the maximum tensile stress on the surface of the AC layer. The LEA was used strictly for predicting stress distribution. For small strain problems in systems that allow for stress relaxation between loading events, as is the case for pavement systems subjected to truck loading, there was no difference in the stress distribution predicted by LEA and viscoelastic analysis. A viscoelastic model, which is part of the HMA-FM-based model, was then used to predict strain and energy based on the predicted stress. Therefore, the error associated with using LEA should be negligible.

The thermal response model was developed based on a thermal stress model for predicting longitudinal thermal stresses and thermal cracking (33). Because top-down cracking (known to occur in the longitudinal direction) is particularly relevant to transverse thermal stresses, the existing thermal stress model was revised to account for transverse thermal stresses, which are limited by the maximum frictional resistance that can develop between the HMA surface and base layers.

4.1.4 Pavement Fracture Model

The pavement fracture model has three sub-models: (1) a crack initiation model, (2) a crack growth model, and (3) a crack amount model. These sub-models are summarized below (details regarding each of these models are presented in Appendix B).

The fracture energy-based crack initiation model was developed to predict the location and time of crack initiation in HMA layers, in conjunction with the material property model and pavement response model.

In the model, the load-associated damage and thermal-associated damage is obtained based on the pavement response models as follows,

- The load-associated damage per cycle (or, $DCSE_L/cycle$) is calculated as

$$DCSE_L / cycle = \int_0^{0.1} \sigma_{AVE} \sin(10\pi t) \dot{\varepsilon}_{pmax} \sin(10\pi t) dt \quad (0-13)$$

where σ_{AVE} is the average stress within the zone being analyzed to determine crack initiation and

$\dot{\varepsilon}_{pmax}$ is the creep strain rate.

- The thermal-associated damage over the time interval from $(t - \Delta t)$ to t (or, $DCSE_T/\Delta t$) is expressed as

$$DCSE_T / \Delta t = [\sigma(t) - \sigma(t - \Delta t)] \cdot [\varepsilon_{cr}(t) - \varepsilon_{cr}(t - \Delta t)] / 2 \quad (0-14)$$

where ε_{cr} is creep strain at time t . It can be expressed as

$$\varepsilon_{cr}(t) = \varepsilon_{cr}(t - \Delta t) + \frac{1}{2 \cdot \eta_v} [\xi(t) - \xi(t - \Delta t)] \cdot [\sigma(t) + \sigma(t - \Delta t)]$$

where ξ is the reduced time and η_v is the coefficient of mixture viscosity.

The energy-based failure criterion for crack initiation is as follows:

$$DCSE_{norm}(t) = \frac{DCSE_{remain}(t)}{DCSE_f(t)} \geq 1.0 \quad (0-15)$$

where, $DCSE_{remain}$ is the accumulated dissipated energy when taking healing into account,

$DCSE_f$ is the DCSE limit accounting for its degradation with aging, and $DCSE_{norm}$ is the

normalized damage accumulation. The threshold for crack initiation is 1.0. The $DCSE_{remain}$

during each time interval Δt can be further expressed as follows:

$$DCSE_{remain}(\Delta t) = (1 - h_{dn}) \cdot [n \cdot (DCSE_L / cycle) + DCSE_T(\Delta t)] \quad (0-16)$$

where n is number of load cycles in Δt .

The crack growth model was developed to predict the increase of crack depth with time in HMA layers, in conjunction with the material property model and thermal response model. In this model, load-induced tensile stresses ahead of the crack tip were predicted using a displacement discontinuity boundary element (DDBE) program (34); near-tip thermal stresses

were estimated by applying the stress intensity factor (SIF) of an edge crack to the thermal stresses predicted using the thermal response model. For each step of crack growth, the load-associated damage and the thermal-associated damage were calculated in the same manner as used in the crack initiation model, and the same failure criteria as used for crack initiation were used for crack propagation. Some key terms used during simulation of the step-wise crack growth follow:

- **Potential crack path:** The potential crack path was predefined in front of the crack tip at the beginning of crack growth simulation. It was composed of a series of zones of constant length heading toward the bottom of the AC layer.
- **Zone (in the potential crack path):** The zone is a means used to discretize the potential crack path to facilitate the calculation of crack growth. A constant zone length was used because it is far more computationally efficient than using variable zone lengths, with relatively little effect on the crack growth prediction. It was measured from lab testing that cracking develops in a stepwise manner in asphalt mixtures. For typical asphalt mixtures with a nominal maximum aggregate size (NMAS) of 12.5 mm, the stepwise developed crack length is about one half of the NMAS, or about 6 mm. Therefore, 6 mm (0.25 inch) was selected as the constant zone length.
- **Critical crack depth (CD_c):** The critical crack depth is the final crack depth in the crack growth model, which was preset to be one-half the depth of the AC layer, as field observations showed that top-down cracking generally does not exceed that depth.

The crack amount model was developed based on the assumption of a linear relationship between the crack amount and the crack depth over AC layer thickness ratio (C/D) because, generally, the crack mouth opening gets wider as a crack gets deeper. Also, for a crack of the same depth (i.e., same C), the crack mouth opening is wider in a thinner layer than in a thicker layer. Therefore, it seems logical to assume that the probability that a crack is visible and counted as a crack (and therefore the probability of increase in crack amount) increases as the C/D ratio increases. The model was used to convert the crack depth versus time relationship to that of crack amount versus time.

4.1.5 Outputs

The outputs for the predictive system are presented in the forms of (1) crack depth versus time and/or (2) crack amount versus time.

4.1.6 Model Integration

The integration of sub-models was performed based on a critical condition concept, which is central to the cracking perform model. It specifies that crack initiation and growth only develop under specific loading, environmental and healing conditions that are critical enough to exceed the mixture's energy threshold. Figure 0-2 shows the stepwise pattern of crack propagation based on this concept, which is in direct contrast to traditional fatigue theory that assumes cracking is a continuous process. The integration process was completed in two phases.

In Phase One, a critical condition identification (CCI) module was developed based on the critical condition concept. Figure 0-3 shows the flowchart of this module and its three components: (1) material property aging sub-models, (2) damage computation process (in terms of normalized dissipated creep strain energy: $DCSE_{norm}$), and (3) a healing model. The critical condition is identified by checking the $DCSE_{norm}$ (after healing) against the threshold. As also shown in Figure 0-3, the damage computation function has two options. Option A is used to compute damage before the onset of cracking and Option B is for damage computation during crack propagation. Accordingly, two follow-up modules were formed: (1) a crack initiation simulation (CIS) module using Option A and (2) a crack growth simulation (CGS) module using Option B. These are described in the following two subsections.

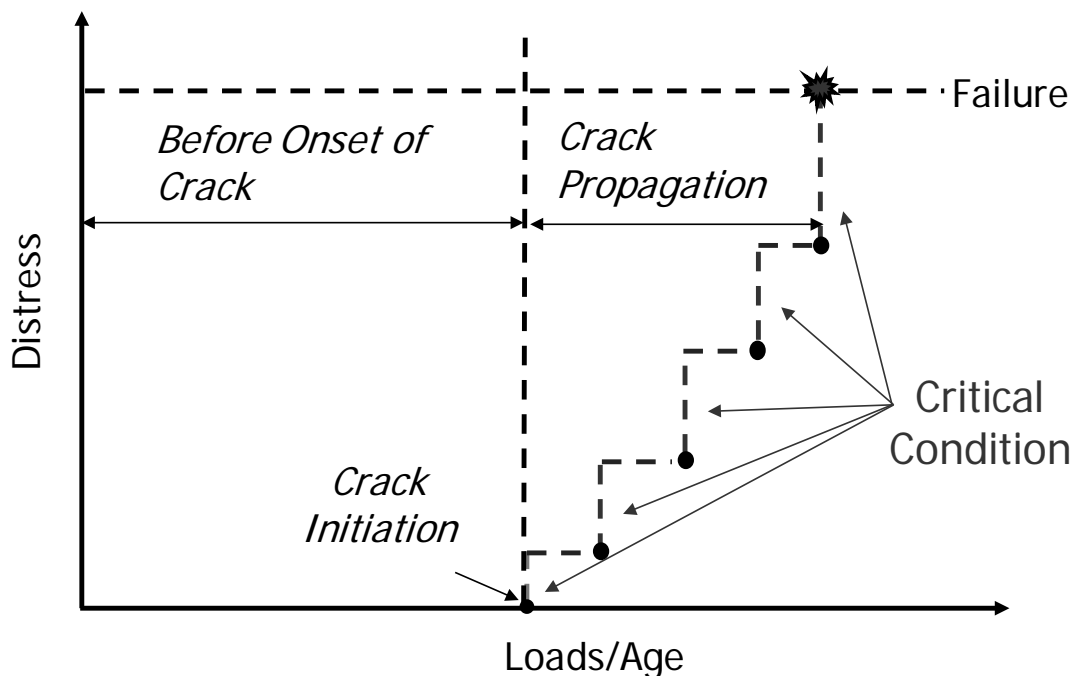


Figure 0-2. Critical conditions for crack initiation and propagation

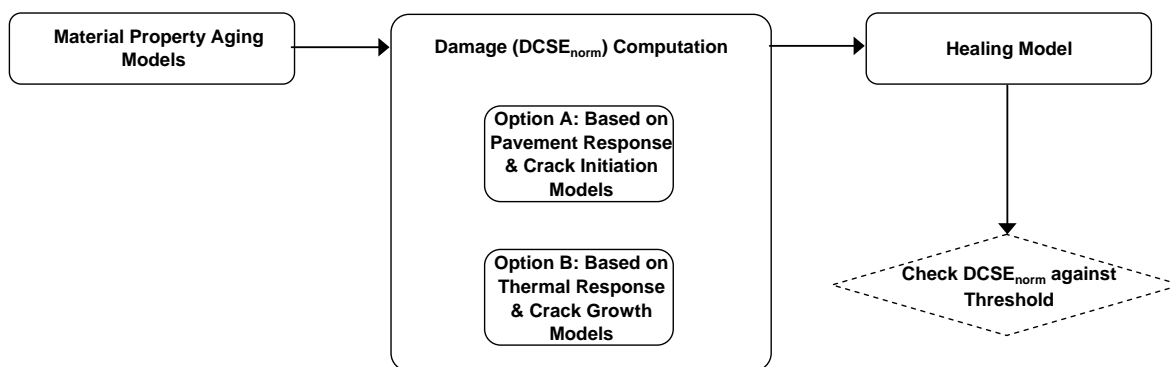


Figure 0-3. Flowchart of CCI module

In phase two, the integration was continued to illustrate the effects of healing and thermal stress using two example simulations: (1) healing effects in one pavement section in FDOT’s APT facility and (2) thermal effects in one pavement section in the Washington D.C. area (see Appendix B).

4.1.6.1 Module for crack initiation simulation (CIS)

The CIS module was developed by directly making use of the CCI module (with Option A for damage computation). As shown in Figure 0-4, the AC pavement structure is analyzed using

a 3-D LEA program. The CCI module is called to compute the amount of induced damage, as well as damage recovery and accumulation in a step-wise manner until the critical condition is identified (usually in several years). Whenever starting a yearly period (which starts from July 1st of each year and ends with June 30th of the following year), mixture properties are updated with the material property aging models. Upon completion of the simulation, crack initiation time, as well as the location of the initial crack will be reported.

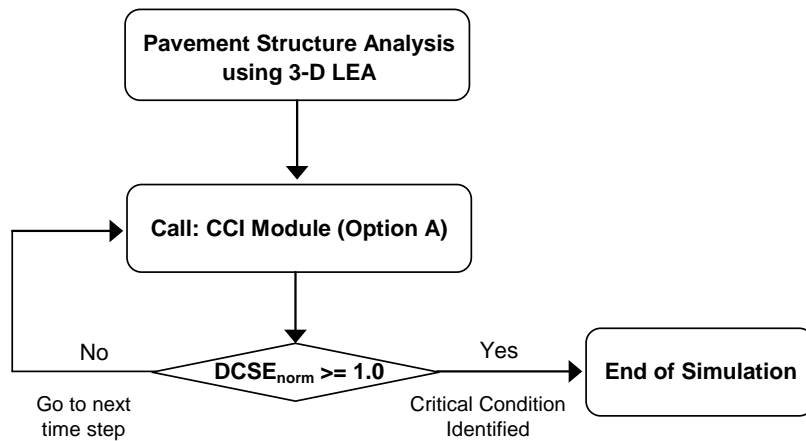


Figure 0-4. Flowchart of CIS module

4.1.6.2 Module for crack growth simulation (CGS)

The CGS module was developed on the basis of the CCI module (with Option B for damage computation). Figure 0-5 shows the flowchart for this module.

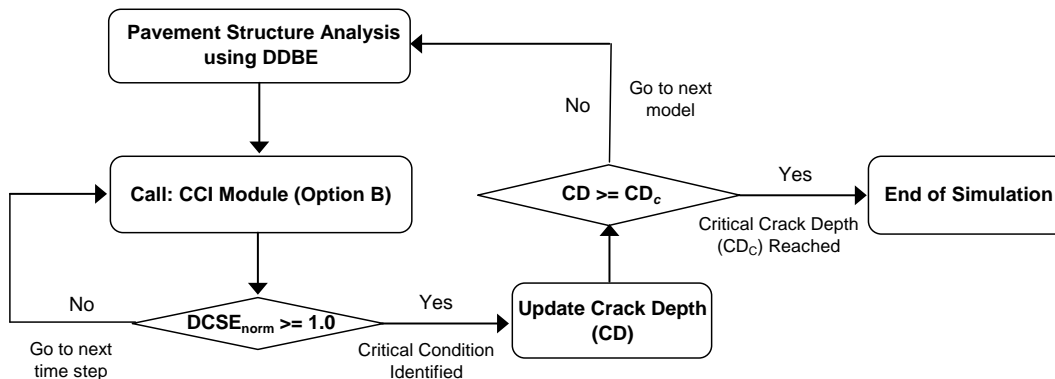


Figure 0-5. Flowchart of CGS module

Knowing the initiation time and location of the initial crack, the CGS module starts by discretizing the pavement structure using 2-D displacement discontinuity boundary elements. The CCI module is then called to compute damage accumulation for each time step. If the critical condition is identified, the crack depth increases by a distance of one zone [selected as 6 mm (0.25 in.)] because lab testing revealed that cracking develops in a stepwise manner in asphalt mixtures. For typical asphalt mixtures with a nominal maximum aggregate size (NMAS) of 12.5 mm, the stepwise-developed crack length is about one half of the NMAS, or about 6 mm.

The updated crack depth is then checked against the critical crack depth (preset to be one-half the depth of the HMA layer as field observations showed that top-down cracking generally does not exceed one-half depth of the layer):

- If the crack depth is less than the critical crack depth, a new pavement structure with the updated crack depth will be discretized and another simulation is performed using the same steps as mentioned above. For modeling using the displacement discontinuity (DD) boundary element method (BEM), remeshing of the whole pavement structure is not required. The increase in crack depth can be simply addressed by replacing the zone next to the current crack-tip with a few DD elements.
- Once the critical crack depth is reached, the simulation is completed and the time and applied loads corresponding to each crack depth increment will be reported.

4.2 Model Evaluation: Parametric Study

The top-down cracking performance model was intended to predict crack initiation (time and location) as well as crack propagation (increase of crack depth or crack amount with time) for calibration and validation using asphalt concrete pavements. However, because of model complexity, it was necessary to know how various factors affected predicted results and which factors had the largest influence on performance. Specifically, it was important to identify factors that could alter the cracking mechanism used in the model (e.g., bending versus near-tire mechanism). Therefore, a parametric study was conducted using a broad range of input

parameters to evaluate these factors. To limit the number of runs, the following conditions were assumed:

- A pavement structure used to demonstrate the thermal effect was selected. As shown in Figure 0-6, it consists of five layers: three asphalt concrete sub-layers, base, and subgrade.
- The base thickness, subgrade modulus and thickness, and Poisson's ratio for each of the layers were not changed for all analyses conducted.
- The variation in AC creep compliance was obtained by varying binder viscosity (i.e., by changing binder type only). However, the other material characteristics (e.g., aggregate gradation, air void, and effective binder content of asphalt mixture), which also influence creep compliance, were not changed.

These conditions reduced the input requirements to parameters in three input categories:

Material and structural properties, including

Initial fracture energy
Fracture energy aging parameter
Binder viscosity
Base modulus
AC layer thickness

Traffic volume: number of ESALs per year.

Climatic information: a mean annual air temperature (MAAT) and its companion hourly temperature data at four different depths of AC layer for a whole year.

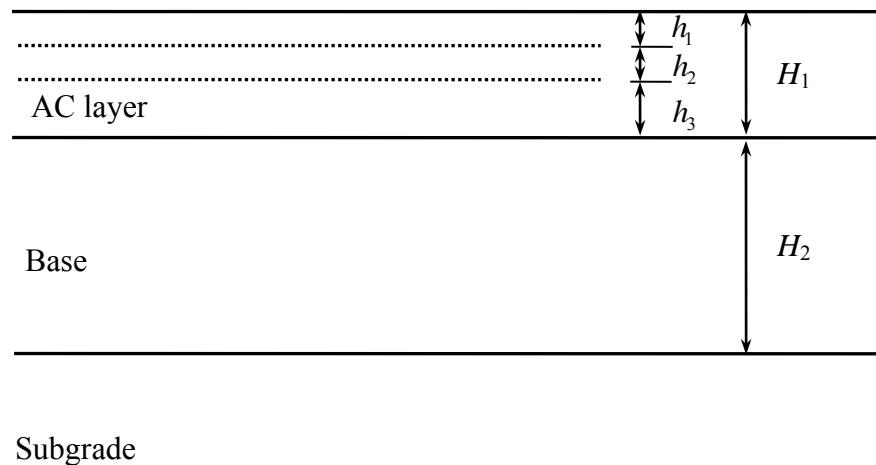


Figure 0-6. Pavement structure selected for use in parametric study

The values selected for each variable are listed in Table 0-2. For each variable, the value used in the example to demonstrate the thermal effect is indicated by shading. In other words, the example was selected as a reference (or baseline) case to illustrate the effects of various factors. So, the input information for this example was reproduced in Table 0-3, which was used in conjunction with Table 0-2 to conduct this analysis.

Then, each parameter included in the analysis was individually varied relative to the values given in Table 0-2, while the remaining parameters were held constant at the values used for the reference case. In total, the influence of individual parameters was investigated using 16 cases including the reference case. However, interactions and combined effects were not considered in this analysis.

Table 0-2. Range of parameters selected for sensitivity analysis

Variables	Values			
Initial Fracture Energy FE_i (Kpa)	2	5	10	
Fracture Energy Aging Parameter k_1	1	3	5	
Binder Type	58-28	67-22	76-22	
Base Modulus (Ksi)	20	40	60	
AC Layer Thickness (in)	2.5	5	7.5	10
Traffic Volume (10^6 ESALs per year)	0.175	0.438	0.876	
MAAT ($^{\circ}$ F)	50	60	75	

Table 0-3. Data for material property aging models

Parameter	Value
Aggregate % passing by weight (sieve size)	100.0 (3/4 in.), 90.0 (3/8 in.), 60.2 (# 4), 4.8 (# 200)
Binder type	67-22
Mean annual air temperature, $^{\circ}$ F	60
Effective binder content, % by volume	12
Air void content, % by volume	7
Initial fracture energy, Kpa	2
Fracture energy aging parameter	3

4.2.1 Effects of Material and Structural Properties

The material and structural properties investigated included initial fracture energy, fracture energy aging parameter, binder viscosity, base modulus, and AC layer thickness. The influence of each is discussed in the following subsections.

4.2.1.1 Effect of Initial Fracture Energy

The initial fracture energy (FE_i) is the starting value (also maximum value) of any fracture energy aging curve (see Figure 0-7) and it controls the initial degradation rate of any maximum healing potential aging curve (see Figure 0-8). Therefore, it was expected to have a strong influence on pavement cracking performance. To examine such influence, a broad range of initial fracture energies was selected.

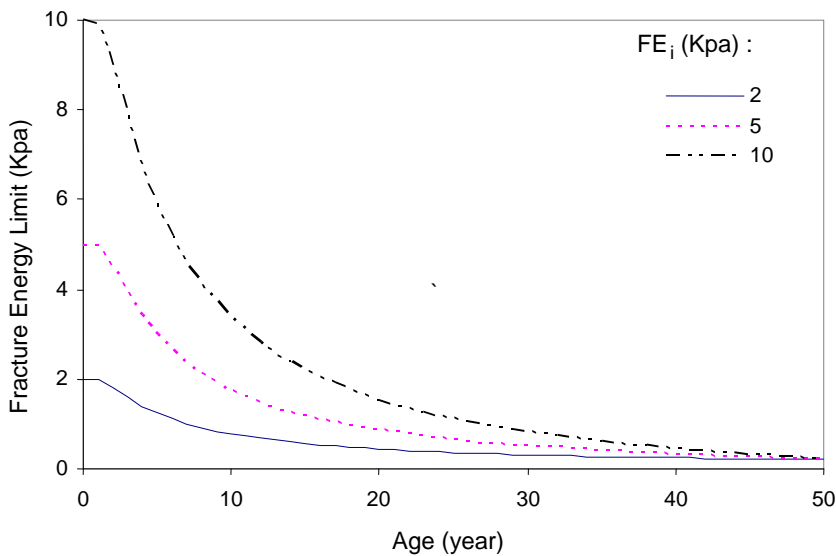


Figure 0-7. FE limit aging curves for different FE_i ($k_1 = 3$)

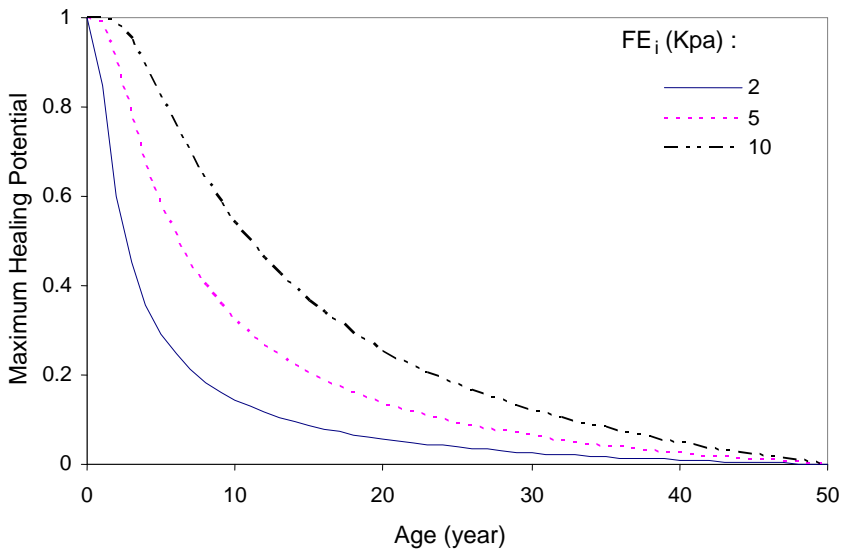


Figure 0-8. Maximum healing potential (surface) aging curves for different FE_i

Plots of crack depth versus time predicted by the model for different values of initial fracture energy are shown in Figure 0-9. As the figure shows, pavement with higher initial fracture energy exhibits better cracking performance (i.e., longer crack initiation time t_i and propagation time). For pavements with the same AC layer thickness, comparison was also made with respect to an average crack growth rate, which was defined as

$$C_t = \frac{CD_c - CD_i}{t_p} \quad (0-1)$$

where, C_t is average crack growth rate, CD_c is critical crack depth, CD_i is initial crack depth of 0.25 inch, and t_p is crack propagation time to the critical crack depth. The average crack growth rate is essentially the slope of the curves shown in Figure 0-9. It is clear from the figure that a higher FE_i value leads to a lower average crack growth rate, representing better cracking performance.

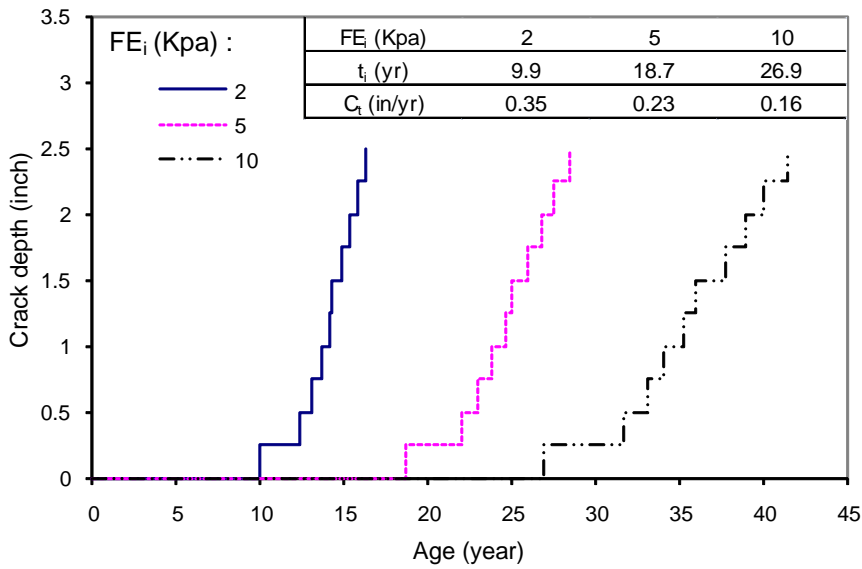


Figure 0-9. Effect of initial fracture energy on cracking performance

4.2.1.2 Effect of Fracture Energy Aging Parameter

Fracture energy aging parameter k_1 is an input parameter that governs the shape of the fracture energy aging curve. For a constant initial fracture energy, a larger k_1 value corresponds to a lower rate of degradation in fracture energy with aging (i.e., higher resistance to fracture, see Figure 0-10).

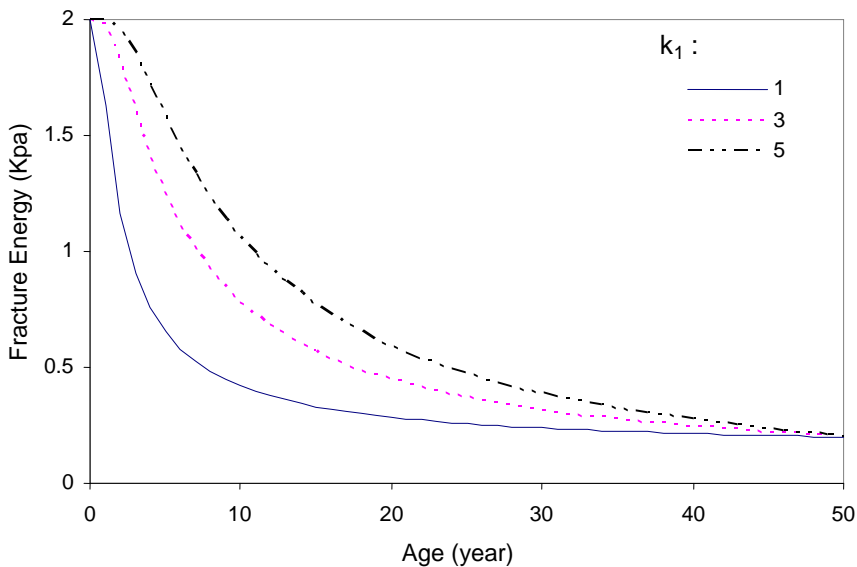


Figure 0-10. FE limit aging curves at different k_1 ($FE_i = 2$ Kpa)

The effect of the fracture energy aging parameter is shown in Figure 0-11. As shown, the increase of k_1 value results in longer time to crack initiation and a shallower slope of the crack growth curve.

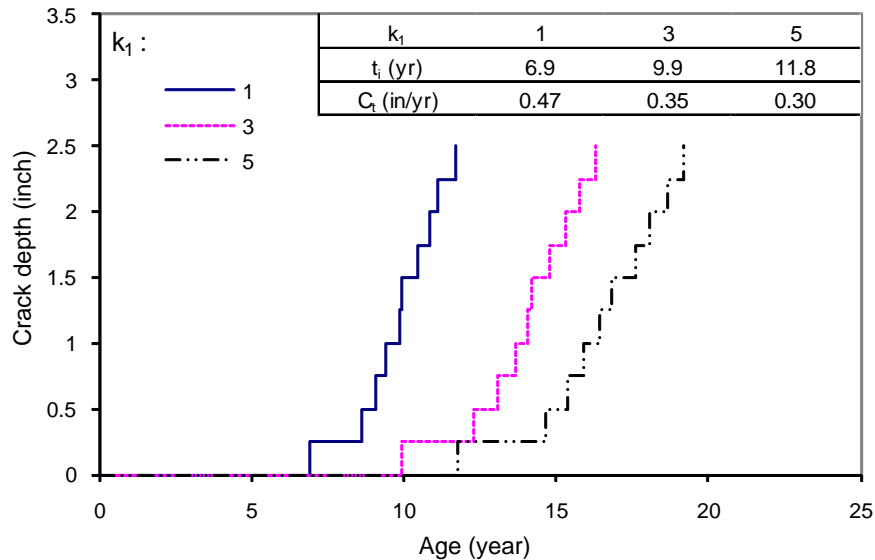


Figure 0-11. Effect of fracture energy aging parameter on cracking performance

4.2.1.3 Effect of Binder Viscosity

A typical range of binder types (from soft to stiff) was selected for the analysis of cracking performance. Figure 0-12 shows that crack initiation time is not affected by the change in binder viscosity. Also a softer binder results in a slightly higher crack growth rate because of the higher creep rate of the mixture with the softer binder. However, binder stiffness also affects AC stiffness such that a softer binder will contribute to lower AC stiffness, which can offset the effect of higher creep rate. Therefore, the overall change in the average crack growth rate is small, and pavement cracking performance is not sensitive to the change of binder viscosity. However, this result does not consider the contribution of the softer binder to an increased mixture fracture energy, which was kept constant in this analysis.

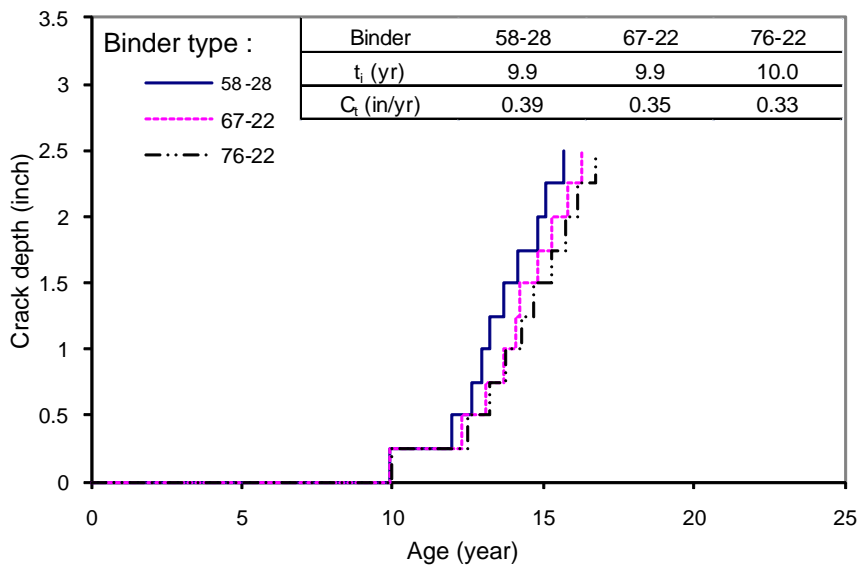


Figure 0-12. Effect of binder type on cracking performance

4.2.1.4 Effect of Base Modulus

The effect of base modulus was investigated using the material properties listed in Table 0-3 and the values of base modulus given in Table 0-2. Pavement cracking performance predicted by the model is given in Figure 0-13, which shows that the pavement with higher base modulus has better performance (i.e., longer crack initiation time and lower crack growth rate). This was expected because a stiffer base tends to reduce the load-induced tensile stresses at the surface of the pavement. For the range of base modulus values studied, the effect of base modulus is fairly strong.

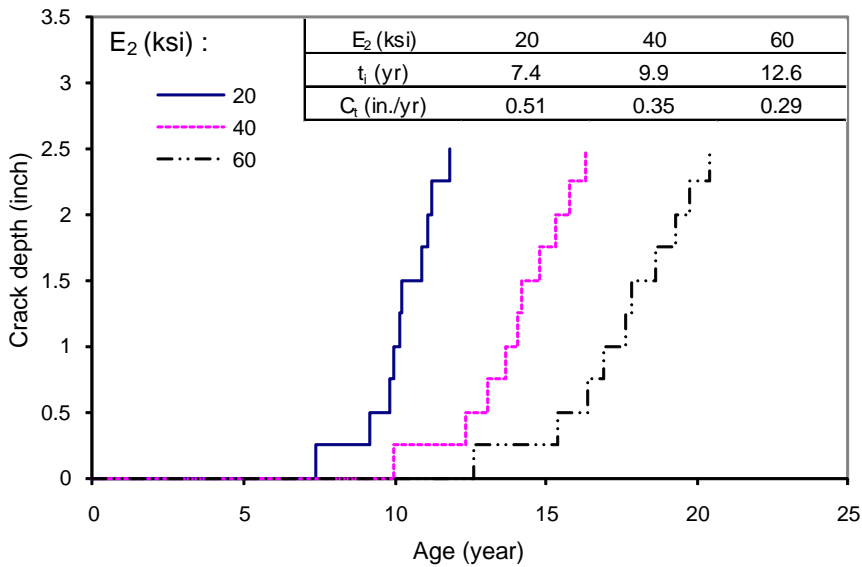


Figure 0-13. Effect of base modulus on cracking performance

4.2.1.5 Effect of AC Layer Thickness

The following AC layer thicknesses were selected for this analysis (see Table 0-2):

- 2.5 in. for a thin AC layer.
- 5 in. for a medium thickness AC layer.
- 7.5 in. and 10 in. for thick AC layers.

The predicted pavement cracking performance for the first three AC layer thickness values are shown in Figure 0-14, which shows that the pavement with thicker AC layer had better cracking performance, i.e., longer time to crack initiation. Because the crack growth rate generally increases with crack length for any crack, it was determined that this parameter was not suitable to be directly compared for pavements with different AC layer thicknesses, which by definition have different total crack lengths. However, the influence of AC layer thickness on crack growth may be examined in the following two cases: (1) Comparison of a staged crack growth rate (C_{11}) for the crack depth of 1.25 in. for all three AC layers (2.5, 5.0, and 7.5 in.), which are 0.25, 0.24, and 0.20 in./year, respectively; and (2) Comparison of another staged crack growth rate (C_{12}) for the crack depth of 2.50 in. for two AC layers (5.0 and 7.5 in.), which are

0.35 and 0.32 in./year. It can be seen from these comparisons that, in general, crack growth is slower in a thicker layer.

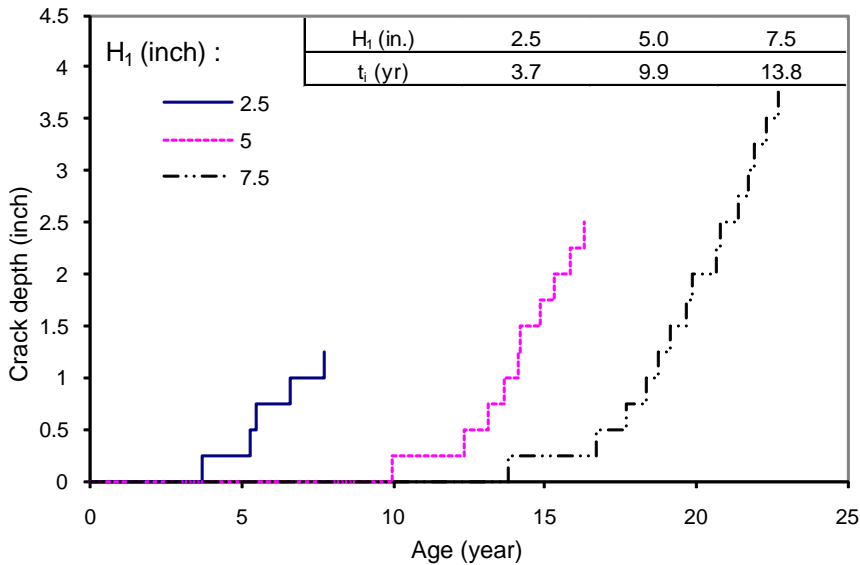


Figure 0-14. Effect of AC layer thickness on cracking performance

However, the predicted location of the initial crack for the thick AC layer was more than 36 inches from the center of one tire. In this case, the initial crack was actually predicted to be either in the other traffic lane or in the compressive zone of the other tire (e.g., location A or C due to Tire 1, as indicated in Figure 0-15), which did not seem realistic. Therefore, the bending mechanism used for model prediction may not be appropriate for the thick AC layer pavement.

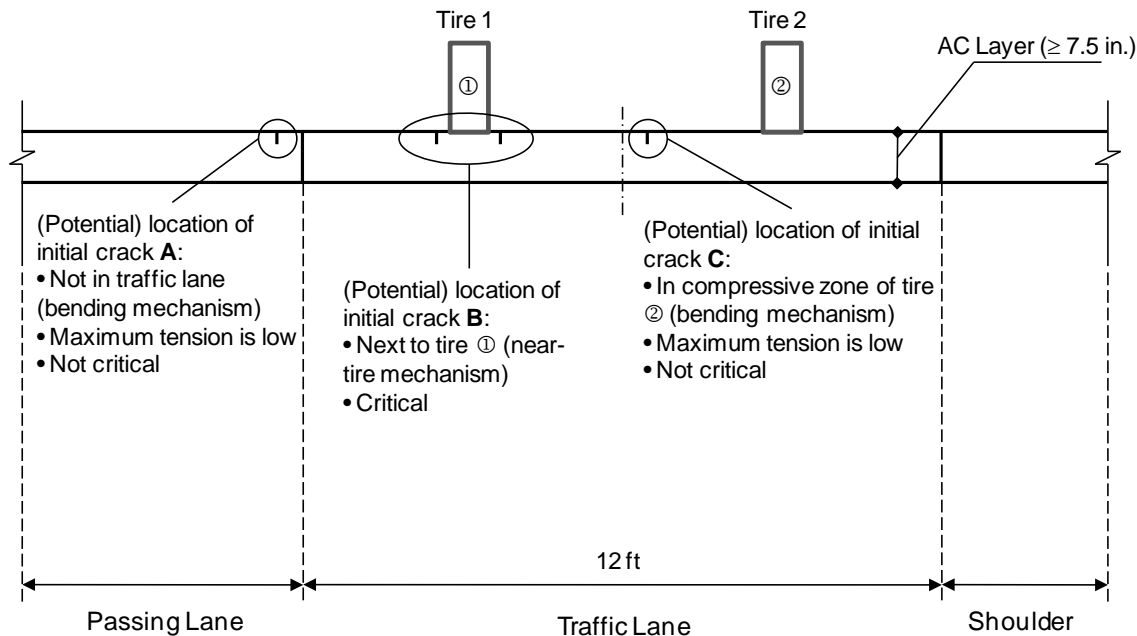


Figure 0-15. Change in top-down cracking mechanism from bending to near-tire

The near-tire mechanism, accounting for shear-induced tension at the tire edge, was thus considered for use in thick AC layer. This mechanism stipulated initial cracks located just next to the tire edge (e.g., location B due to Tire 1 in Figure 0-15). The major driving force for crack initiation and propagation is the shear-induced principal tensile stress. However, a crack growth simulation tool based on this mechanism was not available at this time. Therefore, the CGS module was used as a surrogate to predict crack growth with time. Due to the localized nature of the shear-induced tension at the tire edge, the critical crack depth was redefined to be one fourth of the AC layer depth. Then, a simplified model with the near-tire mechanism was used to predict cracking performance for the 7.5 in. thick AC layer and a 10 in. full depth AC pavement. The predicted cracking performance shown in Figure 0-16 indicates that both pavements have almost identical performance (i.e., same crack initiation time and similar crack propagation time). This is expected because the principal tensile stress of 25 psi predicted based on actual tire stresses was the same for both pavements. In fact, this stress was found to be independent of AC thickness and the stiffness ratio of AC-to-base layer.

A comparison of Figure 0-16 and Figure 0-14 suggests that thick pavements may perform even worse than a pavement with a medium thickness AC layer. However, the simplified model does not address some potential factors affecting the near-tire mechanism, including the effects of the wander and stress state, which will result in less damage than predicted, and therefore, the comparison may not be accurate without considering these factors.

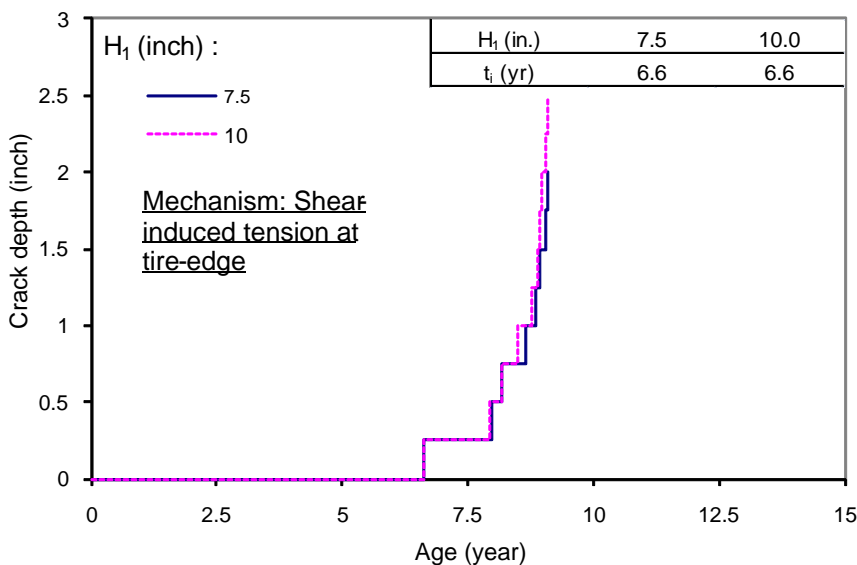


Figure 0-16. Predictions based on tire-edge cracking mechanism

4.2.2 Effect of Traffic

As shown in Table 0-2, three traffic levels were selected for this analysis: a high traffic level with 0.876 million ESALs/year; a medium traffic level with 0.438 million ESALs / year; and a low traffic level with 0.175 million ESALs/year.

The high, medium, and low traffic levels are equivalent to 100, 50, and 20 ESALs / hour, respectively. The predicted pavement performance, shown in Figure 0-17, indicates that the pavement subjected to the highest traffic level had the worst performance (i.e., shortest time to crack initiation and highest crack growth rate). Overall, the effect of traffic is strong.

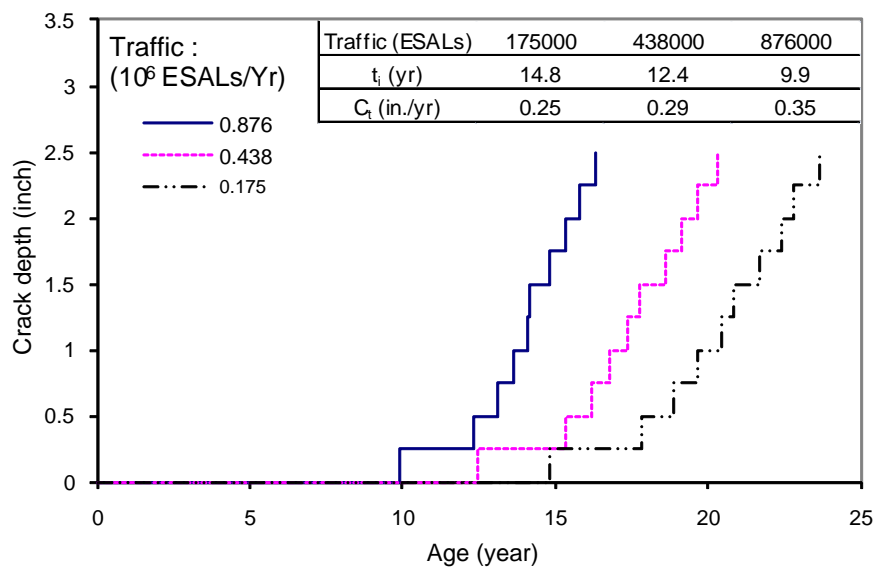


Figure 0-17. Effect of traffic volume on cracking performance

4.2.3 Effect of Climate

Three typical climatic environments were selected for this analysis: a hard-freeze (HF) environment as that of Fargo, ND; a freeze-thaw (FT) environment as that of Washington, DC, and a non-freeze (NF) environment as represented by the climate of Melrose, FL. The mean annual air temperature (MAAT) values for these climatic environments are given in Table 0-2. For each climate, the MAAT value and the corresponding temperature data file containing hourly temperature history at four depths of the AC layer for a whole year were used as input for model prediction. The predicted pavement performance, shown in Figure 0-18, indicates similar pavement cracking performance for both the HF and FT environments. However, the pavement in the NF environment exhibits slightly later time to crack initiation, but a higher crack growth rate than those for the other two environments. Overall, the effect of climatic environment (more specifically, temperature) is not significant.

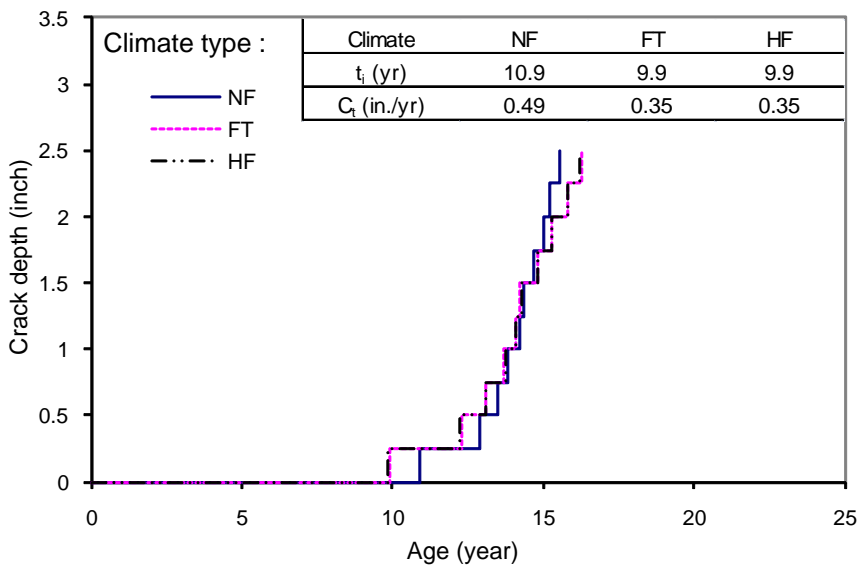


Figure 0-18. Effect of climatic environment on cracking performance

This finding was expected because the climatic environment influences damage development in the pavement in two ways. Colder weather leads to higher thermal stresses and thus higher thermally induced damage. But, colder weather results in lower creep rate and thus lower load-induced damage. However, transverse thermal stresses were used to compute thermally induced damage in the thermal response model. Therefore, the resulting thermally induced damage is not as high as that caused by longitudinal thermal stresses.

When both thermally induced damage and load-induced damage are combined, the two opposite effects of climatic environment tend to offset each other. To verify this trend, the thermal response sub-model was turned off in the top-down cracking performance predictive system, which was then used to predict cracking performance for the same pavement under these three climatic environments (i.e., the climate was allowed to influence load-induced damage only). The results presented in Figure 0-19 indicate that the climate did not have much influence on crack initiation time. However, it did strongly affect the crack growth rate. As can be seen, the pavement in the warmer climatic environment has a higher crack growth rate than the one in

the colder climate because the pavement in the warmer climate is subjected to a higher creep rate for longer time and thus more damage.

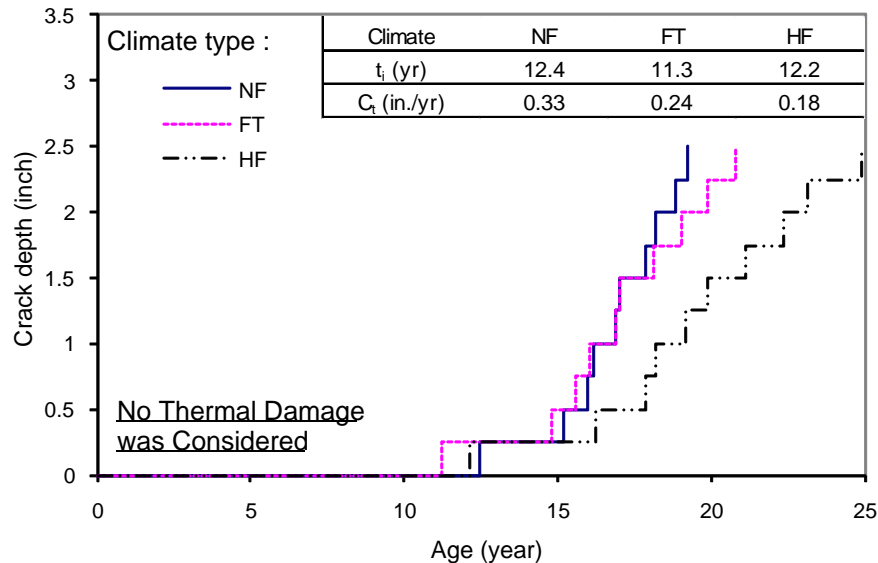


Figure 0-19. Effect of climatic environment (w/o thermally induced damage) on cracking performance

4.3 Model Calibration and Validation

The top-down cracking performance model was calibrated and validated to determine whether the model could reasonably predict the cracking performance of asphalt concrete pavement for different pavement material and structural properties, traffic volume, and climatic information.

4.3.1 Summary of Top-down Cracking Performance Model Data

Calibration of the top-down cracking performance model was conducted by matching as closely as possible top-down cracking predictions with observed cracking performance in the field, more specifically crack initiation time. To complete the calibration, input data were needed to make top-down cracking predictions, and observed field performance data of each pavement section was required for comparison with model predictions. This section presents the data used for model calibration.

4.3.1.1 Selection of pavement sites

Thirteen pavement sections were used for calibration/validation. These sections were selected based on quality of data in terms of both laboratory testing and field observation. Only sections for which material property data obtained from Superpave IDT tests performed on field core were used. In addition, only sections for which pavement performance data could be confirmed through direct field observations were used. According to the climatic condition, these pavement sections fell into two groups. Group I included eleven sections in Florida (Non-Freeze climate), and Group II had two sections in Minnesota (Hard-Freeze climate). The locations of these test sections are presented in Table 0-4.

Table 0-4. Field test sections under Non-Freeze climate of Florida

Group No.	Section No.	Section Name	Code	County	Location / Section Limits
I	1	Interstate 75 Section 1	I75-1A	Charlotte	MP 161.1 - MP 171.3
	2	Interstate 75 Section 1	I75-1B	Charlotte	MP 149.3 - MP 161.1
	3	Interstate 75 Section 3	I75-3	Lee	MP 131.5 - MP 149.3
	4	Interstate 75 Section 2	I75-2	Lee	MP 115.1 - MP 131.5
	5	State Road 80 Section 1	SR 80-1	Lee	From Hickey Creek Bridge To East of Joel Blvd.
	6	State Road 80 Section 2	SR 80-2	Lee	From East of CR 80A To West of Hickey Creek Bridge
	7	Interstate 10 Section 8	I10-8	Suwannee	MP 15.144 - MP 18.000
	8	Interstate 10 Section 9	I10-9	Suwannee	MP 18.000 - MP 21.474
	9	State Road 471	SR471	Sumter	The northbound lane three miles north of the Withlacoochee River
	10	State Road 19	SR19	Lake	The southbound lane five miles south of S.R. 40
	11	State Road 997	SR997	Dade	The northbound lane 7.6 miles south of US-27
II	12	Interstate 94 Cell 4	I94-4	-	located near Albertville, Minnesota (40 miles northwest of the Twin Cities)
	13	Interstate 94 Cell 14	I94-14	-	located near Albertville, Minnesota (40 miles northwest of the Twin Cities)

The parametric study presented in Section 4.2 showed that AC layer thickness governs the cracking mechanism. For pavements with thin to medium thickness AC layers such as those of Group I (which ranges from 2 to 8 in.), the bending mechanism was appropriate. But, for full-depth AC pavements such as those of Group II (which ranges from 8 to 12 in.), the near-tire mechanism had to be used. In this project, Group I was used for calibration/validation of the bending mechanism, and Group II was used to evaluate the reasonableness of the near-tire mechanism.

4.3.1.2 Data obtained from SuperPave IDT

The Superpave indirect tensile test (IDT) developed as part of the Strategic Highway Research Program (SHRP) (29) was used to determine tensile properties on field cores obtained from the 13 test sections (i.e., properties at the age when coring was conducted). Nine specimens (from nine cores) were selected from each section to test the mixture at three temperatures (i.e., three replicate specimens at each temperature). The Superpave IDT includes three types of tests: resilient modulus, creep compliance, and tensile strength.

- The resilient modulus test was performed in a load-controlled mode by applying a repeated haversine waveform load to the specimen for a period of 0.1 second followed by a rest period of 0.9 seconds. The load was selected to keep the repeated horizontal strain between 100 and 300 micro-strain during the test (35). The resilient moduli of mixtures (M_R) determined at 10°C are presented in Table 0-5.
- The creep compliance test was also performed in the load-controlled mode by applying a static load to the specimen for a period of 1000 seconds. The load was selected to maintain the accumulative horizontal strain below 1000 micro-strain (36). The creep compliance master curve power law parameters (m and D_1) (determined based on tests conducted at 0, 10, and 20°C) are presented in Table 0-6. Plots for the master curves are provided in Appendix B (Section B.4).
- The strength test was performed in a displacement-controlled mode, in which loading was applied at a rate of 50 mm/min. The fracture properties determined at 10°C are also shown in Table 0-5, including tensile strength (S_t), failure strain (ϵ_f), FE limit (FE_f), and DCSE limit ($DCSE_f$).

Table 0-5. Data from SuperPave IDT resilient modulus and tensile strength tests at 10°C

Section Code	M_R (Gpa)	S_t (Mpa)	ϵ_f ($\mu\epsilon$)	FE_f (Kpa)	$DCSE_f$ (Kpa)	Aged Time (year)
I75-1A	11.14	1.65	1028.05	1.1	1.0	15
I75-1B	10.91	2.01	1437.44	2.0	1.8	14
I75-3	11.58	1.68	715.74	0.8	0.7	15
I75-2	10.29	1.89	1066.72	1.3	1.1	14
SR80-1	13.39	1.59	495.27	0.3	0.2	16
SR80-2	13.45	2.39	679.15	1.0	0.8	19
I10-8	9.85	1.56	386.00	0.4	0.3	7
I10-9	10.21	1.27	415.00	0.4	0.3	7
SR471	7.67	1.79	2040.00	2.5	2.3	3
SR19	9.30	1.71	1338.00	1.6	1.4	3
SR997	11.74	2.33	594.00	0.9	0.7	40
I94-4	8.18	1.35	1203.56	1.1	1.0	13
I94-14	9.44	1.78	1760.25	2.4	2.2	13

Table 0-6. Data from SuperPave IDT creep compliance tests at 0, 10, and 20°C

Section Code	m	D_1 (1/Gpa)	$AT(3)^*$	$AT(2)$	$AT(1)$
I75-1A	0.441	0.027	251.19	35.48	1
I75-1B	0.471	0.029	177.83	19.95	1
I75-3	0.485	0.022	281.84	14.13	1
I75-2	0.460	0.021	562.34	56.23	1
SR80-1	0.445	0.014	354.81	25.12	1
SR80-2	0.368	0.014	501.19	35.48	1
I10-8	0.441	0.013	112.202	8.913	1
I10-9	0.503	0.006	141.254	14.125	1
SR471	0.783	0.001	223.872	63.096	1
SR19	0.595	0.012	89.125	8.913	1
SR997	0.349	0.019	63.096	3.981	1
I94-4	0.462	0.018	–	44.668	1
I94-14	0.456	0.019	–	79.433	1

* $AT(3)$ denotes the inverse of shift factor at the highest temperature.

4.3.1.3 Data for material property model

As introduced in Section 4.1.2, the material property model consists of four sub-models: the AC stiffness (creep compliance) aging model, the tensile strength aging model, the fracture energy (dissipated creep strain energy) limit aging model, and the healing model.

The AC stiffness aging model estimates the stiffness of the asphalt mixture as a function of temperature and time. The input information for this model is as follows:

- Percent passing 3/4, 3/8, #4, and #200 sieves by weight
- Binder type and mean annual air temperature (MAAT)
- Effective binder content (V_{beff} , % by volume) and air void (V_a , % by volume)

The values used for the above parameters are shown in Table 0-7.

The AC tensile strength aging model uses the stiffness predicted by the stiffness aging model and the correlation between stiffness and strength to calculate the tensile strength of asphalt mixture.

Table 0-7. Data used by the material property model

Section Code	Percent passing by weight				V_{beff} (%)	V_a (%)	MAAT (°F)	Binder type
	3/4 in	3/8 in	# 4	# 200				
I75-1A	100.0	91.8	73.6	5.9	10.7	5.4	75	67-22
I75-1B	100.0	93.7	74.6	5.6	10.7	3.2	75	67-22
I75-3	100.0	86.2	65.1	5.5	8.2	7.2	75	67-22
I75-2	100.0	92.5	68.9	5.0	8.4	6.9	75	67-22
SR80-1	100.0	80.4	59.0	5.8	8.6	5.7	75	67-22
SR80-2	100.0	84.8	64.4	6.2	8.9	7.5	75	67-22
I10-8	100.0	90.0	60.2	4.8	10.3	8.7	75	67-22
I10-9	100.0	90.0	60.2	4.8	9.1	9.9	75	67-22
SR471	100.0	90.0	60.2	4.8	13.3	5.7	75	67-22
SR19	100.0	90.0	60.2	4.8	14.2	4.8	75	67-22
SR997	100.0	90.0	60.2	4.8	11.4	7.6	75	67-22
I94-4	100.0	82.1	65.6	5.2	10.3	4.4	50	58-28
I94-14	100.0	83.4	68.3	5.0	11.1	3.7	50	58-28

The fracture energy limit aging model also uses the stiffness predicted by the stiffness aging model, but in a normalized form. The model has two unknowns: the aging parameter k_1 which is to be determined from calibration, and the initial fracture energy FE_i which is in general obtained from unaged cores using SuperPave IDT tests. However, since unaged mixture was not available for the field sections used in this study, FE_i was backcalculated from tests performed on aged cores. As an example, an FE_f value of 1.1 Kpa is obtained by testing cores from Section

I75-1A, which was 15 years old at the time of coring. Then, the FE_i value of the mixture can be determined by using Equation 0-3, in which the normalized stiffness $S_n(t)$ is estimated on the basis of material characteristics of the mixture (see Table 0-7) and the aging parameter k_1 has to be assumed. For a k_1 value of 3, the FE_i is determined to be 4.5 Kpa, with which the entire FE limit aging curve is determined (see Figure 0-20).

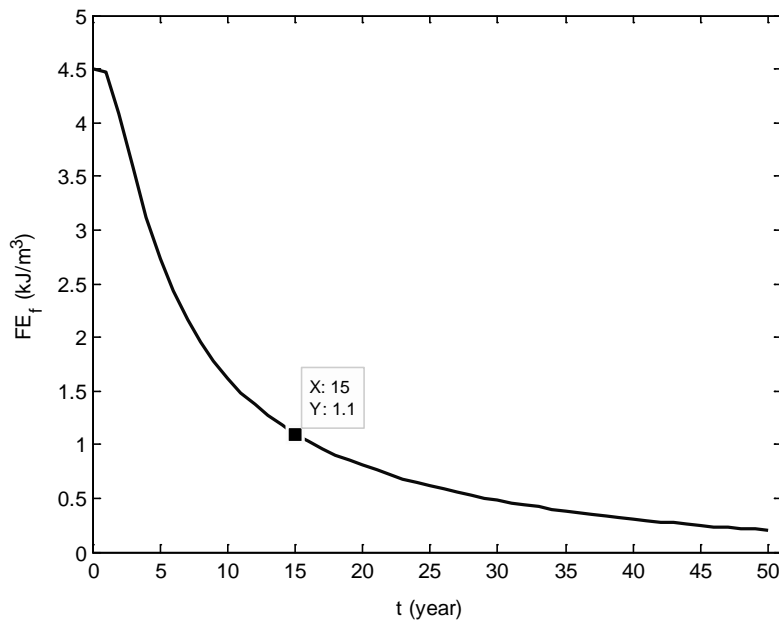


Figure 0-20. FE limit aging curve ($k_1 = 3$) for Section I75-1A

The healing model has three components: the maximum healing potential aging model and two criteria for determining healing by day and by year:

- The maximum healing potential aging model uses the normalized stiffness and initial fracture energy to estimate the loss of maximum healing potential due to aging.
- The criterion for determining healing by day, h_{dn} , uses the lowest stiffness, S_{low} , of any day (predicted by the stiffness aging model) and two critical values, S_{cr1} and S_{cr2} (estimated to be 320 and 2,000 ksi), to determine the healing potential of the day. The daily-based healing is bounded by zero and the maximum value h_{ym} determined by the maximum healing potential aging model.

- The criterion for determination of yearly based healing, h_{yn} , is identical to the criterion for daily based healing except an averaged daily lowest stiffness, S_{lowa} , for a prolonged period was used instead of S_{low} to obtain the healing potential of any year.

Details of these models are provided in Appendix B.

4.3.1.4 Data for pavement response model

The pavement response model consists of two sub-models: (1) a load response model and (2) a thermal-response model.

The load-response model estimates load-induced stresses due to traffic loads. It requires the following input parameters:

- Layer thickness of AC, base, and subbase
- Modulus of base, subbase, and subgrade
- Poisson's ratio of AC, base, subbase, and subgrade
- Equivalent single axle load
- Hourly temperatures within the AC layer

The values used for layer thickness, modulus, and yearly traffic are listed in Table 0-8. Poisson's ratios of 0.3, 0.35, 0.35, and 0.4 were assumed for AC, base, subbase, and subgrade, respectively. It was determined that the effect on load response due to slight changes in Poisson's ratio is negligible. The hourly pavement temperatures were estimated by the enhanced integrated climatic model (EICM), using typical pavement material and structural properties and local climatic information.

The thermal-response model estimates thermally induced stresses caused by changes in pavement temperatures. It requires the following input parameters:

- Thickness of AC layer
- The relaxation modulus master curve parameters
- Hourly pavement temperatures within the AC layer

- The coefficient of thermal contraction of the asphalt concrete mixture

The values used for thickness and hourly pavement temperatures are similar to those described for the load-response model. The coefficient of thermal contraction was assumed to be $1.2\text{E-}5 \text{ } \varepsilon/^{\circ}\text{C}$ for all test sections. It was determined that slight changes in the coefficient of thermal contraction do not significantly influence transverse thermal stresses (predicted by the thermal-response model) which are limited by the maximum frictional resistance that can develop between surface and base layers.

Table 0-8. Data used by the pavement response model

Section Code	Layer thickness (in)			Layer modulus (ksi)			Yearly traffic (10^3 ESAL)
	AC	Base	Sub-base	Base	Sub-base	Sub-grade	
I75-1A	6.54	12	12	54.8	50.1	30.1	573
I75-1B	6.24	12	12	63.6	51.4	36.1	558
I75-3	6.48	12	12	59.6	34.8	36.2	674
I75-2	7.42	12	12	107.4	90.3	31.4	576
SR80-1	3.38	12	12	51.3	40.0	39.7	221
SR80-2	6.30	12	12	57.3	45.6	18.8	207
I10-8	7.20	12	12	55.7	54.5	38.9	392
I10-9	7.40	12	12	65.2	41.4	46.6	392
SR471	2.58	12	12	43.0	34.0	33.6	26
SR19	2.40	12	12	50.7	13.0	12.6	51
SR997	2.18	12	12	109.0	53.0	52.7	89
I94-4	9.10	–	–	–	–	3.2	488
I94-14	10.90	–	–	–	–	3.2	782

4.3.1.5 Data for pavement fracture model

The pavement fracture model consists of three sub-models: (1) a crack initiation model, (2) a crack growth model, and (3) a crack amount model.

The crack initiation model uses (1) the load-induced and thermally-induced stresses predicted by the pavement response model and (2) the rule for determination of crack initiation to predict crack initiation time and location. During the process, the mixture fracture and healing properties determined by the material property model are required.

The crack growth model uses the load-induced stresses predicted by the 2-D DDBE program, thermally induced stresses predicted by the thermal response model combined with the stress intensity function for an edge crack, and the energy-based failure criterion to compute the increase of crack depth with time. The mixture fracture and healing properties determined by the material property model are also required during the process.

The crack amount model converts the crack depth-versus-time relationship predicted by the crack growth model to a crack amount-versus-time relationship.

Detailed information on these models is provided in Appendix B.

4.3.1.6 Observed pavement performance data

The input data presented in Sections 4.3.1.2 to 4.3.1.5 was used to predict the performance of each of the 13 test sections in two phases. In Phase One, the predictions for the 11 sections of Group I were compared with observed performance to calibrate the model. The field performance for each of the sections was obtained from the following two sources:

- Visits were made to each test section to observe and photograph its performance and take cores in 2003. Some sections exhibited a moderate amount of cracking and others showed no cracking. An inspection of core samples from the cracked sections indicated the presence of top-down cracking (i.e., cracks initiated from the surface and moved downward).
- The crack rating history for each test section was obtained from the flexible pavement condition survey database maintained by the Florida Department of Transportation (FDOT) (37). The crack rating is a pavement performance parameter used by the FDOT to monitor cracking development in the field. The index value starts at 10 (indicating no cracking) and drops to 0 with increasing severity of cracking. The crack rating history of the 11 Florida sections used in the project is given in Appendix B.5.

The crack initiation time listed in Table 0-9 for each test section was determined on the basis of the gathered information (see Appendix B).

In Phase Two, predictions obtained using the calibrated model were presented and compared with field observations for all test sections, including those of Group II (also presented in Table 0-9), which was obtained from Minnesota Department of Transportation (MnDOT).

Table 0-9. Observed top-down cracking initiation time

Section No	Section Code	Crack Initiation Time (year)
1	I75-1A	10
2	I75-1B	12
3	I75-3	11
4	I75-2	17
5	SR80-1	13
6	SR80-2	22
7	I10-8	8
8	I10-9	8
9	SR471	2
10	SR19	1
11	SR997	38
12	I94-4	4
13	I94-14	6

Based on the observed crack initiation time, pavement cracking performance can be categorized according to one of five performance levels:

- Level I: 1 to 5 years before crack initiation.
- Level II: 6 to 10 years before crack initiation.
- Level III: 11 to 20 years before crack initiation.
- Level IV: 21 to 30 years before crack initiation.
- Level V: greater than 30 years before crack initiation.

The intent of presenting the performance data according to levels was simply to provide an alternate way to illustrate the goodness of fit of the model, since R^2 values are sometimes difficult to visualize (see Section 4.3.2). Four boundaries (i.e., 5, 10, 20, and 30 years), defining five levels were selected to differentiate the expected range of cracking performance.

Admittedly, the boundaries selected by the research team are not unique. Different boundaries could have been selected and the illustration might have been slightly different. However, the

general message would be the same. In short, slight changes in these boundaries will not significantly affect model calibration/validation results.

4.3.2 Model Calibration

Model calibration was accomplished by matching as closely as possible top-down cracking predictions for 11 pavement sections (Group I) with observed top-down cracking in the field. Given that the aging parameter (k_1) was included as an unknown parameter within the fracture energy aging model, R^2 of the predicted initiation times of top-down cracking was determined for each assumed k_1 value, using linear regression with a constant intercept (more specifically, the error between predicted and measured data was examined relative to the line of equality, which by definition has an intercept of 0). A series of such linear regressions was conducted with k_1 values ranging from 0.5 to 5. The k_1 value resulting in the best fit (highest R^2) of observed initiation times of cracking with predicted times was chosen for the final model. (For brevity, the constant intercept linear regression used in the calibration was simply termed linear regression in the discussion that followed.)

4.3.2.1 Calibration procedure

The calibration procedure included a matrix of runs of the top-down cracking performance model to obtain crack initiation time predictions for each selected section at 8 values of the aging parameter k_1 ranging between 0.5 and 5, as determined by a trial-and-error process. A k_1 value of 0.5 resulted in longer time to crack initiation for most of the pavement sections, including those sections known to have poor observed performance. Similarly, a k_1 value of 5 resulted in shorter time to crack initiation for most of the sections, including those sections known to have good observed performance. The data obtained from these runs is shown in Table 0-10.

Table 0-10. Predicted versus observed cracking performance for different k_1 -values (all test sections in Group I)

Section No.	Observed t_i (year)	Predicted t_i' (year)							
		k_1 -value							
		0.5	1	1.5	2	2.5	3	3.5	5
1	10	14.7	14.7	13.8	12.7	11.8	10.9	10.7	9.6
2	12	13.9	13.9	13.9	13.9	13.8	12.9	12.7	11.0
3	11	8.9	8.0	6.9	6.5	5.9	5.5	4.9	4.0
4	17	19.0	19.0	18.8	17.8	16.8	16.0	15.7	14.6
5	13	3.0	2.3	2.2	1.7	1.3	1.2	1.2	1.1
6	22	25.7	25.7	25.7	24.7	23.7	22.8	22.6	20.9
7	8	7.6	6.6	5.9	5.8	5.6	5.6	4.9	4.6
8	8	7.9	6.9	6.7	6.6	5.9	5.8	5.7	4.7
9	2	6.9	5.8	5.5	4.9	4.8	4.8	4.8	4.7
10	1	5.6	4.6	4.3	3.9	3.8	3.8	3.7	3.5
11	38	34.8	34.8	34.8	34.8	34.8	34.8	34.8	34.7
R^2		0.807	0.803	0.802	0.809	0.802	0.801	0.791	0.767

Also, for each aging parameter, a linear regression routine was used to determine R^2 by examining the error between the observed initiation time and the predicted time of crack initiation relative to the line of equality. The k_1 value that resulted in the largest R^2 (i.e., best match or lowest error between predicted crack initiation time and the time observed in the field) was chosen as the optimum k_1 .

4.3.2.2 Initial calibration results

Linear regressions were performed to determine the R^2 (for each aging parameter k_1). Thus, eight values were obtained (see Table 0-10), and eight models (each of which has different k_1 and R^2 values) were assembled. The model with the highest R^2 value (i.e., 0.809) had a k_1 value of 2.0

Another means for evaluating the goodness of fit of the model is by comparing the predicted levels of cracking performance to those observed, as described in Section 4.3.1.6. The results of this comparison are shown in Figure 0-21 and are summarized as follows:

- Two of the two Level I sections were predicted to be level I sections.
- Two of the three Level II sections were predicted to be Level II sections and one section was predicted to be a Level III section.
- Two of the four Level III sections were predicted to be Level III sections, one was predicted to be a Level II section, and one was predicted to be a Level I section.
- The Level IV section was predicted to be a Level IV section.
- The Level V section was predicted to be a Level V section.

		Observed Cracking Performance Level				
		I	II	III	IV	V
Predicted Cracking Performance Level	I	2		1		
	II		2	1		
	III		1	2		
	IV				1	
	V					1

Figure 0-21. Predicted versus observed cracking performance (All 11 sections)

This comparison shows a strong correlation between predicted and observed cracking performance. As shown in Figure 0-21, eight predictions matched the observed performance, two predictions were off by one level, and only one prediction was off by two levels. Thus, predicted performance in terms of crack initiation time was relatively good for 10 out of 11 sections.

The difference by two levels prediction for Test Section 5 apparently had a strong influence on R^2 , which was not very sensitive to the k_1 value such that the prediction for Test

Section 5 may have overwhelmed the sensitivity of the results. Therefore, Test Section 5 was excluded from the final calibration, but it was included in the validation process.

4.3.2.3 Final calibration

A final calibration that excluded Section 5 was made and linear regressions were performed to determine eight different values of R^2 (one for each aging parameter). The model with the highest R^2 value (i.e., 0.933) had a k_1 value of 3.0 (see Table 0-11).

Table 0-11. Predicted versus observed cracking performance (without Test Section 5 in Group I)

Section No.	Observed t_i (year)	Predicted t_i' (year)							
		k_1 -value							
		0.5	1	1.5	2	2.5	3	3.5	5
1	10	14.7	14.7	13.8	12.7	11.8	10.9	10.7	9.6
2	12	13.9	13.9	13.9	13.9	13.8	12.9	12.7	11.0
3	11	8.9	8.0	6.9	6.5	5.9	5.5	4.9	4.0
4	17	19.0	19.0	18.8	17.8	16.8	16.0	15.7	14.6
6	22	25.7	25.7	25.7	24.7	23.7	22.8	22.6	20.9
7	8	7.6	6.6	5.9	5.8	5.6	5.6	4.9	4.6
8	8	7.9	6.9	6.7	6.6	5.9	5.8	5.7	4.7
9	2	6.9	5.8	5.5	4.9	4.8	4.8	4.8	4.7
10	1	5.6	4.6	4.3	3.9	3.8	3.8	3.7	3.5
11	38	34.8	34.8	34.8	34.8	34.8	34.8	34.8	34.7
R^2		0.902	0.911	0.914	0.930	0.931	0.933	0.924	0.901

A comparison of predicted and observed performance is presented in Figure 0-22, which shows that no prediction was off by more than one level. Eight out of the ten predictions matched the observed performance and the other two were one level off the observed performance. Thus, the predicted performance in terms of crack initiation time was good for all ten test sections. This finding indicates that the top-down cracking performance model appears to adequately represent and account for the most significant factors that influence top-down cracking in the field.

		Observed Cracking Performance				
		I	II	III	IV	V
Predicted Cracking Performance	I	2				
	II		2	1		
	III		1	2		
	IV				1	
	V					1

Figure 0-22. Predicted versus observed cracking performance levels (without Section 5)

4.3.3 Validation of Model

The previous section showed strong correlation between top-down cracking predictions and observed crack initiation time in the field. The final step in the model-development process was validating the model, i.e., assessing its ability to accurately predict top-down cracking for sections other than those used in developing the model.

Three methods are commonly used in validating a regression model: (1) collection of new data, (2) data splitting, and (3) prediction sum of squares (PRESS). The first method requires the use of a different data set. The second requires a large data set that can be divided for calibration and validation. The third method is suitable for small data sets; it has been successfully used in other studies such as validation of the thermal cracking model (29). Because a different data set

could not be obtained in the project and the available data set was small such that it could not be split, the PRESS method was selected for use in this study.

4.3.3.1 PRESS procedure

In the PRESS procedure, the unknown parameters in the model are estimated when one data point is removed at a time from the data set (i.e., for a data set with n data points, the model is calibrated with $(n-1)$ data points at a time). The model is then used to predict the value of the removed point, and the process is repeated for all the data points in the data set. The predicted values obtained are then compared with the actual values. The R^2 (PRESS) is calculated for the predicted and actual values as follows:

$$(R^2)_p = 1 - \frac{\sum (Y_{(i)} - \hat{Y}_{(i)})^2}{\sum (Y_{(i)} - \bar{Y}_{wo(i)})^2} \quad (0-1)$$

Where $Y_{(i)}$ is the observed response for the i th data point,
 $\hat{Y}_{(i)}$ is the predicted response for the i th data point, and
 $\bar{Y}_{wo(i)}$ is the average of the predicted responses of $(n-1)$ data points without the i th data point.

Because the PRESS procedure uses $(n-1)$ data points to estimate the unknown parameters, the R^2 (PRESS) will always be lower than the R^2 obtained from the full model which uses n data points. The degree of closeness of R^2 (PRESS) to R^2 (Full model) serves as a measure of the model's predictive ability (i.e., good models will have an R^2 from the PRESS procedure close to the R^2 from the full model).

4.3.3.2 Validation process using PRESS

For validation purposes, the performance model used to predict crack initiation for any one particular test section was calibrated using data of the other test sections. For example, the model used to predict crack initiation in Test Section 1 was calibrated using the data set without including Section 1.

The validation process involved two steps. First, similar to the final calibration of the performance model presented in the Model Calibration section, Test Section 5 was excluded; only the other ten test sections were included. The calibration procedure (described in the section) was conducted ten times (once for each data set, including nine test sections). The ten models obtained were then used to make independent predictions, and the R^2 (PRESS) was computed using Equation 4-1. In Step Two, the crack initiation time of Test Section 5 was predicted using the model calibrated with all ten test sections and the error associated with this prediction was added to the R^2 (PRESS).

As an example, the top-down cracking performance model used to predict crack initiation for Test Section 1 was calibrated with data from the other nine test sections (i.e., Test Sections 2 through 11 except for Section 5). Linear regressions were performed to determine eight different values of R^2 (one for each aging parameter) using the data from these sections. The performance model used to predict crack initiation for Test Section 1 was selected as the one having the k_1 value that resulted in the highest R^2 . This process was repeated ten times such that a total of 80 linear regressions were performed during this step. A similar process was used in the second step, where linear regressions were performed to determine eight different values of R^2 using the data from all ten test sections used in the first step. The top-down cracking performance model used to predict crack initiation for Test Section 5 was selected as the one that resulted in the highest R^2 . This process was applied once in the second step.

The R^2 for each linear regression is presented in Table 0-12. A shaded area identifies the largest R^2 for each pavement section and the predicted cracking performance level.

The resulting 11 models were used to make an independent prediction of the top-down cracking initiation time for each test section. The independent predictions were compared with

the observed initiation time to evaluate the predictive capability of the model. Results of this evaluation are presented in the following sub-section.

Table 0-12. Predicted cracking performance for various aging parameters using PRESS procedure

Section No.	Observed Performance Level	Predicted Performance							
		Aging Parameter k_1							
		0.5 (R^2)	1.0 (R^2)	1.5 (R^2)	2.0 (R^2)	2.5 (R^2)	3.0 (R^2)	3.5 (R^2)	5.0 (R^2)
1	II	(0.923)	(0.932)	(0.927)	III (0.937)	(0.934)	(0.933)	(0.924)	(0.900)
2	III	(0.906)	(0.915)	(0.917)	(0.934)	III (0.934)	(0.934)	(0.924)	(0.902)
3	III	(0.906)	(0.920)	(0.929)	(0.949)	(0.956)	II (0.962)	(0.959)	(0.948)
4	III	(0.904)	(0.913)	(0.916)	(0.930)	(0.930)	III (0.933)	(0.924)	(0.905)
5	III	(0.902)	(0.911)	(0.914)	(0.930)	(0.931)	I (0.933)	(0.924)	(0.901)
6	IV	(0.907)	(0.917)	(0.920)	IV (0.931)	(0.928)	(0.927)	(0.917)	(0.893)
7	II	(0.900)	(0.911)	(0.916)	(0.934)	(0.935)	II (0.937)	(0.931)	(0.910)
8	II	(0.900)	(0.910)	(0.913)	(0.931)	(0.934)	II (0.936)	(0.927)	(0.909)
9	I	(0.914)	(0.914)	(0.915)	(0.930)	(0.930)	I (0.932)	(0.921)	(0.895)
10	I	(0.909)	(0.911)	(0.911)	(0.928)	(0.928)	I (0.930)	(0.919)	(0.891)
11	V	(0.736)	(0.763)	(0.771)	(0.821)	(0.824)	V (0.829)	(0.802)	(0.734)

* Shaded cells identify the largest R^2 value for each section and the predicted performance level.

4.3.3.3 Validation results

The R^2 value obtained from the PRESS procedure was 0.82; and an R^2 value of 0.93 was obtained for the full model (i.e., the model determined from the final calibration). These values suggest that the performance model has strong predictive ability. Figure 0-23 shows the

independent predictions (using PRESS) for crack initiation time compared with predictions from the full model, which demonstrates the predictive ability of the model.

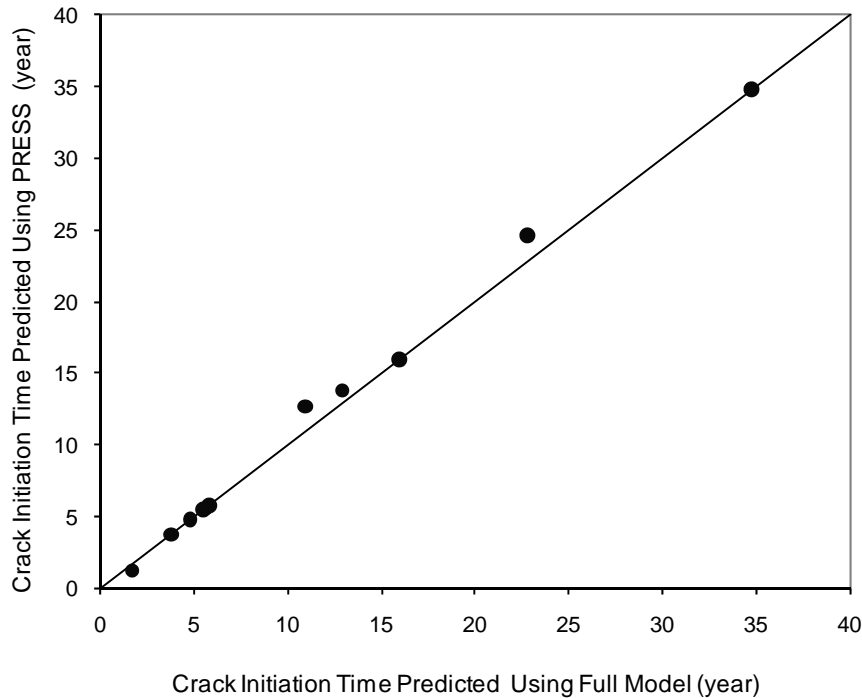


Figure 0-23. Predicted crack initiation time using PRESS versus that using full model

The data were also evaluated by comparing the independent performance predictions with the observed performance levels. The results presented in Figure 0-24 show that only one prediction was off by two levels. Of the other ten predictions, eight matched the observed performance, and two were off by one level. Thus, the predicted cracking performance was good for ten of eleven test sections.

Based on these results and the R^2 (PRESS) value of 0.82, the predictive capability of the model appears to be good. The final predictions using the calibrated/validated model are presented in the next section.

		Observed Cracking Performance Level				
		I	II	III	IV	V
Predicted Cracking Performance Level	I	2		1		
	II		2	1		
	III		1	2		
	IV				1	
	V					1

Figure 0-24. Predicted versus observed cracking performance levels (from PRESS)

4.3.4 Final Model Predictions

Final model predictions were conducted using the calibrated model; the results are presented in Table 0-13. The following sections discuss (1) predicted versus observed cracking performance in terms of both crack initiation time and cracking performance level, (2) predicted crack propagation time versus predicted crack initiation time, and (3) predicted cracking performance of all sections in terms of crack amount development with time.

Table 0-13. Predicted crack depths versus time for an aging parameter (k_1) of 3.0

Section	I75-1A		I75-1B		I75-3		I75-2		SR80-1		SR80-2		
Thickness (inch)	6.54		6.23		6.47		7.42		3.38		6.29		
Year Opened	1988		1989		1988		1989		1987		1984		
Observed Crack Initiation Time (year)	10		12		11		17		13		22		
Predictions	C.D.*	C/D ⁺	Y.C. [@]	C/D	Y.C.	C/D	Y.C.	C/D	Y.C.	C/D	Y.C.	C/D	Y.C.
	0.25	0.04	10.9	0.04	12.9	0.04	5.5	0.03	16.0	0.07	1.2	0.04	22.8
	0.50	0.08	12.7	0.08	14.6	0.08	6.3	0.07	18.4	0.15	1.7	0.08	25.6
	0.75	0.11	13.2	0.12	15.1	0.12	6.8	0.10	18.9	0.22	1.9	0.12	26.5
	1.00	0.15	13.5	0.16	15.4	0.15	6.9	0.13	19.3	0.30	2.0	0.16	26.9
	1.25	0.19	13.7	0.20	15.7	0.19	6.9	0.17	19.6	0.37	2.1	0.20	27.4
	1.50	0.23	13.9	0.24	15.9	0.23	7.0	0.20	19.8	0.44	2.1	0.24	27.7
	1.75	0.27	14.1	0.28	16.0	0.27	7.0	0.24	20.0	0.52	2.4	0.28	27.9
	2.00	0.31	14.2	0.32	16.2	0.31	7.1	0.27	20.1			0.32	28.3
	2.25	0.34	14.3	0.36	16.3	0.35	7.1	0.30	20.3			0.36	28.5
	2.50	0.38	14.5	0.40	16.4	0.39	7.2	0.34	20.4			0.40	28.6
	2.75	0.42	14.7	0.44	16.7	0.43	7.2	0.37	20.6			0.44	28.8
	3.00	0.46	14.8	0.48	17.0	0.46	7.3	0.40	20.7			0.48	29.2
	3.25	0.50	15.1	0.52	17.2	0.50	7.5	0.44	20.8			0.52	29.4
	3.50							0.47	20.9				
	3.75							0.51	21.1				

* C.D. designates Crack Depth (inch); ⁺ C/D designates Crack depth over AC thickness ratio;

[@] Y.C. designates time to each crack depth (year) from opening to traffic.

Table 0-13. Continued

Section	I10-8		I10-9		SR471		SR19		SR997		I94-4		I94-14		
Thickness (inch)	7.20		7.40		2.58		2.39		2.17		9.10		10.90		
Year Opened	1996		1996		2000		2000		1963		1994		1994		
Observed Crack Initiation Time (year)	8		8		2		1		38		4		6		
Predictions	C.D.*	C/D ⁺	Y.C. [@]	C/D	Y.C.	C/D	Y.C.	C/D	Y.C.	C/D	Y.C.	C/D	Y.C.	C/D	Y.C.
	0.25	0.03	5.6	0.03	5.8	0.10	4.8	0.10	3.8	0.12	34.8	0.03	4.2	0.02	6.0
	0.50	0.07	6.6	0.07	6.9	0.19	5.2	0.21	4.7	0.23	39.6	0.05	5.9	0.05	7.2
	0.75	0.10	6.8	0.10	7.3	0.29	5.7	0.31	4.9	0.35	41.4	0.08	6.0	0.07	7.4
	1.00	0.14	7.0	0.14	7.5	0.39	6.0	0.42	5.0	0.46	42.8	0.11	6.2	0.09	7.9
	1.25	0.17	7.1	0.17	7.6	0.48	6.3	0.52	5.1	0.58	43.2	0.14	6.3	0.11	8.0
	1.50	0.21	7.3	0.20	7.7	0.58	7.0					0.16	6.9	0.14	8.3
	1.75	0.24	7.4	0.24	7.8							0.19	7.1	0.16	8.8
	2.00	0.28	7.5	0.27	7.9							0.22	7.2	0.18	9.0
	2.25	0.31	7.5	0.30	8.0							0.25	7.7	0.21	9.2
	2.50	0.35	7.6	0.34	8.1									0.23	9.3
	2.75	0.38	7.7	0.37	8.2									0.25	9.9
	3.00	0.42	7.7	0.41	8.3										
	3.25	0.45	7.7	0.44	8.4										
	3.50	0.49	7.8	0.47	8.5										
	3.75	0.52	7.9	0.51	8.5										

* C.D. designates Crack Depth (inch); ⁺ C/D designates Crack depth over AC thickness ratio;

[@] Y.C. designates time to each crack depth (year) from opening to traffic.

4.3.4.1 Predicted versus observed cracking performance

The predicted cracking performance for all test sections is compared with the observed performance in terms of both crack initiation time and cracking performance level in Figure 0-25. As shown, the predictions generally agree well with the observed performance levels (except for Section SR80-1 which is off by two levels).

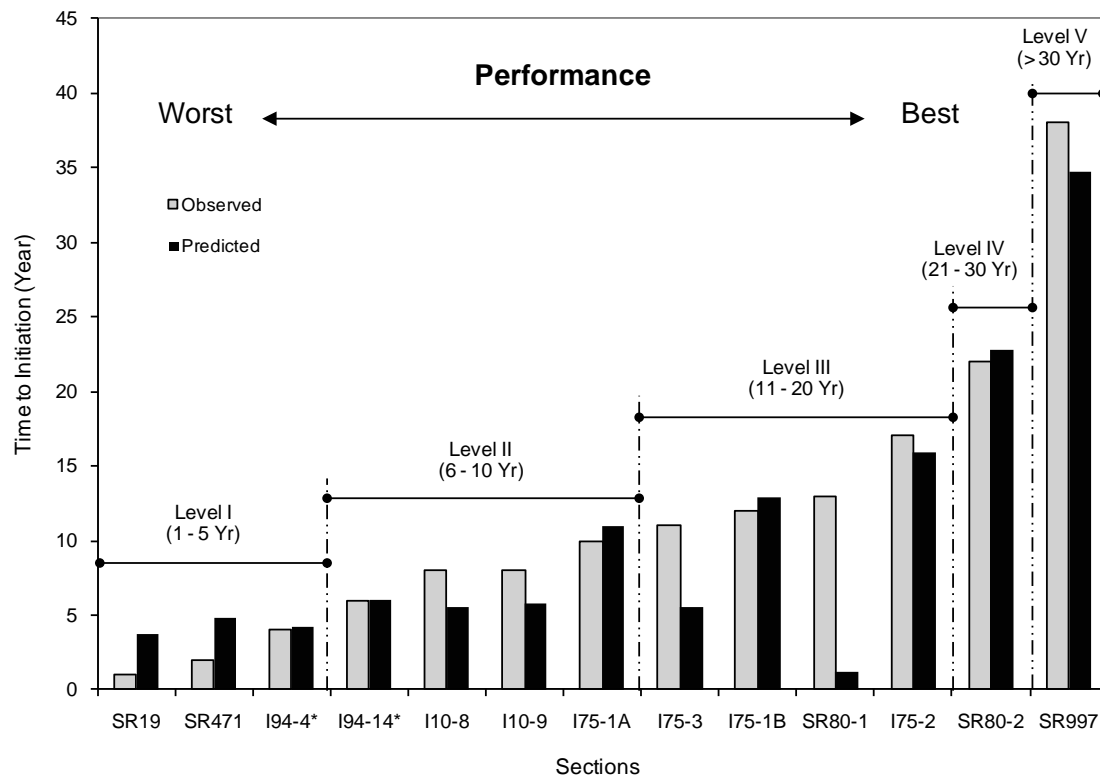


Figure 0-25. Predicted versus observed crack initiation time for all test sections

4.3.4.2 Predicted crack propagation time versus initiation time

The initial depth of top-down cracking was determined to be 6 mm (0.25 in.), and the critical crack depth was defined as the depth equal to one-half of the AC layer thickness (see Appendix B). Therefore, for a vertical crack, the crack propagation time, t_p , can be obtained by computing the difference between the time to initial crack depth (i.e., crack initiation time) and that to critical crack depth.

The crack propagation time determined for each test section using the calibrated model was plotted against the corresponding crack initiation time (Figure 0-26). As shown, the crack propagation time appears to increase linearly with the initiation time such that for pavement sections that start to crack after 10 to 20 years in service, the propagation time to failure is about 4 to 5 years (this is consistent with typical observations in the field). For test sections with an earlier crack initiation, the propagation time tends to be shorter; and for pavements that last for more than 20 years, the time to critical crack depth is longer.

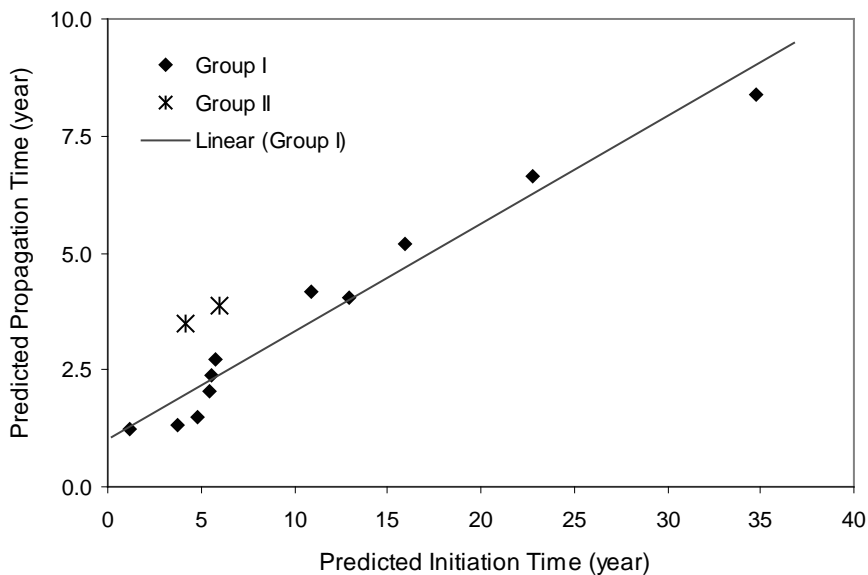


Figure 0-26. Predicted crack propagation time versus crack initiation time

Because reliable field data on crack development cannot be obtained, no further calibration was performed on predicted crack propagation time. However, the comparison shown in Figure 0-26 provides a means for assessing the reasonableness of the model for predicting propagation time.

4.3.4.3 Crack amount development with time

The final model predictions are expressed in terms of crack amount versus time for each test section and presented according to the performance level (I to V) with respect to observed performance in Figures 0-27 to 0-30. These predictions may be summarized as follows:

- The amount of cracking of a thin pavement at initiation is greater than that of a thicker pavement. This indicates that crack initiation may be more easily identified in thinner pavements than in thicker ones in the field.
- For test sections of Group I (governed by the bending mechanism), predictions for sections of lower performance levels are generally consistent with field observations (Figures 0-27 and 0-28). The relatively high creep rate combined with high surface tensile stresses are believed to contribute to the severe cracking conditions in these sections within a relatively short period. Predictions for sections of higher performance levels agree reasonably with observations in the field, except for Section 5 (i.e., SR80-1) (Figures 0-29 and 0-30). The relatively low creep rate and high fracture energy of the asphalt mixtures combined with the relatively low traffic in these sections resulted in longer service life.
- For test sections of Group II (governed by the near-tire mechanism), predictions of crack initiation for both sections of this group agree well with field observations (Figures 0-27 and 0-28). The trend between predicted propagation and predicted initiation time appeared to be different than observed for the bending mechanism. However, this observation should be considered preliminary because there were only two sections in Group II, which did not allow for calibration and/or validation of the near-tire mechanism.

4.4 Summary of Findings

An HMA-FM-based model for predicting top-down cracking propagation in HMA layers was developed in this project. Several key elements were identified, developed, and then incorporated into the existing HMA-FM model, including material property sub-models that account for changes in mixture properties (e.g., fracture energy, creep rate, and healing) with aging, and a thermal-response model that predicts transverse thermal stresses. In addition, a simplified fracture energy-based crack initiation model (without considering damage zone effects) was developed and integrated with the HMA-FM-based model to illustrate the capabilities of a completed system.

Parametric studies have shown that the system can reasonably capture the effects of climate, traffic, and material and structural properties on top-down cracking performance. It was also shown that structural characteristics may define the form of possible top-down cracking mechanisms (bending mechanism – suitable for HMA layers with thin to medium thickness, and near-tire mechanism – dominant for thick HMA layers).

A limited calibration using data from field sections was performed by matching as closely as possible top-down cracking predictions with observed top-down cracking. Only one calibration factor (i.e., the aging parameter, k_1) was included in the calibration process. The results showed that the system appears to reasonably represent and account for the most significant factors that influence top-down cracking. The validation efforts using the PRESS procedure confirmed the viability of the predictive model.

The finalized system was used to predict the increase of crack depth (and crack amount) with time for all 13 field sections included in this project. In general, it was found that the predicted crack propagation time for test sections (Group I) was linearly proportional to the crack initiation time. This relationship indicated that the system can reasonably predict crack propagation time. Predictions for the two full-depth test sections (Group II), governed by the near-tire mechanism, were reasonable. However, some important factors (e.g., wander and effect of stress state on damage rate) were not considered.

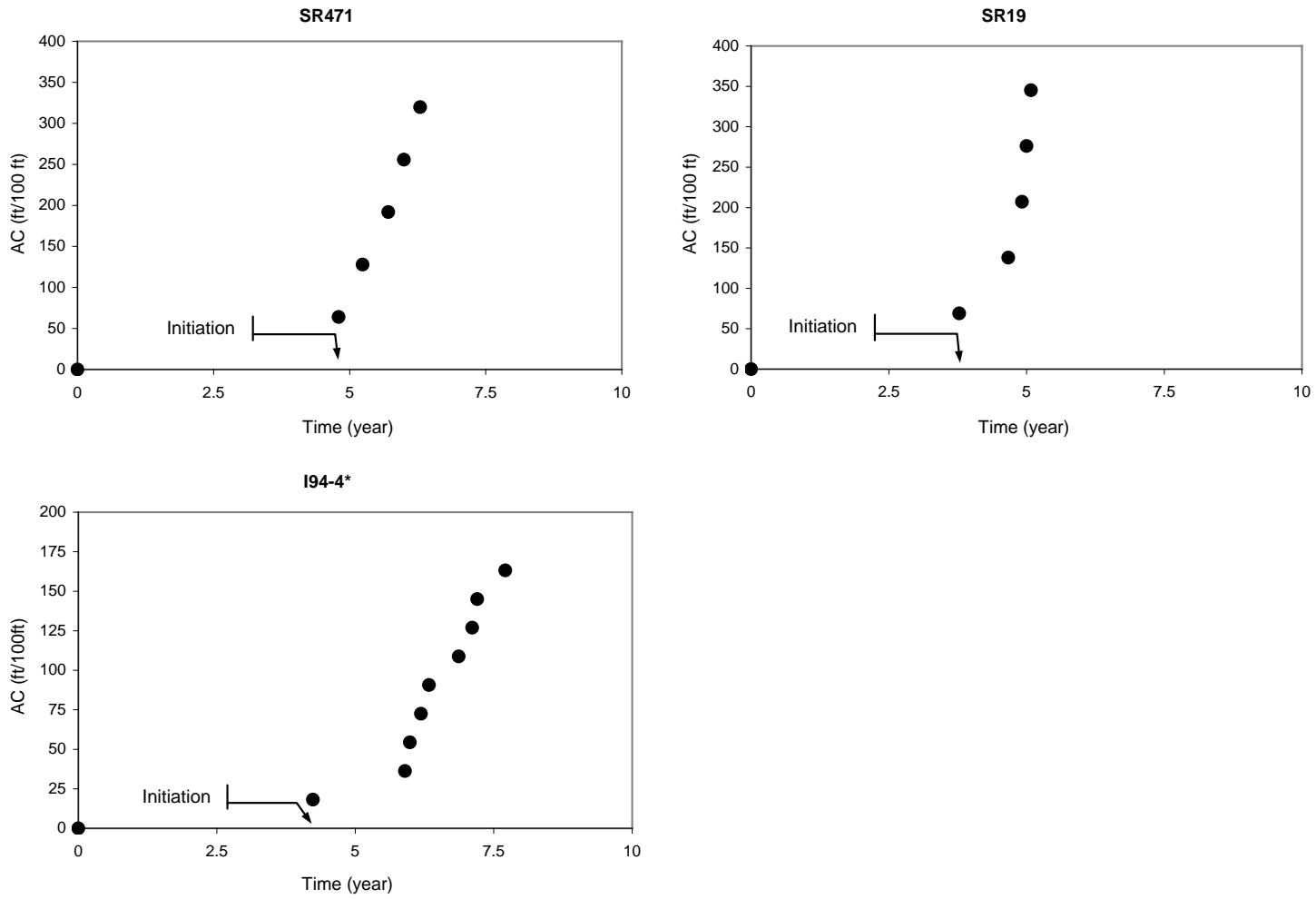


Figure 0-27. Predicted crack amount versus time for test sections of level I

(* The maximum amount of cracking was reduced to 165 ft /100 ft for full depth pavement (near-tire mechanism).)

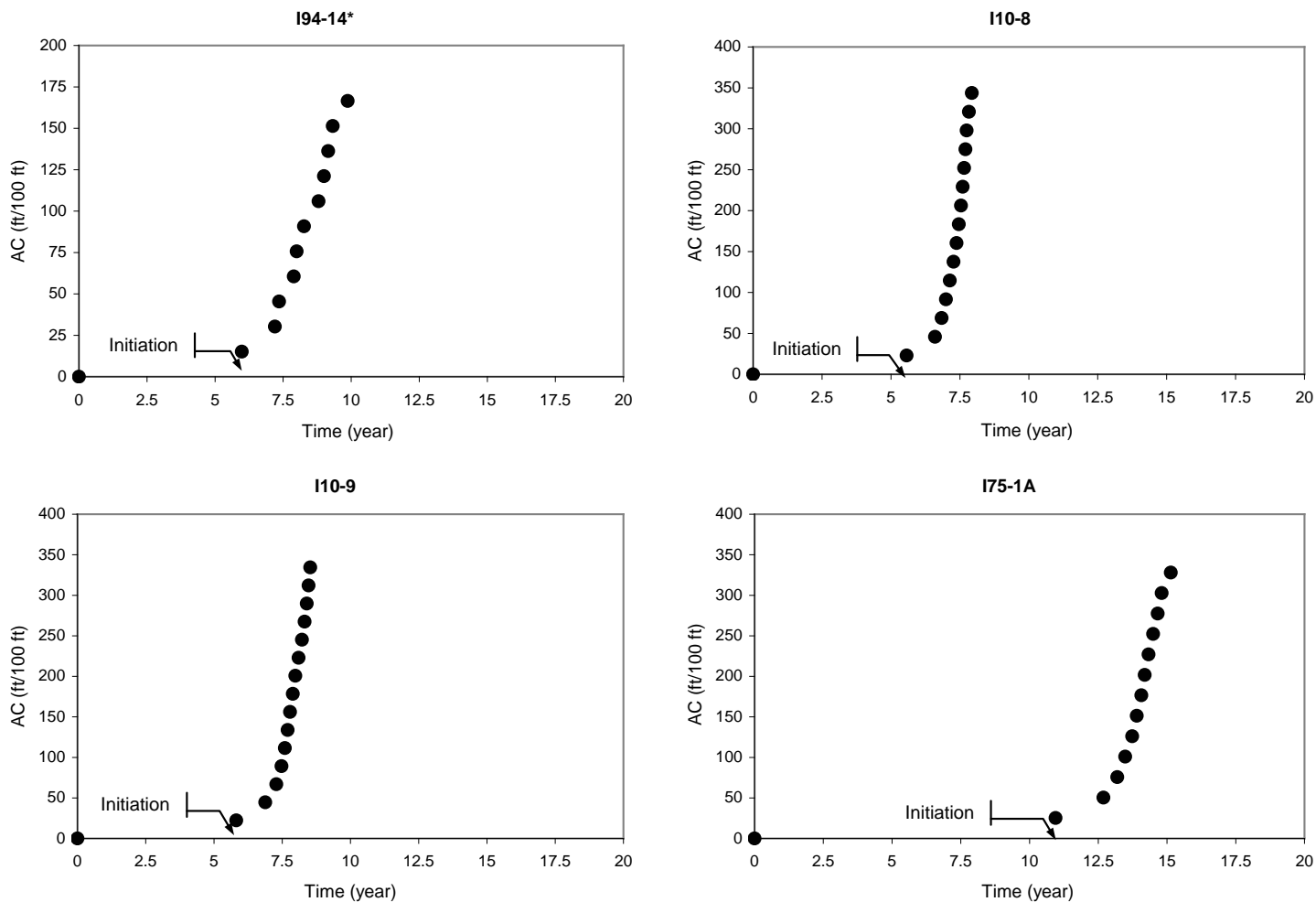


Figure 0-28. Predicted crack amount versus time for test sections of level II

(* The maximum amount of cracking was reduced to 165 ft /100 ft for full depth pavement (near-tire mechanism).)

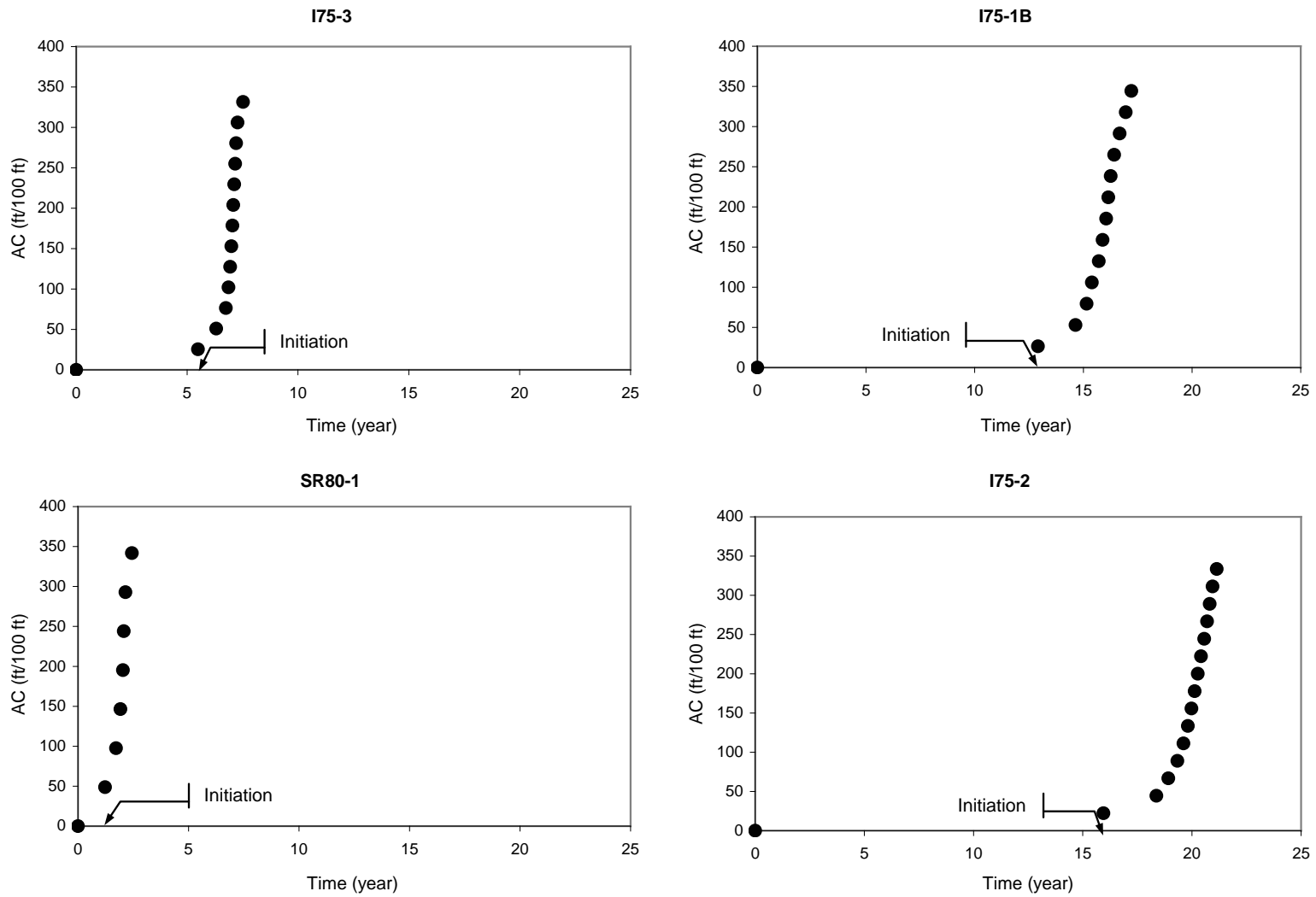


Figure 0-29. Predicted crack amount versus time for test sections of level III

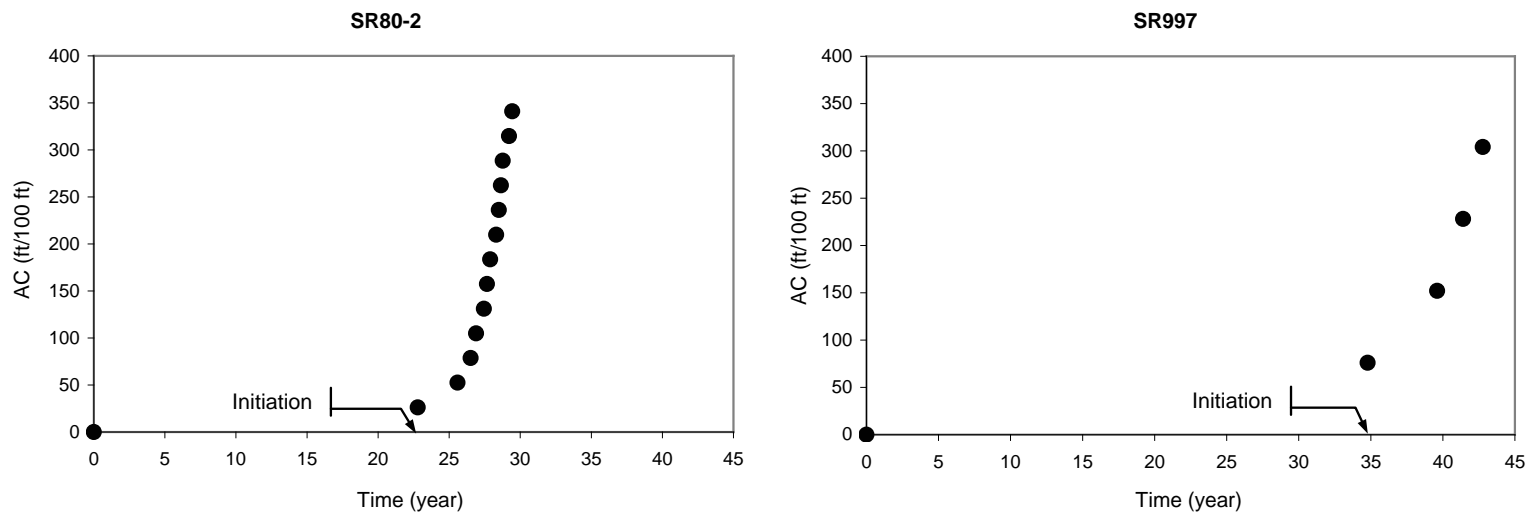


Figure 0-30. Predicted crack amount versus time for test sections of levels IV and V

CHAPTER 5 CONCLUSIONS AND RECOMMENDATIONS FOR FUTURE RESEARCH

5.1 Conclusions

Two model components: (1) a VECD-based crack initiation model and (2) an HMA-FM-based crack propagation model, and one integrated system (i.e., a simplified fracture energy-based approach for crack initiation integrated with the HMA-FM-based crack propagation model) were developed in this project.

The primary role of the VECD-based model is to account for damage zone effects prior to cracking and to identify the time and location of crack initiation sites. Several important material property sub-models (including aging, healing, failure criteria, viscoplasticity, and thermal stress models) were developed, modified, and/or investigated, and then incorporated into the existing VECD model. These material sub-models were then converted into and/or combined with the structural sub-models. The integrated sub-model was implemented in the VECD-FEP++, and an extrapolation method was developed for predicting top-down cracking initiation in HMA pavements. A parametric study was undertaken and shows that the VECD-based model provides reasonable predictions and trends for crack initiation.

The primary role of the HMA-FM-based model is to account for macro crack effects during crack propagation and to predict the propagation of cracks over time. This model consists of the following key elements: (1) a critical condition concept that can accurately capture field observations and significantly reduce the computation time required for long-term pavement performance prediction; (2) material property sub-models that account for changes in near-surface mixture properties with aging, including increase in stiffness (stiffening), reduction in fracture energy (embrittlement), and reduction in healing potential, which together make pavements more susceptible to top-down cracking over time; (3) a thermal-response model that

predicts transverse thermal stresses, which can be an important part of the top-down cracking mechanism; and (4) a pavement fracture model that predicts crack growth over time, accounting for the effect of changes in geometry on stress distributions.

A simplified fracture energy-based approach for predicting crack initiation (i.e., a crack initiation model that does not consider damage zone effects) was developed and integrated with the HMA-FM-based model to form a top-down cracking performance model to demonstrate the capabilities of a completed system. A systematic parametric study showed that the integrated performance model provided reasonable predictions and expected trends for both crack initiation and propagation. A limited calibration and validation using data from field sections indicated that the performance model reasonably represents and accounts for the most significant factors that influence top-down cracking in the field, but it is not ready or intended for immediate implementation because (1) the model eventually implemented in the MEPDG should capture damage zone effects, for which the VECD-based model is needed, and (2) further verification of sub-models is needed.

In summary, the work performed indicates that the VECD-based crack initiation model and the HMA-FM-based crack propagation model developed and evaluated in this project can form the basis for a top-down cracking model suitable for use in the MEPDG. Furthermore, given the general nature of the component models, they can also form the basis for the next-generation MEPDG performance model to predict multiple cracking distresses simultaneously, including top-down cracking, bottom-up cracking, and thermal cracking.

5.2 Recommendations for Future Research

It is recommended that the two primary model components developed in this study (i.e., the VECD-based crack initiation model and the HMA-FM-based crack propagation model) be fully integrated to form a top-down cracking performance model suitable for implementation in

the MEPDG. Full integration of the two models is necessary for accurate performance prediction to establish the confidence needed for implementation of a reliable MEPDG. Furthermore, the resulting model would be a suitable candidate for implementation as the next generation performance model for bottom-up cracking and thermal cracking. The general nature of the targeted system, which can predict damage and crack propagation anywhere in the pavement system, considering the combined effects of both load and environment, forms the basis for a single system to deal with multiple cracking distresses simultaneously.

It is emphasized that the simplified integrated system developed in this study is not ready nor intended for immediate implementation, because (1) it is necessary to evaluate damage zone effects on performance predictions, for which the VECD-based crack initiation model is needed; (2) it is necessary to further verify the material property sub-models developed in this study (i.e., models for aging, healing, damage, and fracture criteria); and (3) validation and calibration of the integrated performance model needs to be performed on a broader range of pavements and environmental conditions. The intent of the simplified integrated system was to demonstrate the potential of a fully integrated system, while gaining experience in dealing with issues relative to integration of model components that involve very different functions (e.g., how to build a reasonable framework for integration) as well as issues relative to calibration and validation of a full system (e.g., issues associated with collection and/or use of field performance data). The experiences gained were of great benefit in helping to formulate a plan for integrating, calibrating, and validating the two model components. It is proposed that future development progress as described in the following two phases:

Phase One: As a minimum, the following considerations are recommended to develop a top-down cracking performance model for the MEPDG based on the two primary model components developed in this study:

- Aging model: There is a need to unify the material property aging submodels developed for the VECD-based and HMA-FM-based component models, including submodels for viscoelastic properties and damage and fracture properties.
- Healing model: There is a need to unify the healing submodels developed for the VECD-based and HMA-FM-based component models. Also, the unified healing model should be verified using data under various conditions that are needed for top-down cracking simulations.
- Failure criteria: It is recommended that the energy-based failure criteria defined and used in the HMA-FM-based model be incorporated into the VECD system, so that a unified and more advanced failure criterion is used by both.
- The near-tire mechanism: There is a need to unify the near-tire mechanism considered by the VECD-based and HMA-FM-based component models. Also, the effects of tire type and cross slope on shear-induced tension near the tire edge should be considered for incorporation into the unified near-tire mechanism.
- Refinement of analysis program: There is a need to reduce the computer run time of the VECD-based model through the improvement, refinement, and calibration of the submodels which are included in the analysis system.
- Model calibration and validation using field data: A calibration and validation effort with a broader range of field sections is needed to ensure the accuracy of the integrated top-down cracking performance model.

Phase Two: The following considerations are recommended to develop a more advanced system for future use in the MEPDG,

- Advanced material models: The model developed in Phase One includes modules for linear-elastic unbound paving materials. For more accurate predictions, enhancements are needed to: include a nonlinear-elastic material model, consider the effects of moisture gradients in pavement systems, and incorporate anisotropy of the HMA and slip elements at the pavement-base interface and/or between HMA layers.
- Traffic: Constant ESAL loading distribution was used in Phase One. It would be more realistic to use an equivalent daily loading history that has a more representative load spectra and distribution (i.e., more trucks during certain times of the day). Also, load wander likely plays a role in performance associated with the near-tire mechanism. Therefore, it should be considered in future model development.

- Generalized cracking mechanism: The VECD-FEP++ models top-down and bottom-up damage propagation simultaneously, but an algorithm to account for the interaction of these two cracking mechanisms in macro crack propagation (or, simultaneous damage and macro crack propagation) needs to be developed for determination of critical conditions.

REFERENCES

1. Roque, R., and B. E. Ruth. "Mechanisms and Modeling of Surface Cracking in Asphalt Pavements." *Journal of the Association of Asphalt Paving Technologists*, Vol. 59, 1990, pp. 397-421.
2. Myers, L., R. Roque, and B. E. Ruth. "Mechanisms of Surface Initiated Longitudinal Wheel Path Cracks in High-type Bituminous Pavements." *Journal of the Association of Asphalt Paving Technologists*, Vol. 67, 1998, pp. 402-432.
3. Uhlmeier, J. S., K. Willoughby, L. M. Pierce, and J. P. Mahoney. "Top-down Cracking in Washington State Asphalt Concrete Wearing Courses." *Transportation Research Record: Journal of the Transportation Research Board*, No. 1730, Transportation Research Board of the National Academies, Washington, DC, 2000, pp. 110-116.
4. Gerritsen, A. H., et al. Prediction and Prevention of Surface Cracking in Asphaltic Pavements. *Proc., 6th International Conference on Structural Design of Asphalt Pavements*, Ann Arbor, Michigan, 1987, pp. 378-391.
5. De Freitas, E. F., P. Pereira, L. Picado-Santos, and A. T. Papagiannakis. "Effect of Construction Quality, Temperature, and Rutting on Initiation of Top-downing Cracking." *Transportation Research Record: Journal of the Transportation Research Board*, No. 1929, Transportation Research Board of the National Academies, Washington, DC, 2005, pp. 174-182.
6. Matsuno, S., and T. Nishizawa. "Mechanism of Longitudinal Surface Cracking in Asphalt Pavement." *Proc., 7th International Conference on Asphalt Pavements*. University of Nottingham, UK, Vol. 2, 1992, pp. 277-291.
7. Raju, S., et al. Analysis of Top-Down Cracking Behavior of Asphalt Pavements. *Transportation Research Board*, Washington, D.C., 2008.
8. Myers, L. A., and R. Roque. "Top-down Crack Propagation in Bituminous Pavements and Implications for Pavement Management." *Journal of the Association of Asphalt Paving Technologists*, Vol. 71, 2002, pp. 651-670.
9. Zhang, Z., R. Roque, and B. Birgisson. "Evaluation of Laboratory-Measured Crack Growth Rate for Asphalt Mixtures." In *Transportation Research Record: Journal of the Transportation Research Board*, No. 1767, Transportation Research Board of the National Academies, Washington, D.C., 2001, pp. 67-75.
10. Kim, B., R. Roque, and B. Birgisson. "Effect of Styrene Butadiene Styrene Modifier on Cracking Resistance of Asphalt Mixture." *Transportation Research Record: Journal of the Transportation Research Board*, No. 1829, Transportation Research Board of the National Academies, Washington, DC, 2003, pp. 8-15.

11. Roque, R., Z. Zhang, and B. Sankar. "Determination of Crack Growth Rate Parameters of Asphalt Mixtures Using the SuperPave Indirect Tensile Test (IDT)." *Journal of the Association of Asphalt Paving Technologists*, Vol. 68, 1999, pp. 404-433.
12. Yoo, P. J., and I. L. Al-Qadi. "The Truth and Myth of Fatigue Cracking Potential in Hot-Mix Asphalt: Numerical Analysis and Validation." *Journal of the Association of Asphalt Paving Technologists*, Vol. 77, 2008, pp. 549-590.
13. Kim, Y. R., et al. Application of Viscoelastic Continuum Damage Model Based Finite Element Analysis to Predict the Fatigue Performance of Asphalt Pavements. KSCE, *Journal of Civil Engineering*, Vol. 12, No. 2, 2008, pp. 109-120.
14. Roque, R., et al. "Evaluation of Surface-initiated Longitudinal Wheel Path Cracking." Final Report for FDOT No. C5978 Contract, Univ. of Florida, Gainesville, Florida, 2006.
15. Daniel, J. S., and Y. R. Kim. "Laboratory Evaluation of Fatigue Damage and Healing of Asphalt Mixtures." *ASCE Journal of Materials in Civil Engineering*, Vol. 13, No. 6, 2001, pp. 434-440.
16. Raghavendra, S., et al. Verification of the Rate of Asphalt Mix Aging Simulated by AASHTO PP2-99 Protocol. In *Transportation Research Record, TRB, CD*. 2006.
17. Bell, C. A., A. J. Wieder, and M. J. Fellin. *Laboratory Aging of Asphalt-Aggregate Mixtures: Field Validation*. SHRP-A-390, Strategic Highway Research Program, National Research Council, Washington, D.C., 1994.
18. AASHTO. AASHTO R30 – 02: Standard Practice for Mixture Conditioning of Hot-Mix Asphalt (HMA). Washington, D.C., 2008.
19. Reese, R. "Properties of Aged Asphalt Binder Related to Asphalt Concrete Fatigue Life." *Journal of the Association of Asphalt Paving Technologists*, Vol. 66, 1997, pp. 604-632.
20. Underwood, B. S., et al. "Response and Fatigue Performance Modeling of ALF Pavements Using 3-D Finite Element Analysis and a Simplified Viscoelastic Continuum Damage Model." *Journal of the Association of Asphalt Paving Technologists*, 2009. In Press.
21. Lee, H. J., and Y. R. Kim. "A Viscoelastic Continuum Damage Model of Asphalt Concrete with Healing." *ASCE Journal of Engineering Mechanics*, Vol. 124, No. 11, 1998, pp. 1224-1232.
22. Kim, Y. R., D. N. Little, and R. L. Lytton. "Fatigue and Healing Characterization of Asphalt Mixtures." *ASCE Journal of Materials in Civil Engineering*, Vol. 15, No.1, 2003, pp. 75-83.

23. Kim, Y. R., D. N. Little and R. L. Lytton. "Use of Dynamic Mechanical Analysis (DMA) to Evaluate the Fatigue and Healing Potential of Asphalt Binders in Sand Asphalt Mixtures." *Journal of the Association of Asphalt Paving Technologists*, Vol. 71, 2002, pp. 176-206.
24. Mirza, M. W., and M. W. Witzak. "Development of a Global Aging System for Short and Long Term Aging of Asphalt Cements." *Journal of the Association of Asphalt Paving Technologists*, Vol. 64, 1995, pp. 393-430.
25. AASHTO. AASHTO Guide for Design of Pavement Structures. Washington, D.C., 1993.
26. Underwood, B. S., Y. R. Kim and M. N. Guddati. "Characterization and Performance Prediction of ALF Mixtures Using a Viscoelastoplastic Continuum Damage Model." *Journal of the Association of Asphalt Paving Technologists*, Vol. 75, 2006, pp. 577-636.
27. Hinterhoelzl, R. M. and R. A. Schapery. "FEM Implementation of a Three-Dimensional Viscoelastic Constitutive Model for Particulate Composites with Damage Growth." *Mechanics of Time Dependent Materials*, Vol. 8, 2004, pp. 65-94.
28. Kutay, M. E., N. Gibson, and J. Youtcheff. "Conventional and Viscoelastic Continuum Damage (VECD) - Based Fatigue Analysis of Polymer Modified Asphalt Pavements." *Journal of the Association of Asphalt Paving Technologists*, Vol. 77, 2008, pp. 395-434.
29. Lytton, R. L., et al. *Development and Validation of Performance Prediction Models and Specifications for Asphalt Binders and Paving Mixes*. SHRP-A-357, Strategic Highway Research Program, National Research Council, Washington, D.C., 1993.
30. Witzak, M. W., and O. A. Fonseca. "Revised Predictive Model for Dynamic (Complex) Modulus of Asphalt Mixtures." *Transportation Research Record: Journal of the Transportation Research Board*, No. 1540, Transportation Research Board of the National Academies, Washington, DC, 1996, pp. 15-23.
31. Deme, I. J., and F. D., Young. "Ste. Anne Test Road Revisited Twenty Years Later." *Proceedings, Canadian Technical Asphalt Association*, Vol. 32, 1987, pp. 254-283.
32. Kim, B., and R. Roque. "Evaluation of Healing Property of Asphalt Mixtures." *Transportation Research Record: Journal of the Transportation Research Board*, No. 1970, Transportation Research Board of the National Academies, Washington, D.C., 2006, pp. 84-91.
33. Hiltunen, D. R., and R. Roque. "A Mechanics-Based Prediction Model for Thermal Cracking of Asphaltic Concrete Pavements." *Journal of the Association of Asphalt Paving Technologists*, Vol. 63, 1994, pp. 81-117.
34. Sangpetngam, B. *Development and Evaluation of a Viscoelastic Boundary Element Method to Predict Asphalt Pavement Cracking*. PhD Dissertation. University of Florida, Gainesville, 2003.

35. Roque, R., and W. G. Buttlar. "The Development of a Measurement and Analysis System to Accurately Determine Asphalt Concrete Properties Using the Indirect Tensile Mode." *Journal of the Association of Asphalt Paving Technologists*, Vol. 61, 1992, pp. 304-332.
36. Buttlar, W. G., and R. Roque. "Development and Evaluation of the Strategic Highway Research Program Measurement and Analysis System for Indirect Tensile Testing at Low Temperatures." In *Transportation Research Record: Journal of the Transportation Research Board*, No. 1454, Transportation Research Board of the National Academies, Washington, D.C., 1994, pp. 163-171.
37. *Flexible Pavement Condition Survey Handbook*. State Materials Office, Florida Department of Transportation, 2003.

APPENDIX A. DEVELOPMENT OF THE VECD-BASED MODEL

TABLE OF CONTENTS

	<u>page</u>
TABLE OF CONTENTS.....	A-ii
APPENDIX	
A DEVELOPMENT OF THE VECD-BASED MODEL	A-1
A.1 Development of Model Components.....	A-3
A.1.1 Laboratory Specimen Fabrication and Test Method	A-3
A.1.2 Material Property Sub-models.....	A-5
A.1.2.1 Linear viscoelastic (LVE) model	A-5
A.1.2.2 Viscoelastic continuum damage model (VECD)	A-9
A.1.2.3 Fatigue life prediction	A-14
A.1.2.4 Statistical analysis for dynamic modulus test results of the AL mix	A-25
A.1.2.5 Viscoplasticity	A-27
A.1.2.6 Thermal stress.....	A-30
A.2 Reasonableness and Sensitivity Checks	A-32
A.2.1 Reasonableness.....	A-32
A.2.2 Sensitivity	A-39
A.2.2.1 Support condition effect	A-39
A.2.2.2 Aging effect.....	A-41
A.2.2.3 Thermal stress effect	A-42
A.2.2.4 Viscoplastic effect	A-43
A.3 Example Simulation and Parametric Study Contour Plots	A-45
A.3.1 Example Simulation Contour Plots	A-45
A.3.2 Parametric Study Contour Plots	A-46
A.4 List of References	A-55

CHAPTER 1 DEVELOPMENT OF THE VECD-BASED MODEL

Top-down cracking has been proven to be one of the major distresses in hot-mix asphalt (HMA) pavements in the United States. Many field studies have shown that different patterns of top-down cracking exist, including cracks that start from the pavement surface and propagate downward, cracks that start as a top-down crack and propagate horizontally at the layer interface, and cracks that start from both the top and bottom simultaneously, forming a conjoined cracking pattern. The complex state of stress that exists in HMA pavements with various layer materials and thicknesses makes it difficult to determine the location of crack initiation and to predict crack propagation. For example, a crack may initiate at the bottom of the HMA layer, but changes in the state of stress during the propagation of that crack may result in the initiation and propagation of another crack at the top of the HMA layer. These complex mechanisms involved in crack initiation and propagation can make it difficult to reliably predict the service life of HMA pavements using conventional HMA performance prediction models and pavement response models.

With the goal of accurate pavement performance evaluation, researchers at North Carolina State University (NCSU) have been developing advanced models for HMA under complex loading conditions. Over the past decade, they have successfully developed material models that can accurately capture various critical phenomena, such as: microcrack-induced damage, which is critical in fatigue modeling; strain rate-temperature interdependence; and viscoplastic flow, which is critical in high temperature modeling. The resulting single model is termed the viscoelastoplastic continuum damage (VEPCD) model.

To extend the strengths of the VEPCD model to the fatigue cracking evaluation of pavement systems, the viscoelastic continuum damage (VECD) model has been incorporated

into the public domain finite element code, FEP++. The resulting product, the so-called VECD-FEP++, allows the accurate evaluation of boundary condition effects (e.g., layer thickness) on the material behavior. In the VECD-FEP++, the damage is calculated for each element based on its state of stress, temperature, loading rate, and boundary conditions. Therefore, it is not necessary to assume *a priori* the location of distress initiation, nor the path of distress evolution. Not having to make such assumptions is a feature of the VECD-FEP++ that is essential in modeling top-down cracking initiation in various HMA pavements. The flexible nature of the VECD-FEP++ modeling technique allows cracks to initiate wherever the fundamental material law suggests. As a result, much more realistic and accurate cracking simulations can be accomplished using the VECD-FEP++.

The capability of the VECD-FEP++ to predict the performance of the pavement structure has been validated using different pavement structures. One example uses the Federal Highway Administration Accelerated Load Facility (FHWA ALF) pavements and another example is the Korea Express Highway (KEC) test road in South Korea (13). In the FHWA ALF research, twelve asphalt pavement lanes (that use various binders) were constructed at the FHWA Turner-Fairbanks Highway Research Center to rapidly collect data on pavement performance under conditions in which axle loading and climatic conditions are controlled. The KEC test road was constructed in December 2002 to serve as the basis for Korea's new pavement design guide, giving consideration to actual traffic loads and environmental changes. This test road is a 7.7 km two-lane highway consisting of 25 Portland cement concrete (PCC) pavement sections and 15 asphalt concrete (AC) pavement sections as well as three bridges and two geotechnical structures. The variables considered in the Korean study for AC pavements are surface layer type, base layer type, base layer thickness, and sublayer properties. Field performance surveys

have been performed since the test road was constructed and will be continued. Predictions made using the VECD-FEP++ for the KEC test road sections demonstrate field performance trends and also reveal a generally positive relationship between model predictions and field observations for all the sections.

In an attempt to demonstrate the ability of the VECD-FEP++ to integrate the effects of variables that are important in top-down cracking behavior, several sub-models are refined from existing models and incorporated into the VECD-FEP++. These models account for aging, healing, thermal stress, viscoplasticity and mode-of-loading. The Enhanced Integrated Climatic Model (EICM) is also integrated into the framework. It must be noted that these sub-models are incorporated into the VECD-FEP++ framework as place-holders only. Their accuracy needs to be verified and calibrated with further testing using various mixtures and in-depth analysis of the results. However, the reasonableness of the VECD-FEP++ with these sub-models is demonstrated using sensitivity analysis and a parametric study.

A.1 Development of Model Components

A.1.1 Laboratory Specimen Fabrication and Test Method

All specimens were compacted by the Servopac Superpave gyratory compactor, manufactured by IPC Global of Australia, to dimensions of 178 mm in height and 150 mm in diameter. To obtain specimens of uniform quality for testing, these samples were cored and cut to a height of 150 mm and a diameter of 75 mm.

After obtaining specimens of the appropriate dimensions, air void measurements were taken via the Core-Lok method, and specimens were stored until testing. It is noted that the air voids for all tests in this research are between 3.5% and 4.5%. During storage, specimens were sealed in bags and placed in an unlit cabinet to reduce the aging effects. Further, no test specimens were stored for longer than two weeks before testing.

Prior to all testing, the steel end plates were glued to the specimen using DEVCON steel putty. Extreme care was taken to completely clean both the end plates and the specimen ends before each application to prevent failure at the glued area. To ensure the specimens were properly aligned, a special gluing jig was employed so that the end plates were parallel, thus minimizing any eccentricity that might occur during the test.

Measurements of axial deformations were taken during testing at 90° intervals over the middle 100 mm of the specimen using loose-core linear variable displacement transducers (LVDTs). Load, crosshead movement and specimen deformation data were acquired using a 16-bit National Instruments data acquisition board and collected using LabVIEW software. The data acquisition rate varied depending on the nature of the test so that the appropriate amount of data could be acquired for analysis. A MTS closed-loop servo-hydraulic loading frame was used for all the tests. Depending on the nature of the test, either an 8.9 kN or 25 kN load cell was used. An environmental chamber, equipped with liquid nitrogen coolant and a feedback system, was used to control and maintain the test temperature.

Three different types of laboratory testing were performed for the aging study: the complex modulus test, constant crosshead rate test, and cyclic fatigue test. The complex modulus test and constant crosshead rate test were carried out with the aim of capturing the aging effects in the current VECD model. For a more direct investigation of aging effects, cyclic fatigue tests were performed in controlled crosshead (CX) and controlled stress (CS) modes.

The complex modulus test was performed in stress-controlled uniaxial tension-compression mode. The test was performed at frequencies of 25, 10, 5, 1, 0.5, and 0.1 Hz and temperatures of -10°, 5°, 20°, 40°, and 54°C. The load level was adjusted for each condition to produce total strain amplitudes of about 50 to 70 microstrains, which is in the linear viscoelastic

(LVE) range. The constant crosshead rate test was conducted in uniaxial tension mode at different on-specimen LVDT strain rates at both 5°C and 40°C until failure. Instead of testing several replicates at a limited set of rates and temperatures, tests were conducted at three different rates with one replicate per rate.

Both types of cyclic fatigue tests, CX and CS, were conducted only in tension mode with a haversine loading at a fixed level. Because a true controlled strain test using cylindrical specimens is difficult to run and can damage equipment if improperly performed, the CX test was utilized. Such a test results in a mixed mode of loading that is neither controlled stress nor controlled strain.

A.1.2 Material Property Sub-models

A.1.2.1 Linear viscoelastic (LVE) model

A.1.2.1.1 Linear viscoelasticity

Viscoelastic materials exhibit time and temperature dependence, meaning that the material response is not only a function of the current input, but the entire input history. By contrast, the response of an elastic material is dependent only on the current input. For the uniaxial loading considered in this research, the non-aging, LVE constitutive relationships are expressed in the convolution integral form, as shown in Equations (A-33) and (A-34):

$$\sigma = \int_0^t E(t-\tau) \frac{d\varepsilon}{d\tau} d\tau \quad \text{and} \quad (\text{A-33})$$

$$\varepsilon = \int_0^t D(t-\tau) \frac{d\sigma}{d\tau} d\tau, \quad (\text{A-34})$$

where $E(t)$ and $D(t)$ are the relaxation modulus and creep compliance, respectively (the τ term is the integration variable). The relaxation modulus and creep compliance are important material

properties, along with the complex modulus, in LVE theory. Because these two properties are the responses for respective unit inputs, they are called *unit response functions*. These unit response functions can be obtained either by experimental tests performed in the LVE range or by converting another unit response function, as suggested by Park and Schapery (2).

A.1.2.1.2 Unit response functions and their interrelationships

The unit response functions presented in Equations (A-33) and (A-34) are often measured in the frequency domain via the complex modulus test, because it is often difficult to obtain unit response functions in the time domain due to the limitations of the machine capacity or testing time. The complex modulus provides the constitutive relationship between the stress and strain of a material loaded in a steady-state sinusoidal manner, e.g., in the frequency domain. The storage modulus can be determined from the complex modulus and it can be converted to a time-dependent property, such as $E(t)$ and $D(t)$, through LVE theory. When the storage modulus is expressed in terms of reduced angular frequency, ω_R , as shown in Equation (A-35), it can be expressed using the Prony series representation given in Equation (A-36) (2, 3).

$$E'(\omega_R) = |E^*(\omega_R)| \sin(\phi(\omega_R)) \quad \text{and} \quad (\text{A-35})$$

$$E'(\omega_R) = E_\infty + \sum_{i=1}^m \frac{\omega_R^2 \rho_i E_i}{\omega_R^2 \rho_i^2 + 1}, \quad (\text{A-36})$$

where

- E_∞ = the elastic modulus,
- ω_R = the angular frequency ($= 2\pi f_R \Delta t$),
- Δt = the time lag between the stress and strain,
- E_i = the modulus of the i^{th} Maxwell element (fitting coefficient), and
- ρ_i = the relaxation time (fitting coefficient).

The coefficients determined from this process are then used with Equation (A-37) to find the relaxation modulus.

$$E(t) = E_{\infty} + \sum_{i=1}^m E_i e^{-t/\rho_i} \quad (\text{A-37})$$

Using the theory of viscoelasticity, the exact relationship between the creep compliance and the relaxation modulus is given by Equation (A-38).

$$\int_0^t E(t-\tau) \frac{dD(\tau)}{d\tau} d\tau = 1 \quad (\text{A-38})$$

If the creep compliance can be written in terms of the Prony representation (Equation (A-39)), substituted into Equation (A-38) along with Equation (A-37) and simplified, the result can be expressed as a linear algebraic equation, Equation (A-40). The coefficients, $\{D\}$ in this equation, are solved by any proper numerical method.

$$D(t) = D_g + \sum_{j=1}^n D_j \left(1 - e^{-t/\tau_j}\right) \quad \text{and} \quad (\text{A-39})$$

$$[A]\{D\} = [B], \quad (\text{A-40})$$

where

$$[A] = \sum_{j=1}^M \left[\sum_{m=1}^N \frac{\rho_m E_m}{\rho_m - \tau_j} \left(e^{-\frac{t}{\rho_m}} - e^{-\frac{t}{\tau_j}} \right) + E_{\infty} \left(1 - e^{-\frac{t}{\tau_j}} \right) \right],$$

$$\{D\} = D_j; \text{ and}$$

$$[B] = 1 - \frac{1}{E_{\infty} + \sum_{m=1}^N E_m} \left(E_{\infty} + \sum_{m=1}^N E_m e^{-\frac{t}{\rho_m}} \right)$$

Once the coefficients, D_j , are determined, they are substituted into Equation (A-39) to find the creep compliance.

A.1.2.1.3 Time-temperature superposition principle for linear viscoelastic material

The effects of time and temperature on viscoelastic material behavior can be combined into a single parameter, called *reduced time*, through the time-temperature superposition principle.

Viscoelastic properties obtained in the LVE range at different temperatures can be superposed to develop a single mastercurve by shifting them horizontally to a certain reference temperature.

The horizontal distance required to superpose a curve to a reference curve in logarithmic space is the log of the time-temperature shift factor (a_T). A material that exhibits a single mastercurve by this method is called *thermorheologically simple*. Equation (A-41) represents the general

mathematical definition of reduced time.

$$\xi(t) = \int_0^t \frac{1}{a_T(\tau)} d\tau, \quad (\text{A-41})$$

where

a_T = the time-temperature shift factor.

When the temperature is constant, for example in a relaxation modulus experiment, Equation (A-41) simplifies to the more common form shown in Equation (A-42). For frequency domain conditions, such as when measurements are taken in a dynamic modulus test, the reduced frequency is similarly computed using Equation (A-43).

$$\xi = \frac{t}{a_T} \quad (\text{A-42})$$

$$f_{red} = f * a_T \quad (\text{A-43})$$

A.1.2.2 Viscoelastic continuum damage model (VECD)

A.1.2.2.1 Continuum damage

On the simplest level, continuum damage mechanics considers a damaged body with some stiffness as an undamaged body with a reduced stiffness. Continuum damage theories thus attempt to quantify two values: damage and effective stiffness. Further, these theories ignore specific microscale behaviors and, instead, characterize a material using macroscale observations, i.e., the net effect of microstructural changes on observable properties. In the macroscale, the most convenient method to assess the effective stiffness is to use the instantaneous secant modulus. As discussed in the subsequent sections, direct use of the stress-strain secant modulus in asphalt concrete (AC) is complicated by time dependence. Damage is oftentimes more difficult to quantify and generally relies on macroscale measurements combined with rigorous theoretical considerations. For the VECD model, Schapery's work potential theory, which is based on thermodynamic principles, is appropriate for the purpose of quantifying damage. Within Schapery's theory, damage is quantified by an internal state variable (S) that accounts for microstructural changes in the material.

A.1.2.2.2 Correspondence principle

The correspondence principle states that viscoelastic problems can be solved with elastic solutions when physical strain is replaced by pseudo strain.

$$\varepsilon^R = \frac{1}{E_R} \int_0^t E(t-\tau) \frac{d\varepsilon}{d\tau} d\tau, \quad (\text{A-44})$$

where E_R is a particular reference modulus included for dimensional compatibility and typically taken as one. Using pseudo strain in place of physical strain, the constitutive relationship presented in Equation (A-33) can be rewritten as

$$\sigma = E_R \varepsilon^R \quad (A-45)$$

It is seen from Equation (A-45) that a form corresponding to that of a linear elastic material (Hooke's Law) is used when strain is replaced by pseudo strain. In a practical sense, pseudo strain is simply the LVE stress response to a particular strain input. The most important effect of pseudo strain is seen when plotting stress, because any time effects are removed from the resulting graph. This property of the stress-pseudo strain relationship is used in the modeling approach presented here.

The basic consideration of the continuum damage theory is that any reduction in stiffness is related to damage. Graphically, this phenomenon is seen in a reduction of the stress-strain modulus; recall that continuum damage theories typically use a secant modulus to quantify the effect of damage. For viscoelastic materials, a reduction in the secant modulus is also related to the time effects. However, in stress-pseudo strain space the time effects are removed, and any reduction in the pseudo secant modulus (the secant modulus in the stress-pseudo strain space) is a direct consequence of damage.

A.1.2.2.3 Viscoelastic continuum damage theory

Continuum damage theory states that the stiffness reduction is defined by the pseudo secant modulus (pseudo stiffness). This quantity is typically normalized for specimen-to-specimen variability by the factor, I , and denoted as C (Equation (A-46)).

$$C = \frac{\sigma}{\varepsilon^R \times I} \quad (A-46)$$

The LVE relationship represented by the pseudo strain in Equation (A-45) can be modified to Equation (A-47) when the microcracking damage grows (4). Then, by substituting Equation (A-47) into Equation (A-34), the nonlinear constitutive relationship for strain is given in Equation (A-48).

$$\sigma = C(S) \varepsilon^R \quad (\text{A-47})$$

$$\varepsilon_{ve} = E_R \int_0^t D(t-\tau) \frac{d\left(\frac{\sigma}{C(S)}\right)}{d\tau} d\tau \quad (\text{A-48})$$

Equations (A-47) and (A-48) require the determination of an internal state variable, S . This internal state variable quantifies any microstructural changes that result in observed stiffness reduction. The relationship between damage (S) and the normalized pseudo secant modulus (C) is known as the damage characteristic relationship and is a material property that is independent of loading conditions.

A.1.2.2.4: Simplified VECD model

Recently, a new simplified model for the analysis and prediction of cyclic data has been developed using the current VECD model constitutive functions. The major difference between this simplified VECD (S-VECD) model and the more rigorous VECD model is the use of a simplified pseudo strain calculation methodology for the cyclic portion, as shown in Equation (A-49). The overall effect of such a simplification on the value of pseudo strain is found to be small, but the simplification is found to save a great deal of computational time without causing a large error in the calculations. In addition, the resulting formulation unifies the results of the CS, CX, and monotonic testing and supports earlier findings that the damage characteristic curve

is a material property independent of temperature and test type. The simplified model formulations are shown in the following equations with descriptions of the variables (20).

$$\varepsilon^R = \begin{cases} \varepsilon^R = \frac{1}{E_R} \int_0^{\xi} E(\xi - \tau) \frac{d(\varepsilon)}{d\tau} d\tau & \xi \leq \xi_p \\ (\varepsilon_{0,ta}^R)_i = \frac{\beta + 1}{2} \left((\varepsilon_{0,pp})_i * |E^*|_{LVE} \right) & \xi > \xi_p \end{cases} \quad (\text{A-49})$$

$$dS = \begin{cases} (dS_{Transient})_{\text{timestep } j} = \left(-\frac{1}{2} (\varepsilon^R)_j^2 \Delta C_j \right)^{\alpha/1+\alpha} \times (\Delta \xi)_j^{1/\alpha} & \xi \leq \xi_p \\ (dS_{cyclic})_{\text{cycle } i} = \left(-\frac{I}{2} (\varepsilon_{0,ta}^R)_i^2 \Delta C^*_i \right)^{\alpha/1+\alpha} \times (\Delta \xi_p)_i^{1/\alpha} \times (R)^{1/\alpha} & \xi > \xi_p \end{cases} \quad (\text{A-50})$$

$$C = \begin{cases} C = \frac{\sigma}{\varepsilon^R I} & \xi \leq \xi_p \\ C^* = \frac{\sigma_{0,ta}}{\varepsilon_{0,ta}^R I} & \xi > \xi_p \end{cases} \quad (\text{A-51})$$

$$\beta_i = \frac{(\sigma_{peak})_i + (\sigma_{valley})_i}{|\sigma_{peak}|_i + |\sigma_{valley}|_i} \quad (\text{A-52})$$

$$R = \frac{1}{\xi_f - \xi_i} * \int_{\xi_i}^{\xi_f} (f(\xi))^{2\alpha} * d\xi \quad (\text{A-53})$$

where

- ξ_p = reduced pulse time of the loading pulse,
- ε_0^R = cyclic pseudo strain amplitude,
- $|E^*|_{LVE}$ = linear viscoelastic dynamic modulus of the material at the particular temperature and frequency of the test,
- C^* = cyclic pseudo stiffness,
- ε_0 = cyclic strain amplitude,
- β = a factor that allows direct quantification of the duration that a given stress history is tensile,
- R = form adjustment factor,
- ξ_i = reduced time within loading cycle when tensile loading begins,
- ξ_f = reduced time within loading cycle when tensile loading ends,
- $f(\xi)$ = normalized time function found from loading type assumption,

$\Delta\sigma_{pp}$ = peak-to-peak amplitude, and
 $\Delta\sigma_{ta}$ = tension amplitude.

The transient portion of the loading history, i.e., the first half of the first cycle, is important because it is used to define the specimen-to-specimen correction factor, I , and because damage growth in this first loading path can be significant. The α in the simplified model formulations is defined as $(1/u+1)$ for the constant rate and CX tests, and as $(1/u)$ for the CS tests. This definition of α is based on theoretical arguments and has been verified using short-term aged (STA) materials only. Its universality with regard to materials tested at other aging conditions was not verified in the original work (20).

Because the CS and CX tests fail in different patterns, two different criteria are necessary. From the study by Underwood et al. (20), two criteria have been adopted to define the cycle in which data can be used in the VECD characterization process: 1) the phase angle criterion, and 2) the threshold criterion. The phase angle criterion is the same as that used in defining the number of cycles to failure (N_f) suggested by Reese (19). The concept of the threshold criterion is that when processes other than damage mechanisms, such as viscoplasticity, begin to have a significant effect, then a test no longer can be used directly for characterization. It is believed that the onset of other mechanisms is closely related to the total amount of permanent strain experienced by the specimen. From experience with the constant crosshead rate tests at 5°C, it is known that for any given mixture, tests performed at certain rates show similar strain levels at the peak stress, as shown in Figure 1-1 (a). In this figure, the straight lines represent the averaged strain levels for each aged mixture, and these strain levels are clearly ranked according to aging level. These mixture-dependent strain levels represent a known level below which VECD mechanisms dominate. The cycle in the fatigue tests at which the permanent strain (backcalculated from the measured permanent pseudo strain) exceeds this threshold is taken as

the point after which the data cannot be used for VECD characterization. Figure 1-1 (b) shows the cut-off point schematic for the AL-STA mix. As can be seen, the cut-off criterion is applied only to the CS tests.

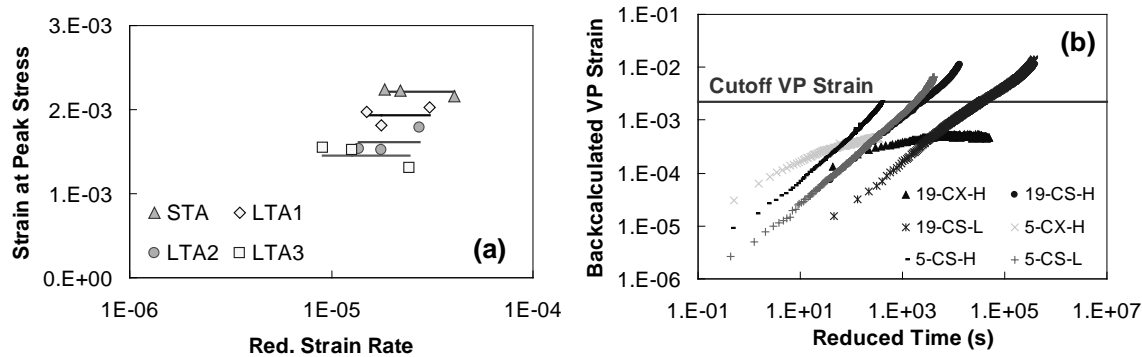


Figure 1-1. (a) Strain at peak stress and (b) Cut-off viscoplastic strain level for AL-STA mix

A.1.2.3 Fatigue life prediction

The most recent study of material model simulations using the simplified VECD model is presented in this subsection for a better understanding of the verification and/or the application of the simplified VECD model, including the general failure criterion (7).

A.1.2.3.1 Simplified VECD model

Controlled strain test simulation

All the cyclic fatigue test data were fitted to analytical forms to obtain the damage characteristic curves for each mixture. The power law function (Equation (A-54)) was found to fit the experimental results better than the exponential function (Equation (A-55)). Once the simplified VECD model was calibrated, i.e., the C_{11} and C_{12} coefficients in Equation (A-54) were found for each mixture, the analytical function of the damage characteristic curve could be substituted into Equation (A-50) to derive the function needed to simulate the cyclic tests, as shown in Equation (A-56).

$$C^* = 1 - C_{11} S^{C_{12}} \quad (\text{A-54})$$

$$C = e^{mS^n} \tag{A-55}$$

$$S_{i+1} = S_i + \left(\frac{1}{2} (\varepsilon_{0,ta}^R)^2 C_{11} C_{12} S^{C_{12}-1} \right)^\alpha R(d\xi) \tag{A-56}$$

In these simulations the pseudo strain history was taken directly from the measured pseudo strain and the pseudo stiffness, and hence, the stress response was predicted. The predicted and measured pseudo stiffness values for a typical good prediction are shown in Figure 1-2, and the results from a typical bad prediction are shown in Figure 1-3.

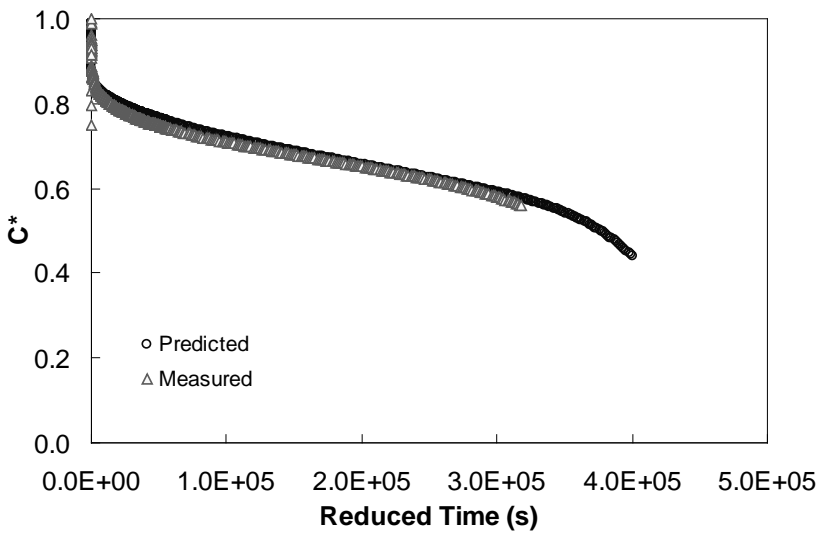


Figure 1-2. Typical good pseudo stiffness prediction (RI19B-5)

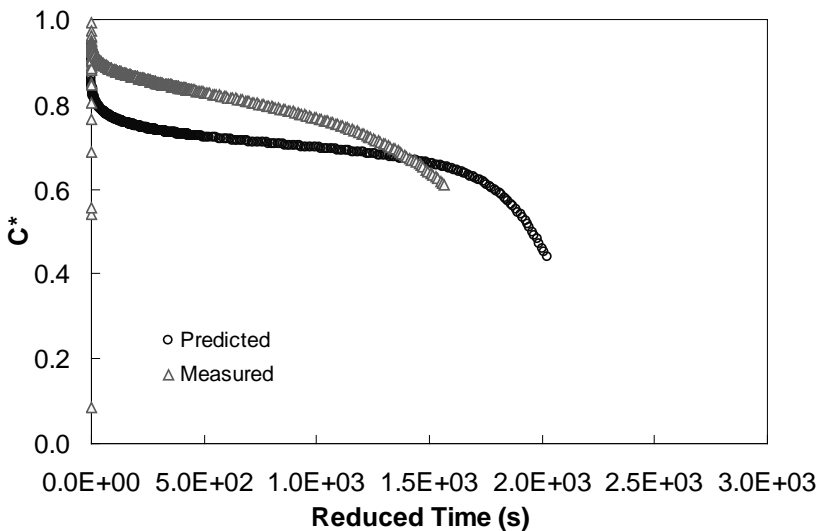


Figure 1-3. Typical bad pseudo stiffness prediction (I19C-10)

Simulation failure criterion

The simplified fatigue model does not account for changing time dependency and, therefore, it was not possible to observe a sudden decrease of the phase angle in the simulation. For this reason, an empirical observation of all the tested mixtures was made to determine the failure criterion. The observation is shown in Figure 1-4 where the pseudo stiffness at failure (C_f^*) is plotted against reduced frequency for multiple mixtures. Reduced frequency, f_R , is computed by multiplying the actual test frequency, f , by the shift factor for the temperature of the test, Equation (A-57), where the coefficients α_1 , α_2 , and α_3 are all characterized as part of the LVE characterization process.

$$f_R = f * a_T = f * 10^{\alpha_1 T^2 + \alpha_2 T + \alpha_3} \tag{A-57}$$

Note that only mid-failure test results are used here, because the goal is to predict localization failure, not pre-localization failure.

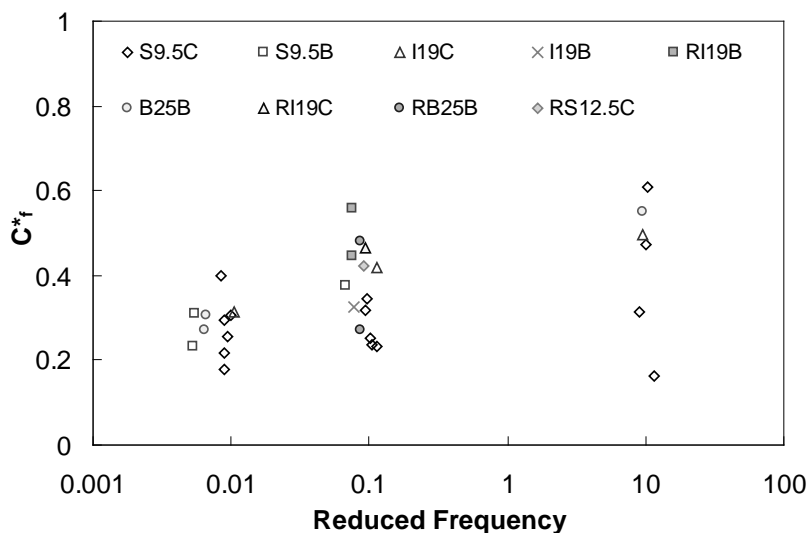


Figure 1-4. Experimental observation of pseudo stiffness values at failure against reduced frequency

It is found from Figure 1-4 that, in general, the pseudo stiffness at failure (C_f^*) value increases with reduced frequency. It is also found that for the non-RAP mixtures at reduced frequencies at or below 0.01 Hz (a condition that corresponds physically to a temperature of approximately 27°C and frequency of 10 Hz), failure occurs at a pseudo stiffness value of approximately 0.28. This value is similar to that observed by Daniel and Kim (8) for their tests, which were performed at 25°C. As the reduced frequency increases, failure tends to occur at a higher level of pseudo stiffness. Although the data scatter is significant, it is also observed that the rate of this increment is aggregate size-dependent. From the data obtained at a reduced frequency of around 0.1 Hz, it is found that RAP mixtures have a higher failure pseudo stiffness value than non-RAP mixtures. These observations lead to the piecewise failure function, given in Equation (A-58).

$$C_f^* = \begin{cases} b & f_R < 0.01 \\ a \cdot (\log(f_R) - \log(0.01)) + b & 0.01 \leq f_R < 10 \end{cases} \quad (\text{A-58})$$

Note that: the failure criterion is a linear function, dependent on nominal maximum aggregate size (NMAS), in semi-log space between the reduced frequencies of 0.01 to 10 Hz; the failure criterion is constant, as a function of RAP or non-RAP mixtures, at reduced frequencies lower than this range; and at temperatures above this range no interpretation is made.

To characterize the coefficients of this function an optimization approach is taken. In this approach, the error between the measured and predicted fatigue life is minimized by systematically changing the coefficients of Equation (A-58) as a function of NMAS and for RAP versus non-RAP mixtures. Due to the inherent complexity involved in this optimization program,

a genetic algorithm technique is used. A commercial Excel-based macro language add-in, *Evolver*, is used for this purpose.

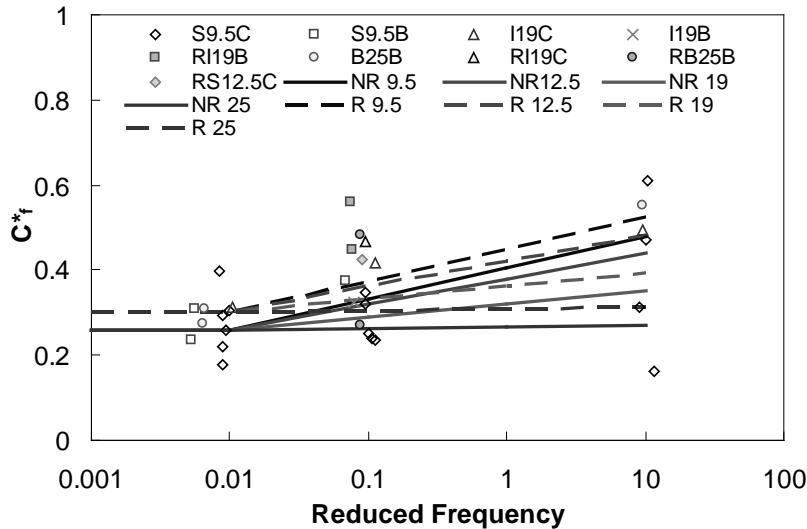


Figure 1-5. Optimized failure criterion

The results in Figure 1-5 show that the optimized failure criterion matches with the experimental data points. The value of the intercept coefficient, b , for the RAP mixtures is greater than that for non-RAP mixtures, and the value of the slope coefficient, a , decreases with the increase in nominal maximum aggregate size (NMAS). The final functional forms for these coefficients are shown in Equations (A-59) and (A-60).

$$a = -0.0045(NMAS) + 0.12 \quad (\text{A-59})$$

$$b = \begin{cases} 0.26 & \text{non-RAP} \\ 0.30 & \text{RAP} \end{cases} \quad (\text{A-60})$$

Fatigue life prediction results

The simulation failure criterion developed in the previous section is applied to predict the fatigue life for the mid-failure cyclic tests. The results of this prediction process are shown in the form of line-of-equality (LOE) plots in both arithmetic and logarithmic space in Figure 1-6.

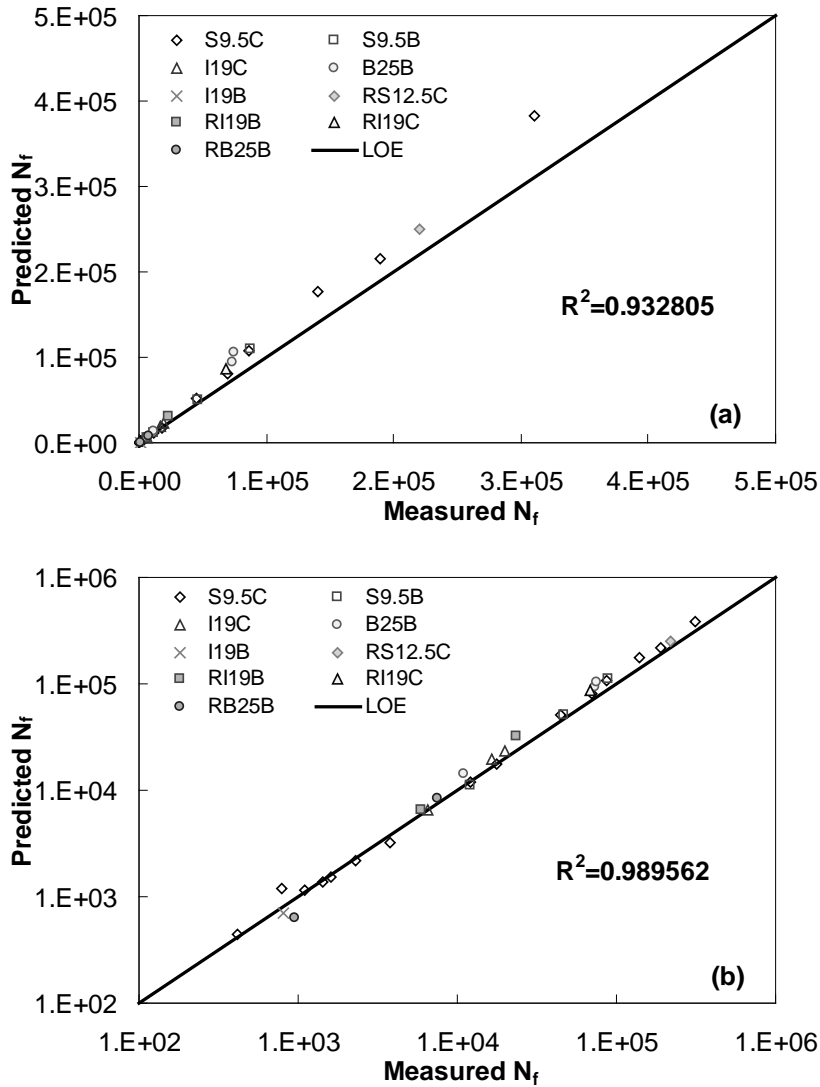


Figure 1-6. Comparison of measured and predicted fatigue life for mid-failure cyclic tests in (a) arithmetic and (b) logarithmic space

The findings from Figure 1-6 are encouraging, as the relationship shows a high degree of statistical significance as evidenced by the high correlation coefficients in both arithmetic and logarithmic scales. Although it cannot be assessed directly from this figure, the arithmetic fatigue life prediction error for all the available mid-failure cyclic tests is $17 \pm 12\%$. A slight tendency to over-predict is evident, which may be caused by the viscoplasticity in some of the high temperature and low strain level tests.

To validate the failure criterion, fatigue test results from mixtures not used in the calibration of Equations (A-58) through (A-60) are utilized. In total, three mixtures, each from the FHWA ALF experiment, are included in this effort: CRTB, Terpolymer, and Control mixtures. Details of these mixtures, including the experimental results used to generate the data in Figure 1-7, are given elsewhere (26, 10). The measured and predicted cycles to failure for these mixtures are shown in both arithmetic and logarithmic space in Figure 1-7.

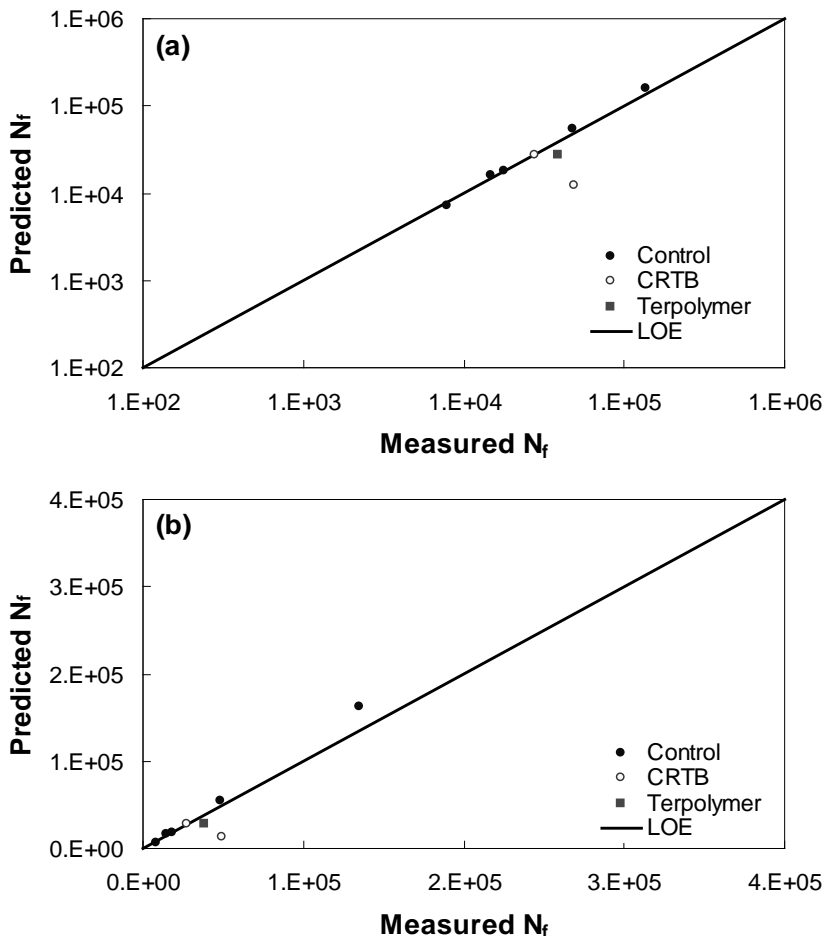


Figure 1-7. Validation of calibrated failure criterion with non-calibration mixture cyclic tests in (a) arithmetic and (b) logarithmic space

Overall, the agreement between the measured and predicted number of cycles to failure (N_f) is very good. One major exception occurred for one of the CRTB tests, which shows a significant under-prediction. After examining the measured and predicted behaviors more closely

for the CRTB experiments, it was found that the number of cycles to failure values for the two tests do not follow the expected trends. Specifically, the test with the higher input strain values produced a larger number of cycles to failure than the experiment with the lower input strain values. In light of this anomaly and in light of the fact that, besides the single CRTB test, all other predictions agree favorably with the measured data, the failure criterion is deemed acceptable. Further validation and improvement of this failure criterion is part of further research work.

A.1.2.3.2: Direct tension fatigue simulation using simplified VECD model

Having verified the simplified VECD model for the case of mixed loading mode, attention now turns to its use for simulating pure controlled strain and controlled stress direct tension fatigue tests.

Controlled Strain Test Simulation

Starting with the simplified VECD model formulation (Equation (A-50)), assuming the power law damage model (Equation (A-54)), and after rearranging, integrating and simplifying, the following relationship can be obtained to find the fatigue life for a pure controlled strain direct tension cyclic test:

$$N_f = \frac{(f_R)(2^{3\alpha})S_f^{\alpha-\alpha C_{12}+1}}{(\alpha-\alpha C_{12}+1)(C_{11}C_{12})^\alpha [(\beta+1)(\varepsilon_{0,pp})(|E^*|_{LVE})]^{2\alpha} R}, \quad (\text{A-61})$$

where S_f is the value of the damage parameter at failure. This equation is derived based on the assumption that the damage at failure is much greater than the initial damage at the first cycle of loading, i.e., $S_f \gg S_i$, and the assumption that the fatigue life value is much greater than one. Both of these assumptions are true for most real experiments.

Equation (A-61) can be used directly to find the effect of strain amplitude, loading frequency and testing temperature on fatigue life. Analysis was performed to simulate fatigue tests at 5°, 19° and 27°C. Figure 1-8 presents the simulation results for the S9.5C mixture in the plot of the standard logarithmic strain level versus the fatigue life. Note that similar plots are generated when empirically characterizing the fatigue resistance of AC mixtures. Also note that all simulated tests are in a zero mean strain condition, i.e., $\beta = 0$, and the loading frequency is 10 Hz. The value of the damage parameter at failure, S_f , is determined based on the same mixture type-dependent failure criterion proposed in Equation (A-58). Figure 1-8 also shows that Equation (A-61) effectively captures the same major trends suggested by other empirical research (11-16). That is, the fatigue life decreases as the strain level increases, and stiffer materials (i.e., materials at a low temperature) fail earlier than softer materials for the same strain level. The model also suggests that the effect of temperature (when the frequency and material type are fixed) is to shift the fatigue envelopes such that the curves become parallel. Anecdotal evidence of this behavior is supported in the literature by the form taken for various empirical predictive models (14, 16, 17-22).

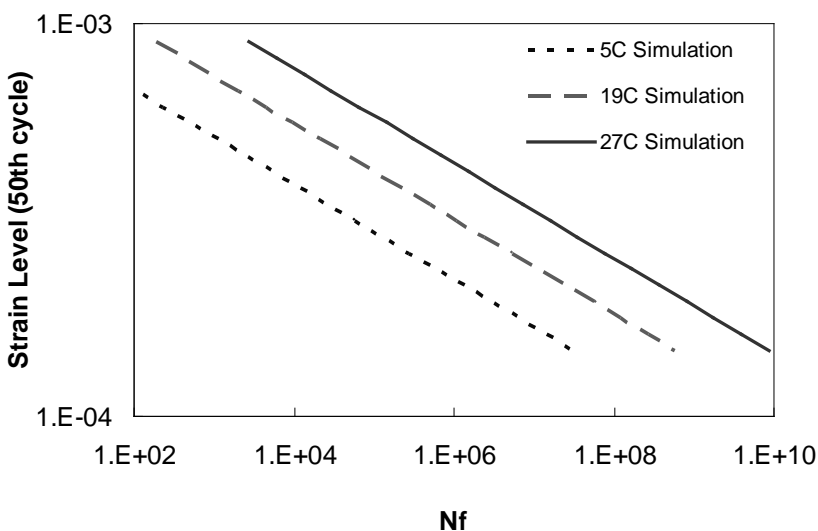


Figure 1-8. Controlled strain direct tension fatigue simulation results for S9.5C mixture

Controlled Stress Test Simulation

The simplified VECD model is also applied to simulate the controlled stress direct tension fatigue test. The formulation of the stress-based model is not as straightforward as that of the strain-based model due to the complexity of the integration, as evident in Equation (A-62).

$$N_f = \frac{f \cdot 2^{3\alpha} \cdot |E^*|^{2\alpha}}{\left[(\sigma_{0,pp}) (\beta + 1) \right]^{2\alpha}} K_1 \int_{\hat{s}_i}^{\hat{s}_f} \left(\frac{\left(1 - \hat{C}_{11} (S)^{C_{12}} \right)^2}{\hat{C}_{11} C_{12} S^{C_{12}-1}} \right)^\alpha (d\hat{S}) \quad , \quad (\text{A-62})$$

where \hat{s} is pseudo stress-based damage as compared to the pseudo strain-based damage, S . The two damage parameters are simply related by a factor, K_2 .

$$(\Delta S)_{cycle\ i} = (\Delta \hat{S})_{cycle\ i} * (K_2) \quad (\text{A-63})$$

The K_2 factor and \hat{C}_{11} term can be obtained using Equations (A-32) and (A-33), respectively.

$$K_2 = \left(|E^*|_{LVE} \right)^{2\alpha/\alpha+1} \quad (\text{A-64})$$

$$\hat{C}_{11} = C_{11} (K_2)^{C_{12}} \quad (\text{A-65})$$

Similar to the controlled strain test simulation, different fatigue life values are found at different stress levels and testing temperatures using Equation (A-62). This analysis was performed at 5°, 19° and 27°C with a constant loading frequency of 10 Hz. For these simulations the load levels were assumed to be constant and tensile, i.e., $\beta = 1$. Typical results from this type of simulation are shown in Figure 1-9.

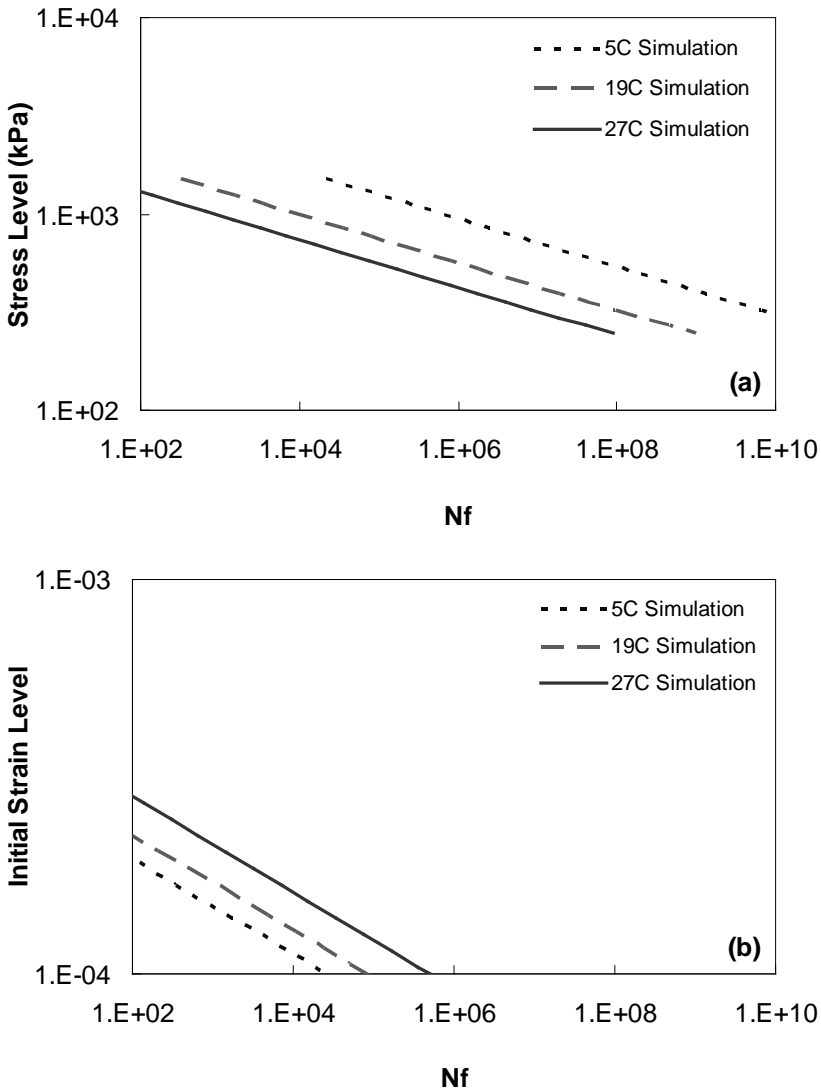


Figure 1-9. Controlled stress direct tension fatigue simulation results for S9.5C mixture in plots for: (a) stress vs. fatigue life, and (b) strain vs. fatigue life

Figure 1-9 (a) shows the simulated fatigue envelope for the S9.5C mixture in the stress level versus fatigue life plot. At the same testing temperature, the fatigue life decreases as the input stress level increases. Also, it is interesting to see that the position of the fatigue envelopes at different temperatures flips, as compared to the controlled strain test simulation results shown in Figure 1-8. That is, under the same stress level input, the fatigue life increases as the temperature decreases. This behavior is also consistent with the controlled stress flexural

bending test results from the SHRP project A-003A (13) and also consistent with findings from material level testing on the ALF mixtures (26).

Figure 1-9 (b) plots the same simulation results, but in a different way. Here, the initial strain level is shown instead of the initial stress level. This initial strain level is obtained by dividing the stress level by the material's LVE modulus value. For comparative purposes, Figure 1-9 (b) is plotted in the same scale as Figure 1-8. It is found that now the positions of the fatigue envelopes at different temperatures are in the same order that appeared in the controlled strain simulation. However, the fatigue life obtained from the controlled stress test is much shorter than that from the controlled strain test. This observation is reasonable, because during a pure controlled stress test, the material's stiffness decreases with the number of loading cycles, and the actual on-specimen strain amplitude increases. This situation eventually causes earlier failure than the controlled strain test with the same initial on-specimen strain level. This phenomenon has also been identified with beam fatigue experiments (12, 21).

A.1.2.4 Statistical analysis for dynamic modulus test results of the AL mix

A statistical analysis of the dynamic modulus ($|E^*|$) data at different aging levels for the AL mixture has been performed to determine the significance of the graphical observations. Because all the tests were not conducted under exactly the same conditions, each replicate was first processed using interpolation to build a data set for precisely the same temperature and frequency conditions. The specific temperatures and frequency combinations that were compiled are: -10°C , 5°C , 20°C , 40°C , and 54°C and 25, 10, 5, 1, 0.5, and 0.1 Hz, respectively.

As a first cut analysis, the average dynamic modulus value from each long-term aging level (LTA1, LTA2, and LTA3) is plotted against STA dynamic modulus values at a consistent temperature and frequency condition, as shown in Figure 1-10 (a) and (b). Error bars are shown in these figures and represent a single standard deviation from the mean. The analysis of these

figures clearly shows that the test results, i.e., the means plus a single standard deviation, of the LTA specimens are higher overall than those from the STA specimens.

Although this graphical technique led the research team to conclude that the differences between the STA and LTA samples are significant, a more comprehensive statistical analysis of these values using the step-down bootstrap method has also been performed. This method is used in lieu of multiple paired t-tests due to the effect of experiment-wise error rates, which can result in incorrect conclusions when making multiple comparisons. Failing to account for this error rate increases the probability of finding significance when none is present. The statistical analysis results are shown by temperature and frequency in Table 1-14. Note that in this table, the conditions under which the means are statistically similar (based on a 95% significance level) are highlighted.

From Table 1-14 the first comparisons to review are those between adjacent aging level test results, i.e., STA versus LTA1, LTA1 versus LTA2, and LTA2 versus LTA3. Overall, statistically different values are found between each adjacent aging level except at the extreme conditions, i.e., a fast frequency at a low temperature and a slow frequency at a high temperature. Based on the standard deviation values shown in Figure 1-10, this finding may be explained by the higher degree of replicate variation under extreme conditions as compared to that under less extreme conditions. A comparison of the two extreme aging conditions, STA versus LTA3, shows that significant differences exist for almost all the conditions except 0.1 Hz at 54°C. Because this condition has the highest amount of variability and is also the most likely to contain experimental errors due to accumulated permanent strain, it is reasonable to conclude that overall a statistically significant effect on the dynamic modulus values exists due to the laboratory aging procedures.

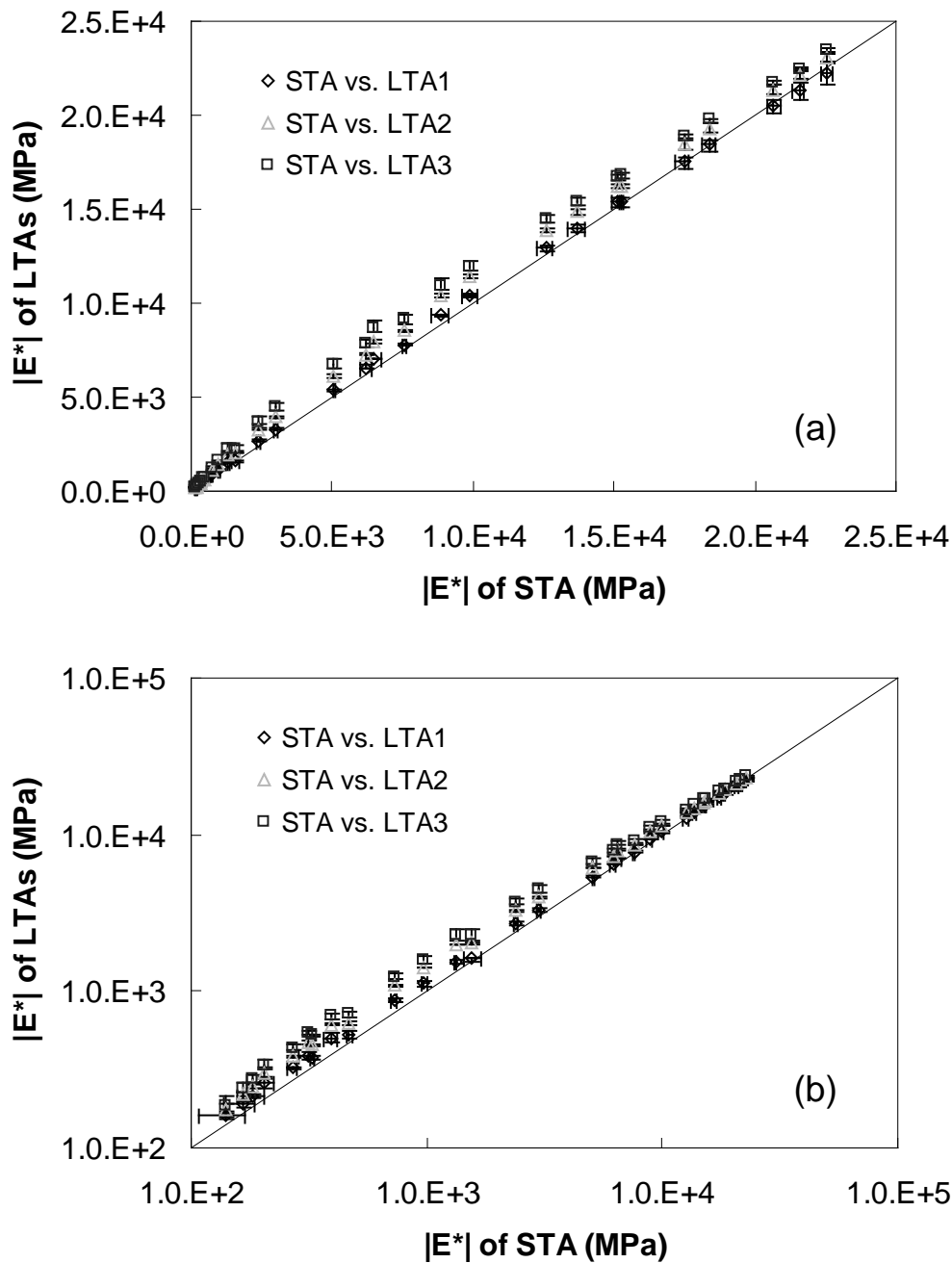


Figure 1-10. Comparison of dynamic modulus of long-term aging levels against the short-term aging level in (a) arithmetic scale and (b) logarithmic scale

A.1.2.5 Viscoplasticity

Viscoplasticity is commonly considered to be a material level factor related to rutting distress. However, as results from the NCHRP 9-30A project suggest, viscoplasticity may interact with the pavement structure to change the distribution of stress and strain within the

pavement. Modifications to these distributions may drastically alter the potential for bottom-up cracking because these structural viscoplastic effects have been shown to be the most drastic near the pavement base.

Table 1-14. Statistical Analysis Summary of Dynamic Modulus of AL Mix

Temperature (°C)	Frequency (Hz)	p-value					
		STA vs. LTA1	LTA1 vs. LTA2	LTA2 vs. LTA3	STA vs. LTA2	LTA1 vs. LTA3	STA vs. LTA3
-10	25	0.486	0.070	0.100	0.045	0.019	0.019
-10	10	0.589	0.071	0.105	0.044	0.016	0.005
-10	5	0.694	0.047	0.087	0.040	0.014	0.004
-10	1	0.855	0.038	0.034	0.023	0.005	0.005
-10	0.5	0.730	0.035	0.033	0.022	0.006	0.003
-10	0.1	0.460	0.005	0.015	0.001	0.003	0.001
5	25	0.241	0.008	0.031	0.004	0.009	0.009
5	10	0.194	0.012	0.026	0.005	0.010	0.006
5	5	0.142	0.010	0.025	0.004	0.003	0.005
5	1	0.029	0.002	0.040	0.002	0.003	0.006
5	0.5	0.021	0.001	0.033	0.003	0.002	0.008
5	0.1	0.012	0.001	0.024	0.003	0.006	0.011
20	25	0.031	0.004	0.011	0.004	0.006	0.006
20	10	0.047	0.003	0.008	0.006	0.003	0.008
20	5	0.009	0.002	0.012	0.001	0.005	0.005
20	1	0.019	0.002	0.013	0.001	0.003	0.003
20	0.5	0.014	0.003	0.013	0.001	0.003	0.004
20	0.1	0.002	0.000	0.029	0.001	0.008	0.006
40	25	0.429	0.003	0.026	0.006	0.007	0.020
40	10	0.015	0.002	0.011	0.003	0.003	0.001
40	5	0.020	0.001	0.008	0.001	0.003	0.001
40	1	0.023	0.006	0.011	0.002	0.010	0.025
40	0.5	0.025	0.006	0.008	0.001	0.004	0.001
40	0.1	0.054	0.066	0.048	0.017	0.022	0.006
54	25	0.022	0.013	0.021	0.002	0.013	0.002
54	10	0.009	0.001	0.002	0.001	0.003	0.001
54	5	0.022	0.007	0.029	0.002	0.006	0.005
54	1	0.074	0.022	0.140	0.016	0.009	0.016
54	0.5	0.151	0.038	0.132	0.032	0.014	0.023
54	0.1	0.419	0.265	0.507	0.199	0.147	0.132

To develop and implement a rigorous viscoplastic model into the FEP++ code would require substantial effort beyond the scope of the current project. Therefore, viscoplasticity is considered in terms of the sensitivity ratio to viscoplasticity of the given material and structure, the so-called *damage correction factor* (DCF). The DCF is calculated by using a simple strain-

hardening viscoplastic material model and pavement responses predicted using the FEP++ without damage for the pavement structure under evaluation.

To model the viscoplastic behavior of AC under tensile loading Uzan (23) and Schapery (24) suggest a simple relationship, evidenced by Equation (A-66), which assumes that viscosity obeys a power law in viscoplasticity. Several researchers (24, 25) have shown that the model is applicable to monotonic behavior in tension.

$$\dot{\varepsilon}_{vp} = \frac{g(\sigma)}{\eta(\varepsilon_{vp})}, \quad (\text{A-66})$$

where

$$\begin{aligned} g(\sigma) &= \text{stress function and} \\ \eta &= \text{viscosity.} \end{aligned}$$

Assuming that η is a power law in the viscoplastic strain, Equation (A-67) becomes

$$\dot{\varepsilon}_{vp} = \frac{g(\sigma)}{A\varepsilon_{vp}^p}, \quad (\text{A-67})$$

where A and p are model coefficients. Rearranging and integrating yield

$$\varepsilon_{vp}^p d\varepsilon_{vp} = \frac{g(\sigma) dt}{A} \quad \text{and} \quad (\text{A-68})$$

$$\varepsilon_{vp}^{p+1} = \frac{p+1}{A} \int_0^t g(\sigma) dt. \quad (\text{A-69})$$

Raising both sides of Equation (A-69) to the $1/(p+1)$ power yields

$$\varepsilon_{vp} = \left(\frac{p+1}{A} \right)^{\frac{1}{p+1}} \left(\int_0^t g(\sigma) dt \right)^{\frac{1}{p+1}}. \quad (\text{A-70})$$

Letting $g(\sigma) = B\sigma^q$, and coupling coefficients A and B into coefficient Y , Equation (A-70)

becomes

$$\varepsilon_{vp} = \left(\frac{p+1}{Y} \right)^{\frac{1}{p+1}} \left(\int_0^t \sigma^q dt \right)^{\frac{1}{p+1}}. \quad (\text{A-71})$$

In the current work, the coefficients, p , q and Y , are pressure-dependent quantities.

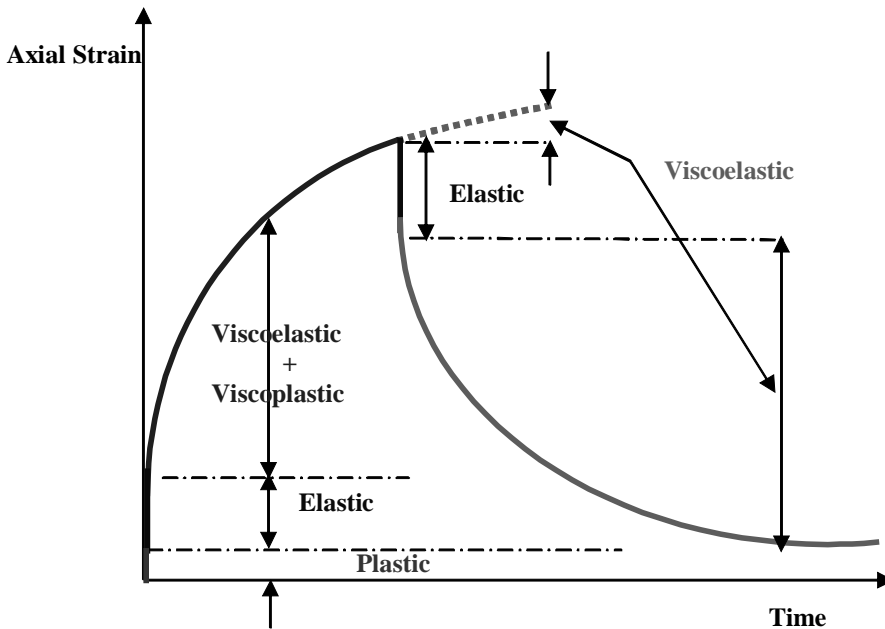


Figure 1-11. Strain decomposition from creep and recovery testing

Typically, viscoplastic models are characterized using creep and recovery tests. These tests allow relatively easy separation of the viscoplastic and viscoelastic components, as shown in Figure 1-11. However, it is difficult (if not impossible using some machines) to maintain zero load during the recovery period of the creep and recovery test in tension. Therefore, in tension, viscoplastic characterization uses constant rate tests in which the VECD model is used first to predict the viscoelastic strain. This viscoelastic strain is then subtracted from the measured strain to provide the viscoplastic strain that is needed for curve fitting to Equation (A-71).

A.1.2.6 Thermal stress

Another main source of top-down cracking in asphalt pavements is thermal stress. Thermal stress can contribute to top-down cracking in two ways: (1) through thermal fatigue, expressed

by repeated, thermally-induced tensile stress at the pavement surface, which can gradually damage the pavement and contribute to surface-induced cracking; and (2) through acute thermal cracking, where very low temperatures cause sudden fracture of the pavement surface.

In evaluating thermal cracking and traditional bottom-up cracking, failure is determined when the maximum tensile stress exceeds the tensile strength of the asphalt concrete. However, the situation is more complicated in top-down cracking analysis, because the stress induced at the surface of the pavement involves both normal and shear components.

The ability of the viscoelastoplastic continuum damage (VEPCD) model to accurately characterize the tensile behavior of AC under thermally induced loading has been confirmed by Chehab and Kim (26). Measured responses and fracture parameters from thermal strain-restrained specimen tensile (TSRST) strength tests were compared with those predicted using the VEPCD, VECD, and LVE models. Excellent agreement between the measured and predicted responses was found, especially in the VEPCD and VECD models, as explained in the next paragraph.

The stress histories predicted for the three cooling rates via the three models are plotted in Figure 1-12 as a function of time. Also plotted are the average measured stress values from all replicates tested at each rate. As is apparent from visual inspection, the stress predicted using the LVE model is greater than the measured stress, with the difference increasing as time increases and the cooling rate decreases. This discrepancy is due to the fact that the LVE model does not account for stress relaxation due to microcracking. The error between the VECD-predicted stress and the measured stress is much smaller than that for the LVE case for all cooling rates. Moreover, the error lessens with an increase in time and a decrease in cooling rate. The VEPCD-predicted stress matches the measured stress very well, with discrepancies being greatest at the

slowest cooling rate. From a comparison of the predicted stresses among each other, it is evident that the VEPCD model yields the most accurate predictions, slightly better than the VECD model. Another important observation is that the rate of increase in VECD-predicted stress with time deviates from stress that corresponds to the measured and other predictions.

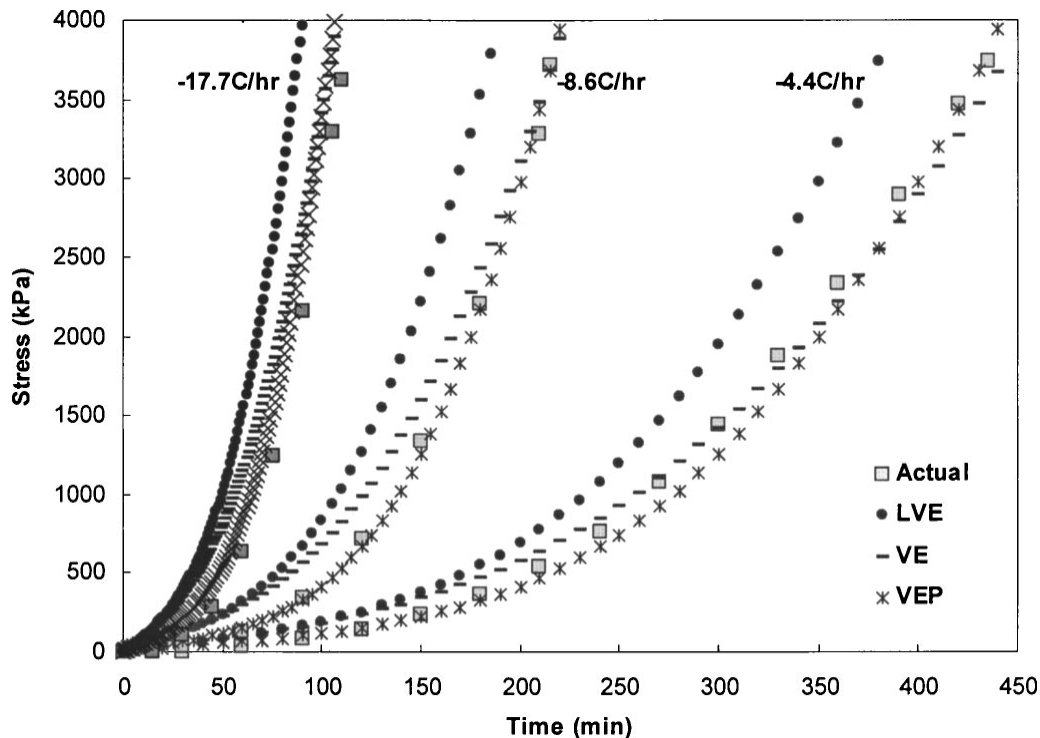


Figure 1-12. Average measured and predicted stress histories for different material models and cooling rates

A.2 Reasonableness and Sensitivity Checks

A.2.1 Reasonableness

To verify the modeling framework, first a reasonableness check is performed. Because the purpose here is to verify that the VECD model is implemented correctly, the analytical sub-models (healing, aging, thermal damage, etc.) are not included. Table 1-15 summarizes the simulation details for the analysis to verify reasonableness. Three factors were chosen based on the general effects that are expected of such factors from experience. Four temperature profiles were selected to represent the critical conditions: Tallahassee, Florida in the summer (FL-Jun) at

5:00 AM (5:00) and at 2:00 PM (14:00), and Laramie, Wyoming in the winter (WY-Dec) at 5:00 AM and at 2:00 PM. The temperature profiles for these four conditions are shown in Figure 1-13. For both geographical locations, the 5:00 AM temperature profile shows a low temperature at the top of the pavement and a high temperature at the bottom. Due to heat from the sun, the opposite trend occurs for both locations at 2:00 PM. Differences between the average temperatures for the two locations are also evident from Figure 1-13. The two pavement structures shown in Figure 3-34 and the two asphalt mixtures from the ALF study (Control and SBS) were utilized in these simulations.

Table 1-15. Simulation Details for Reasonableness Check

Item	Number of Cases	Detail
Region	4	FL-Jun-5:00, FL-Jun-14:00, WY-Dec-5:00, WY-Dec-14:00
Structure	2	Thin (127 mm or 5 in.), Thick (304.8 mm or 12 in.)
AC Material	2	ALF Control, ALF SBS
Support Condition	1	Moderate
Aging	1	No Aging
Healing	1	None
Thermal Stress	1	None
DCF	1	None
Total Number of Cases	16	

Simulation results are presented in Table 1-16 to Table 1-18 in terms of the tensile stress and radial strain at the peak loading time (0.05 sec) for all 16 test cases. For easier comparisons, all contours for the same variables (stress or strain) are plotted using the same scale. From the contours shown in Table 1-16 to Table 1-18, the following comparisons can be made:

- Highest versus lowest temperature profile by region (Florida and Wyoming)
- Florida versus Wyoming by time of day (5:00 AM or 2:00 PM)
- Control versus SBS mixtures under the same condition(s)
- Thin versus thick structure under the same condition(s)

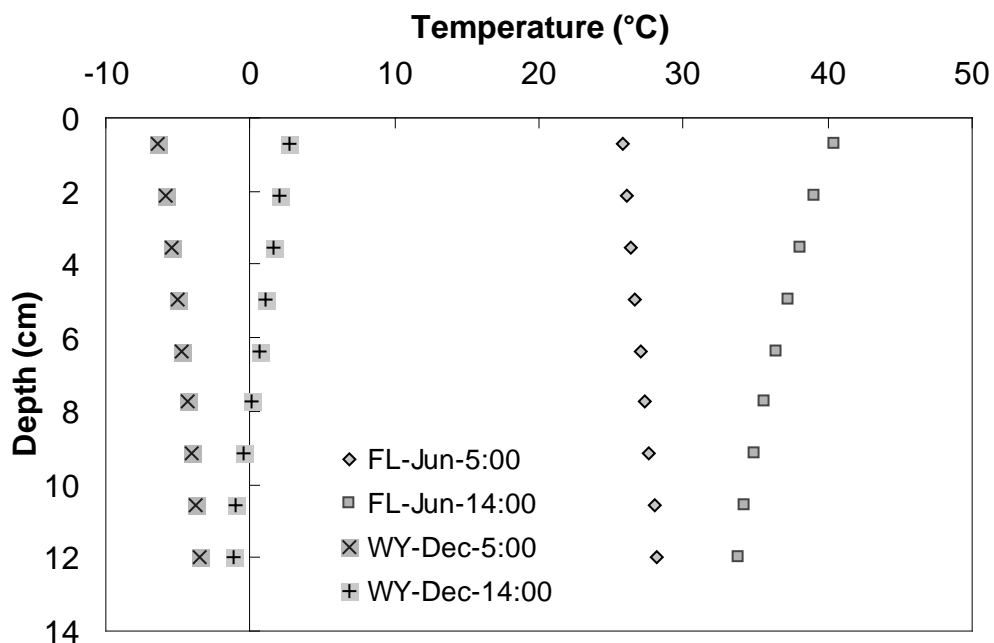


Figure 1-13. Temperature profile for reasonableness check

A key observation from the plots shown in Table 1-16 to Table 1-18 is that the tensile strain at the pavement bottom is greater at higher temperatures. The magnitude of stress also shows a change, a decrease, with increasing temperatures. This effect is expected because the support conditions are constant for all cases, and the modulus value of the asphalt layer increases with reductions in temperature. However, it is interesting that daily temperature variations have little effect on the stress distribution. Instead, a large difference in the mean temperature is needed in order to change the stress distribution noticeably. This effect is more obvious in the thin pavement section than in the thick pavement section, and results from increased bending-related stress in the thin sections. Of course, because the stress distribution changes very little due to temperature variations, the strain magnitude increases with the temperature because the material is softer at higher temperatures. Unlike the stress distributions, though, these changes in strain magnitude may be noticeably different during daily temperature fluctuations.

Comparisons of material type reveal that when the SBS materials are used, higher strain magnitudes result. If the temperatures shown in Figure 1-13 are combined with the data shown in Figure 3-35, i.e., the mastercurve, appropriate time temperature shift factors, and a quasi-approximate time-frequency conversion (27), it can be seen that the most extreme temperature in the simulations, 41°C, and the loading time of 0.1 second, correspond approximately to a reduced frequency of 6.0×10^{-5} Hz. At this reduced frequency, the SBS material shows a softer LVE response than the Control mixture, as seen in Figure 3-35. If, on the other hand, the simulation is performed at the high temperature PG grade (continuous grade-based) of the two mixtures, 72°C, then the approximate equivalent reduced frequency would be 1.5×10^{-7} Hz. At this reduced frequency, the SBS mixture is stiffer (in terms of linear viscoelasticity) than the Control mixture, and it should be expected that the radial strain would be less for the SBS mixture than for the Control mixture. Table 1-19 shows the contours for a thin pavement at 0.05 second and at 72°C for both the SBS and the Control mixtures. From this table it is seen that the SBS mixture shows less total strain than the Control mixture, which, along with the data in Table 1-16 to Table 1-18 and Figure 3-35, confirms the reasonableness of the response predictions with regard to material type.

Finally, comparisons between the thin and thick pavements show that the magnitude of the tensile strain at the bottom of the thin pavement is always greater than the strain in the equivalent thick pavement case. The difference is more noticeable in the Wyoming simulations because of the scaling used in the contours and because the Wyoming conditions result in a mixture with a high modulus. The Florida simulations show similar gray scale patterns of the thick and thin pavements, which is a result of setting a scale capable of delineating strain under all of the conditions shown. These cases are thus misleading; in reality, the strain in the thin pavement

case is greater than in the simulations. It is also observed that the approximate pavement shear center, as indicated by a bulb of radial strain extending near the loading edge, is relatively higher in the thick pavement (at 20% of total depth) than it is in the thin pavement case (at 40% of total depth). This behavior is to be expected in layered analysis.

Table 1-16. Tensile Stress and Strain Contours for Reasonableness Check: Thin Pavements – Florida and Wyoming

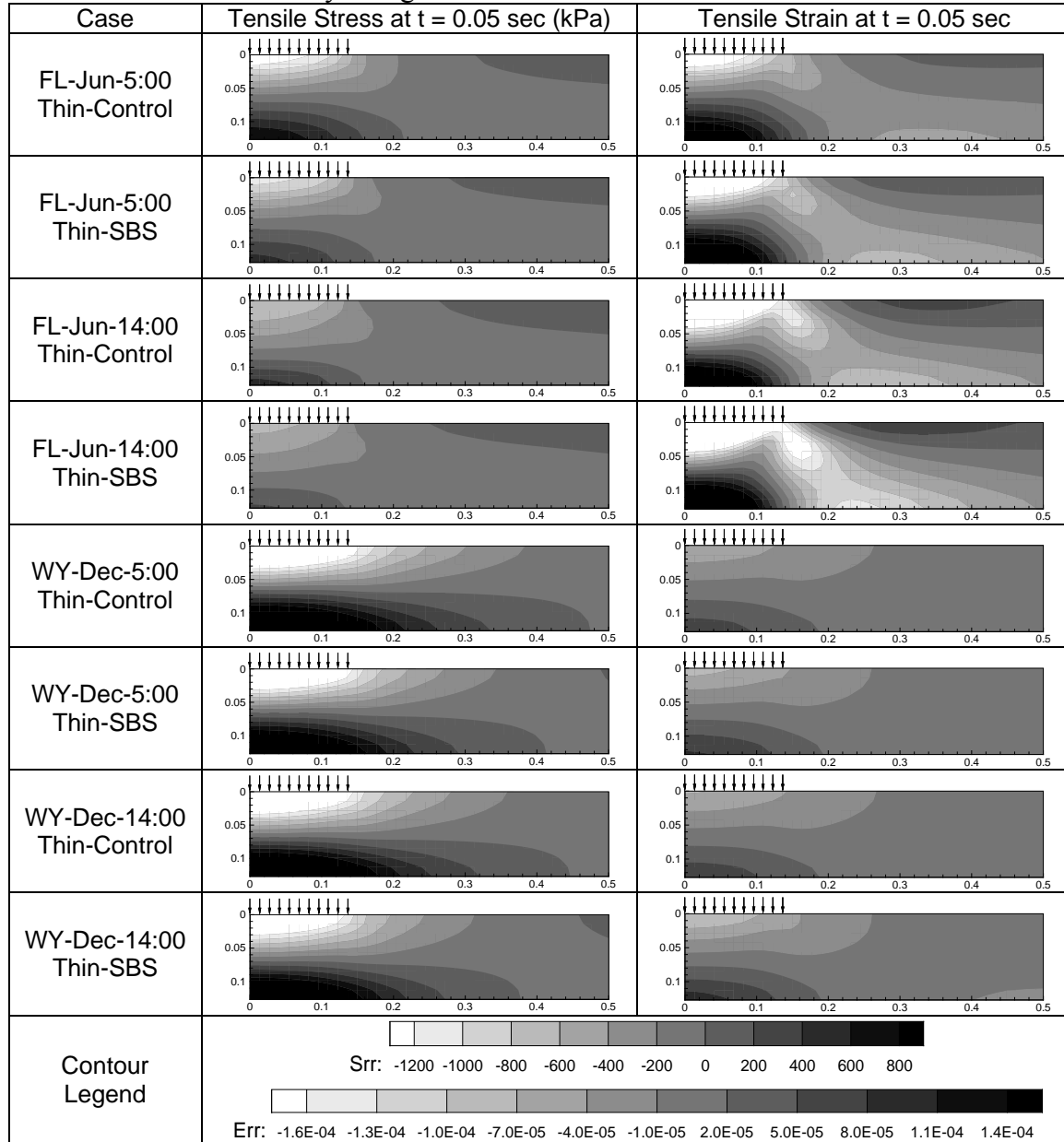


Table 1-17. Tensile Stress and Strain Contours for Reasonableness Check: Thick Pavements - Florida

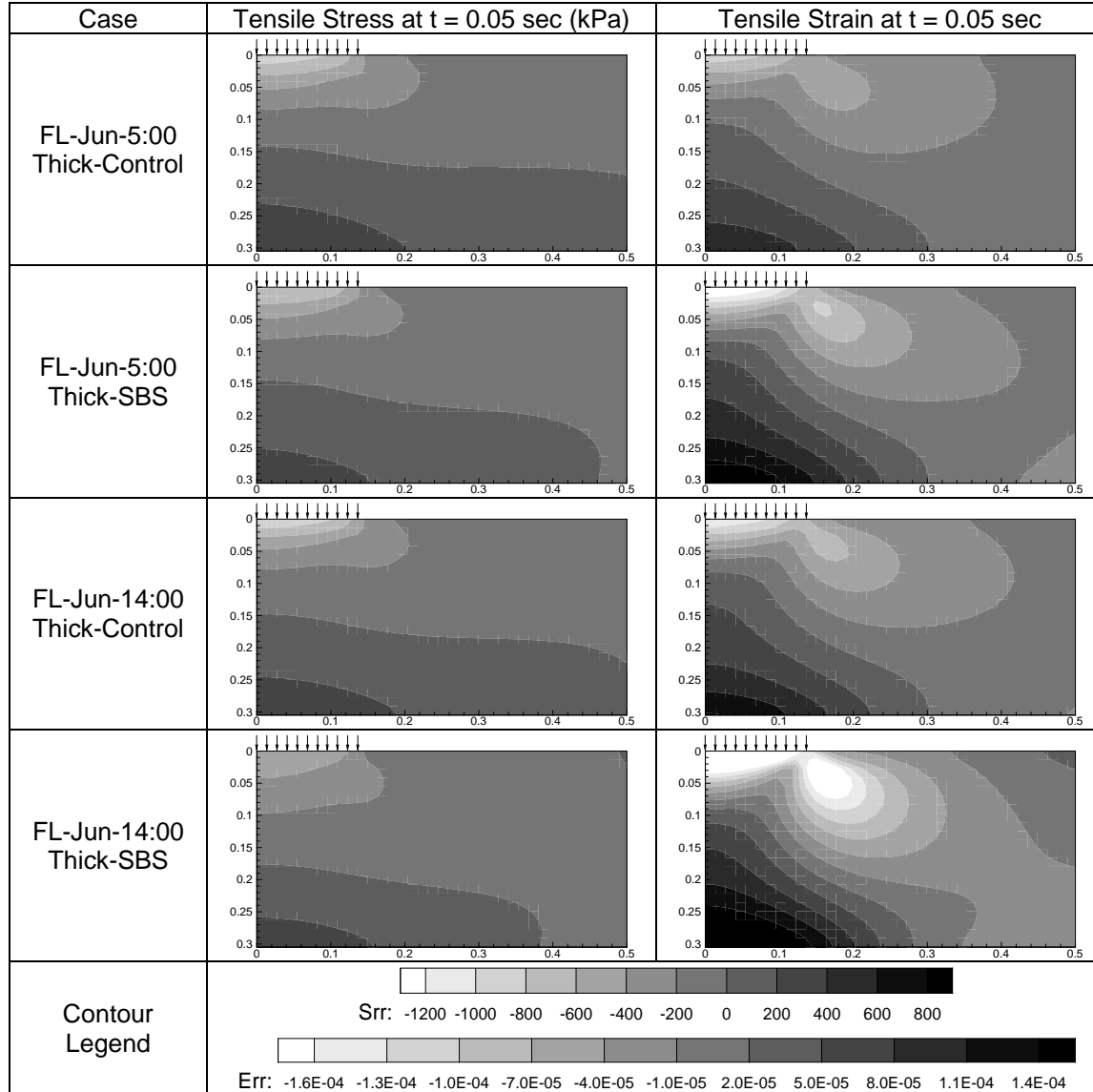


Table 1-18. Tensile Stress and Strain Contours for Reasonableness Check: Thick Pavements - Wyoming

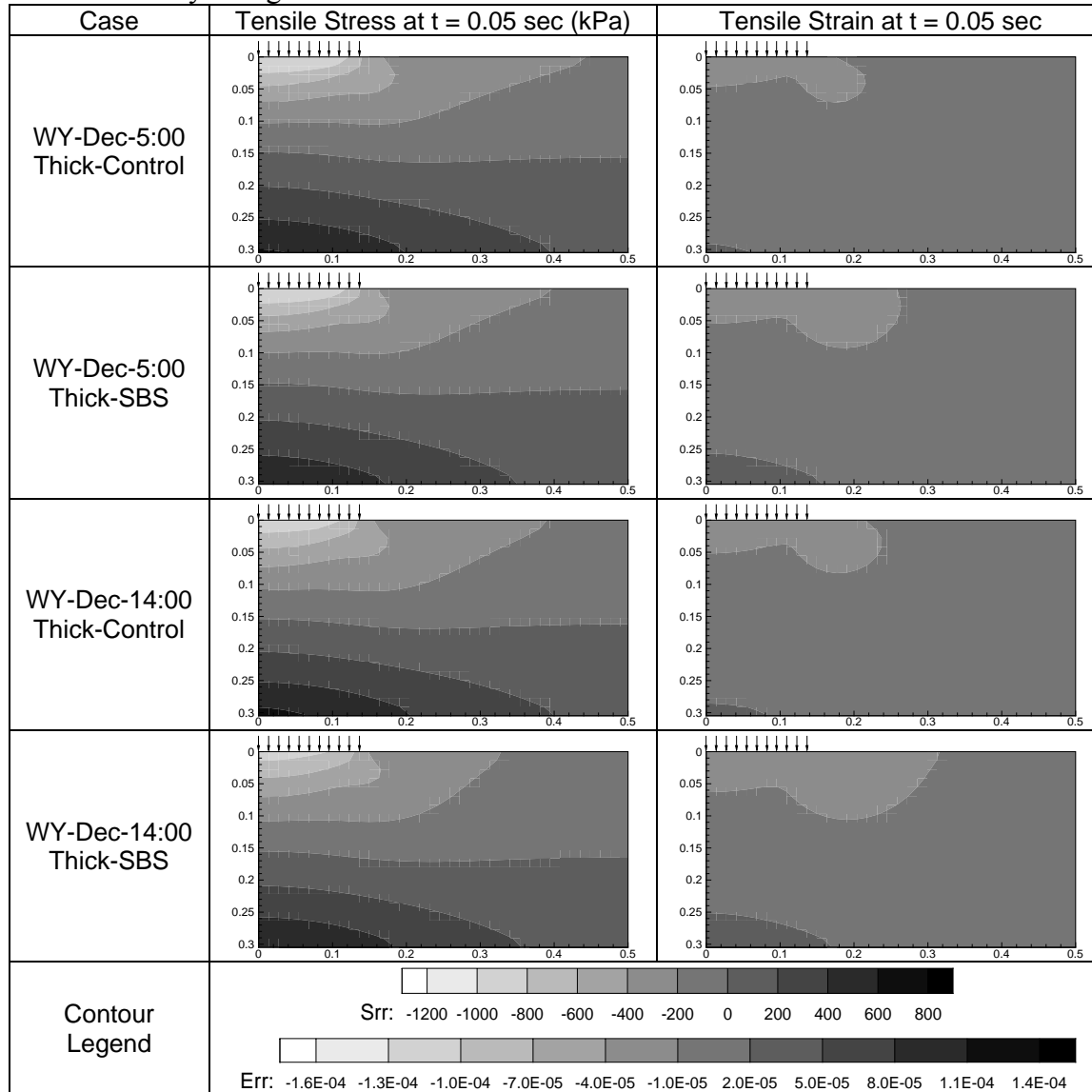
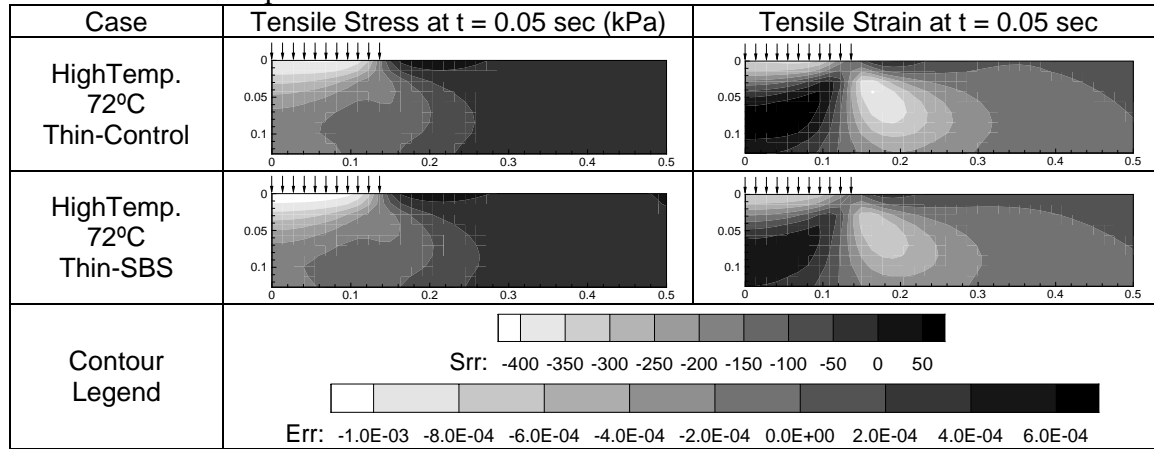


Table 1-19. Tensile Stress and Strain Contours for Reasonableness Check: Thin Pavements – Full Depth 72°C



A.2.2 Sensitivity

This section discusses in detail the effect of each analytical sub-model on pavement performance. Simulation details are shown in Table 1-20. Here, the pavement structure and asphalt material are fixed as the thick pavement and Control mix, respectively. Temperature data for two regions (Florida and Wyoming) are utilized for 1 year or 20 years, depending on the purpose. It was decided that the DCF should be included in all cases, because this factor has a significant effect, especially in Florida, which experiences relatively higher temperatures than Wyoming. For the support condition, sensitivity is evaluated independently of the other factors, but a specific condition was chosen for the sensitivity analysis of each variable (i.e., a weak support condition was used to assess the DCF, and a moderate support condition was used to assess aging). The rationale behind selecting which support condition to use for which variable is to amplify the effect of the variable under investigation; i.e., the support condition is chosen to represent the worst case scenario.

A.2.2.1 Support condition effect

Table 1-21 displays a comparison of the damage contours for Florida and Wyoming to show the effects of varying the support condition. From this table it is evident that a strong

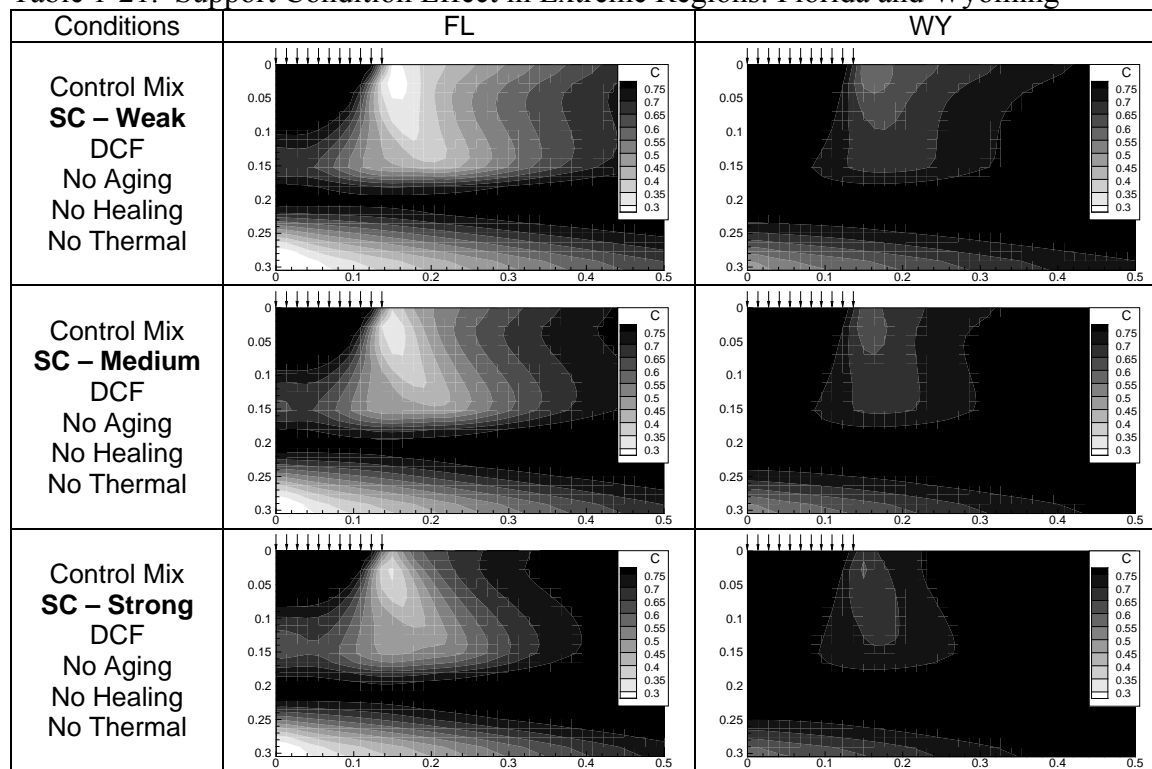
support condition leads to an overall reduction in damage distribution. The effect is most significant for the top-down damage, but also affects the damage at the bottom of the pavement. It is also seen that the effect of the support condition is most noticeable in the case of the Wyoming climatic condition.

Table 1-20. Simulation Details for Sensitivity Check

Item	Number of Cases	Details
Region	2	FL, WY
Structure	1	Thick (304.8 mm or 12 in.)
AC Material	1	ALF Control
Support Condition	3	Weak, Moderate, Strong
Aging	2	No Aging, Aging
Healing	0	--*
Thermal Stress	2	High vs. Low Thermal Coefficient
DCF	2	1-yr EICM or 10-yr EICM
Total Number of Cases	32	

* Not assessed due to time and resource limitations

Table 1-21. Support Condition Effect in Extreme Regions: Florida and Wyoming

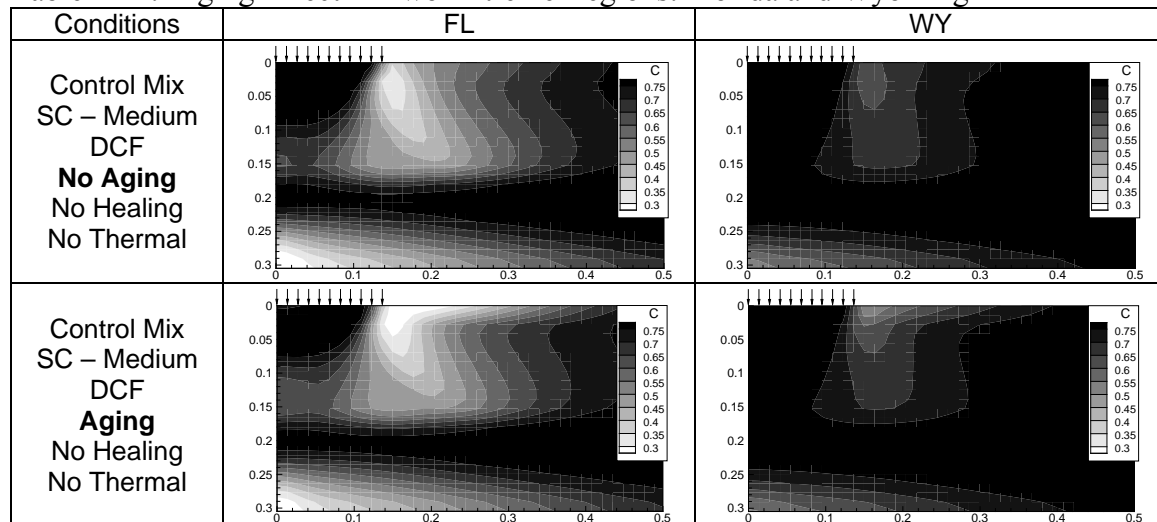


A.2.2.2 Aging effect

To investigate the effect of aging, FEP++ simulations were conducted, and the results are shown in Table 1-22. In the simulations a single year run was performed, but the input material properties correspond to either the un-aged properties (denoted as No Aging in Table 1-22) or the 20 year-aged properties (denoted as Aging in Table 1-22). Because the amount of field aging is related directly to environmental conditions, two extreme cases, Laramie, Wyoming and Tallahassee, Florida, were used in this sensitivity analysis. The ALF Control mixture was used for both cases. Note that, because the purpose of the first simulation runs was to assess only the sensitivity of the aging model, the healing and thermal damage models were not active. The following observations can be made from the contours shown in Table 1-22:

- Aging can have a noticeable effect on the damage growth in a pavement, particularly at the pavement surface;
- The effects of aging are more significant in climates with higher annual pavement temperatures (Florida) than in cooler climates (Wyoming);
- Although the effects of aging are most noticeable at the pavement surface, aging affects the way stress distributes throughout the pavement and, thus, the way that damage accumulates throughout the whole pavement structure.

Table 1-22. Aging Effect in Two Extreme Regions: Florida and Wyoming



A.2.2.3 Thermal stress effect

Thermal stress is the direct result of structural constraints on material expansion. When a material is heated or cooled it tends to expand or contract by an amount directly proportional to the change in temperature. The constant of proportionality is known as the *thermal coefficient*, and for the purposes here is assumed to be a material constant. This parameter is not typically measured for AC, but it can be estimated from Equation (A-72) (29). A parametric study using this equation with typical in-service input values shows that this property may range from 1.3×10^{-5} to $2.5 \times 10^{-5} \text{ } \varepsilon/\text{ }^\circ\text{C}$. This range was further truncated for this study, and two α_{mix} values, 1.2×10^{-5} and 2.1×10^{-5} , were used in the sensitivity analysis.

$$\alpha_{mix} = \frac{VMA * \alpha_{AC} + V_{AGG} * \alpha_{agg}}{3 * V_{Total}}, \quad (\text{A-72})$$

where

- α_{mix} = thermal coefficient of the mixture,
- α_{AC} = thermal coefficient of the asphalt cement ($3.45 \times 10^{-4} \text{ } \varepsilon/\text{ }^\circ\text{C}$),
- α_{agg} = thermal coefficient of the aggregate particles ($6.5 \times 10^{-6} \text{ } \varepsilon/\text{ }^\circ\text{C}$),
- VMA = percentage of voids in the mineral aggregate,
- V_{AGG} = percentage of aggregate in the mixture, by volume, and
- V_{Total} = percentage of total volume, 100.

Laramie, Wyoming and Tallahassee Florida are the regions selected for these simulations. Because thermal damage is most severe during the winter months when the material is stiff and cools relatively rapidly, only the damage that occurs during December was simulated. The results are shown in Figure 1-14 for the four different conditions. From this figure it is clearly observed that the damage is greater with the larger thermal coefficient. The effect of the thermal coefficient varies by region because the modulus is affected by the mean temperature. In the case of the Florida simulation, the material is much more viscous than it is in the Wyoming case. As a

result, the material is more likely to relax and absorb thermally-induced dimensional changes and, therefore, experience less damage. Because the overall effect of thermal damage is reduced, the apparent effect of the thermal coefficient is also reduced for Florida. In Wyoming, most of the damage in December occurs due to thermal damage and, as a result, it is concluded that the total damage growth for Wyoming is quite sensitive to the thermal coefficient. Similar ratios of damage growth for the two coefficients would be observed for other months, but the total damage growth for those months might not be as large as is seen for December, so the thermal stress effect may be smaller.

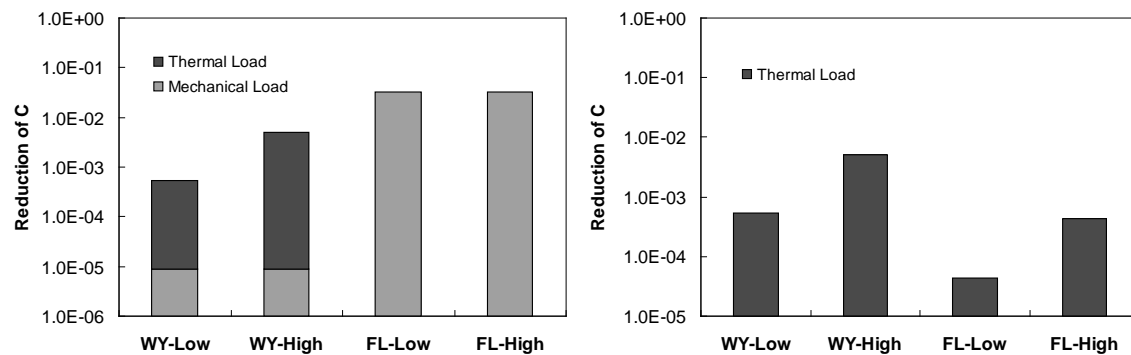


Figure 1-14. Sensitivity of thermal damage growth to selected thermal coefficient: (a) thermal and mechanical, and (b) thermal damage only

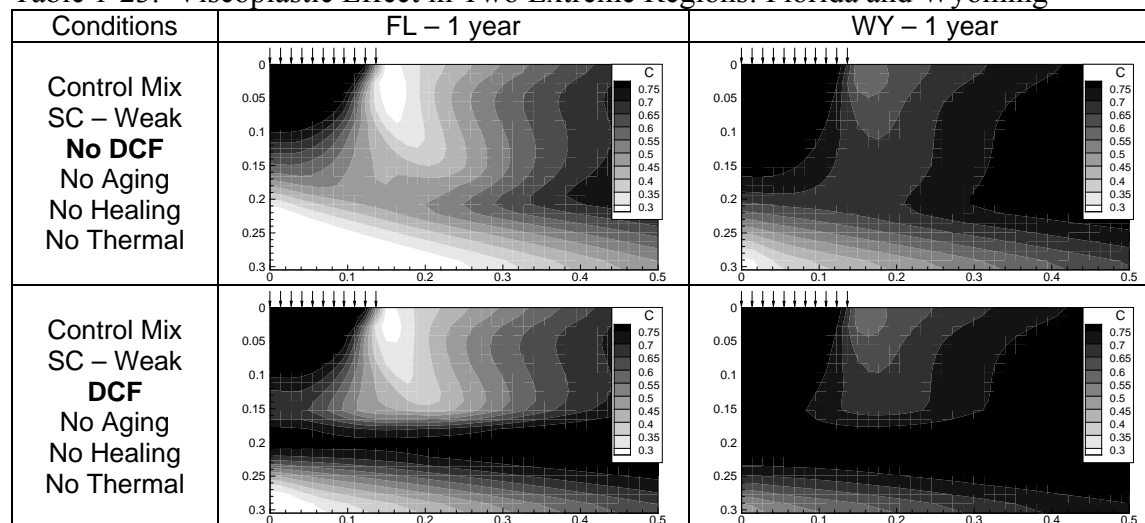
A.2.2.4 Viscoplastic effect

The effect of viscoplasticity on pavement performance, especially cracking, could be significant, depending on the material, structure, and/or temperature. As described in Section 1.2.3.2, the effect of viscoplasticity on the pavement performance can be handled through the DCF.

To evaluate the viscoplastic effect, simulations were conducted by making only the DCF analytical model active. The other sub-models – healing, aging and thermal – were inactive. Some typical results are shown in Table 1-23. To amplify the effects of the DCF, the support conditions for the contours are all weak, as shown in Table 1-23. These simulations were run for

one year with and without the DCF. As is clearly seen in Table 1-23, the DCF noticeably reduces the total damage growth for both the Wyoming and Florida regions. The effects of the DCF are somewhat more pronounced in the Florida case and much more pronounced near the pavement base.

Table 1-23. Viscoplastic Effect in Two Extreme Regions: Florida and Wyoming



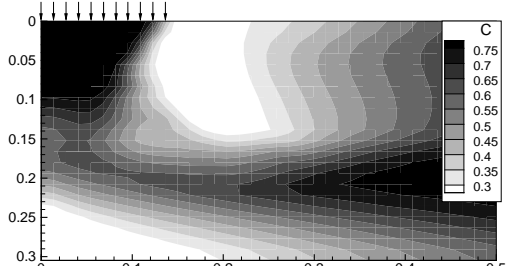
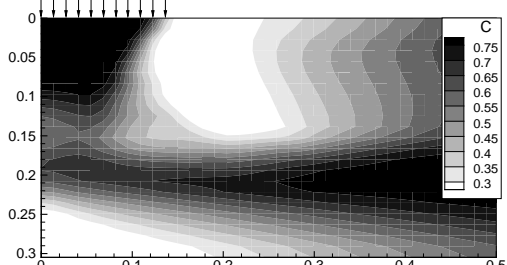
Another important aspect of the DCF that should be examined is the temperature used in the computations. This issue is important because most of the temperature data compiled in the EICM are less than 10-year data, and to simulate a pavement condition requires repeating the data. The effect of sequential year temperature data on the DCF calculation was evaluated. Two methods to calculate the DCF were chosen:

- Calculate the DCF using 1-year EICM data and repeat both the temperature profiles and the DCF 20 times.
- Calculate the DCF year by year and use annual specific temperature profiles by repeating the 10-year EICM data.

As with the other DCF sensitivity analysis, no other analytical sub-models were active in these simulations. For simulation purposes, the D.C. temperature data were selected as representative for all regions. The ALF Control mix and a moderate modulus were utilized for

the asphalt layer and subgrade, respectively. As shown in Table 1-24, the two methods generate similar results. As a result of the analysis shown in Table 1-24, it is concluded that the DCF calculation is not sensitive to yearly temperature fluctuations and, as a result, only a single annual temperature profile needs to be used in computing its value. Because thermal effects were considered by sequentially repeating five years of EICM data, the DCF was computed based on the average of five years of EICM data.

Table 1-24. Sensitivity of the Damage Factor Calculation

Conditions	Method	DC -20 years
Control Mix SC – Medium DCF No Aging No Healing No Thermal	EICM-1 yr DCF-1 yr	
	EICM-10 yr DCF-20 yr	

A.3 Example Simulation and Parametric Study Contour Plots

A.3.1 Example Simulation Contour Plots

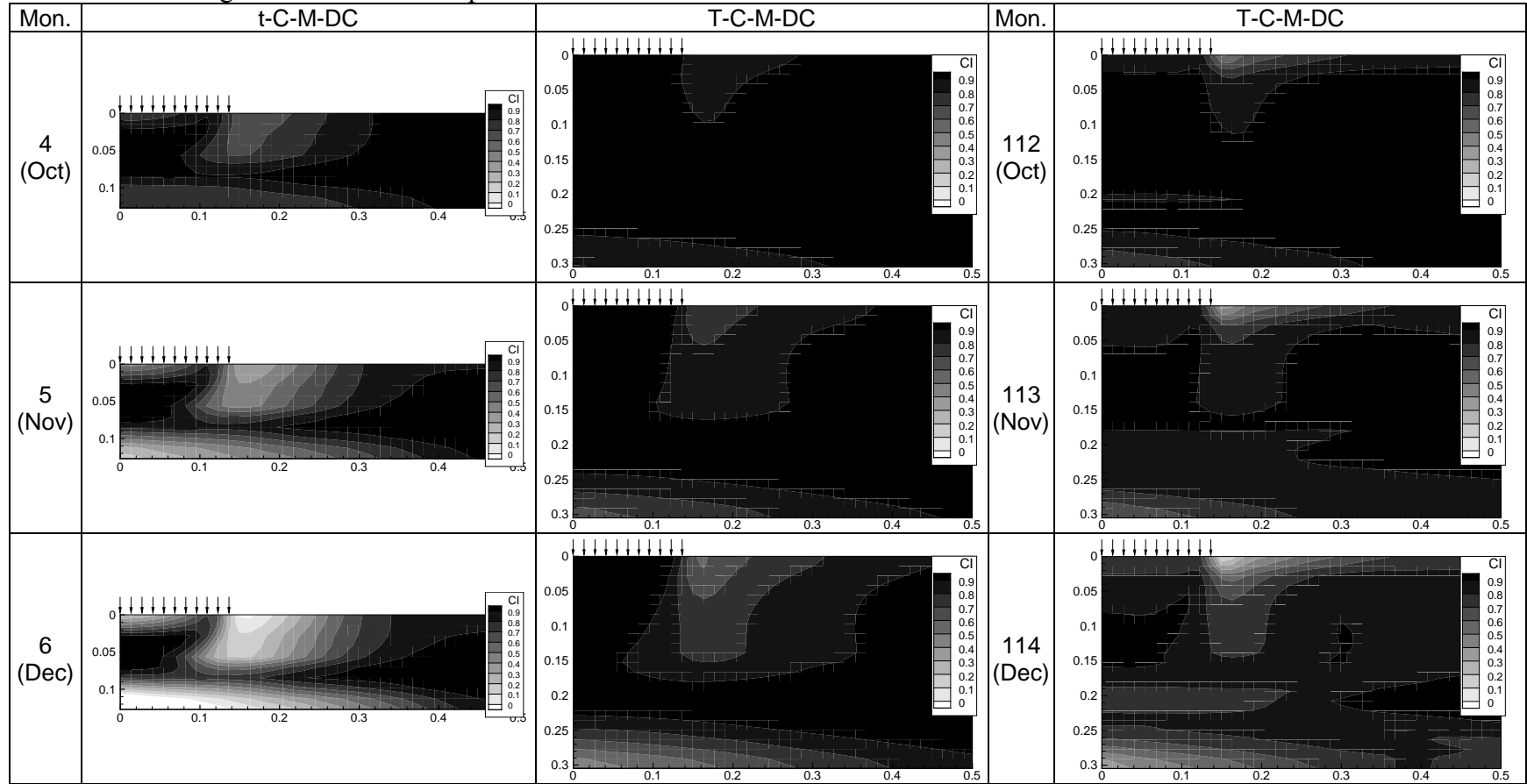
Results from the simulations are shown as a series of contour plots. The variable of interest in these contours is the condition index (CI). The resulting contour plots for this simulation condition are summarized in Table 1-25. In this table, the month column contains two items of information: the simulation month number (all simulations began in July) and the abbreviated month that corresponds to the simulation. Simulations for all cases were performed until one element reached a pseudo stiffness value of 0.25 or until ten years had been simulated. In the

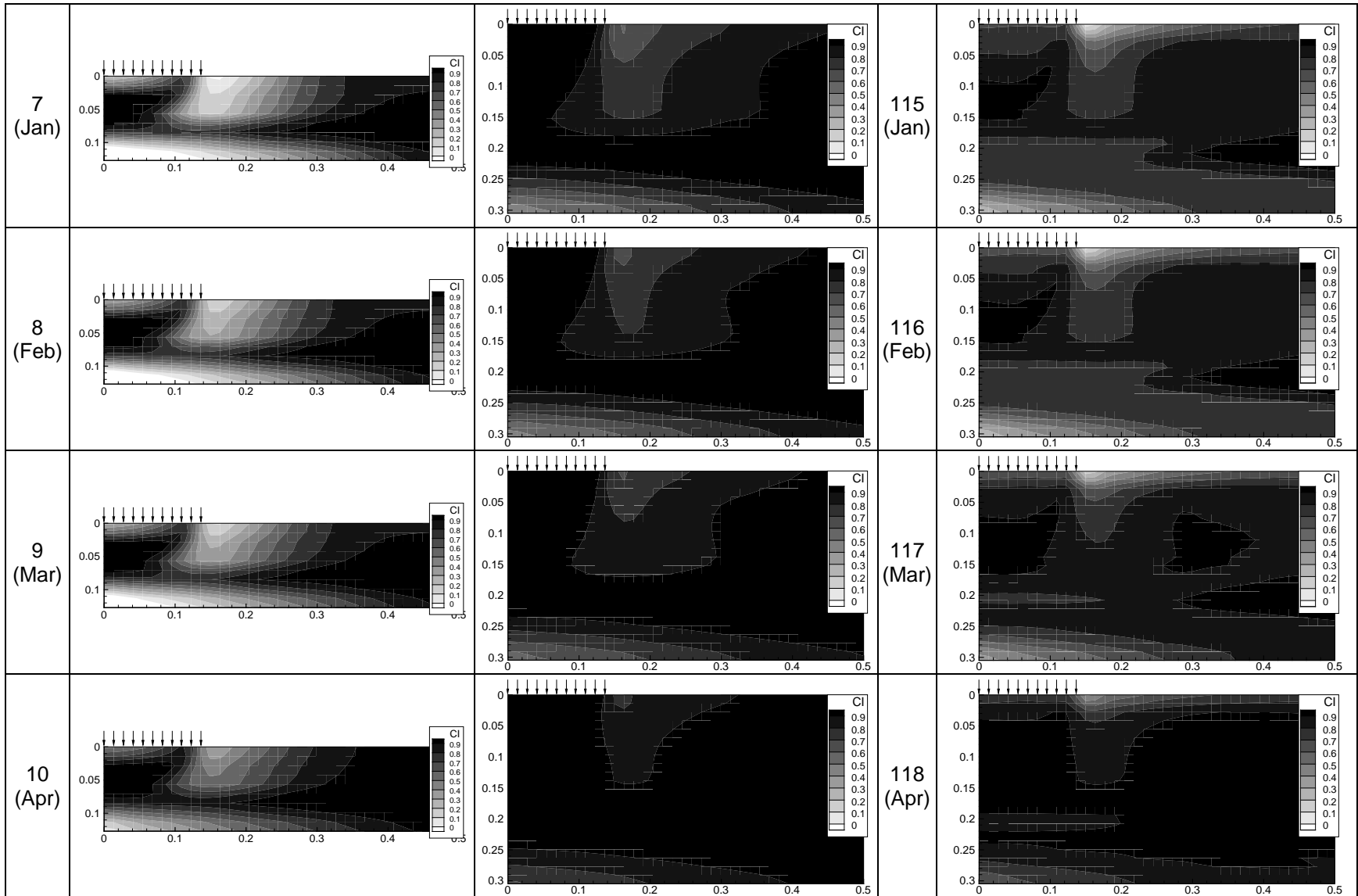
case of the thin pavement, the length of time was somewhat longer than a full year, but the thick pavement was simulated for the full ten years. Table 1-25 shows the contours for the months of October through July of the first simulation year for both the thick pavement and the thin pavement. In addition, the final nine months of the thick pavement simulation are shown in the far right column of the table. All contours are interpreted in terms of the extent and severity of the damage.

A.3.2 Parametric Study Contour Plots

The simulated CI contours are shown for the thin pavements in Table 1-26 and for the thick pavements in Table 1-27 through Table 1-29. Note that the contours in Table 1-26 and Table 1-27 are all at the end of the ninth month (March), whereas the contours in Table 1-28 and Table 1-29 are also for March, but at year 5 and year 10, respectively. Also note the naming convention used for the different simulations. For the evaluation of the effect of asphalt mixture properties, the damage progression contours from October through June are shown in Table 1-30. The letters stand for, in order: pavement type, thick (T) or thin (t); material type, ALF control (C) or ALF SBS (S); and support condition, weak (W) or strong (S).

Table 1-25. Damage Contours for Example Simulations





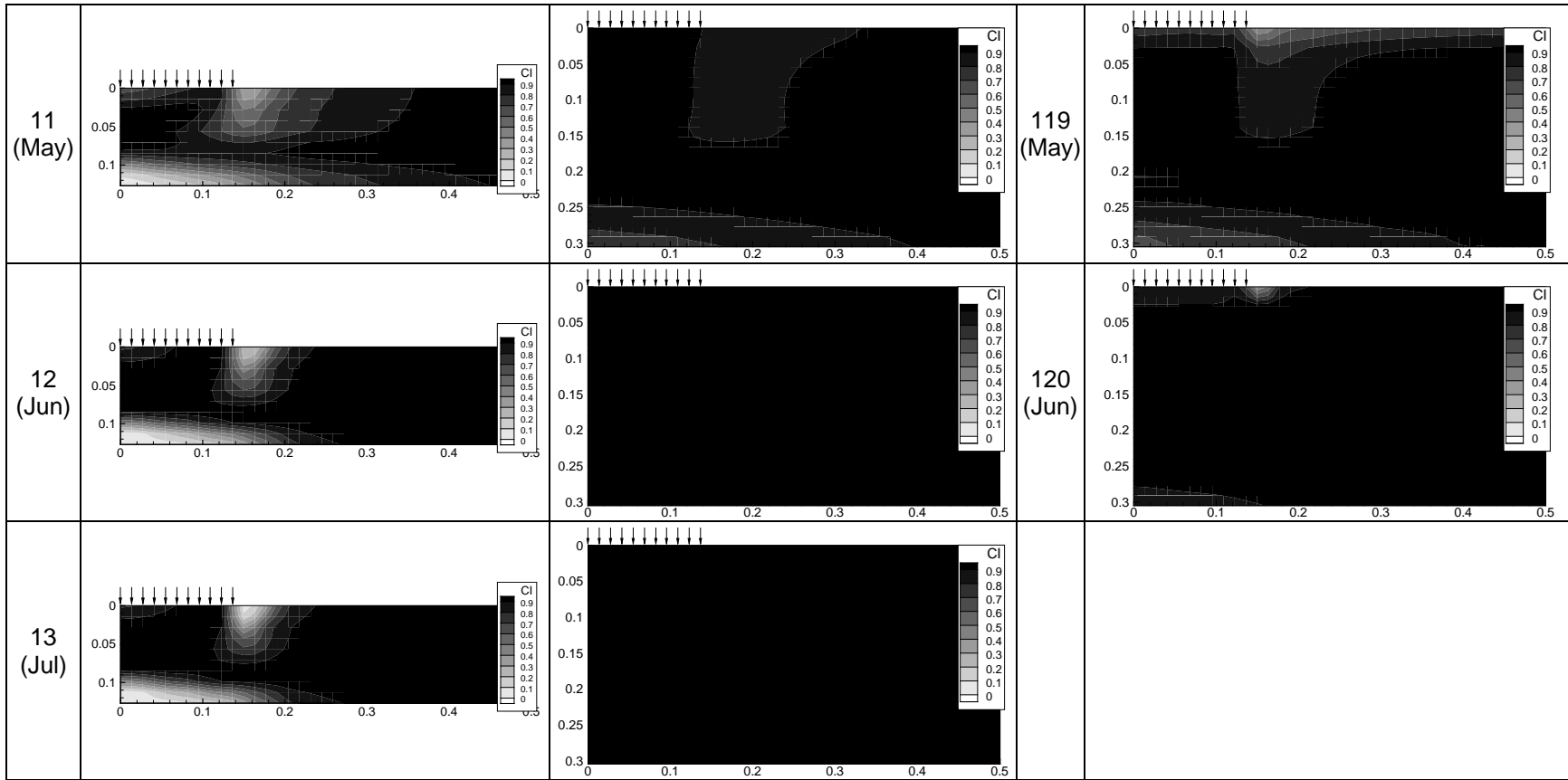
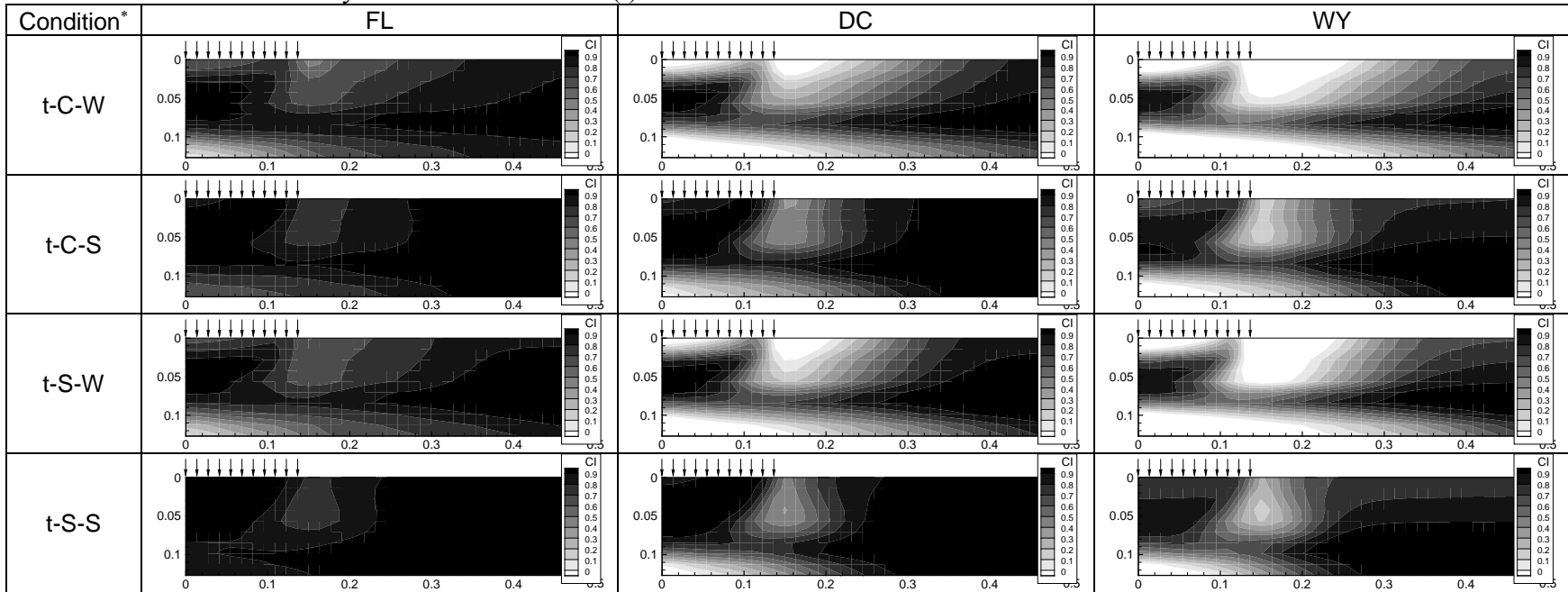


Table 1-26. Parametric Study Simulations for Thin (t) Pavements



* Four conditions were considered for thin pavements: 1) t-C-W stands for a thin pavement with an ALF Control material layer over a weak supporting layer; 2) t-C-S stands for a thin pavement with an ALF Control material layer on a strong supporting layer; 3) t-S-W stands for a thin pavement with an ALF SBS material layer over a weak supporting layer; and 4) t-S-S stands for a thin pavement with an ALF SBS material layer on a strong supporting layer. Similar conditions were considered for thick pavements (see Tables 1-27 to 1-29), except that t (thin) was replaced by T (thick).

Table 1-27. Parametric Study Simulations for Thick (T) Pavements: Year 1

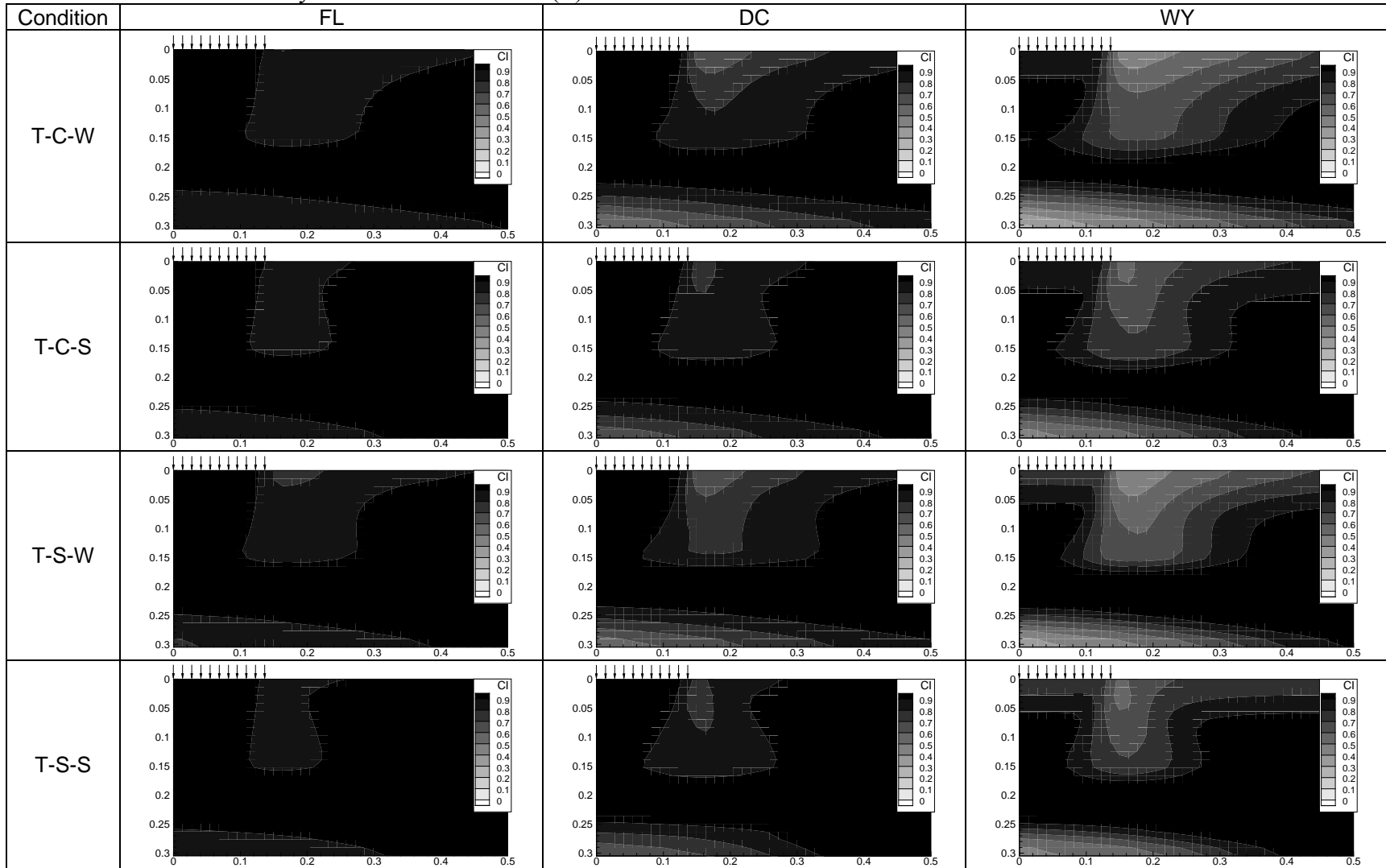


Table 1-28. Parametric Study Simulations for Thick (T) Pavements: Year 5

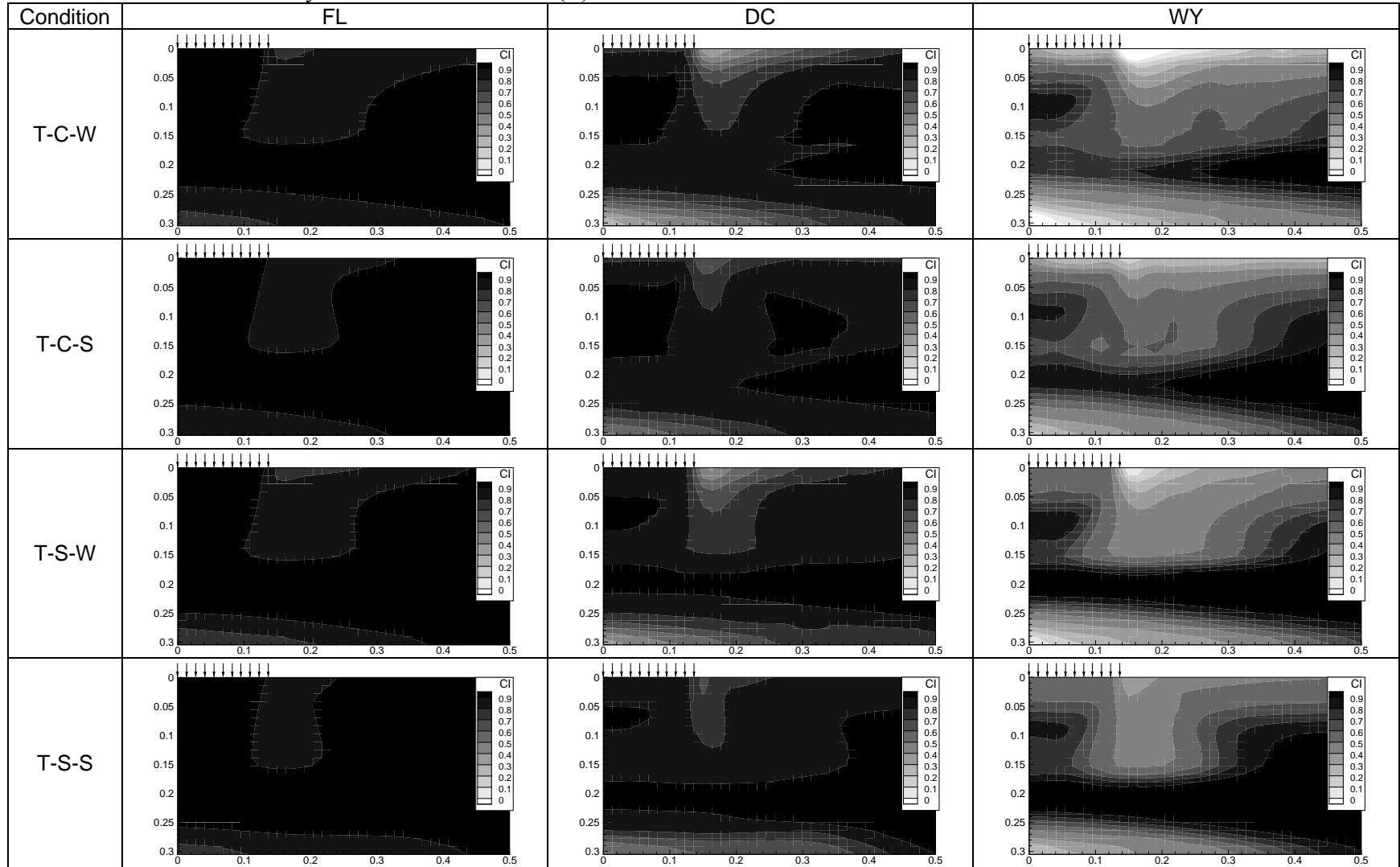


Table 1-29. Parametric Study Simulations for Thick (T) Pavements: Year 10

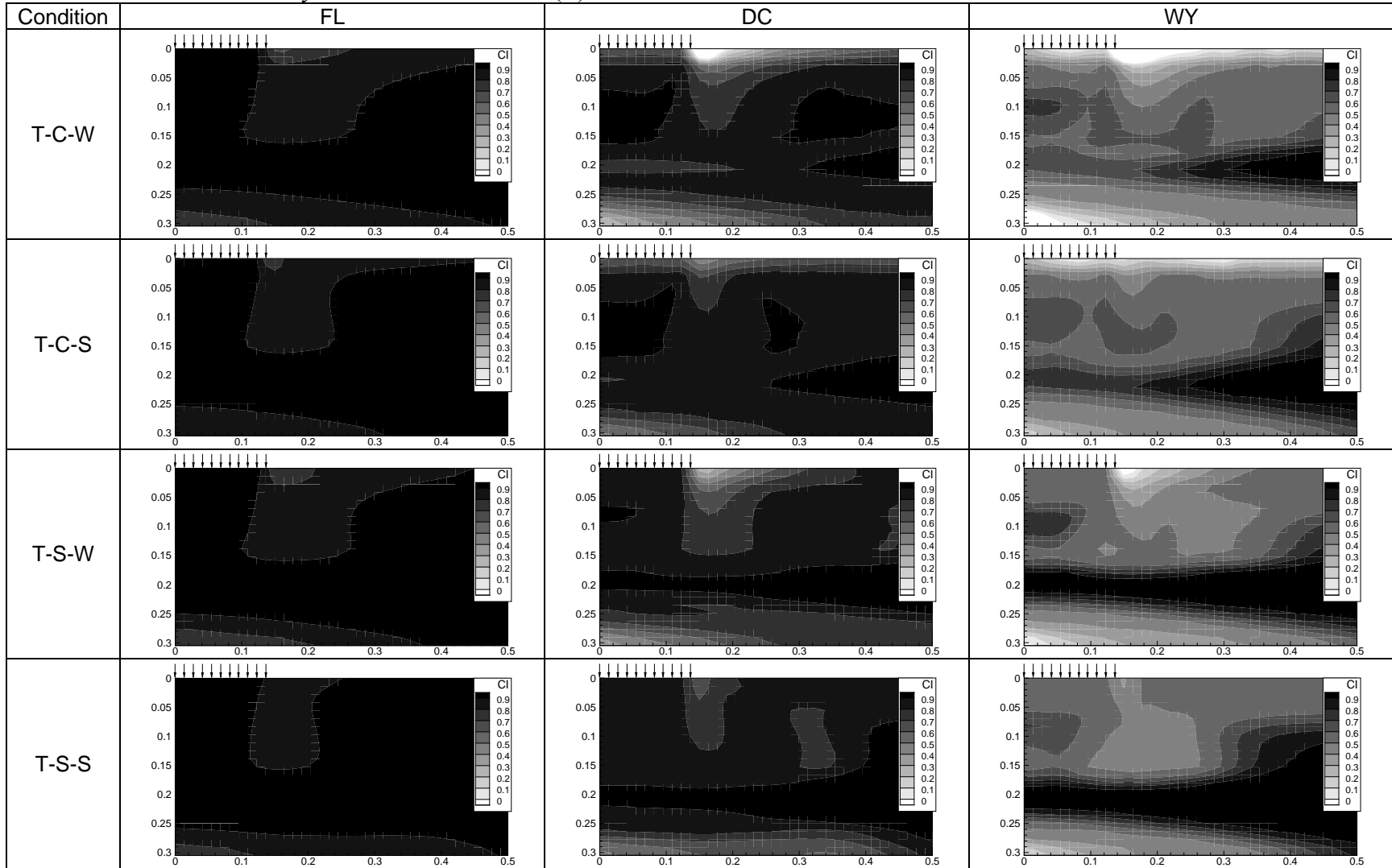
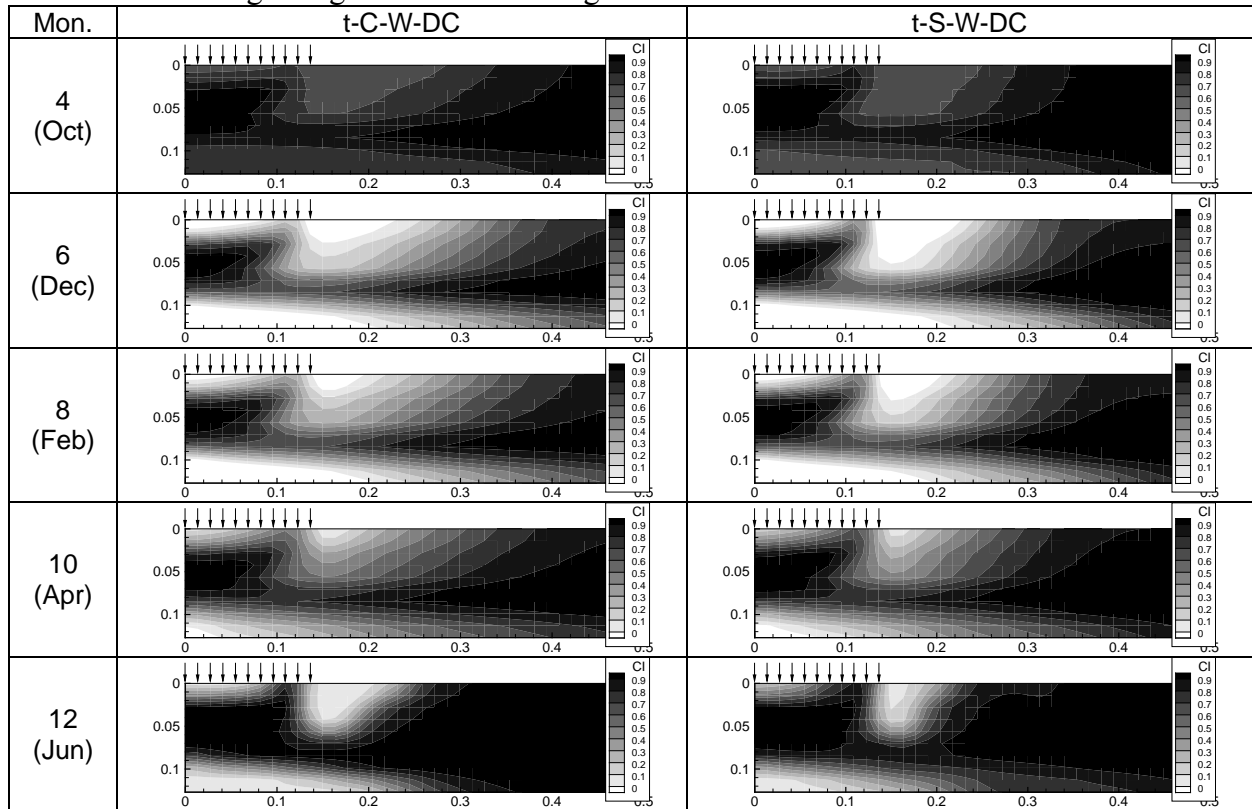


Table 1-30. Damage Progression and Healing in SBS and Control Pavements



A.4 List of References

1. Kim, Y. R., C. Baek, B. S. Underwood, V. Subramanian, M. N. Guddati, and K. Lee. Application of Viscoelastic Continuum Damage Model Based Finite Element Analysis to Predict the Fatigue Performance of Asphalt Pavements. KSCE, *Journal of Civil Engineering*, Vol. 12, No. 2, 2008, pp. 109-120.
2. Park, S. W. and R. A. Schapery. Methods of Interconversion between Linear Viscoelastic Material Functions. Part I – A Numerical Method based on Prony Series. *International Journal of Solids and Structures*, Vol. 36, 1999, pp. 1653-1657.
3. Schapery, R. A. A Simple Collocation Method for Fitting Viscoelastic Models to Experimental Data. *GALCIT SM 61-23A*. California Institute of Technology, Pasadena, CA. 1961.
4. Schapery, R. A. Correspondence Principles and a Generalized J-integral for Large Deformation and Fracture Analysis of Viscoelastic Media. *International Journal of Fracture*, Vol. 25, 1984, pp. 195-223.
5. Underwood, B. S., Y. R. Kim, S. Savadatti, S. Thirunavukkarasu, M. N. Guddati. Response and Fatigue Performance Modeling of ALF Pavements Using 3-D Finite Element Analysis and a Simplified Viscoelastic Continuum Damage Model. *Journal of the Association of Asphalt Paving Technologists*, 2009. In Press.
6. Reese, R. Properties of Aged Asphalt Binder Related to Asphalt Concrete Fatigue Life. *Journal of the Association of Asphalt Paving Technologists*, Vol. 66, 1997, pp. 604-632.
7. Hou, T., B. S. Underwood, and Y. R. Kim. Fatigue Performance Prediction of North Carolina Mixtures Using the Simplified Viscoelastic Continuum Damage Model. *Journal of the Association of Asphalt Paving Technologists*, Vol. 79, 2010. In press.
8. Daniel, J. S. and Y. R. Kim. Development of a Simplified Fatigue Test and Analysis Procedure Using a Viscoelastic Continuum Damage Model. *Journal of the Association of Asphalt Paving Technologists*, Vol. 71, 2002, pp. 619-650.
9. Underwood, B. S., Y. R. Kim and M. N. Guddati. Characterization and Performance Prediction of ALF Mixtures Using a Viscoelastoplastic Continuum Damage Model. *Journal of the Association of Asphalt Paving Technologists*, Vol. 75, 2006, pp. 577-636.
10. Underwood, B. S., Y. R. Kim, and M. N. Guddati. Improved Calculation Method of Damage Parameter in Viscoelastic Continuum Damage Model. *International Journal of Pavement Engineering*, 2009. In Press.
11. Tangella, S. C. S. R., J. Craus, J. A. Deacon, and C. L. Monismith. Summary Report on Fatigue Response of Asphalt Mixtures. Prepared for *SHRP Project A-003-A*. Strategic Highway Research Program, National Research Council, Washington, D.C., 1990.

12. Strategic Highway Research Program (SHRP). Fatigue Response of Asphalt-Aggregate Mixes. *SHRP-A-404*, National Research Council, Washington, D.C., 1994.
13. Tayebali, A. A., J. A. Deacon, and C. L. Monismith. Development and Evaluation of Surrogate Fatigue Models for SHRP A-003A: Abridged Mix Design Procedure. *Journal of the Association of Asphalt Paving Technologists*, Vol. 64, 1995, pp. 340-364.
14. Asphalt Institute. Research and Development of the Asphalt Institute's Thickness Design Manual (MS-1), 9th edition. Research Report 82-2. 1982.
15. Tayebali, A. A., J. A. Deacon, J. S. Coplantz, and C. L. Monismith. Modeling Fatigue Response for Asphalt-Aggregate Mixtures. *Journal of the Association of Asphalt Paving Technologists*, Vol. 62, 1993, pp. 385-421.
16. Huang, Y. *Material Characterization and Performance Properties of Superpave Mixtures*. Ph.D. Dissertation, North Carolina State University, Raleigh, NC. 2004.
17. Finn, F., C. L. Saraf, K. Kulkarni, K. Nair, W. Smith, and A. Abdullah. Development of Pavement Structural Subsystems. *Final Report NCHRP 1-10B*, National Cooperative Highway Research Program, National Research Council, Washington, D.C., 1977.
18. Shell International Petroleum. *Shell Pavement Design Manual: Asphalt Pavements and Overlays for Road Traffic*. London. 1978.
19. Craus, J., R. Yuce, and C. L. Monismith. Fatigue Behavior of Thin Asphalt Concrete Layers in Flexible Pavement Structures. *Journal of the Association of Asphalt Paving Technologists*, Vol. 53, 1984, pp. 559-582.
20. Advanced Research Associates. *2002 Design Guide: Design of New and Rehabilitated Pavement Structures*. NCHRP 1-37A Project, National Cooperative Highway Research Program. National Research Council. Washington, D.C., 2004.
21. Epps, J. A. and C. L. Monismith. Influence of Mixture Variables on the Flexural Fatigue. *Journal of the Association of Asphalt Paving Technologists*, Vol. 38, 1969, pp. 423-464.
22. Pell, P. S. and K. E. Cooper. The Effect of Testing and Mix Variables on the Fatigue Performance of Bituminous Materials. *Journal of the Association of Asphalt Paving Technologists*, Vol. 44, 1975, pp. 1-37.
23. Uzan, J., M. Perl, and A. Sides. Viscoelastoplastic Model for Predicting Performance of Asphalt Mixtures. In *Transportation Research Record: Journal of the Transportation Research Board, No. 1043*, Transportation Research Board of the National Academies, Washington, D.C., 1985, pp. 78-79.

24. Schapery, R. A. Nonlinear Viscoelastic and Viscoplastic Constitutive Equations with Growing Damage. *International Journal of Fracture*, Vol. 97, 1999, pp. 33-66.
25. Chehab, G. R., Y. R. Kim, R. A. Schapery, M. Witzack, and R. Bonaquist. Characterization of Asphalt Concrete in Uniaxial Tension Using a Viscoelastoplastic Model. *Journal of the Association of Asphalt Paving Technologists*, Vol. 72, 2003, pp. 315-355.
26. Chehab, G. R. and Y. R. Kim. Viscoelastoplastic Continuum Damage Model Application to Thermal Cracking of Asphalt Concrete. *ASCE Journal of Materials in Civil Engineering*, Vol. 17, No. 4, 2003, pp. 384-392.
27. Underwood, B. S. and Y. R. Kim. Determination of the Appropriate Representative Elastic Modulus for Asphalt Concrete. *International Journal of Pavement Engineering*, Vol. 10, No. 2, 2009, pp. 77-86.
28. Lytton, R. L., J. Uzan, E. G. Fernando, R. Roque, D. Hiltunen, and S. M. Stoffels. *Development and Validation of Performance Prediction Models and Specifications for Asphalt Binders and Paving Mixes*. SHRP-A-357, Strategic Highway Research Program, National Research Council, Washington, D.C., 1993.

APPENDIX B. DEVELOPMENT OF THE HMA-FM-BASED MODEL

TABLE OF CONTENTS

	<u>page</u>
TABLE OF CONTENTS.....	B-ii
APPENDIX	
B DEVELOPMENT OF THE HMA-FM-BASED MODEL.....	B-1
B.1 Introduction.....	B-1
B.1.1 HMA Fracture Mechanics Model.....	B-1
B.1.1.1 HMA fracture mechanics.....	B-1
B.1.1.2 HMA fracture mechanics-based crack growth simulator.....	B-2
B.1.1.3 Energy ratio approach.....	B-4
B.1.1.4 Modified energy ratio approach.....	B-5
B.1.1.5 Summary of existing HMA-FM model.....	B-6
B.1.2 Material Property Models.....	B-6
B.1.2.1 Binder aging model.....	B-7
B.1.2.2 Dynamic modulus model.....	B-7
B.1.2.3 Tensile strength model.....	B-8
B.1.2.4 Healing model.....	B-8
B.2 Development of Model Components.....	B-11
B.2.1 Material Property Model.....	B-11
B.2.1.1 AC stiffness (creep compliance) aging model.....	B-11
B.2.1.2 AC tensile strength aging model.....	B-13
B.2.1.3 FE limit (DCSE limit) aging model.....	B-14
B.2.1.4 Healing model.....	B-17
B.2.2 Pavement Response Model.....	B-24
B.2.2.1 Load response model.....	B-24
B.2.2.2 Thermal response model.....	B-25
B.2.3 Pavement Fracture Model.....	B-27
B.2.3.1 Crack initiation model.....	B-27
B.2.3.2 Crack growth model.....	B-29
B.2.3.3 Crack amount model.....	B-30
B.3 Integration of Model Components.....	B-31
B.3.1 Integration of Healing Model.....	B-31
B.3.1.1 Background of experiments for evaluating healing effect.....	B-31
B.3.1.2 Material and structural properties.....	B-32
B.3.1.3 Model predictions without healing.....	B-35
B.3.1.4 Determination of critical values for daily lowest AC stiffness.....	B-38
B.3.1.5 Model predictions with healing.....	B-39
B.3.2 Integration of Thermal Response Model.....	B-42
B.3.2.1 Selection of climatic environment.....	B-42
B.3.2.2 Material and structural properties.....	B-43
B.3.2.3 Traffic information.....	B-46

B.3.2.4 Model predictions without thermally induced damage	B-46
B.3.2.5 Model predictions with thermally induced damage	B-48
B.4 Creep Compliance Master Curves from the SuperPave IDT	B-52
B.5 Determination of Crack Initiation Time.....	B-55
B.6 List of References	B-59

CHAPTER 2 DEVELOPMENT OF THE HMA-FM-BASED MODEL

B.1 Introduction

B.1.1 HMA Fracture Mechanics Model

The continuing development of the HMA fracture mechanics (HMA-FM) model, which was determined to be necessary to include effects of aging, healing, and thermal stress on top-down cracking performance, represented a significant proportion of the effort of the researchers at the University of Florida (UF). The enhancements made to this model to make it suitable for use in a MEPDG framework will be reviewed following the sequence of each new development.

B.1.1.1 HMA fracture mechanics

Recently, researchers at UF (1, 2) developed the HMA fracture mechanics model. In this model, a fundamental crack growth law (named HMA fracture mechanics) was developed that allows for predicting the initiation and propagation of cracking, including top-down cracking, in asphalt mixture. This law is based on a critical condition concept which specifies that crack initiation and growth only develop under specific loading, environmental, and healing conditions that are critical enough to exceed the mixture's energy threshold/limit. A dissipated creep strain energy limit ($DCSE_f$) has been identified suitable to serve as the energy limit in the law, which can be determined using the SuperPave Indirect Tension Test (IDT). Figure 2-1 shows a typical stress-strain response of mixture from IDT tensile strength test. The fracture energy limit (FE_f) is determined as the area under the stress-strain curve (Area OAB). The elastic energy at fracture (EE) is calculated as the triangular area (CAB), in which the elastic modulus of the mixture (M_R) is determined using IDT resilient modulus test. The $DCSE_f$ is then obtained by subtracting the EE from the FE_f , which can be expressed as following,

$$DCSE_f = FE_f - S_t^2 / (2 \cdot M_R) \quad (2-1)$$

Where, S_t is the tensile strength of the mixture. It has been shown that $DCSE_f$ is independent of mode of loading. Once the damage in asphalt mixture is equal to (or larger than) the threshold, the critical condition is triggered, which results in crack initiation (or propagation).

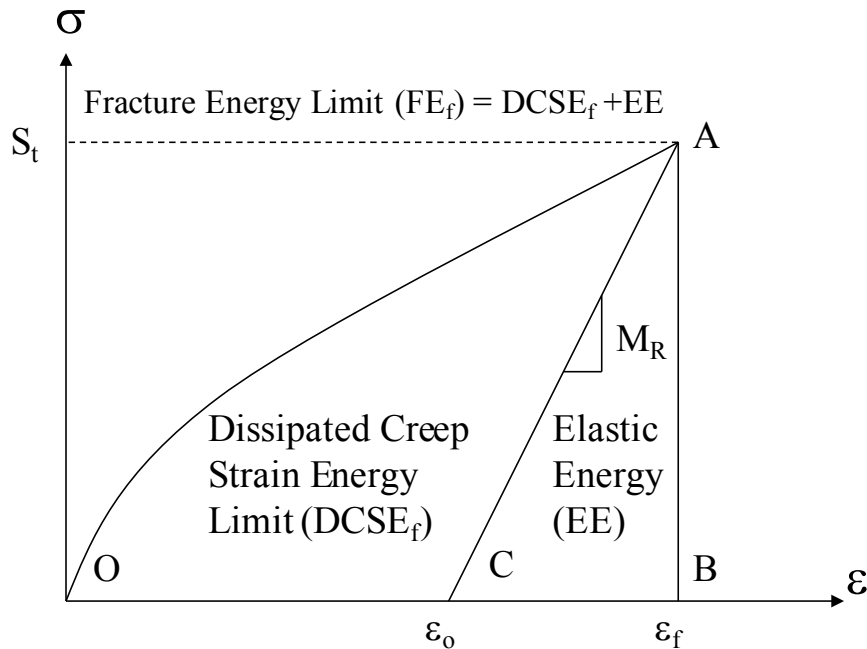


Figure 2-1. Determination of dissipated creep strain energy

B.1.1.2 HMA fracture mechanics-based crack growth simulator

Based on the HMA fracture mechanics, Sangpetngam et al. (3, 4) developed a crack growth simulator to predict crack propagation in HMA pavements. In this simulator, the displacements and stresses at any point of a pavement section are determined using the displacement discontinuity boundary element method (DDBEM). The DDBEM requires meshes only on the boundaries of an object (including cracks), and addresses crack growth by simply adding a few elements in the region of crack propagation. Figure 2-2 shows the typical boundary discretization in a two-dimensional BEM model for a pavement structure.

Figure 2-3 illustrates the structure of the simulator and the associated modeling steps: (i) model the problem by placing displacement discontinuity (DD) elements on the boundaries, with

the location(s) of possible crack initiation specified; (ii) define the process zone in front of the critical location(s); (iii) use the BEM to calculate the tensile-mode dissipated creep strain energy (DCSE) step by step; (iv) check the accumulated DCSE to determine whether the crack will grow or not: if the accumulated DCSE reaches or exceeds the damage threshold (i.e., DCSE limit), a macro-crack forms in the critical zone and causes the crack to grow by length of the zone (6 mm or 0.25 in.). The resulting simulator is capable of evaluating relative cracking performance among asphalt pavements of similar ages.

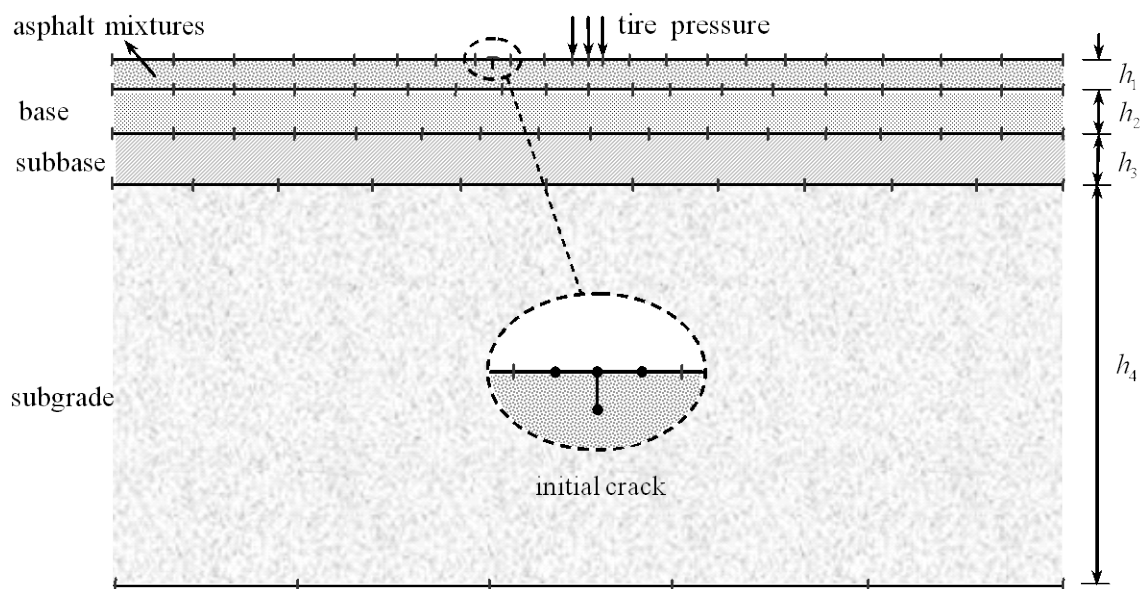


Figure 2-2. BEM model for a typical four-layer pavement structure

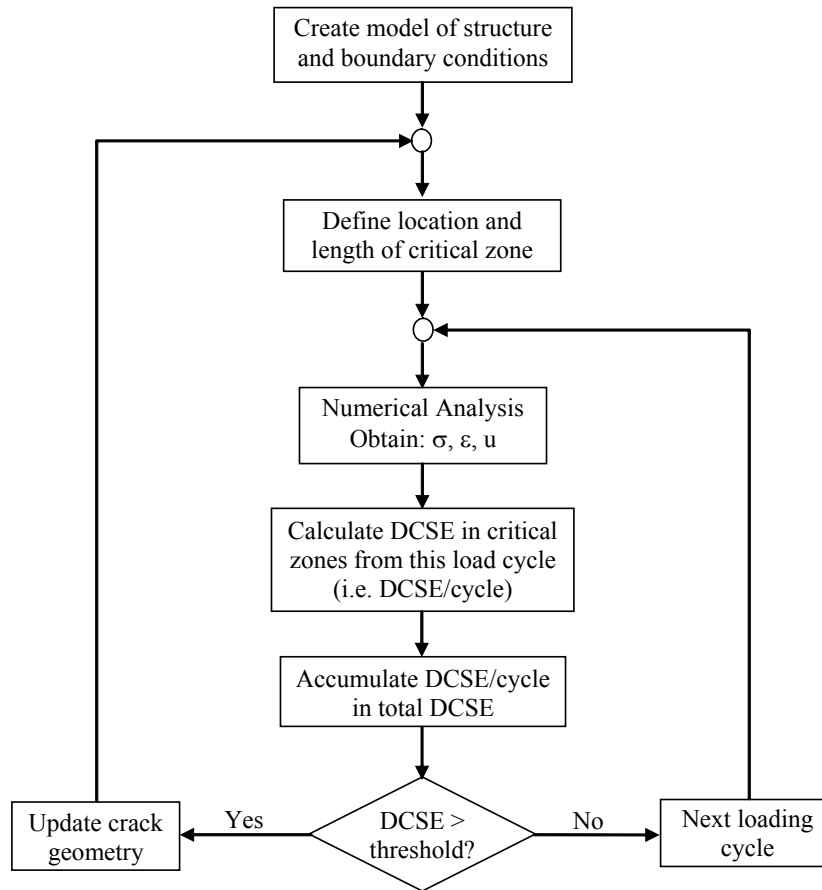


Figure 2-3. Flowchart of the HMA fracture mechanics-based crack growth simulator

B.1.1.3 Energy ratio approach

Roque et al. (5) derived a parameter termed the energy ratio (ER) based on a detailed analysis and evaluation of 22 field test sections in Florida using the HMA fracture mechanics (HMA-FM) model. The ER was defined as follows:

$$ER = DCSE_f / DCSE_{\min} \quad (2-2)$$

Where, $DCSE_f$ is the dissipated creep strain energy limit of the mixture, and $DCSE_{\min}$ is the minimum dissipated creep strain energy required for the number of cycles to failure to exceed 6000, which can be determined as follows:

$$DCSE_{\min} = m^{2.98} \cdot D_1 / A \quad (2-3)$$

Where, m and D_1 are the creep compliance power law parameters (determined using SuperPave IDT creep compliance test at 10 °C), and parameter A is a function of tensile strength S_t and tensile stress in the asphalt concrete pavement, which is expressed as follows:

$$A = 0.0299 \cdot \sigma^{-3.10} \cdot (6.36 - S_t) + 2.46 \times 10^{-8} \quad (2-4)$$

It is noted that the SuperPave IDT tensile strength and resilient modulus tests at 10 °C are required to determine S_t and resilient modulus M_R . The tensile stress is predicted using the measured M_R and other layer moduli as determined from falling weight deflectometer (FWD) tests for a typical pavement structure.

As can be seen from the above definitions, the ER accounts for effects of both damage and fracture properties on top-down cracking performance. A higher ER implies better cracking performance.

B.1.1.4 Modified energy ratio approach

Due to the fact that ER was developed based on the evaluation of load-induced cracking performance, it may not provide a reliable basis to assess pavements located in areas where the thermal effect cannot be neglected. In order to combine the effects of load and thermal, Kim et al. (6) developed a method to calculate thermally induced damage and the failure time (FT) to 100 mm crack length for a thin plate subject to specified thermal loading conditions. This method was then used in conjunction with the HMA-FM model to perform a detailed analysis and evaluation of 11 field test sections in Florida, which resulted in a new parameter termed the modified energy ratio (MER) defined as follows:

$$MER = IFT / MTR \quad (2-5)$$

Where, MTR is the minimum time requirement used to discriminate the performance of cracked and uncracked pavement sections. IFT is the integrated failure time expressed as follows:

$$IFT = FT \cdot (AMT / MTV) \cdot ER \quad (2-6)$$

Where, AMT is the annual mean air temperature and MTV is the mean temperature variation, which are correction factors to account for temperature inputs other than the single harmonic function used to calculate FT. ER is the energy ratio.

It is clear that the MER approach essentially introduced a correction factor into the ER equation such that both load and thermal effects can be accounted for during evaluation of top-down cracking performance.

B.1.1.5 Summary of existing HMA-FM model

In summary, these research efforts formed the existing HMA-FM model. However, the effect of aging and healing on top-down cracking performance during the entire service life of asphalt concrete pavements was not considered, which certainly cannot be ignored for more accurate prediction of top-down cracking. Furthermore, transverse, instead of longitudinal, thermal stresses needed to be considered for prediction of top-down cracking, since unlike thermal cracking, top-down cracking generally occurs in the longitudinal direction. In addition, the thermally induced damage needed to be directly involved in the computation of damage accumulation, so that damage recovery due to healing can be applied in a more consistent way as compared with the indirect approach used in the MER method.

B.1.2 Material Property Models

In this part, several existing mixture property sub-models, which were suitable for further development into mixture aging and healing models for incorporation into the HMA-FM model, are reviewed.

B.1.2.1 Binder aging model

Asphalt aging is sometimes quantified by change in binder viscosity, which is directly related to the prediction of dynamic modulus and the creep properties, as discussed below. The binder viscosity at mix/laydown condition ($t = 0$) is estimated using the following equation (24):

$$\log \log (\eta) = A + VTS \times \log (T_R) \quad (2-7)$$

where η is the binder viscosity in centipoises (10^{-2} poise), T_R is the temperature in Rankine, and A and VTS are regression constants. Typical values of A and VTS for three commonly used asphalt binders are given below (see NCHRP 1-37A design guide):

PG 64-22:	$A = 10.98$	$VTS = -3.68$
PG 67-22:	$A = 10.6316$	$VTS = -3.548$
PG 76-22:	$A = 9.715$	$VTS = -3.208$

For aged conditions, the viscosity of the asphalt binder at the pavement surface (depth $z = \frac{1}{4}$ in) can be estimated from the following in-service surface aging model (24):

$$\log \log (\eta_{aged}) = F_{AV} \times \frac{\log \log (\eta_{t=0}) + A_f t}{1 + B_f t} \quad (2-8)$$

where t is the time in months, F_{AV} is the air void adjustment factor, and A_f and B_f are field aging parameters that are functions of the in-service temperature and the mean annual air temperature (MAAT). The expressions for these parameters can be found in the current design guide (8). The viscosity-depth relation is given as:

$$\eta_{t,z} = \frac{\eta_t (4 + E) - E(\eta_{t=0})(1 - 4z)}{4(1 + E \cdot z)} \quad \text{and} \quad E = 23.82 \exp(-0.0308 \cdot Maat) \quad (2-9)$$

B.1.2.2 Dynamic modulus model

The dynamic modulus $|E^*|$ of asphalt concrete is used to analyze the response of pavement systems. Numerous attempts have been made to develop regression equations to calculate the dynamic modulus from conventional mixture volumetric properties. The predictive equation

developed by Witczak and Fonseca (30) is one of the most comprehensive mixture dynamic modulus models available today. This model is used in the current ME design guide. According to Witczak's model, the dynamic modulus $|E^*|$ can be represented by a sigmoidal function as follows:

$$\log|E^*| = \delta + \frac{\alpha}{1 + \exp(\beta + \gamma \log t_r)} \quad (2-10)$$

where $|E^*|$ is in psi; t_r is reduced time in seconds ($1/f$, f is loading frequency) at a reference temperature; δ , α , β , γ are fitting parameters. Detailed expressions for δ , α , β , γ in terms of the gradation and volumetric properties of the mixture can be found in Witczak and Fonseca (30).

B.1.2.3 Tensile strength model

In their work on evaluation of mixture low temperature cracking performance, Deme and Young (31) found that the tensile strength of mixture (S_t) is well correlated with the mixture stiffness at a loading time of 1800 second, i.e., S_{1800} . They had extensive data in the temperature range of -40 to 25 °C. Based on these data, the following relation was obtained between the mixture stiffness (in psi) and the tensile strength (in Mpa) through regression:

$$S_t = \sum_{n=0}^5 a_n \cdot (\log S_f)^n \quad (2-11)$$

Where S_f is the tensile stiffness that can be obtained from the dynamic modulus $|E^*|$ by taking $t = 1800$ s. The constants a_n are shown as follows,

$$\begin{aligned} a_0 &= 284.01, & a_1 &= -330.02, & a_2 &= 151.02, & a_3 &= -34.03, \\ a_4 &= 3.7786, & a_5 &= -0.1652 \end{aligned}$$

B.1.2.4 Healing model

The concept of healing to increase mixture fatigue life has been observed and has been more widely accepted by researchers (11 - 22) in recent years. Button et al. (11) conducted

controlled displacement crack growth testing in asphalt concrete mixes modified with various additives. They found an increase in work was required to open cracks after rest periods due to both relaxation in the uncracked body and chemical healing at the micro-crack and macro-crack interface. Zhang (12) conducted fracture tests using the Indirect Tensile Test and showed there is a critical energy level that distinguishes micro-damage from macro-damage; micro-damage is healable and macro-damage is not. Daniel and Kim (15) used a third point bending beam machine to induce flexural damage in beam specimens subjected to cyclic loading. They found the calculated flexural stiffness increased after the specimens were subject to rest periods. Figure 2-4 shows that healing increased the ultimate number of cycles the specimen endured before failure at 20 °C.

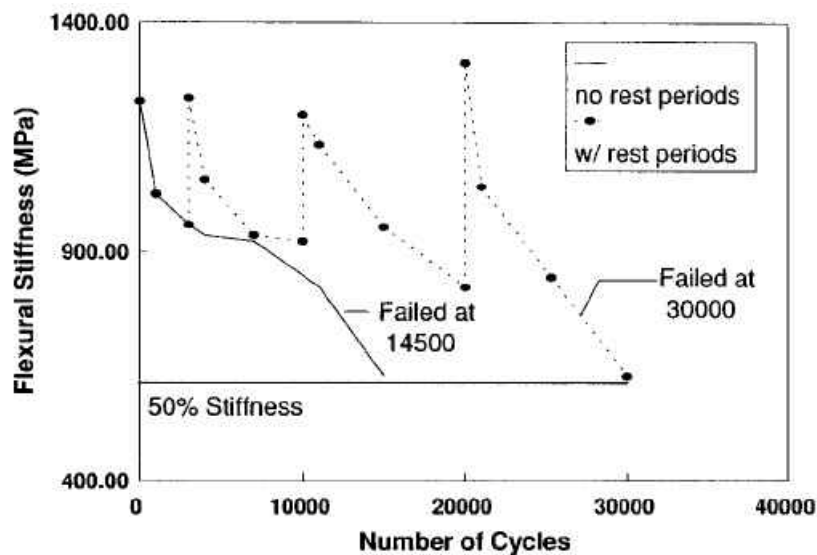


Figure 2-4. Flexural stiffness versus number of cycles to failure with and without rest periods (after Daniel and Kim (15))

Recent research by Kim and Roque (32) focused on development of experimental methods to evaluate healing properties of asphalt mixture. First, the DCSE associated with healing during unloading was determined by developing relationships between changes in resilient deformation and DCSE. The healing process was then expressed in terms of DCSE versus time. Figure 2-5

presents healing results at 20 °C for different applied DCSEs in the same mixture. Based on these results, they defined a healing rate h_r , which can be expressed as

$$h_r = DCSE_{healed}(t) / \ln(t) \tag{2-12}$$

where, $DCSE_{healed}(t)$ is the recovered DCSE at time t , which is defined as,

$$DCSE_{healed}(t) = DCSE_{induced} - DCSE_{remain}(t) \tag{2-13}$$

where, $DCSE_{induced}$ is the total energy dissipated at the end of the loading period, and

$DCSE_{remain}(t)$ is the dissipated energy remaining at time t during the rest period. As a further step, they identified a normalized healing rate h_{nr} , which was defined as,

$$h_{nr} = h_r / DCSE_{induced} \tag{2-14}$$

Substituting Eqn (2-12) into Eqn (2-14), leads to the following form,

$$h_{nr} = \left[1 - \frac{DCSE_{remain}(t)}{DCSE_{induced}} \right] / \ln(t) \tag{2-15}$$

The normalized healing rate was found to be independent of the amount of damage incurred in the asphalt mixture. It was also found to increase with increasing temperature.

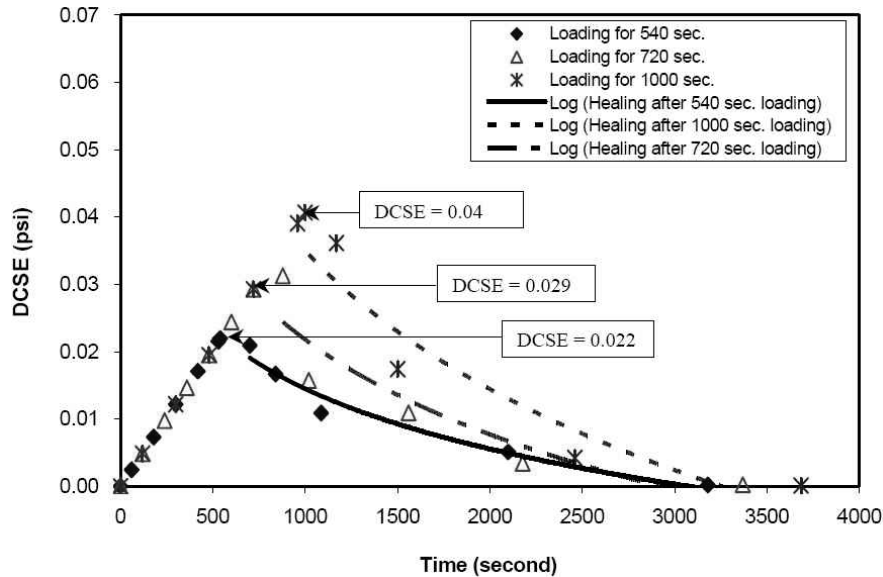


Figure 2-5. Healing tests at different DCSE for modified mixture: loading with 55 psi & healing at 20 °C (after Kim and Roque (32))

B.2 Development of Model Components

The model components developed in this project included: material property models, pavement response models, and pavement fracture models. Detailed descriptions of each of the developments are summarized in the sections below:

B.2.1 Material Property Model

As can be seen from Section B.1 (Introduction), no existing model is available to predict damage and fracture properties, or the changes of these properties with aging. However, development, calibration, and validation of a mixture model to predict damage, healing, and fracture properties is clearly a major research effort in its own right, and well beyond the scope of the current study. Therefore, the goal of this research was to develop rudimentary (placeholder) relationships between basic mixture characteristic and these properties for use when measured properties cannot be obtained.

The material property aging models and healing model developed for this purpose will be introduced in the following sub-sections. The plots used to illustrate the implementation of the models were generated using material and structural properties of one pavement section in the Washington D.C. area (see Section B.3.2 for detailed information of that pavement).

B.2.1.1 AC stiffness (creep compliance) aging model

An AC stiffness aging model was developed on the basis of binder aging model and dynamic modulus model (at a loading time of 0.1 s). In this model, the aging effect on mixture stiffness was considered using the following empirical equation,

$$|E^*|_t = |E^*|_0 \frac{\log \eta_t}{\log \eta_0} \quad (2-16)$$

where $|E^*|_t$ and $|E^*|_0$ represent the stiffnesses corresponding to aged and unaged conditions, respectively; η_t and η_0 correspond to the aged and unaged binder viscosity.

As an example, Figure 2-6 gives three predicted AC stiffness curves as a function of time (in days), i.e., daily lowest, mean, and highest AC stiffness at surface of the pavement section of Washington D.C. area during Year one (started from July 1st). The AC stiffness curves of the same mixture at Year five (i.e., after being aged for five years), are shown in Figure 2-7. It can be seen from a comparison of these two plots that the effect of aging on AC stiffness is considerable, as expected.

With the AC stiffness aging model, creep compliance values at 1, 2, 5, 10, 20, 50, 100, 200, 500, and 1000 sec for three temperatures (e.g., 0, 10, and 20°C) were obtained by taking inverse of the AC stiffness values at the corresponding time and temperature, which resulted in three creep compliance curves for 1000 sec. Figure 2-8 shows the predicted creep compliance curves at multiple temperatures for the same pavement section at Year one. These were used to generate master curve (17) to obtain creep compliance rate, and to predict thermal stresses (33, 19, 20).

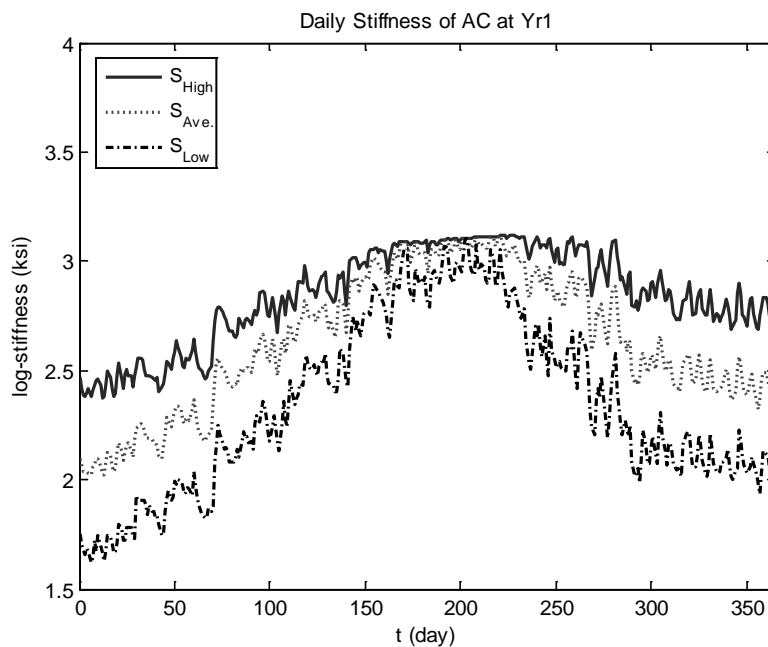


Figure 2-6. Daily AC stiffness of one pavement section in Washington D.C. area (Year one)

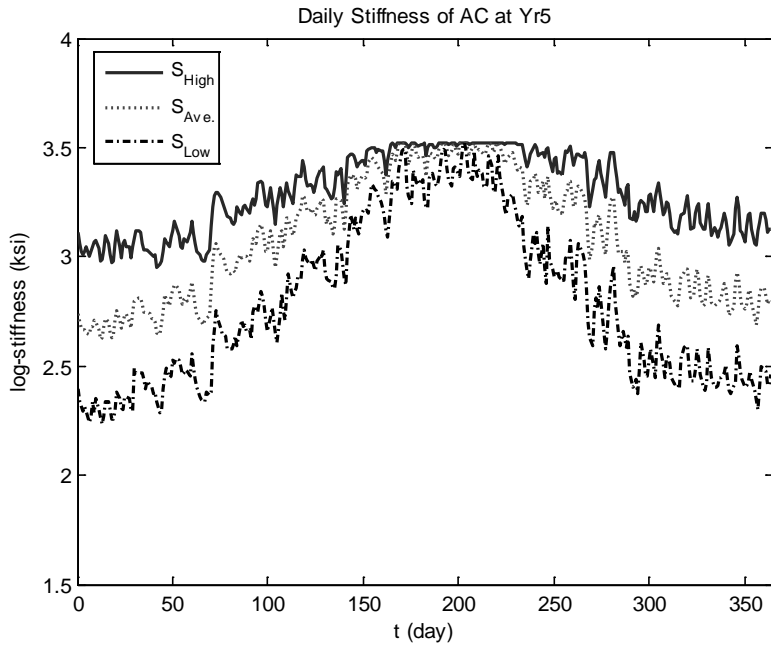


Figure 2-7. Daily AC stiffness of one pavement section in Washington D.C. area (Year five)

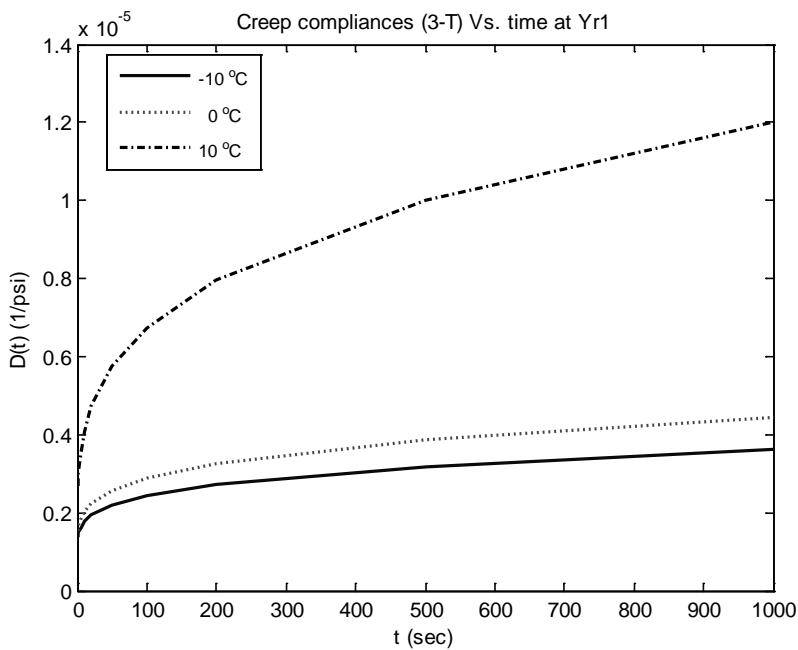


Figure 2-8. 1000 second creep compliance curves at three temperatures

B.2.1.2 AC tensile strength aging model

The AC tensile strength aging model was developed by directly relating tensile strength to the AC stiffness aging model based on the relationship developed by Deme and Young (31). As

an example, Figure 2-9 (c) shows the variation of AC tensile strength with age at the surface of the pavement section. It was obtained based on the AC stiffness aging curve determined at 10°C, as shown in Figure 2-9 (d).

B.2.1.3 FE limit (DCSE limit) aging model

It was shown by our testing results (21) that fracture energy limit (FE_f) generally decreases at a decreasing rate with age, and reaches some minimum value after sufficiently long time. So, the FE limit function was assumed to begin with an initial fracture energy (FE_i) at the starting point of Year one ($t = 0$), and end with a minimum value (FE_{min}) after a sufficiently long aging time (t_{inf}). Also, it was assumed that the normalized change of FE limit was related to the normalized change of stiffness by a power of k_1 , which are expressed as following,

$$\frac{FE_i - FE_f(t)}{FE_i - FE_{min}} = [S_n(t)]^{k_1} \quad (2-17)$$

The item on the left hand side of Equation (2-17) represents the normalized change of FE limit, in which FE_i is the initial fracture energy. FE_{min} is the minimum value after an aging period of t_{inf} . In this research, FE_{min} was determined to be 0.2 kJ/m³ based on experience from field specimens, and t_{inf} was chosen as 50 years. On the right hand side, k_1 is an aging parameter to be determined from calibration. $S_n(t)$ is the normalized change of stiffness at the surface of the AC layer, and is expressed as,

$$S_n(t) = \frac{S(t) - S_0}{S_{max} - S_0} \quad (2-18)$$

where, $S(t)$ is the stiffness at the surface of the AC layer. S_0 and S_{max} are $S(t)$ when t is 0 and 50 years, respectively. It can be seen that $S_n(t)$ is a parameter that varies between zero and one.

With a simple manipulation, the FE limit surface aging function was then obtained from Equation (2-17) as follows:

$$FE_f(t) = FE_i - (FE_i - FE_{\min}) \cdot [S_n(t)]^{k1} \quad (2-19)$$

It was also observed from testing of field cores that FE limit ($FE_f(t,z)$) generally increases with depth after a period of aging. So, at $t = 0$ when no aging is applied, $FE_f(0,z)$ (or, FE_i) was assumed to be independent of depth. Then, at any age after that (i.e., $t > 0$), the $FE_f(t,z)$ was assumed to increase with depth such that the ratio of the difference between FE_i and FE limit at depth z to the difference between FE_i and FE limit at surface ($z = 0$) was equal to the ratio of the stiffness at depth z to the stiffness at surface ($z = 0$), which are expressed as following,

$$\frac{FE_i - FE_f(t, z)}{FE_i - FE_f(t)} = \frac{S(t, z)}{S(t)} \quad (2-20)$$

where, $FE_f(t,z)$ and $S(t,z)$ are FE limit and AC stiffness at depth z , respectively. With a simple manipulation, the FE limit aging function at depth z was obtained from Equation (2-20) as follows:

$$FE_f(t, z) = FE_i - [FE_i - FE_f(t)] \cdot S(t, z) / S(t) \quad (2-21)$$

Based on the FE limit aging function, the DCSE limit aging function was developed and is expressed as follows,

$$DCSE_f(t, z) = FE_f(t, z) - [S_t(t, z)]^2 / [2 \cdot S(t, z)] \quad (2-22)$$

where, $S_t(t,z)$ is a general expression for AC tensile strength. It is noted that this equation is a generalized form of Equation (2-1), in which M_R is approximated by AC stiffness (at 10 Hz).

As an example, Figure 2-9 (a) shows the variation of FE limit with age at the surface of the pavement in the Washington D.C. area. Correspondingly, the DCSE limit aging curve is given in Figure 2-9 (b).

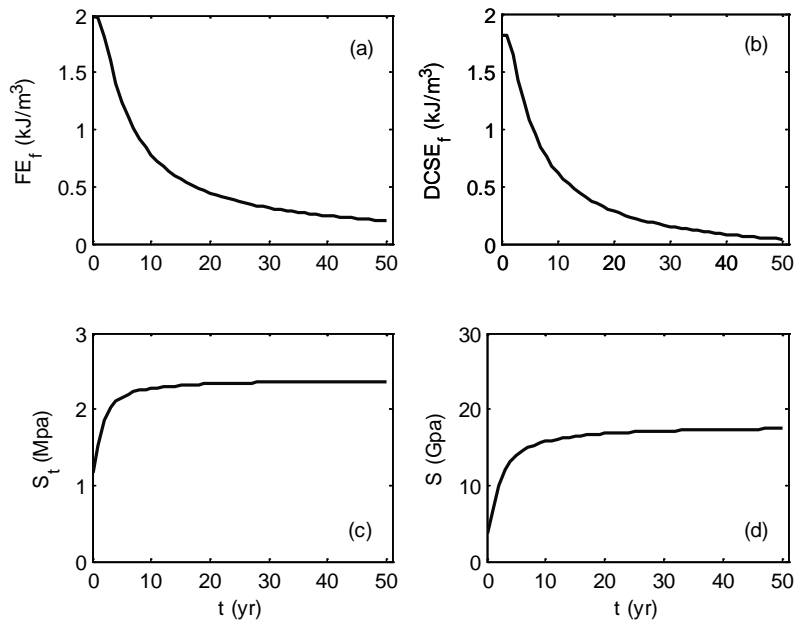


Figure 2-9. Variation of energy limits, tensile strength and stiffness with age

Clearly, the initial fracture energy FE_i and aging parameter k_1 of Equation (0-3) are key parameters that govern the trend of the FE limit aging curve. Figure 0-7 gives FE limit curves at three different values of FE_i (for a constant k_1 value of 3). As shown, generally the FE limit value decreases with time. For a larger FE_i , the entire FE limit curve moves upward (in the plot). But, the initial degradation rate of the curve also becomes larger. Figure 0-10 presents FE limit curves at three different values of k_1 for a constant FE_i value of 2. It can be seen that a larger FE limit value is associated with a larger k_1 . And, the initial degradation rate of the curve is smaller for a larger k_1 value.

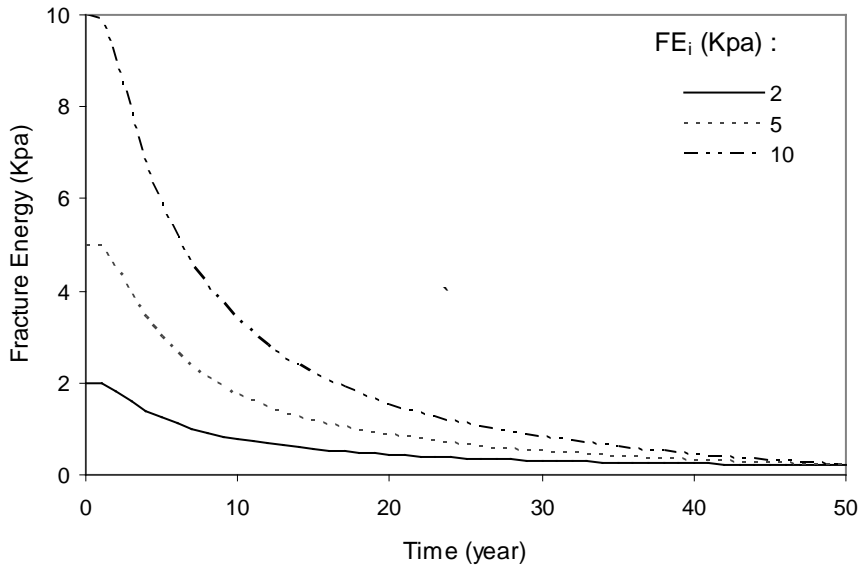


Figure 2-10. FE limit aging curves at different FE_i ($k_1 = 3$)

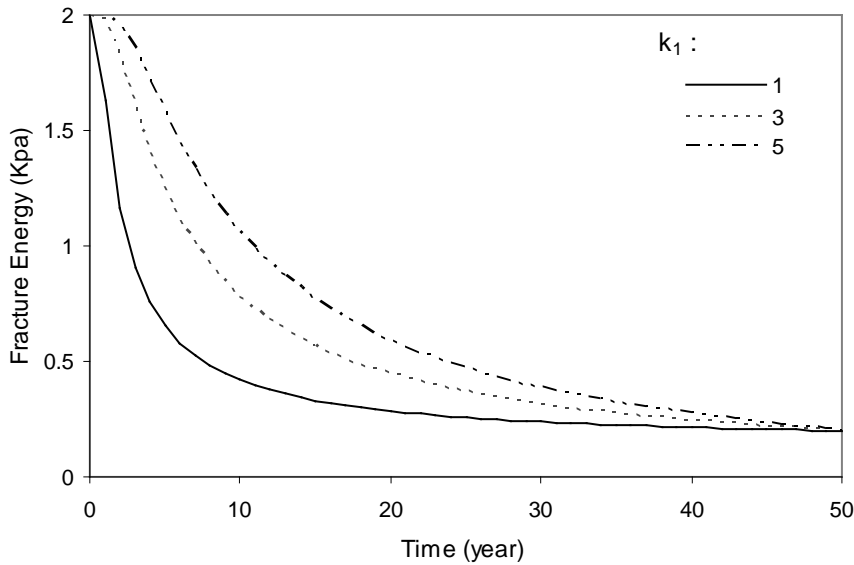


Figure 2-11. FE limit aging curves at different k_1 ($FE_i = 2$ Kpa)

B.2.1.4 Healing model

The development of a healing model for use in this research was completed in two steps. First, a mixture level healing model was obtained based on the research by Kim and Roque (32). The application of this model was illustrated using a simulated SuperPave IDT repeated load test on an HMA specimen.

As a further step, possible improvements to this model for application in real pavement sections were investigated, which resulted in the development of a simplified empirically-based healing model for use in this research.

A model based on laboratory healing tests

As stated in Section B.1 (Introduction), the normalized healing rate h_{nr} is a mixture-dependent material property, which can be determined using the laboratory healing test developed at the University of Florida (32).

If h_{nr} is known a priori, the remaining dissipated energy after healing time t can be estimated using the following equation, which was derived from Equation (2-15),

$$DCSE_{remain}(t) = DCSE_{induced} \cdot [1 - h_{nr} \cdot \ln(t)] \quad (2-23)$$

where, $DCSE_{induced}$ is the dissipated energy at the end of the loading period.

Based on Equation (2-23), a healing model was developed with the following assumptions,

- Micro-damage can only be healed during rest periods.
- For cyclic loading condition with more than one rest period, the damage induced during one loading period continuous to be healed during any successive rest period, until it vanishes.
- A constant temperature condition was assumed for this healing model since shift factors for computing normalized healing rate at different temperatures had not been established because of limited test results.
- The normalized healing rate is independent of mixture aging.

This model was then used in conjunction with the existing HMA-FM model to predict crack initiation for an HMA specimen during a simulated IDT repeated load fracture test. The input information is given in Table 2-31.

As shown in the table, a constant healing period of 300 s was introduced between every 300 loading cycles. Each of the loading cycles was composed of 0.1 s of haversine loading and 0.9 s rest period. It was assumed that no healing occurred during loading.

Table 2-31. Input for a synthetic IDT test

Parameter	Value
Loading period* (sec)	300
Healing period (sec)	300
Temperature (°C)	10
m	0.505
D1 (10^{-6} 1/Kpa)	0.101
DCSE _f (Kpa)	0.978
h_{nr} (1/ln(sec))	0.1

* It includes 300 loading cycles. Each cycle lasts 1-second.

Figure 2-12 shows the predicted DCSE versus number of load cycles for the with and without healing conditions. As shown, the damage accumulation when healing was accounted for is much slower than that without considering healing. The healing model based on Equation (2-23) was then incorporated into the existing HMA-FM model to more accurately predict cracking performance.

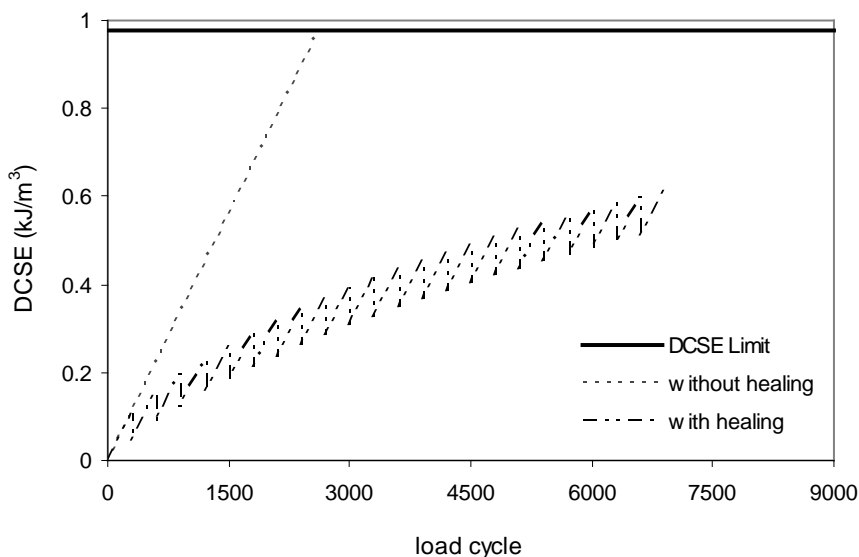


Figure 2-12. Predicted damage accumulations with and without healing

However, it is emphasized that this model may not be suitable for direct application in field conditions due to the following reasons:

- Variation of h_{nr} (i.e., healing rate) with age was not taken into account in the model.
- Similarly, variation of h_{nr} with temperature was not considered in the model.
- It is very hard to determine healing period and loading period in the field, which have varying lengths and are randomly distributed.
- Even if constant healing periods and loading periods are assumed, it is not trivial to track the decrement of damage generated in each loading period with time. In other words, the current model is somewhat computationally inefficient.

Healing model for use in this research

Since the lab test based healing model is not suitable for application in real pavements, possible improvements were investigated, which resulted in the development of an empirically-based and less computationally involved healing model, which is composed of three components:

- Maximum healing potential aging model.
- Daily-based healing criterion.
- Yearly-based healing criterion.

Each of the components is introduced as follows.

Maximum healing potential aging model

The following relationship describes the maximum healing potential surface aging model:

$$h_{ym}(t) = 1 - [S_n(t)]^{FE_i/1.67} \quad (2-24)$$

where, FE_i is the initial fracture energy, $S_n(t)$ is the normalized change of stiffness at the surface of the AC layer, and t is time in years. The maximum healing potential versus depth relation is:

$$h_{ym}(t, z) = 1 - [1 - h_{ym}(t)] \cdot \frac{S(t, z)}{S(t)} \quad (2-25)$$

where, $S(t,z)$ is the general expression for AC stiffness, and $S(t)$ is the stiffness at surface of AC layer.

As shown in Eqn (0-7), the maximum healing potential h_{ym} was controlled by the initial fracture energy. As an example, Figure 0-8 gives maximum healing potential surface aging curves for three different values of FE_i . As shown, a higher h_{ym} is generally associated with a larger FE_i . And, the initial degradation rate of h_{ym} decreases with the increase of FE_i value.

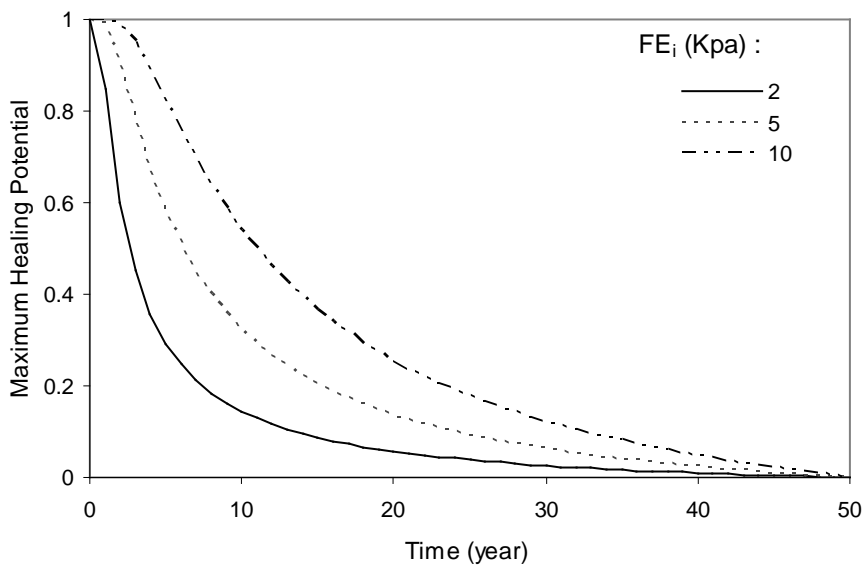


Figure 2-13. Max. healing potential surface aging curves at different FE_i

Daily-based healing criterion

A daily-based healing criterion was developed to estimate the recovered damage on any particular day. It was assumed that the damage generated in a day would be healed according to a daily normalized healing parameter h_{dn} which is defined as,

$$h_{dn} = 1 - \frac{DCSE_{d_remain}}{DCSE_{d_induced}} \quad (2-26)$$

where, $DCSE_{d_induced}$ is the dissipated energy induced during the day, and $DCSE_{d_remain}$ is the dissipated energy remaining at the end of the day after healing, which can be obtained by rearranging Eqn (0-9) as follows,

$$DCSE_{d_remain} = DCSE_{d_induced} \cdot (1 - h_{dn}) \quad (2-27)$$

The daily normalized healing parameter is dependent on depth, time, and temperature. In this study, h_{dn} was correlated with the daily lowest stiffness S_{low} of the AC layer. The rationale is that healing potential is believed to be closely related to the AC material's capacity to flow. Since S_{low} is the lowest stiffness of a day, it represents the highest flow capacity of the material on that day, which was used to estimate the material's healing potential.

The daily lowest stiffness can be determined using the daily highest temperature at any depth of the AC layer (refer to AC stiffness aging model). As an example, Figure 2-14 gives the variation of daily highest temperature at the surface of the pavement in the Washington D.C. area.

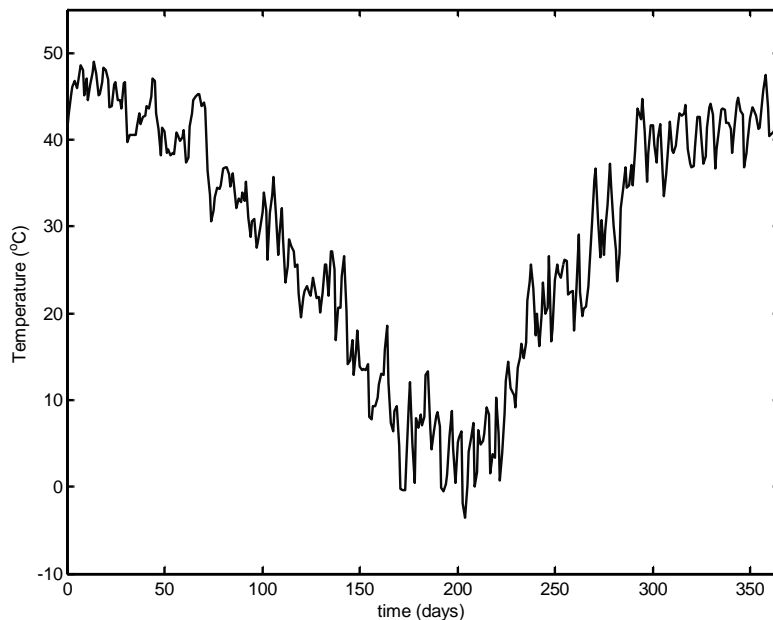


Figure 2-14. Variation of daily highest temperature

The corresponding daily lowest stiffness S_{low} for five successive years (each year was started from July 1st), after taking the effects of aging into account, are plotted in Figure 2-15. In addition, two critical stiffness values S_{cr1} and S_{cr2} are also shown in the figure, which divide the S_{low} profile into three zones,

- S_{cr1} is the Lower Bound Value. It was assumed that the daily normalized healing parameter h_{dn} reached the maximum value of a year, i.e., h_{ym} representing the highest healing potential of the mixture for that year, when: $S_{low} \leq S_{cr1}$ (i.e., when S_{low} falls into Zone A). h_{ym} was determined using the maximum healing potential aging model.
- S_{cr2} is the Upper Bound Value. It was assumed that h_{dn} reached the minimum value of a year, i.e., zero representing the lowest healing potential of the mixture, when: $S_{low} \geq S_{cr2}$ (i.e., when S_{low} falls into Zone C).
- For any S_{low} value that is between S_{cr1} and S_{cr2} (i.e., when S_{low} is in Zone B), h_{dn} can be determined by linear interpolation between zero and h_{ym} , representing intermediate healing potentials.
- Determination of S_{cr1} and S_{cr2} is discussed in Subsection B.3.1.

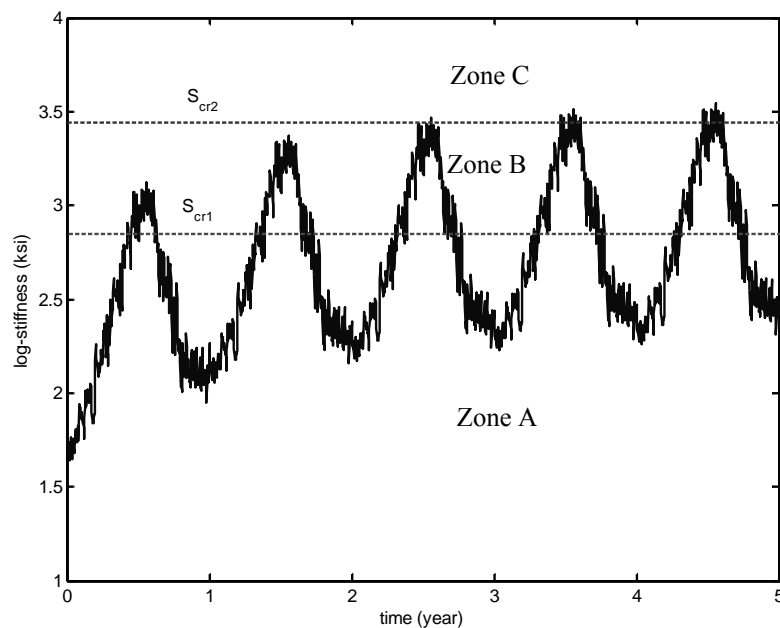


Figure 2-15. Daily lowest AC stiffness (S_{low}) profile and two critical values (S_{cr1} & S_{cr2})

Yearly-based healing criterion

In the daily-based healing criterion, the damage generated in any particular day will be healed only once during that day, after which no healing will be applied to remaining damage. This does not agree well with the observation from laboratory healing tests (32) which indicated that damage can be healed successively during any rest period that follows. Thus, a yearly-based healing criterion was developed to address continuous healing.

In this healing criterion, it was assumed that all damage accumulated during a yearly period (started from July 1st) can be at least partially healed according to a yearly normalized healing parameter h_{yn} which is defined as,

$$h_{yn} = 1 - \frac{DCSE_{y_remain}}{DCSE_{y_induced}} \quad (2-28)$$

where, $DCSE_{y_induced}$ is the dissipated energy induced during the year, and $DCSE_{y_remain}$ is the dissipated energy remaining at the end of the year after healing, which can be obtained by rearranging Eqn (0-11) as follows,

$$DCSE_{y_remain} = DCSE_{y_induced} \cdot (1 - h_{yn}) \quad (2-29)$$

The yearly normalized healing parameter h_{yn} was determined based on an averaged daily lowest stiffness S_{lowa} over a prolonged period T_p (i.e., the last 40 days of the yearly period being analyzed).

B.2.2 Pavement Response Model

The pavement response model is composed of two sub-models: load response model and thermal response model. Details of each are explained below.

B.2.2.1 Load response model

The load response model was primarily aimed to predict bending-induced maximum surface tensile stresses, since the bending mechanism was the main focus of the HMA-FM-based

model. A 9-kip circular load was applied repeatedly to the surface of a pavement to simulate the cyclic traffic load. Each cycle included 0.1 s haversine loading period and 0.9 s resting period. The model first estimated the AC modulus (see Section B.2.1) based on the temperature profiles and aging conditions. The stiffness gradient due to the temperature and aging effects was taken into account by dividing the AC layer into multiple sub-layers with different stiffnesses. The bending-induced tensile stresses at the pavement surface were then predicted using 3-dimensional (3-D) linear elastic analyses (LEA). The model also automatically searched for the maximum tensile stress on the surface of the AC layer. Figure 2-16 shows the bending-induced surface tensile stress away from the tire.

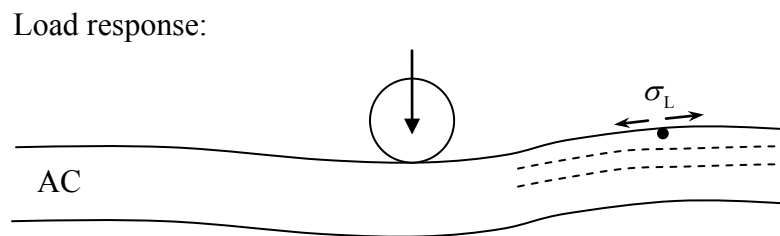


Figure 2-16. Schematic plot for load response at the surface of the AC layer

B.2.2.2 Thermal response model

The thermal response model predicts the thermally induced stresses in the transverse direction of asphalt concrete pavement. It was developed based on a thermal stress model for predicting thermal cracking (33).

The existing thermal stress model was developed on the basis of the theory of linear viscoelasticity. In this model, the asphalt layer was modeled as a thermorheologically simple material. Based upon Boltzmann superposition principle for linear viscoelastic materials, the time-temperature constitutive equation at time t can be expressed as follows,

$$\sigma(t) = \int_0^t E(\xi(t) - \xi(t')) \cdot \frac{d\varepsilon(t')}{dt'} dt' \quad (2-30)$$

where $E(\xi - \xi')$ is the relaxation modulus at reduced time $\xi - \xi'$; and the reduced time ξ is:

$$\xi = t / a_T$$

where a_T is the temperature shift factor. The strain $\varepsilon(t')$ can be expressed as

$$\varepsilon(t') = \alpha [T(t') - T_0]$$

where α is the linear coefficient of thermal contraction, $T(t')$ and T_0 are pavement temperature at time t' and the reference temperature corresponding to stress-free condition.

The following finite difference solution to Equation (2-30) can be obtained by using the generalized Maxwell model representation of the relaxation modulus (Equation (2-32)) which was converted from the Prony series representation for creep compliance (Equation (2-33)),

$$\sigma(t) = \sum_{i=1}^{N+1} \sigma_i(t) \quad (2-31)$$

where

$$\sigma_i(t) = e^{-\Delta\xi/\lambda_i} \sigma_i(t - \Delta t) + \Delta\varepsilon E_i \frac{\lambda_i}{\Delta\xi} (1 - e^{-\Delta\xi/\lambda_i})$$

and $\Delta\varepsilon$, $\Delta\xi$ are the changes in strain and reduced time, respectively.

$$E(t) = E_1 \exp\left(-\frac{t}{\lambda_1}\right) + E_2 \exp\left(-\frac{t}{\lambda_2}\right) + \dots + E_{N+1} \exp\left(-\frac{t}{\lambda_{N+1}}\right) = \sum_{i=1}^{N+1} E_i \exp\left(-\frac{t}{\lambda_i}\right) \quad (2-32)$$

$$D(\xi) = D_0 + \sum_{i=1}^N D_i (1 - e^{-\xi/\tau_i}) + \frac{\xi}{\eta_v} \quad (2-33)$$

where E_i and λ_i are relaxation moduli and relaxation times. D_i , τ_i , η_v are Prony series parameters.

The existing model was intended to predict thermal stresses in the longitudinal direction. However, top-down cracking is known to occur in the longitudinal direction, so transverse, as opposed to longitudinal, thermal stresses are of particular relevance. The difference in transverse

and longitudinal thermal stresses was caused by different boundary conditions to which the AC layer is subjected in these two directions:

- The AC layer is subjected to a fixed boundary condition in the longitudinal direction, which can induce very high longitudinal thermal stresses, which are the main cause of thermal cracking.
- However, the AC layer can move in the transverse direction once the maximum friction provided by the base is reached.

Therefore, the transverse thermal stress, which contributes to top-down cracking, cannot exceed the friction limit. The limit value was determined to be 10 psi for typical HMA and base materials based on a separate calculation. Figure 2-17 shows the transverse thermal stresses due to change of temperature in an AC layer.

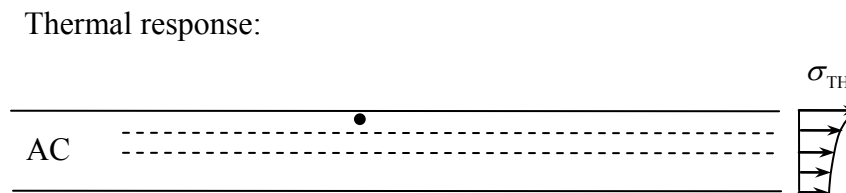


Figure 2-17. Schematic plot for thermal response in the AC layer

B.2.3 Pavement Fracture Model

The pavement fracture model consists of three sub-models: (i) crack initiation model, (ii) crack growth model, and (iii) crack amount model.

B.2.3.1 Crack initiation model

The crack initiation model was developed on the basis of the threshold concept of the existing HMA fracture model. It was used to predict the crack initiation time and location in asphalt pavement sections, in conjunction with the material property model and pavement response model. Details regarding the joint use of all mentioned models were presented in Section 4.1.6 (Main Body).

In the crack initiation model, the load-associated damage and thermal-associated damage is obtained based on the pavement response models as follows,

- The load-associated damage per cycle (or, $DCSE_L/cycle$) is calculated as:

$$DCSE_L / cycle = \int_0^{0.1} \sigma_{AVE} \sin(10\pi t) \dot{\varepsilon}_{pmax} \sin(10\pi t) dt \quad (2-34)$$

where σ_{AVE} is the average stress within the zone being analyzed to determine crack initiation, and $\dot{\varepsilon}_{pmax}$ is the creep strain rate, which is determined from IDT creep tests at 1000 second loading time.

- The thermal-associated damage over the time interval from $(t - \Delta t)$ to t (or, $DCSE_T/\Delta t$) is expressed as:

$$DCSE_T / \Delta t = [\sigma(t) - \sigma(t - \Delta t)] \cdot [\varepsilon_{cr}(t) - \varepsilon_{cr}(t - \Delta t)] / 2 \quad (2-35)$$

where ε_{cr} is creep strain at time t . It can be expressed as:

$$\varepsilon_{cr}(t) = \varepsilon_{cr}(t - \Delta t) + \frac{1}{2 \cdot \eta_v} [\xi(t) - \xi(t - \Delta t)] \cdot [\sigma(t) + \sigma(t - \Delta t)]$$

In the crack initiation model, the rule for crack initiation is given as follows,

$$DCSE_{norm}(t) = \frac{DCSE_{remain}(t)}{DCSE_f(t)} \geq 1.0 \quad (2-36)$$

where, $DCSE_{remain}$ is the accumulated dissipated energy when taking healing into account, $DCSE_f$ is the DCSE limit accounting for its degradation with aging, and $DCSE_{norm}$ is the normalized damage accumulation. The threshold for crack initiation is 1.0. The $DCSE_{remain}$ during each time interval Δt can be further expressed as follows,

$$DCSE_{remain}(\Delta t) = (1 - h_{dn}) \cdot [n \cdot (DCSE_L / cycle) + DCSE_T(\Delta t)] \quad (2-37)$$

where n is number of load cycles in Δt .

B.2.3.2 Crack growth model

The crack growth model was developed on the basis of a two-dimensional (2-D) displacement discontinuity boundary element (DDBE) program (34) and the threshold concept of the existing HMA fracture mechanics model. It was used in conjunction with the material property model and thermal response model to predict increase of crack depth with time in asphalt concrete pavement. Details regarding the joint use of all models were presented in Section 4.1.6 (Main Body).

In the crack growth model, load induced tensile stresses ahead of the crack tip were predicted using the DDBE model as follows:

- The pavement structure was discretized using quadratic displacement discontinuity (DD) boundary elements.
- An initial crack was assumed to have a length of 6 mm (0.25 inch), which is about one half of the nominal maximum aggregate size of typical asphalt mixtures. It was placed vertically at the location of the maximum surface tensile stress and discretized using DD boundary elements.
- The load used for the 2-D model was adjusted so that the maximum tensile stress at surface of the pavement predicted by the 2-D model can be matched with the prediction by the 3-D LEA program. A similar strategy was used by Myers et al. (23) to account for 3-D effects on stress distribution by adjusting load applied to a 2-D pavement model.

Meanwhile, the near-tip thermal stresses were estimated by applying the stress intensity factor (SIF) of an edge crack to the thermal stresses predicted using the thermal response model.

The load associated damage and thermal associated damage were then calculated in a same manner as introduced in the crack initiation model. The same rule as used for determination of crack initiation was adopted in the crack growth model. Once the rule was satisfied (i.e., the $DCSE_{norm}$ reached 1.0), the crack started to grow. Some key terms used during simulation of step-wise crack growth are explained below:

- Potential crack path: The potential crack path was predefined in front of the crack tip at the beginning of crack growth simulation. It was composed of a series of zones of constant length heading toward the bottom of the AC layer.
- Zone (in the potential crack path): The zone is a means used to discretize the potential crack path to facilitate the calculation of crack growth. A constant zone length was used because it is far more computationally efficient than using variable zone lengths, with relatively little effect on the crack growth prediction. It was measured from lab testing that cracking develops in a stepwise manner in asphalt mixtures. For typical asphalt mixtures with a nominal maximum aggregate size (NMAS) of 12.5 mm, the stepwise developed crack length is about one half of the NMAS, which is about 6 mm. So, 6 mm (0.25 inch) was selected as the constant zone length.
- Critical crack depth (CD_c): The critical crack depth is the final crack depth in the crack growth model, which was preset to be one-half the depth of the AC layer, as field observations showed that top-down cracking generally does not exceed that depth.

B.2.3.3 Crack amount model

The crack amount model was developed based on the following assumptions:

- For a 100 feet long pavement section, the maximum crack amount was assumed to be 330 feet. In other words, the pavement was determined to be severely cracked if total crack amount exceeded 330 feet.
- The crack amount, between zero and the specified maximum value, was assumed to be linearly proportional to the crack depth over AC layer thickness ratio (C/D), which ranges from zero to 0.5 (i.e., when crack depth is equal to CD_c). The rationale is that generally, as a crack gets deeper, the crack mouth opening gets wider. Also, for a crack of the same depth (i.e., same C), the crack mouth opening is wider in a thinner layer than in a thicker layer. Therefore, it seems logical to assume that the probability that a crack is visible and counted as a crack (and therefore the probability of increase in crack amount) increases as the C/D ratio increases. The assumption that the relationship is linear is a first order approximation.
- In accordance with the definition for crack initiation in terms of the crack depth (refer to crack initiation model), the onset of a crack in terms of the crack amount was assumed to be triggered by observing an amount of cracking of at least 12 feet.

Based on the above assumptions, the crack amount versus time relationship can be obtained from the crack depth versus time relation predicted by the crack growth model. Using this model, the predicted amount of cracking at initiation is greater than 12 feet for any pavement that has an HMA layer thickness of no larger than 12 inch.

B.3 Integration of Model Components

B.3.1 Integration of Healing Model

The material healing model was integrated into the performance model by determining the two critical values for daily lowest AC stiffness on the basis of a full-scale test conducted in the FDOT's APT facility using the HVS.

B.3.1.1 Background of experiments for evaluating healing effect

Since Accelerated Pavement Testing (APT) offers great potential for evaluation of performance of asphalt mixture and pavement in relatively short periods of time, the Florida Department of Transportation (FDOT) has built an APT facility in Gainesville, Florida. The system includes a fully mobile Heavy Vehicle Simulator (HVS), and eight linear tracks (150 ft long by 12 ft wide). Figure 2-18 shows one typical test section subjected to HVS loading in FDOT's APT facility.



Figure 2-18. A typical HVS test section

The University of Florida (UF) has been working on a research project with FDOT to assess cracking potential of asphalt mixture (21). In an effort to simulate aging of in-service pavement, a unit called the Accelerated Pavement Aging System (APAS) was developed and used to induce artificial aging of asphalt pavement test sections in the APT facility. One lane

(testing track 1) composed of a dense-graded mixture on limestone base and sand subgrade was divided into three test sections: 1A, 1B, and 1C. Each section was subjected to different levels of aging and HVS loading. Sections 1B and 1C were tested first to assess the capability of the APAS system and to determine whether top-down cracking could be induced within a reasonable period of time. It was found that these two sections, which were subjected to extensive loading with moderate aging, could not be cracked even after many heavy loads were applied. In addition to the excellent properties of the mixture and structure, healing was thought to be playing a major role.

Therefore, an experiment was devised to severely age one part of section 1A so as to minimize healing potential. This severely aged part and a companion unaged part were subjected to the same loading conditions (load and temperature) to more definitively evaluate the effects of healing.

The paired portions of section 1A, which were simply called the aged and unaged sections for brevity, were subjected to 18-kip HVS loads to maximize the potential for cracking within a reasonable period of time. Loading on both sections started on February 06, 2007. During February 16 to 19, transverse surface cracks were found in the aged section after around 140,000 passes (see Figure 2-19). Loading was continued until March 27, 2007 with around 488,358 passes, when cracks in the aged section were believed to have approached about half-depth of the AC layer (this was later verified by coring the cracked AC layer). No crack was observed in the unaged section for the entire loading period.

B.3.1.2 Material and structural properties

PG 67-22 binder was used in this study. Figure 2-20 shows binder recovery and viscosity measurements performed on cores obtained from the aged section at 0, 1, and 20 heating cycles of artificial aging. The binder viscosity of the unaged section corresponds to zero heating cycle

(i.e., only slightly aged). As can be seen, the aging level induced in the top of the aged section after 20 healing cycles was extremely high, the viscosity at which was much greater than any value determined from field cores in typical Florida pavement. Figure 2-20 also shows that the APAS was able to effectively create a stiffness gradient through the asphalt layer.



Figure 2-19. Cracks observed in the aged section

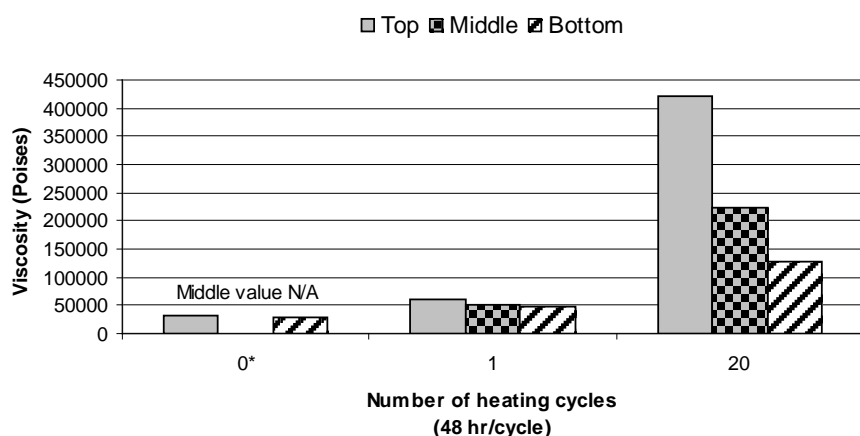


Figure 2-20. Recovered viscosity at different levels of aging

Table 2-32 summarizes the Superpave Indirect Tension Test (IDT) results on cores from the paired sections. The same asphalt mixture with Georgia granite aggregate and 4.6% binder content was used for both sections.

Table 2-32. IDT test results (at 10°C)

APAS		m-value	D ₁	Creep compliance at 1000 sec	Creep rate 1/GPa	FE	DCSE HMA	ER
Unaged	Top	0.491	4.90E-07	2.15	7.13E-09	2.7	2.4	1.88
	Bottom	0.537	5.43E-07	3.27	1.19E-08	2.4	2.2	1.22
Aged	Top	0.355	1.40E-07	0.29	5.74E-10	1.0	0.8	5.68
	Bottom	0.377	4.16E-07	0.88	2.12E-09	1.1	1.0	2.03

The pavement structural and material properties for each layer of the aged section are given in Table 2-33. As shown, the AC layer was further divided into three sub-layers accounting for stiffness gradients due to aging and temperature. Table 2-34 shows creep compliance readings measured at 0, 10, and 20°C during 1000 second Superpave IDT creep tests. They were used to generate master curves for use in modeling viscoelastic material behavior.

Table 2-33. Pavement structure and material properties in the aged section

	E (psi)		H (in)
AC-Top	2.40E+06	0.35	1.5
AC-Mid	1.20E+06	0.35	1.5
AC-Bot	6.00E+05	0.35	3
Base	4.00E+04	0.35	10.5
Subgrade	3.10E+04	0.4	Inf.

Table 2-34. Creep compliance values for aged samples at 0, 10, and 20°C

TIME (SEC)	TOP			BOTTOM		
	0°C	10°C	20°C	0°C	10°C	20°C
1	0.054	0.069	0.129	0.076	0.126	0.248
2	0.059	0.075	0.152	0.076	0.145	0.296
5	0.057	0.084	0.169	0.096	0.171	0.379
10	0.059	0.096	0.196	0.098	0.198	0.443
20	0.065	0.114	0.262	0.111	0.257	0.503
50	0.085	0.126	0.328	0.127	0.296	0.828
100	0.092	0.148	0.425	0.136	0.378	1.154
200	0.095	0.176	0.597	0.146	0.471	1.607
500	0.109	0.238	0.873	0.162	0.669	2.484
1000	0.110	0.282	1.168	0.160	0.884	3.443

B.3.1.3 Model predictions without healing

Stage one: crack initiation

When healing effect was not considered, the predicted load passes to induce crack initiation for the aged and unaged sections are given in Figure 2-21. As seen in the figure, predicted number of loads to cracking for the unaged section was only about 41,700, which was much less than the 128,300 loads for the aged section. The predictions in Figure 2-22 in terms of $DCSE_{norm}$ versus time showed the same trend: the unaged section required less time for crack initiation than the aged one.

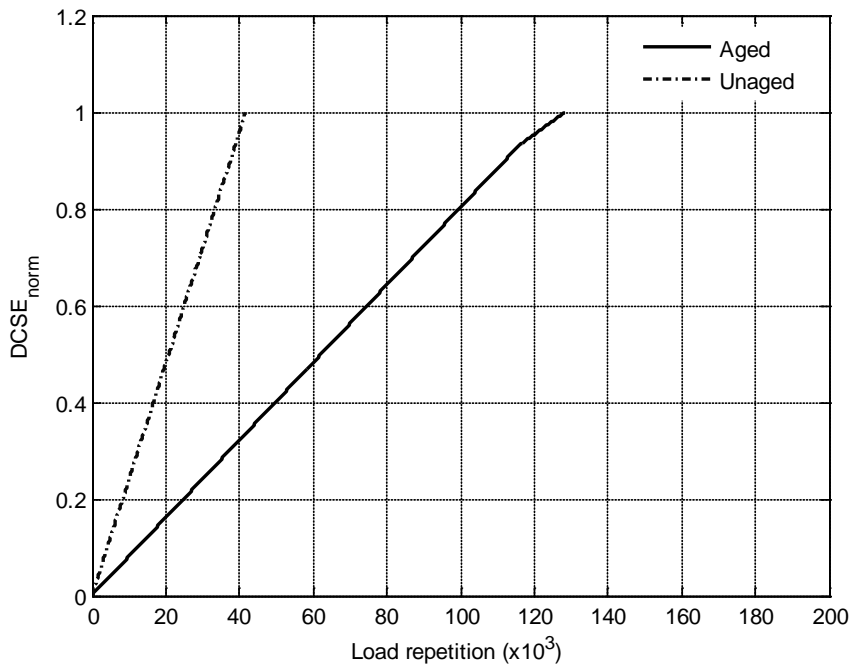


Figure 2-21. Prediction of crack initiation w/o healing: damage versus load repetition

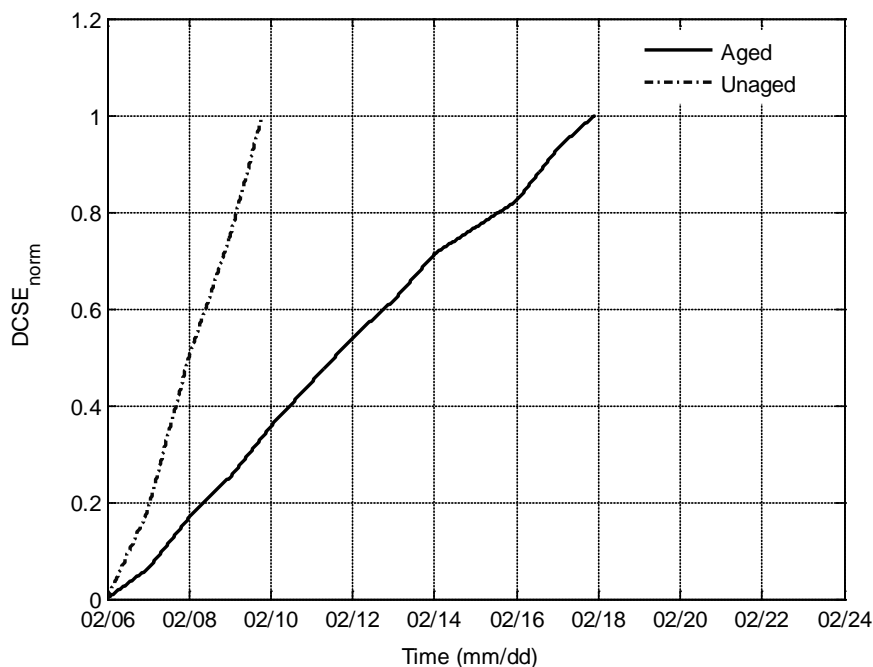


Figure 2-22. Prediction of crack initiation w/o healing: damage versus time

Stage two: crack propagation

Figure 2-23 shows the step-wise increase of crack depth with load passes for both the aged and unaged sections. In general, the crack propagates at a relatively low rate initially (e.g., for the first zone). The rate of growth then increases for the next few zones, beyond which the rate slows down again. As also shown in Figure 2-23, the load repetition to the critical crack depth (i.e., 3 inch for these two sections) is about 129,200 for the unaged section. Meanwhile, the load to 3 inch depth of the aged section is about 295,900, which was much more than that for the aged section. Similar trends can be found from Figure 2-24, which shows crack growth as a function of time. Given the time to crack initiation obtained in stage I, an average crack growth rate in the unaged section can be estimated to be 0.34 in/day, which is more than 1.5 times of the value, i.e., 0.20 in/day obtained for the aged section.

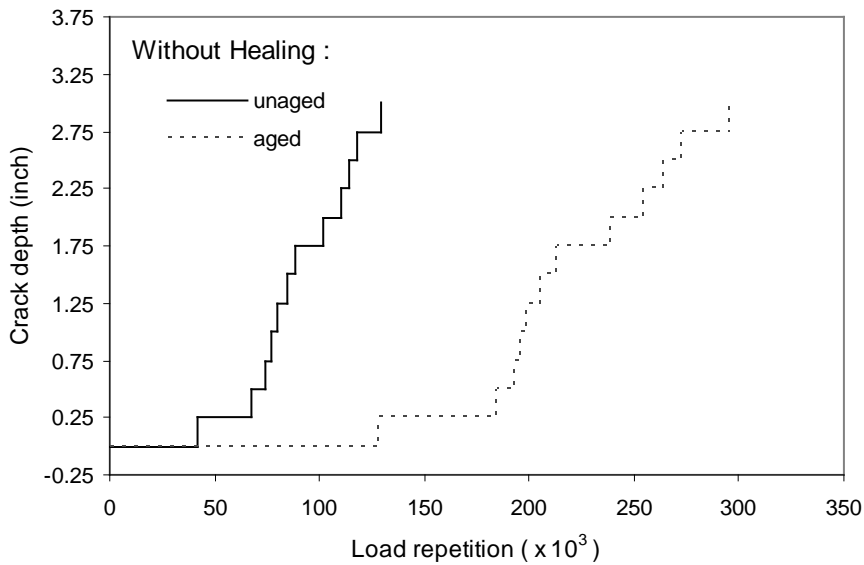


Figure 2-23. Prediction of crack growth w/o healing: crack depth versus load repetition

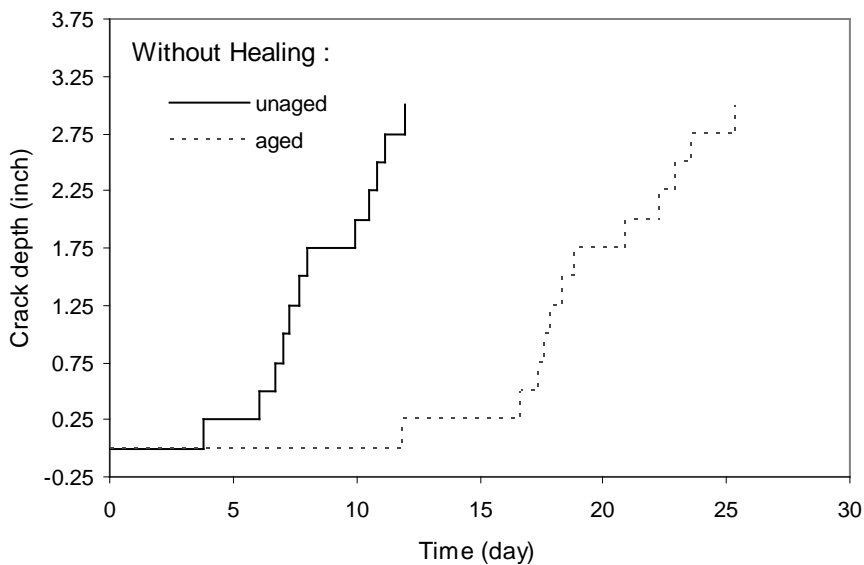


Figure 2-24. Prediction of crack growth w/o healing: crack depth versus time

It is clear that the predicted results in terms of both crack initiation and propagation in the unaged section do not make sense, since as mentioned before, no crack was observed in that section during the entire loading period. Therefore, a mixture healing model must be included in the top-down cracking performance model. However, the two critical values S_{cr1} and S_{cr2} of the healing model have to be estimated before it can be used.

B.3.1.4 Determination of critical values for daily lowest AC stiffness

In order to determine these two critical values S_{cr1} and S_{cr2} , the daily lowest AC stiffness curves in the aged and unaged sections are plotted in Figures 2-25 and 2-26, respectively. As shown, the stiffnesses of the aged section are much higher than the unaged section.

Since the asphalt mixture at surface of the aged section was extensively aged, as indicated by the measured binder viscosity which was much greater than any value determined from field cores in typical Florida pavement, it was believed that no healing would occur in the mixture of this section. According to the definitions of healing zones (see Section B.2.1), the S_{low} values for this section should be close to S_{cr2} . Therefore, the value for S_{cr2} was selected to be 2,000 ksi (see Figure 2-25).

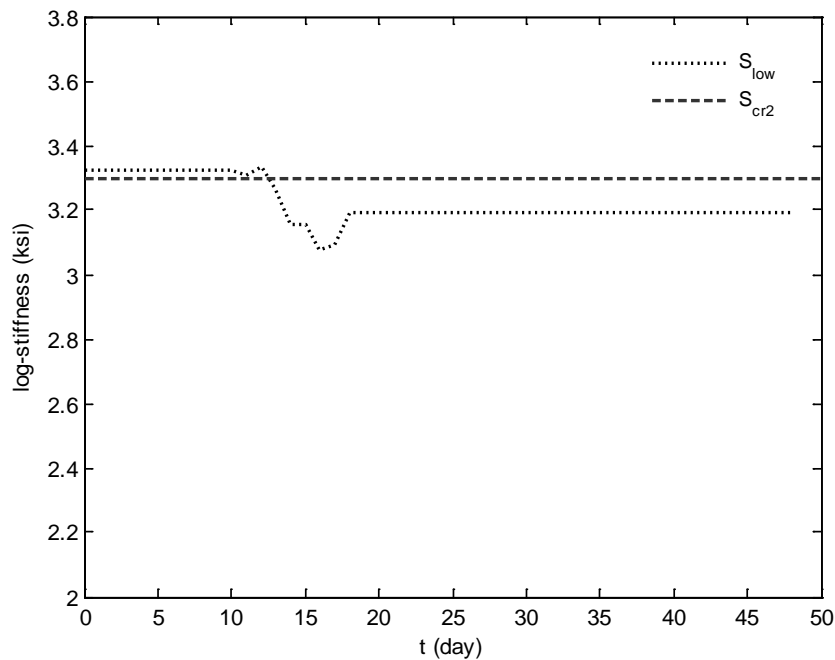


Figure 2-25. Daily AC stiffness of the aged section

On the other hand, mixture in the unaged section was only slightly aged, as shown by viscosity test results. The mixture was thus believed to have full healing potential. According to

the definitions of healing zones, the S_{low} values for this section should be close to S_{cr1} . As a result, S_{cr1} was selected to be 320 ksi (see Figure 2-26).

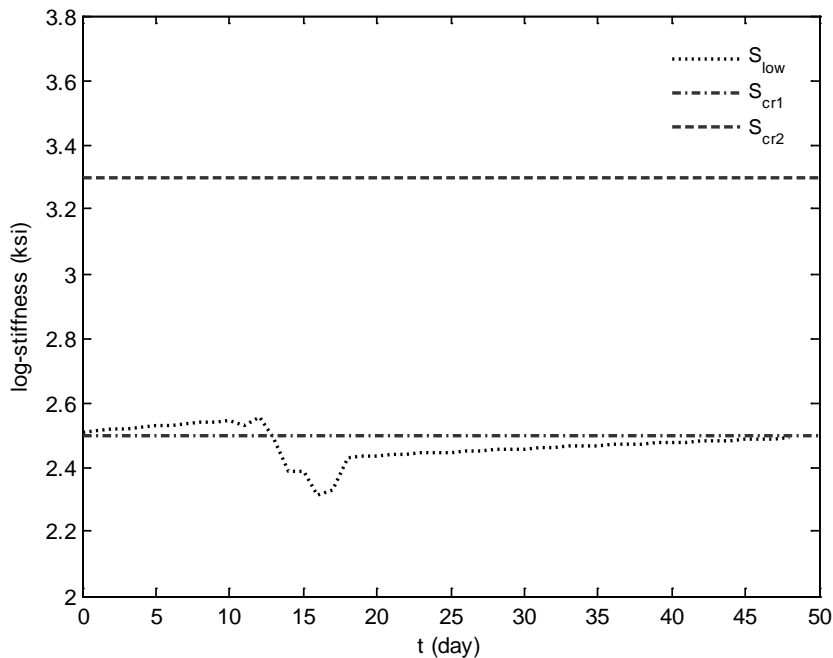


Figure 2-26. Daily AC stiffness of the unaged section

B.3.1.5 Model predictions with healing

Another set of predictions was made using the performance model after incorporating the healing model.

Stage one: crack initiation

The predicted damage in terms of $DCSE_{norm}$ versus load passes for the paired sections are given in Figure 2-27. The figure clearly shows that no crack occurred in the unaged section, which is consistent with the observation in the full-scale HVS test. On the other hand, the predicted load passes to crack initiation for the aged section remained at 128,300. The similar prediction for the aged section using performance models with and without the healing model is expected, since the aged section had no healing potential due to extensive aging applied in the test. The predicted load passes of 128,300 were also found to be close to the actual number of

passes of 140,000 when the first crack was observed. The predictions in Figure 2-28 show the same trend: crack occurred in the aged section after about 12 days, and no crack occurred in the unaged section.

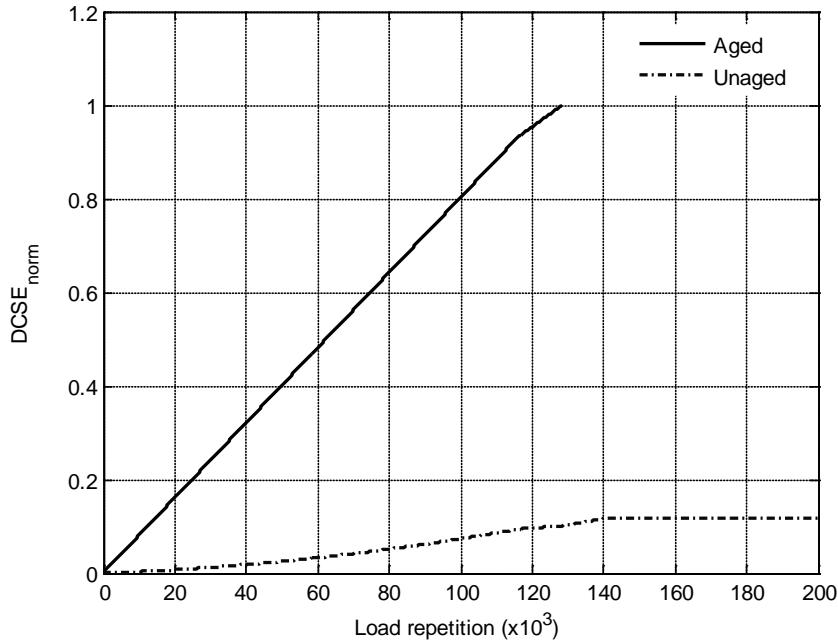


Figure 2-27. Prediction of crack initiation with healing: damage versus load repetition

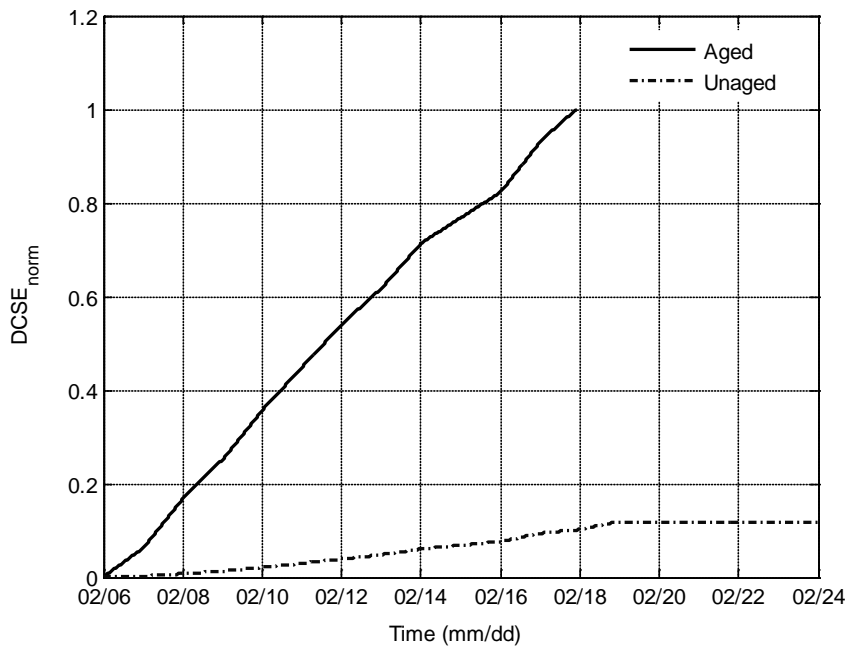


Figure 2-28. Prediction of crack initiation with healing: damage versus time

Stage two: crack propagation

Performance predictions accounting for healing were continued in the crack propagation stage. As shown in Figure 2-29, the crack in the aged section reached the critical crack depth after 296,600 passes of HVS loading. As expected, the number of load passes was slightly greater than the one predicted by the model without healing, since the healing potential, which increases with depth helped to prolong fatigue life. Figure 2-30 shows predicted crack growth in terms of crack depth versus time in the aged section, which follows a similar pattern as that of Figure 2-29. It took another 14 days for the crack to reach the critical crack depth.

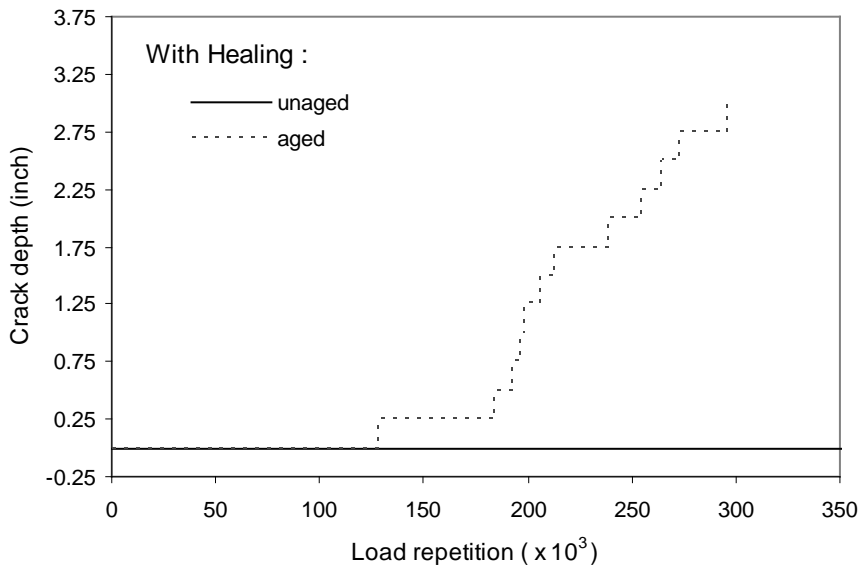


Figure 2-29. Prediction of crack growth with healing: crack depth versus load pass

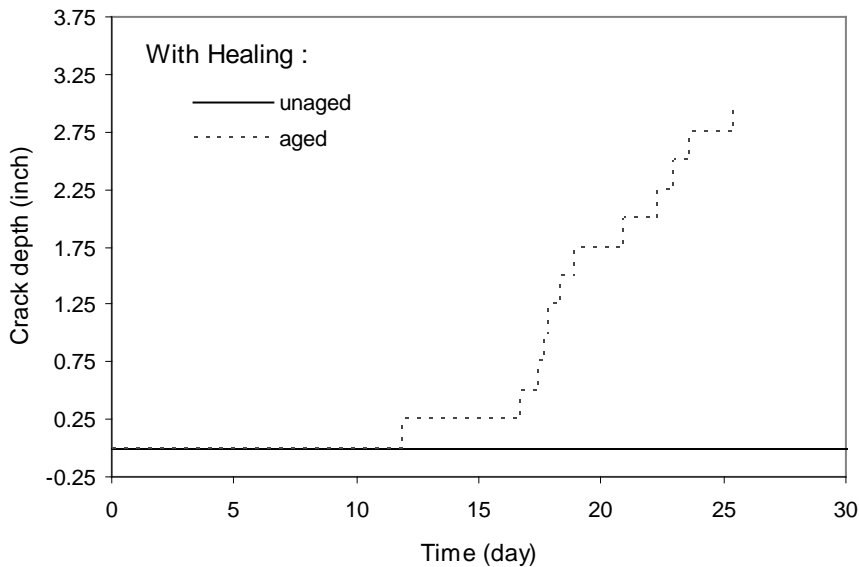


Figure 2-30. Prediction of crack growth with healing: crack depth versus time

In summary, the predictions after incorporation of the healing model seemed quite reasonable, as they agreed well with observations from cores, which indicated that the crack had propagated to about half-depth of the AC layer of the aged section.

B.3.2 Integration of Thermal Response Model

Integration of the thermal response model was completed by simply activating this model in the CCI module. The significance of the thermal response model was illustrated by predicting cracking performance of one pavement section in the Washington D. C. area with and without thermally induced damage accounted for in the performance model.

B.3.2.1 Selection of climatic environment

Since the thermal response model was fully developed, the key for successful integration of this model was to show that the performance model cannot predict cracking performance accurately without accounting for thermal effects. In other words, it was necessary to demonstrate the need to include the thermal response model.

A limited investigation indicated that thermal damage induced in pavement sections subjected to a non-freeze climate as that of Florida was not high enough to alter the predicted top-down cracking performance of these sections. Therefore, a freeze-thaw climate as that of Washington, D.C., was selected to demonstrate the importance of including the thermal response model. The corresponding temperature data file was used as input for model prediction, containing hourly temperatures at different depths of the AC layer. The temperature data was generated based on the climatic condition and typical pavement material and structural properties using the enhanced integrated climatic model (EICM). Other types of climatic environment such as the hard-freeze climate of North Dakota were evaluated in Section 4.2 (Main Body).

B.3.2.2 Material and structural properties

The geometry and material properties for the pavement section are illustrated in Figure 2-31. To account for the effects of stiffness gradient due to temperature and aging, the AC layer was divided into 3 sub-layers with thickness h_1 , h_2 , and h_3 , respectively. Since the temperature and aging gradients are greatest near the surface and reduce with depth, the thickness values of the AC sub-layers were taken as $h_1 = h_2 = H_1/4$ and $h_3 = H_1/2$.

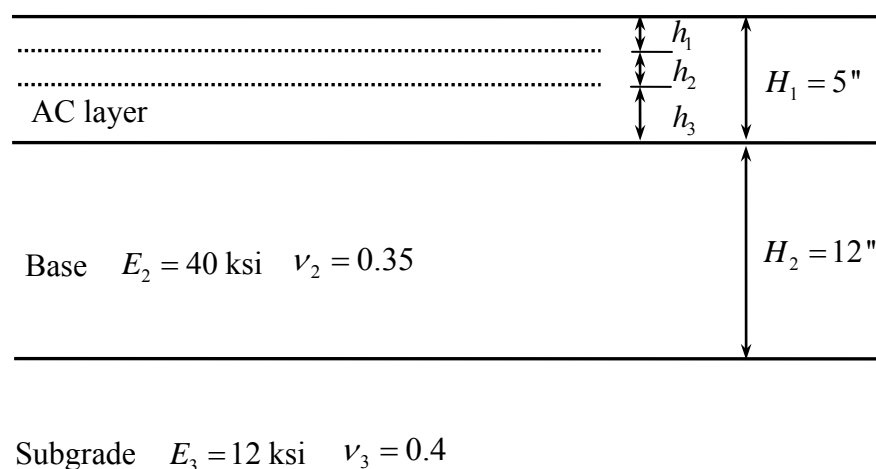


Figure 2-31. Geometry and material properties of a 3-layer pavement structure

The variation of asphalt concrete (AC) modulus with time was estimated using the AC stiffness (creep compliance) aging model. Meanwhile, the degradation of AC fracture properties and healing potential with time were predicted using the FE limit (DCSE limit) aging model and the healing model, respectively. The input information for these material property models is listed in Table 0-3.

Table 2-35. Data for material property aging models

Parameter	Value
Aggregate % passing by weight (seive size)	100.0 (3/4 in.), 90.0 (3/8 in.), 60.2 (# 4), 4.8 (# 200)
Binder type	67-22
Mean annual air temperature, °F	60
Effective binder content, % by volume	12
Air void content, % by volume	7
Initial fracture energy, Kpa	2
Fracture energy aging parameter	3

Figure 2-32 shows the one-year temperature profile at the surface of the AC layer in the Washington D.C. area generated from the EICM. The first day shown in the figure corresponds to July 1st of the year. As an illustration, Figure 2-33 shows the estimated dynamic modulus at year one based on the temperature profile in Figure 2-32. The stiffness was calculated at a load frequency of 10 Hz (i.e., loading time 0.1 s).

The variation of FE limit, DCSE limit, tensile strength and maximum healing potential with age (and depth) are given in Figure 2-34.

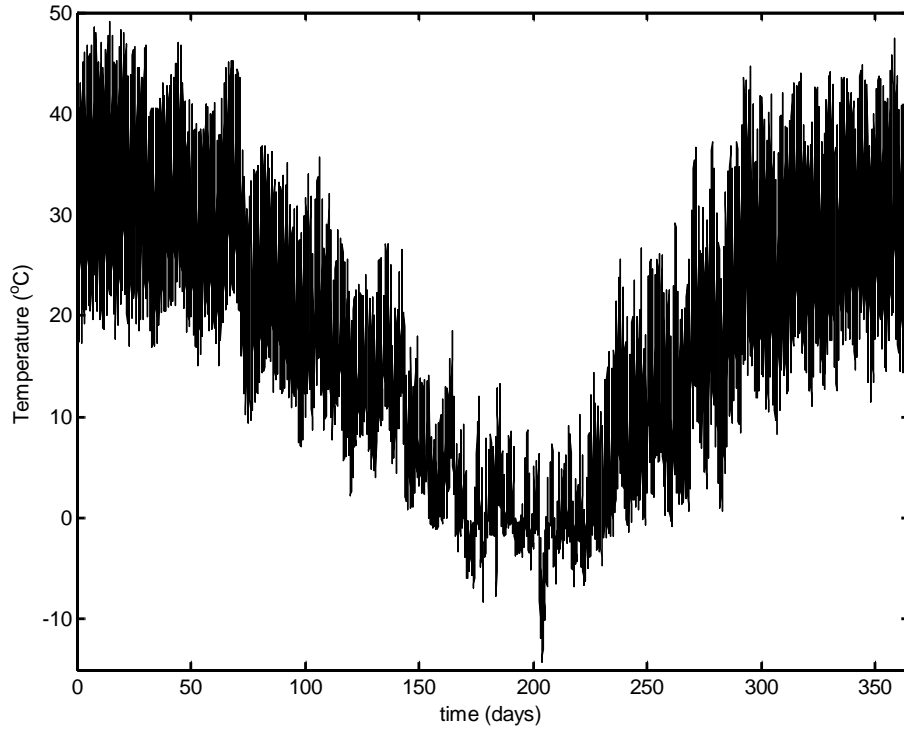


Figure 2-32. One-year temperature profile at the pavement surface (Washington D.C.)

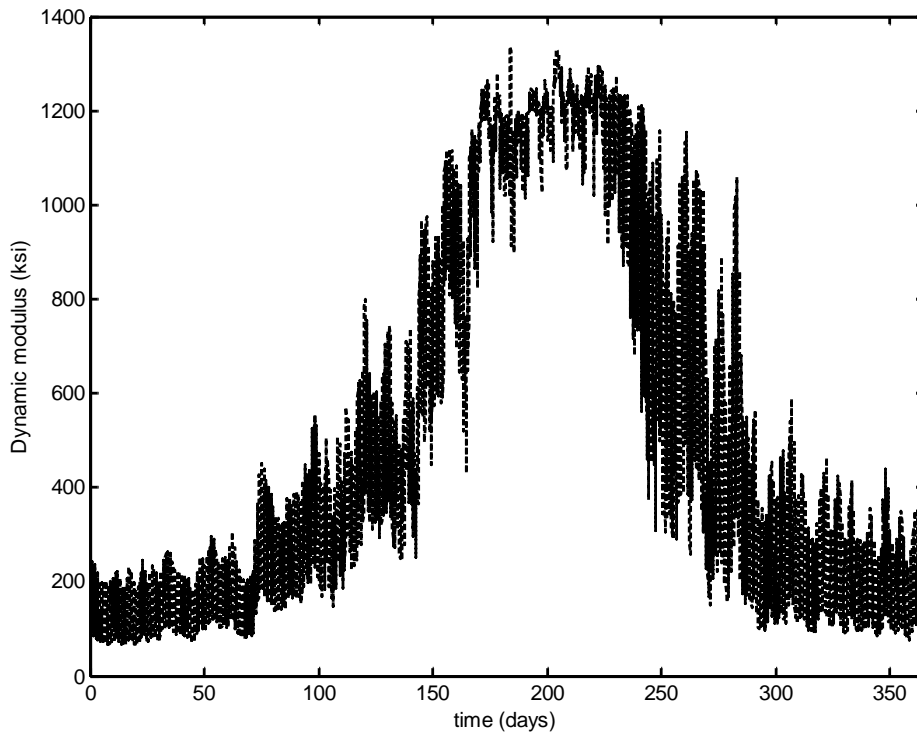


Figure 2-33. Variation of AC stiffness with time

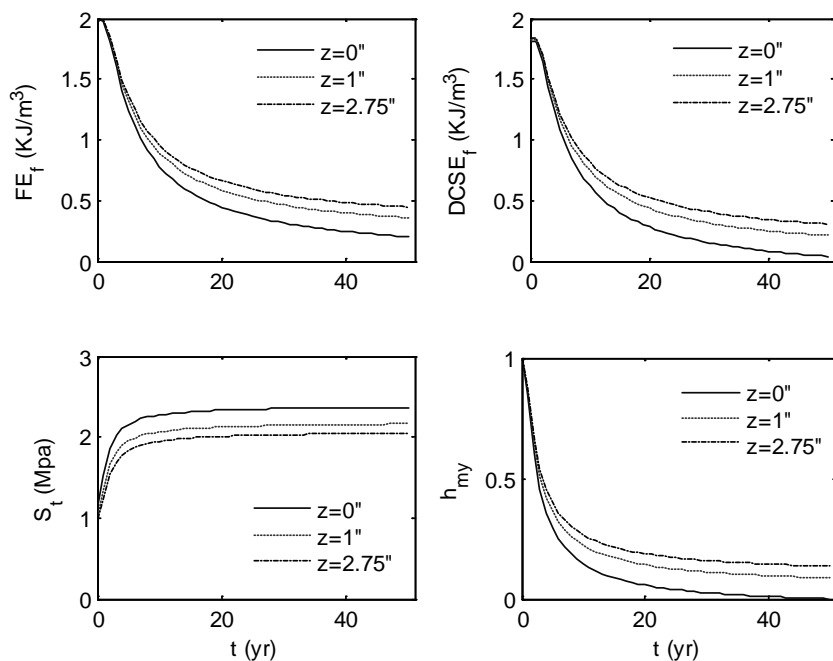


Figure 2-34. Variation of fracture and healing properties with age (and depth)

B.3.2.3 Traffic information

The pavement section was assumed to be subjected to 18 kip single axle wheel load at a rate of 100 cycles per hour, which is equivalent to 17.5 million ESALs per 20 years.

B.3.2.4 Model predictions without thermally induced damage

In this section, predictions for crack initiation and propagation in the pavement section were made without activation of the thermal response model.

Stage one: crack initiation

Figure 2-35 gives the results of load induced damage accumulation versus time during Year 12. As shown, crack initiation occurred in early October of that Year. The total load passes leading to crack initiation is about 9.9 million ESALs, which were obtained by adding the load passes predicted in Year 12, i.e., 223,700 to the product of the yearly traffic (i.e., 0.876 million ESALs) and 11 (meaning the past 11 years).

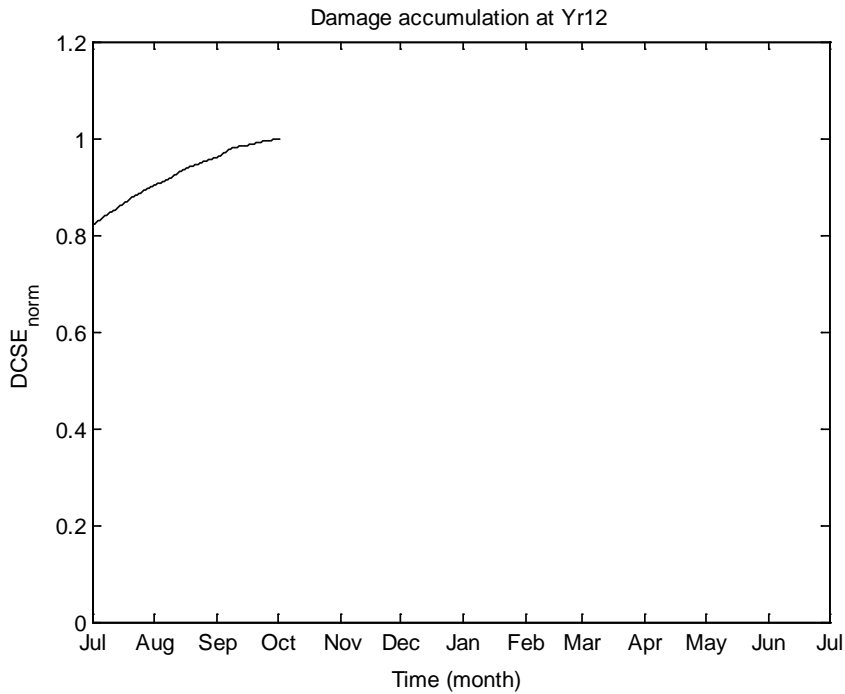


Figure 2-35. Prediction of crack initiation w/o thermally induced damage

Stage two: crack propagation

The predicted crack propagation without thermally induced damage is shown in Figure 2-36. It started at a slow rate for the first few zones. Subsequently, it sped up and maintained a faster rate until it reached the critical crack depth (i.e., 2.5 in for this case). The process took about 9.5 years.

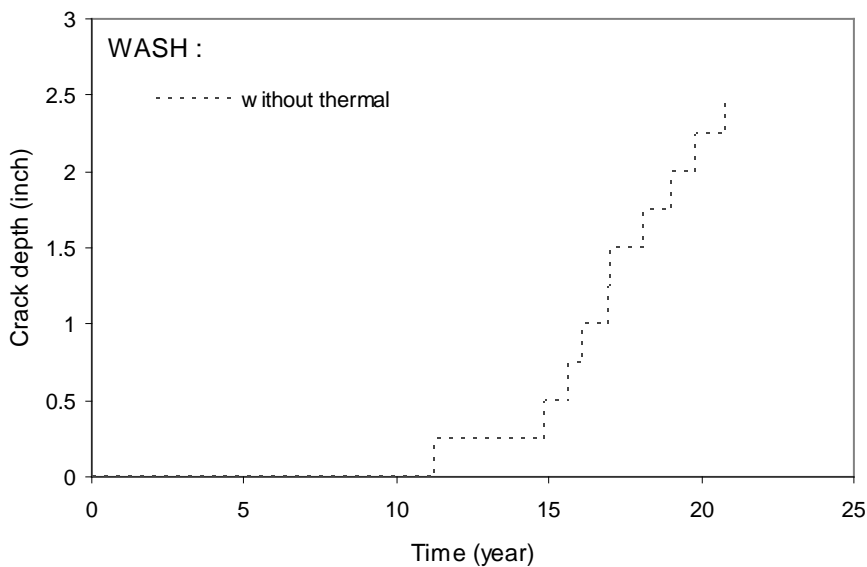


Figure 2-36. Prediction of crack propagation w/o thermally induced damage

B.3.2.5 Model predictions with thermally induced damage

Another set of predictions were made when both load and thermally induced damage were accounted in the performance model. The thermal effect on predicted cracking performance was then evaluated based on a comparison of these results with those of the prior section.

Stage one: crack initiation

Figure 2-37 gives the predicted thermal stresses at four depths of the AC layer using the thermal response model. As shown, the thermal stresses at any depth of the AC layer were almost negligible during warmer months (i.e., Jul. to Sep., and Apr. to Jun.), but they were kept at 10 psi during most of the cold times (i.e., the other half of the yearly period), during which significant amount of thermally induced damage can be generated. It can also be seen from the figure that thermal stresses decrease with depth.

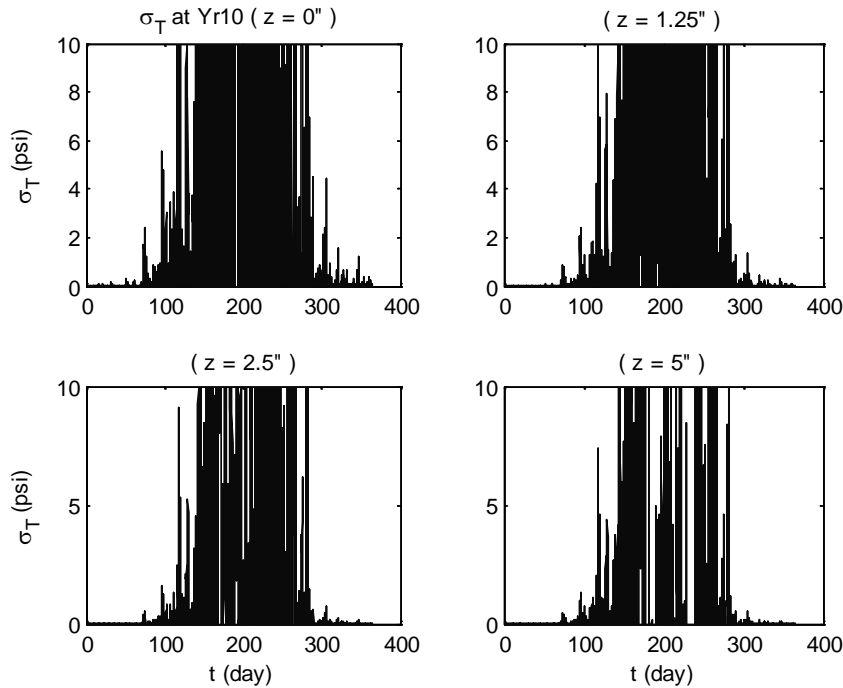


Figure 2-37. Predicted thermal stresses at four depths of AC layer during Year 10

The damage accumulation during Year 10 is shown in Figure 2-38. It can be seen that crack initiation occurred in early June of that Year. After accounting for loads applied in prior years, the total loads leading to crack initiation were about 8.7 million.

Stage two: crack propagation

Figure 2-39 shows the increment of crack depth with time when thermally induced damage was considered (refer to the solid line). Again, the crack propagated at a relatively low growth rate through the first few zones. It then accelerated until it reached the critical crack depth. The process took about 6.4 years. For comparison purpose, the prediction for crack depth versus time without considering thermally induced damage was also presented in the same figure (see the dashed line).

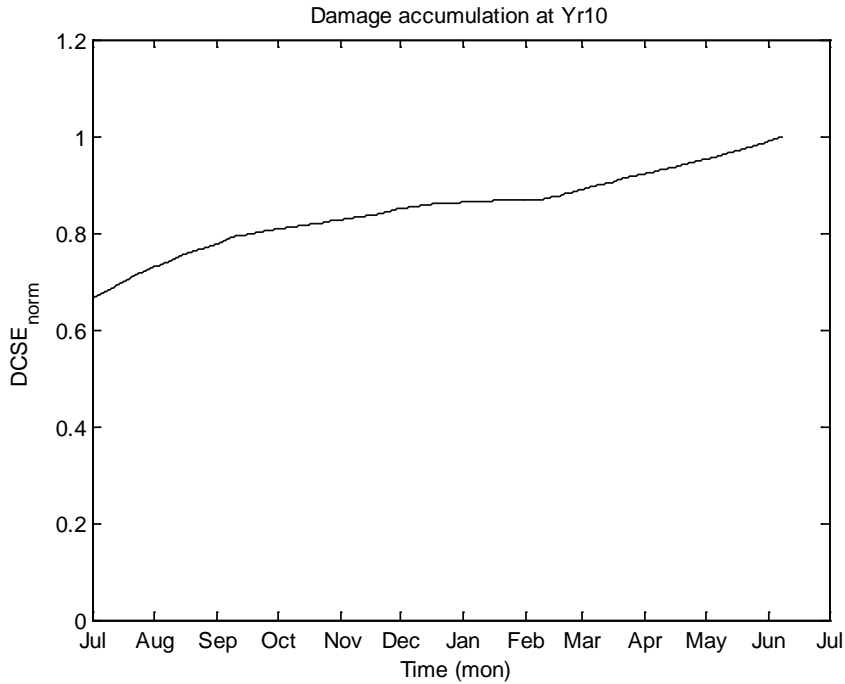


Figure 2-38. Prediction of crack initiation with thermally induced damage

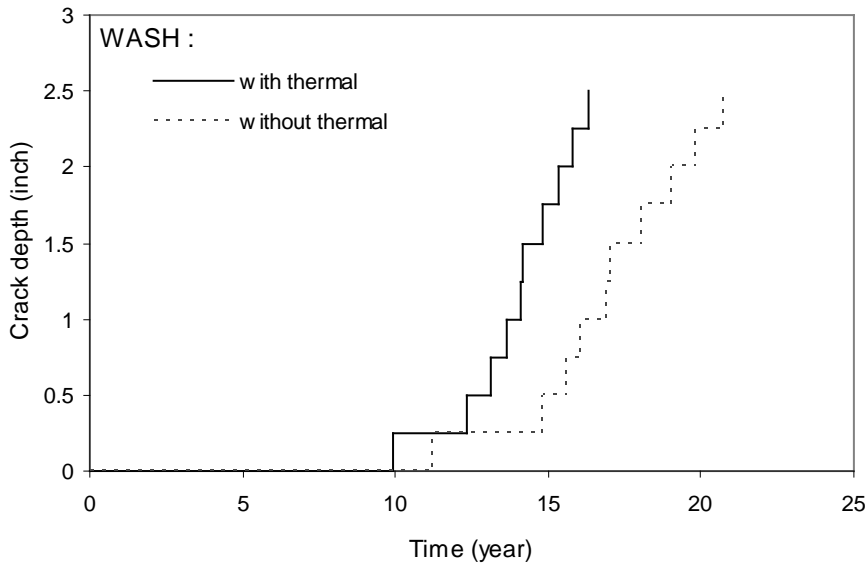


Figure 2-39. Prediction of crack propagation with and without thermally induced damage

Table 2-36 summarizes the predicted number of years (nyrs) and number of load passes (npas) leading to crack initiation, and location of the initial crack (xs) for two conditions: (a) with and (b) without thermally induced damage. It can be seen that without accounting for thermally induced damage, an additional 1.4 years or 1.2 million loads are needed to see

cracking in this pavement. Clearly, the thermal effect cannot be ignored for accurate prediction of crack initiation.

Table 2-36. Thermal effect on crack initiation

WASH	nyrs	npas ($\times 10^6$)	xs (in.)
a: with thermal	9.9	8.7	27.5
b: without thermal	11.3	9.9	27.5

Table 2-37 summarizes the predicted number of years (nyrs), number of load passes (npas), and total increment of crack depth (Δa) for these two conditions during the crack propagation stage.

Table 2-37. Thermal effect on crack propagation

WASH	nyrs	npas ($\times 10^6$)	Δa (in.)
a: with thermal	6.4	5.6	2.25
b: without thermal	9.5	8.3	2.25

Without thermally induced damage, an additional 3.1 years or 2.7 million loads are required to complete the propagation stage. Therefore, the importance of incorporation of thermally induced damage in crack propagation was also emphasized. It is noted that the time for crack initiation will affect the propagation time, since FE limit (DCSE limit) reduces with age. For example, if the FE limit of Year 10 (when crack initiation was identified under condition (a)) was used as the starting FE value for predicting crack propagation under condition (b), additional time or loads are expected.

In summary, predicted top-down cracking performance of one pavement section in the Washington D.C. area was compared for two different conditions: with and without thermally induced damage. Based on the comparison for both crack initiation and propagation, it was found that thermal effect is important for an accurate prediction. Therefore, it is necessary to incorporate the thermal response model into the performance model. The results also indicated

that the FE limit (DCSE limit) aging model played an important role in determining the time of crack initiation and the average crack grow rate.

B.4 Creep Compliance Master Curves from the SuperPave IDT

The creep compliance master curves in the form of power law determined based on SuperPave IDT tests are presented in Figures 2-40 to 2-45.

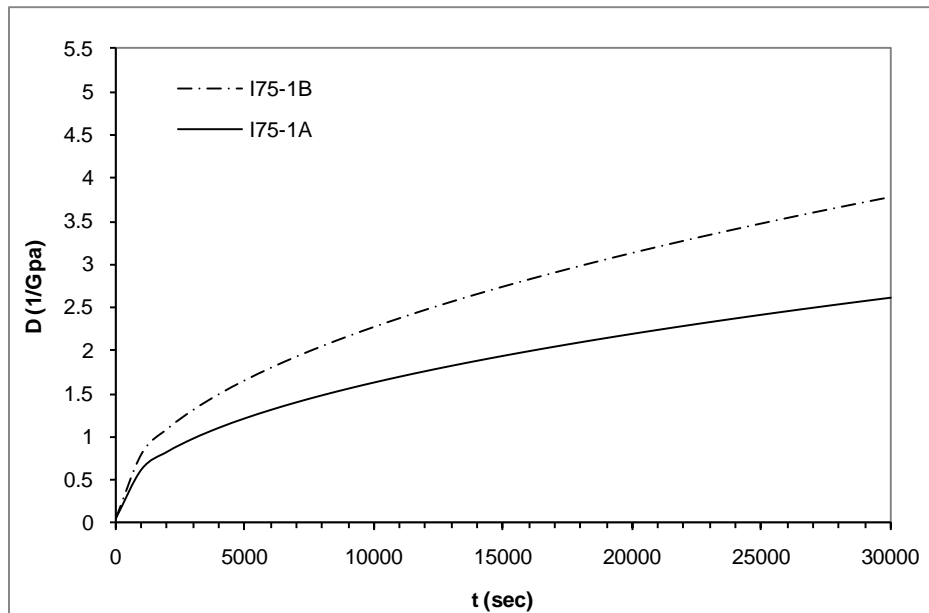


Figure 2-40. Sections I75-1A and I75-1B: Crack Rating History and Crack Initiation Time

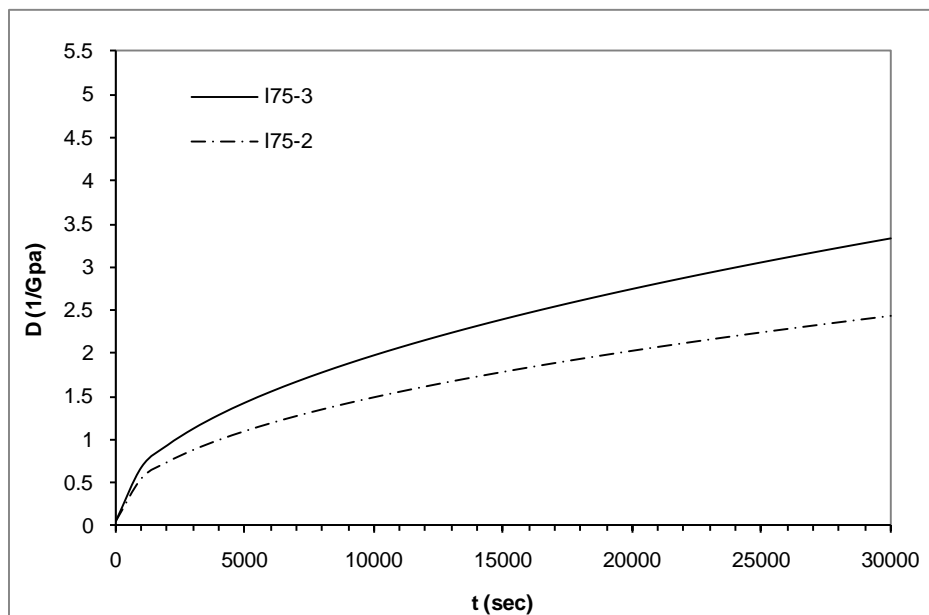


Figure 2-41. Creep compliance master curves for cores from Sections I75-2 and I75-3

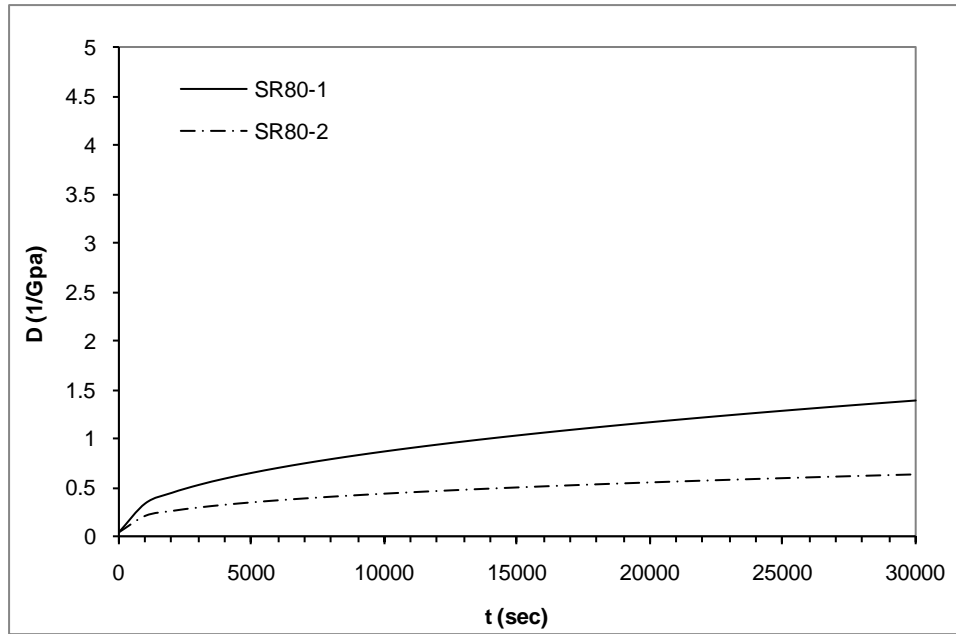


Figure 2-42. Creep compliance master curves for cores from Sections SR80-1 and SR80-2

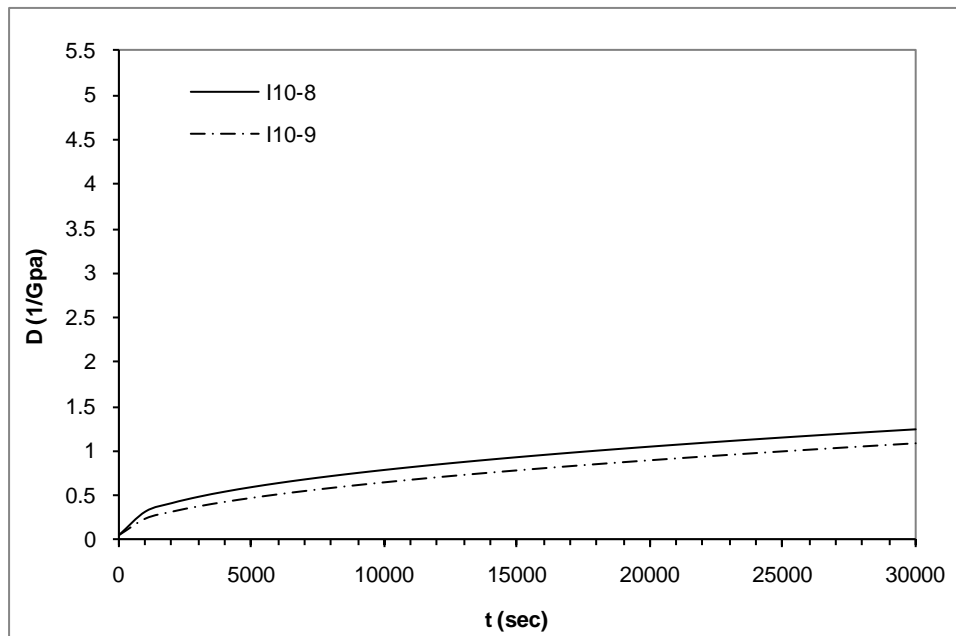


Figure 2-43. Creep compliance master curves for cores from Sections I10-8 and I10-9

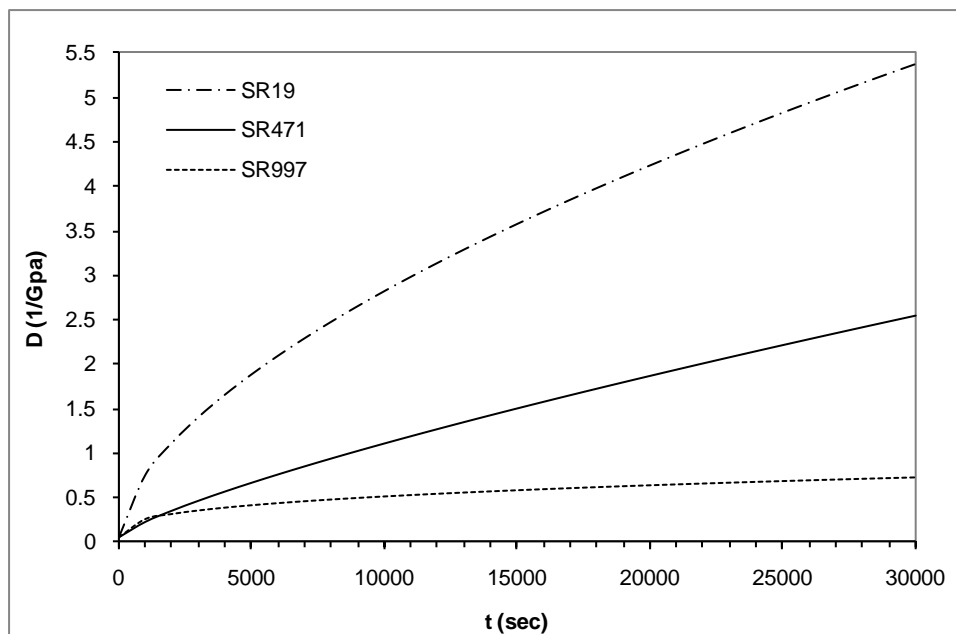


Figure 2-44. Creep compliance master curves for cores from Sections SR471, SR19 and SR997

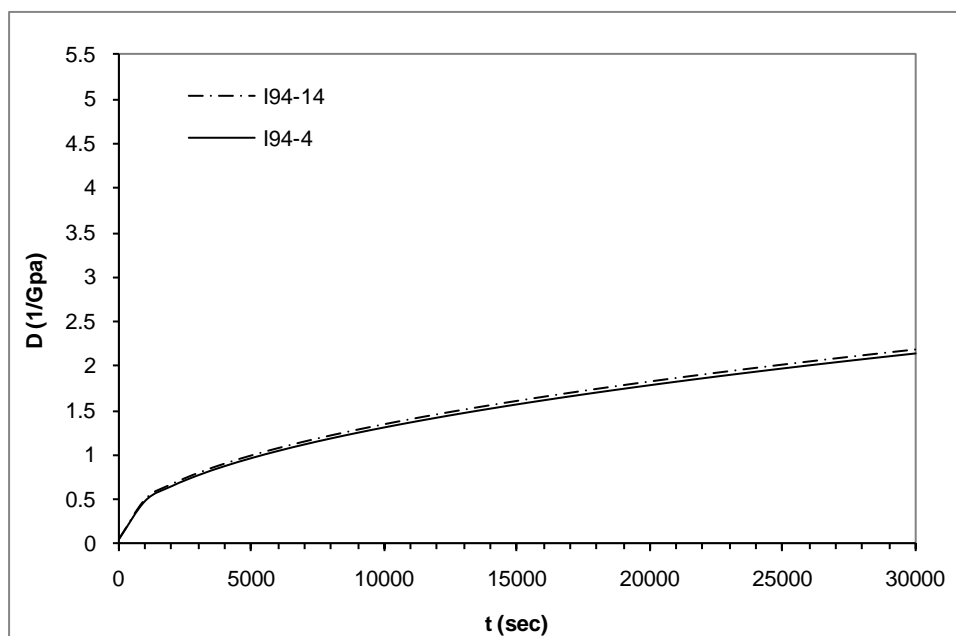


Figure 2-45. Creep compliance master curves for cores from Section I94-4 and I94-14

B.5 Determination of Crack Initiation Time

The crack initiation time for each of the eleven Florida sections (see Table 2-38) was determined on the basis of crack rating history (see Figures 2-46 to 2-51) obtained from the flexible pavement condition survey database maintained by the Florida Department of Transportation (FDOT) (37) and observations from our visits to the field sections in 2003. The approach taken was described as follows:

- Data evaluation:
 - The crack rating is a pavement performance parameter used by the FDOT to monitor cracking development in the field. The index value starts from 10 (indicating no cracking) and reduces to 0 with increasing severity of cracking. Due to the inherent inaccuracy of crack measurements and the uncertainty in relating reported crack measurements to specific amounts of top-down cracking, the crack rating history was only suitable for use in determining crack initiation.
 - The observed cracking status at the time of our visits to field sections (see also Table 2-38) can serve as an independent data point to make confirmation with the crack rating data.
- Threshold determination: a crack rating of 8 was determined to be the threshold for crack initiation.
- Crack initiation determination: in general, the onset of cracking for each pavement section can be determined using the threshold. For cases in which crack initiation was not possible within the range of available data, linear extrapolation was used.

Table 2-38. Top-down cracking initiation time

Section No	Section Code	Year Opened	Cracking Status* (at time of visit)	Crack Initiation Time (year)
1	I75-1A	1988	C	10
2	I75-1B	1989	C	12
3	I75-3	1988	C	11
4	I75-2	1989	U	17
5	SR80-1	1987	C	13
6	SR80-2	1984	U	22
7	I10-8	1996	C	8
8	I10-9	1996	C	8
9	SR471	2000	C	2
10	SR19	2000	C	1
11	SR997	1963	C	38

* C stands for cracking; U stands for no cracking.

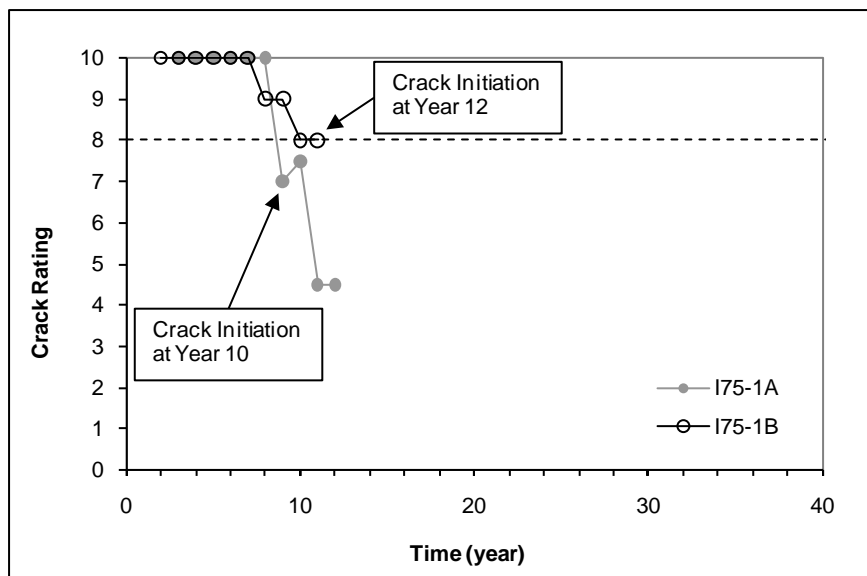


Figure 2-46. Sections I75-1A and I75-1B: Crack Rating History and Crack Initiation Time

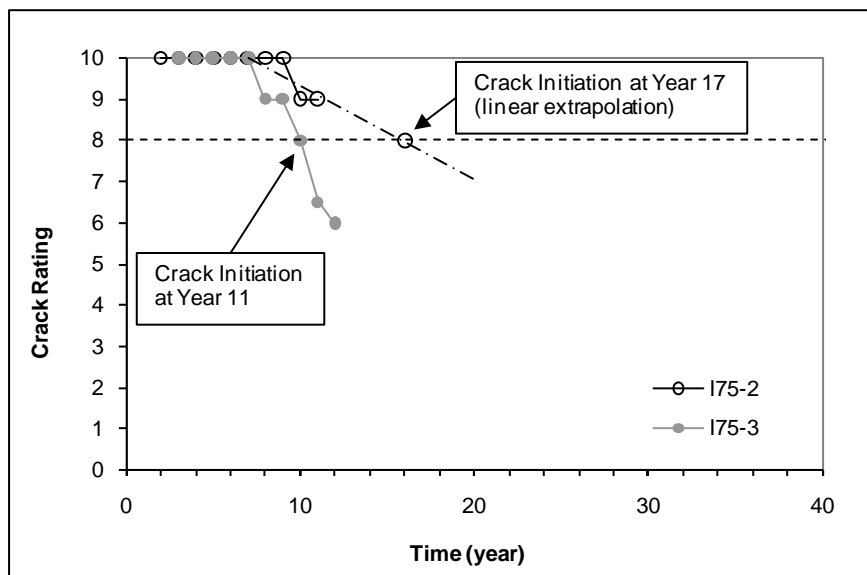


Figure 2-47. Sections I75-2 and I75-3: Crack Rating History and Crack Initiation Time

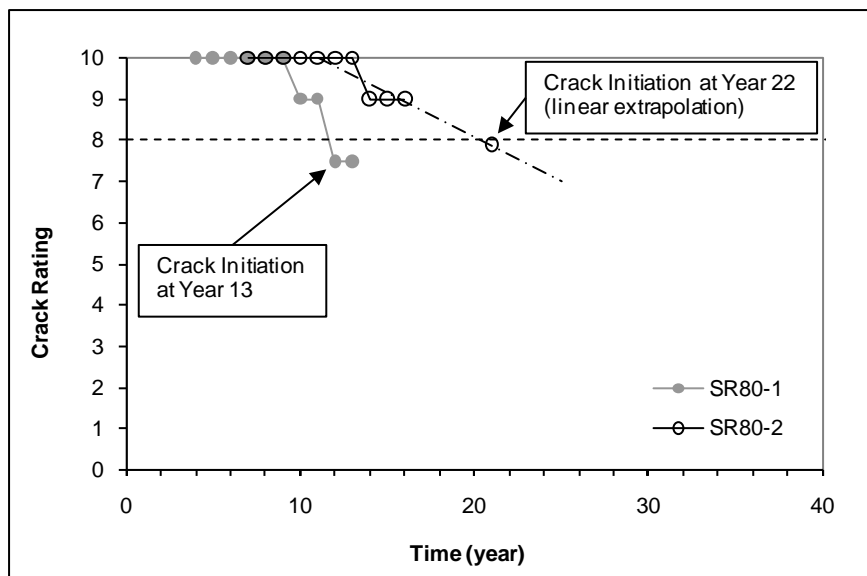


Figure 2-48. Sections SR80-1 and SR80-2: Crack Rating History and Crack Initiation Time

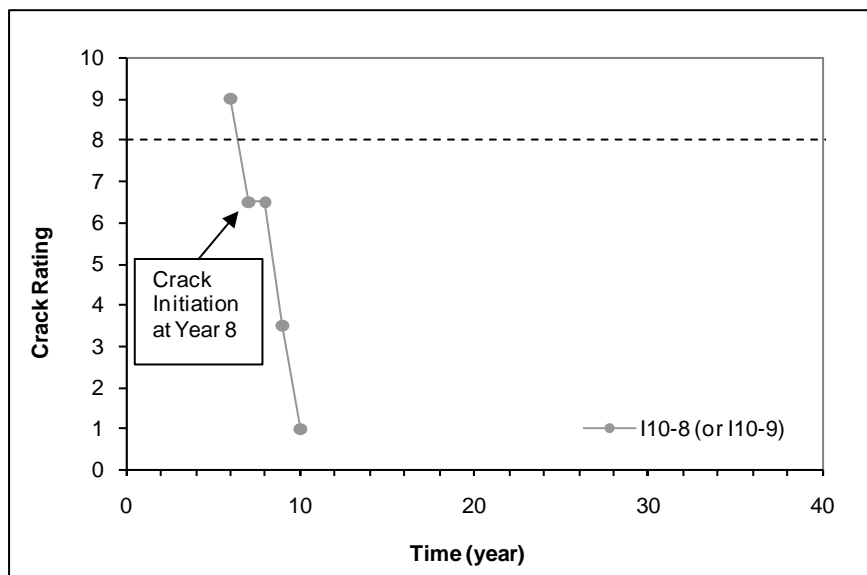


Figure 2-49. Sections I10-8 and I10-9: Crack Rating History and Crack Initiation Time

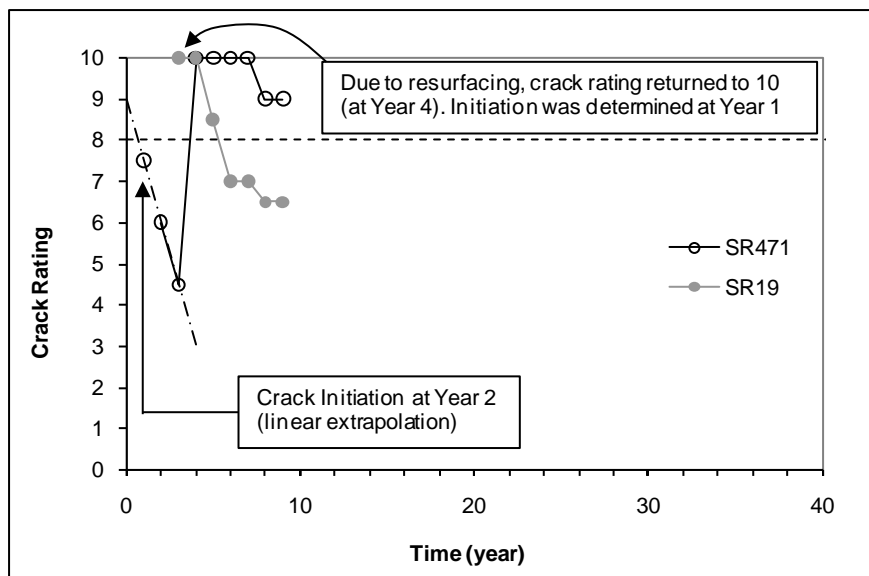


Figure 2-50. Sections SR471 and SR19: Crack Rating History and Crack Initiation Time

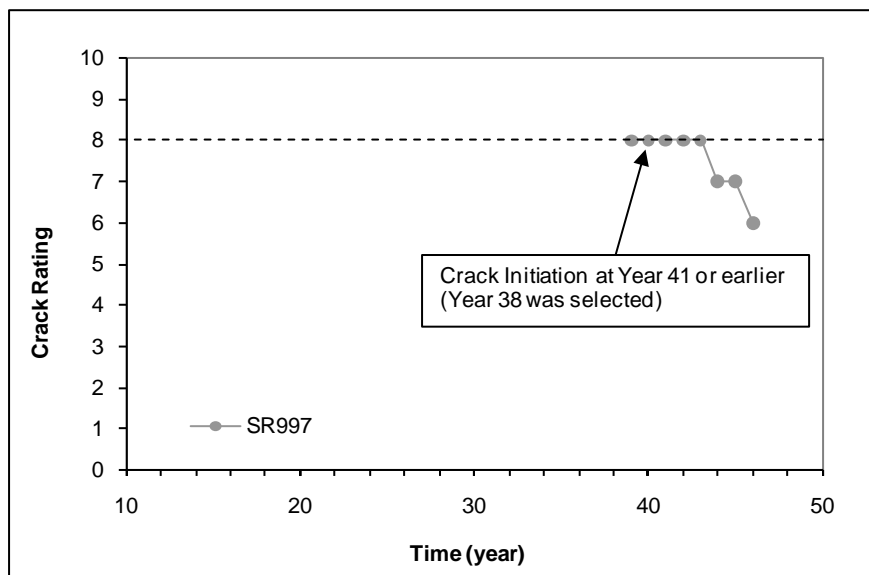


Figure 2-51. Section SR997: Crack Rating History and Crack Initiation Time

B.6 List of References

1. Zhang, Z., R. Roque, B. Birgisson, and B. Sangpetngam. Identification and Verification of a Suitable Crack Growth Law. *Journal of the Association of Asphalt Paving Technologists*, Vol. 70, 2001, pp. 206-241.
2. Roque, R., B. Birgisson, B. Sangpetngam, and Z. Zhang. Hot Mix Asphalt Fracture Mechanics: A Fundamental Crack Growth Law for Asphalt mixtures. *Journal of the Association of Asphalt Paving Technologists*, Vol. 71, 2002, pp. 816-827.
3. Sangpetngam, B., B. Birgisson, and R. Roque. Development of Efficient Crack Growth Simulator Based on Hot-mix Asphalt Fracture Mechanics. In *Transportation Research Record: Journal of the Transportation Research Board, No. 1832*, Transportation Research Board of the National Academies, Washington, D.C., 2003, pp. 105-112.
4. Sangpetngam, B., B. Birgisson, and R. Roque. Multilayer Boundary-element Method for Evaluating Top-down Cracking in Hot-mix Asphalt Pavements. In *Transportation Research Record: Journal of the Transportation Research Board, No. 1896*, Transportation Research Board of the National Academies, Washington, D.C., 2004, pp. 129-137.
5. Roque, R., B. Birgisson, C. Drakos, and B. Dietrich. Development and Field Evaluation of Energy-Based Criteria for Top-down Cracking Performance of Hot Mix Asphalt. *Journal of the Association of Asphalt Paving Technologists*, Vol. 73, 2004, pp. 229-260.
6. Kim, J., R. Roque, and B. Birgisson. Integration of Thermal Fracture in the HMA Fracture Model. *Journal of the Association of Asphalt Paving Technologists*, Vol. 77, 2008, pp. 631-662.
7. Mirza, M. W., and M. W. Witzak. Development of a Global Aging System for Short and Long Term Aging of Asphalt Cements. *Journal of the Association of Asphalt Paving Technologists*, Vol. 64, 1995, pp. 393-430.
8. ARA, Inc., *Guide for Mechanistic-Empirical Design of New and Rehabilitated Pavement Structures*. Final Report - NCHRP Project 1-37A. National Cooperative Highway Research Program, Transportation Research Board, Washington, D.C., 2004.
9. Witzak, M. W., and O. A. Fonseca. Revised Predictive Model for Dynamic (Complex) Modulus of Asphalt Mixtures. In *Transportation Research Record: Journal of the Transportation Research Board, No. 1540*, Transportation Research Board of the National Academies, Washington, D.C., 1996, pp. 15-23.
10. Deme, I. J., and F. D., Young. Ste. Anne Test Road Revisited Twenty Years Later. *Proceedings, Canadian Technical Asphalt Association*, Vol. 32, 1987, pp. 254-283.

11. Button, J. W., D. N. Little, Y. Kim, and J. Ahmed. Mechanistic Evaluation of Selected Asphalt Additives. *Journal of the Association of Asphalt Paving Technologists*, Vol. 56, 1987, pp. 62-90.
12. Zhang, Z. *Identification of Crack Growth Law for Asphalt Mixtures Using the Superpave Indirect Tensile Test (IDT)*. PhD Dissertation. University of Florida, Gainesville, 2000.
13. Daniel, J. S., and Y. R. Kim. Laboratory Evaluation of Fatigue Damage and Healing of Asphalt Mixtures. *ASCE Journal of Materials in Civil Engineering*, Vol. 13, No. 6, 2001, pp. 434-440.
14. Kim, B., and R. Roque. Evaluation of Healing Property of Asphalt Mixture. In *Transportation Research Record: Journal of the Transportation Research Board, No. 1970*, Transportation Research Board of the National Academies, Washington, D.C., 2006, pp. 84-91.
15. Si, Z., D. N. Little, and R. L. Lytton. Characterization of Microdamage and Healing of Asphalt Concrete Mixture. *ASCE Journal of Materials in Civil Engineering*, Vol. 14, No.6, 2002, pp. 461-470.
16. Kim, Y. R., D. N. Little, and R. L. Lytton. Fatigue and Healing Characterization of Asphalt Mixtures. *ASCE Journal of Materials in Civil Engineering*, Vol. 15, No.1, 2003, pp. 75-83.
17. Buttlar, W. G., R. Roque, and B. Reid. Automated Procedure for Generation of Creep Compliance Master Curve for Asphalt Mixtures. In *Transportation Research Record: Journal of the Transportation Research Board, No. 1630*, Transportation Research Board of the National Academies, Washington, D.C., 1998, pp. 28-36.
18. Hiltunen, D. R., and R. Roque. A Mechanics-Based Prediction Model for Thermal Cracking of Asphaltic Concrete Pavements. *Journal of the Association of Asphalt Paving Technologists*, Vol. 63, 1994, pp. 81-117.
19. Park, S. W., and Y. R. Kim. Interconversion between Relaxation Modulus and Creep Compliance for Viscoelastic Solids. *ASCE Journal of Materials in Civil Engineering*, Vol. 11, No. 1, 1999, pp. 76-82.
20. Park, S. W., and Y. R. Kim. Fitting Prony-series Viscoelastic Models with Power-law Presmoothing. *ASCE Journal of Materials in Civil Engineering*, Vol. 13, No. 1, 2001, pp. 26-32.
21. Roque, R., A. Guarin, G. Wang, J. Zou, and H. Mork. *Develop Methodologies/Protocols to Assess Cracking Potential of Asphalt Mixtures Using Accelerated Pavement Testing*. Final Report, FDOT-BD545-49, University of Florida, Gainesville, 2007.

22. Sangpetngam, B. *Development and Evaluation of a Viscoelastic Boundary Element Method to Predict Asphalt Pavement Cracking*. PhD Dissertation. University of Florida, Gainesville, 2003.
23. Myers, L. A., R. Roque, and B. Birgisson. Use of Two-dimensional Finite Element Analysis to Represent Bending Response of Asphalt Pavement Structures. *International Journal of Pavement Engineering*, Vol. 2, 2001, pp. 201-214.
24. *Flexible Pavement Condition Survey Handbook*. State Materials Office, Florida Department of Transportation, 2003.

APPENDIX C. SIMULATION TOOLS

TABLE OF CONTENTS

	<u>page</u>
TABLE OF CONTENTS.....	C-ii
APPENDIX	
C SIMULATION TOOLS.....	C-1
C.1 Simulation Tools for the VECD-Based Model.....	C-1
C.2 Simulation Tools for the HMA-FM-Based Model	C-2
C.2.1 Instructions regarding Use	C-3
C.2.1.1 Installation of the simulation package	C-3
C.2.1.2 Crack initiation simulation (CIS)	C-4
C.2.1.3 Crack growth simulation (CGS).....	C-4

CHAPTER 3 SIMULATION TOOLS

C.1 Simulation Tools for the VECD-Based Model

The VECD-based model was programmed in C++ and compiled using Microsoft Visual Studio. The resulting product, named the VECD-FEP++ (or simply FEP++) simulation package, allows the evaluation of top-down cracking mechanisms and the prediction of crack initiation. This simulation package has been compressed into one installer file, i.e., 'FEP++.exe', and stored in a CD entitled "Simulation Tools and Report Appendices for NCHRP Project 01-42A" (under the directory: CD_NCHRP1-42A\1.VECD\).

The FEP++ can be installed in the target machine by double-clicking the installer file, which will launch the installation wizard. The wizard then guides the rest of the installation procedure. Once the installation is completed successfully, an entry for the FEP++ should appear in the Start Menu of Windows. At the same time, a folder named FEP++ should appear under the installation directory which includes:

- doc (Word help files)
 - FEP++_Manual.doc
 - Tutorial to Run the Examples.doc
- Example (example database files)
 - Four sub-folders, each of which includes an example
 - One output sub-folder (output files for all example cases)
- FEP++ (finite element engine)
- images (bitmap and icon files)
- default (default database file)
- Gui.exe (preprocessor GUI)
- license

- msvc70d.dll (and other dll-files)
- README

Information regarding the FEP++ program design and a demonstration of the data entry windows is provided in the 'FEP++ manual.doc' file. Detailed explanations for running FEP++ simulations are provided in the 'Tutorial to Run the Examples.doc' file. Both of these files are located in the "doc" folder of the installation directory.

In addition, a postprocessor must be installed in the target machine before launching the graphic user interface (GUI) of the FEP++, i.e., the preprocessor. Currently, Tecplot 360 (a trial version) is used as the postprocessor, which can be downloaded from the Tecplot website, i.e., <http://tecplot.com/>. The instructions to be followed for installation are provided on the website. Once the postprocessor is installed in the target machine successfully, the path to Tec360.exe should be <Tecplot_root>\Tec360 2009\bin (which must be verified in the PATH variable of the user's particular system). It should be noted that the Tecplot free trial version works for 14 days only.

C.2 Simulation Tools for the HMA-FM-Based Model

The HMA-FM-based model, after being integrated with the simplified crack initiation model, was programmed and compiled using the commercial software MATLAB (v7.0.4). The resulting product, named the enhanced HMA fracture mechanics (HMA-FM-E) simulation package, allows the prediction of top-down cracking initiation and propagation in HMA layers. The HMA-FM-E simulator is provided on the same CD as mentioned above (under the directory: CD_NCHRP1-42A\2.HMAFM\), including the following contents:

- An executive file, i.e., 'MCRInstaller.exe'. The MATLAB Compiler Runtime (MCR) is a standalone set of shared libraries that enable the execution of M-files. It provides complete support for all features of MATLAB without the MATLAB Graphical User Interface (GUI). Therefore, it is required to run 'MCRInstaller.exe' to install the MCR (v7.2) if it is not available in the target computer.

- A folder (named EHMAFM_Model) which was divided into following two sub-folders according to the specific function of each,
 - "CIS_Files", containing executable codes to perform crack initiation simulation.
 - "CGS_Files", including executable codes to simulate crack propagation.
- An MSWord file, i.e., 'Example Simulation.doc' which documented one example used to demonstrate the capabilities of the predictive model.
- A read-me file ('Readme.doc') explains how to install the MCR into the target machine if needed, and how to use the executable codes (placed in the EHMAFM_Model folder) to simulate the example problem documented in 'Example Simulation.doc'.

C.2.1 Instructions regarding Use

C.2.1.1 Installation of the simulation package

- Verify that 1) a MATLAB Compiler Runtime (MCR) is installed on the target computer, and 2) the installed version is 7.2.
- If any one of the above conditions is not satisfied, copy the 'MCRInstaller.exe' file to the target computer and install the MCR on the computer by double clicking the icon and then proceed as follows:
 - When the MATLAB Component Runtime startup screen appears, click Next to begin the installation.
 - The setup wizard starts. Click Next to continue.
 - The Select Installation Folder dialog lets you choose where you want to install the MCR. This dialog also lets you view available and required disk space on your system. You can also choose whether you want to install the MCR for just yourself or others. Select your options, and then click Next to continue.
 - Confirm your selections by clicking Next. The installation begins. The process takes some time due to the quantity of files that are installed.
 - When the installation completes, click Close on the Installation Completed dialog to exit.
- After the MCR is installed, add the MCR directory to the system path specified by the target system's environment variable.

On windows system:

Add the following pathname: <mcr_root>\v72\runtime\win32 to the PATH environment variable, by doing the following:

- Select the My Computer icon on your desktop.
- Right-click the icon and select Properties from the menu.
- Select the Advanced tab.

- Click Environment Variables.

Note: <mcr_root> is the directory where MCR is installed on the target machine. For example, it is C:\Program Files\MathWorks\MATLAB Component Runtime, if you choose the default location for installation.

- Copy the folder EHMAFM_Model directly to C drive.

C.2.1.2 Crack initiation simulation (CIS)

- Go to <EHAMFM root>, Click CIS_Files
(Note: <EHMAFM root> is the directory of C:\EHMAFM_Model\).
- Prepare Inputs. Go to CIS_Files\examples\ex1_i\input\, including two files:
 - tmpt.dat (data file for asphalt concrete layer temperatures)
 - Example1_I.xls (other information required for example 1, also refer to the doc-file: 'Example Simulation')
- Copy these two files back to <EHMAFM root>\CIS_Files\, and then make changes in them if necessary for your simulation purpose.
- Run 'CracInitSmuA.exe' (in DOS-mode, under <EHAMFM root>\CIS_Files\).
- After the simulation is completed, Find and Copy 'CIShistory.out' to <EHAMFM root>\CGS_Files\examples\ex1_p\input\, which will be used as one of the inputs for Crack Growth Simulation).

C.2.1.3 Crack growth simulation (CGS)

- Go to <EHAMFM root>, Click CGS_Files.
- Prepare Inputs. Go to CGS_Files\examples\ex1_p\input\, including three files:
 - tmpt.dat (data file for asphalt concrete layer temperatures)
 - Example1_P.xls (other information required for example 1, also refer to the doc-file: 'Example Simulation')
 - CIShistory.out
- Copy these files back to <EHMAFM root>\CGS_Files\, and then make changes in the first two files if necessary for your simulation purpose.
- Run 'CracGrowSmuA2.exe' (in DOS-mode, under <EHMAFM root>\CGS_Files\).
- After the simulation is completed, Save 'CGhistory.out' (and other outputs if necessary).